

Observation of CP Violation in the Neutral B Meson System^{*}

Stephen Levy

Stanford Linear Accelerator Center
Stanford University
Stanford, CA 94309

SLAC-Report-729

Prepared for the Department of Energy
under contract number DE-AC03-76SF00515

Printed in the United States of America. Available from the National Technical Information Service, U.S. Department of Commerce, 5285 Port Royal Road, Springfield, VA 22161.

^{*} Ph.D. Thesis, University of California, Santa Barbara

UNIVERSITY of CALIFORNIA
Santa Barbara

Observation of CP Violation in the Neutral B Meson System

A Dissertation submitted in partial satisfaction of the
requirements for the degree

Doctor of Philosophy
in
Physics

by

Stephen Levy

Committee in charge:

Professor Claudio Campagnari, Chair

Professor Harry Nelson

Professor Robert Sugar

September 2003

The dissertation of Stephen Levy is approved:

Chair

September 2003

This dissertation is dedicated to my mom and dad for their
unfailing support these last 28 years. All my love.

ACKNOWLEDGMENTS

Throughout my study of physics, I have had the good fortune to be guided and encouraged by many excellent teachers to whom I owe a debt of gratitude. I would like to thank Mr. Berryann for opening my eyes to the world of physics; Dr. Gilfoyle for inspiring me to become a physicist; and Dr. Rubin for demonstrating the integrity required to fulfill that goal. Most importantly, I'd like to thank my adviser Claudio Campagnari for teaching me what it means to be a physicist. His wisdom and assistance have been invaluable.

There were days and late nights when the pressure of producing a timely $\sin 2\beta$ result (you mean we're publishing *again*) was intense. But the spirits of the "sin2 β crew" were always cheerful and they were a fantastic group to work with. Thanks to Riccardo, David, Fernando, and Söeren. Special thanks to Owen and Wouter for taking so much time to teach me and for never tiring of my questions. And also to Shahram for his dual role of co-worker and friend.

Also thanks to my many officemates through the years, Kevin, Bryan, Natalia, and most recently Adam and Tae, for putting up with my voluminous insane ravings.

I have had some great friends and roommates during my graduate school years, which began with Brookie breaking and entering and ended with him egg-kicking (they can't be cracked if you squeeze from the poles, I swear). I am especially grateful to have mastered his elegant polytheistic theory of religious begging. The days at Quinientos with Hilah, (begin deep Southern accent) Hemingway (end accent), and Pandora were unforgettable (Feb. 14 Day cat omission was not an oversight). As was my initiation to the world of Mudders provided by fresh Doug F. (on the steel horse I ride). Lots of fun times with J. Murray in the ghetto (man, your room is cold). And too many good memories of Courtney C. during the SF years (dummy seeking to be what?). The La Bamba (ZZZ) girls, L.S. and T.I., have made the final stretch an adventure even if their house escapes the glorious egging crescendo I've predicted for these

many months.

Grandma Levy and Grandma Roy provided me with excellent modes of transportation and much love for which I am extremely thankful.

Finally, I must thank my parents. The love and support they have provided has allowed me to pursue my dreams. For this I will be forever grateful. Their faith in me has remained unshakable despite some infamous incidents in my youth (think mailbox) and that faith has kept me steady through darker moments than I've admitted to. They remain always in my heart.

Curriculum Vitæ

Stephen Levy

Education

Doctor of Philosophy in Physics, University of California Santa Barbara (UCSB), California, June 2003 (expected)

Bachelor of Science in Physics and Math, University of Richmond (UR), Richmond, VA, May 1997 (*Magna cum laude*)

Professional Employment

UCSB Research Assistant, Member of BABAR collaboration at the Stanford Linear Accelerator Center (Summer 1998-Present)

UCSB Teaching Assistant, Graduate Particle Physics (Fall 2002-Winter 2002)

UCSB Teaching Assistant, Physics for Majors (Winter 1999-Spring 2000)

Primary Publications

B. Aubert *et al.* [BABAR Collaboration], “Measurement of the CP-violating asymmetry amplitude $\sin 2\beta$,” *Phys. Rev. Lett.* **89**, 201802 (2002).

B. Aubert *et al.* [BABAR Collaboration], “A study of time dependent CP-violating asymmetries and flavor oscillations in neutral B decays at the Upsilon(4S),” *Phys. Rev. D* **66**, 032003 (2002).

B. Aubert *et al.* [BABAR Collaboration], “Observation of CP violation in the B₀ meson system,” *Phys. Rev. Lett.* **87**, 091801 (2001).

B. Aubert *et al.* [BABAR Collaboration], “Measurement of CP violating asymmetries in B₀ decays to CP eigenstates,” *Phys. Rev. Lett.* **86**, 2515 (2001).

G. P. Gilfoyle, S. Levy, and M. Mestayer, “Spatial resolution of the nose cone prototype drift chamber”, CLAS-Note-96-009 (1997).

Awards

GANN Fellowship recipient, UCSB (1998)

Phi Beta Kappa, UR (1997)

R. Loving Award, most promising graduating physics major, UR (1997)

Sigma Xi, scientific research society (1997)

Pi Mu Epsilon, mathematics honor society (1996)

Sigma Pi Sigma, physics honor society (1996)

National Merit Finalist, UR (1993)

Varsity Tennis Scholarship, UR (1993)

Abstract

Observation of CP Violation in the Neutral B Meson System

by

Stephen Levy

This dissertation presents a measurement of time-dependent CP -violating asymmetries in neutral B meson decays collected with the *BABAR* detector at the PEP-II asymmetric-energy B Factory at the Stanford Linear Accelerator Center. The data sample consists of about 88 million $\Upsilon(4S) \rightarrow B\bar{B}$ decays collected between 1999 and 2002. We study events in which one neutral B meson decay to the CP -eigenstates $J/\psi K_S^0$, $\psi(2S)K_S^0$, $\chi_{c1}K_S^0$, and $\eta_c K_S^0$, or to flavor-eigenstates involving $D^{(*)}\pi/\rho/a_1$ and $J/\psi K^{*0}$ ($K^{*0} \rightarrow K^+ \pi^-$), is fully reconstructed. The flavor of the other neutral B meson is tagged at the time of its decay, mainly using the charge of identified leptons and kaons. The proper time elapsed between the meson decays is determined by measuring the distance between the decay vertices. The amplitude of the CP -violating asymmetry, which in the Standard Model is proportional to $\sin 2\beta$, is determined from a simultaneous maximum-likelihood fit to the time-difference distribution of the flavor- and CP -eigenstate samples. We measure $\sin 2\beta = 0.755 \pm 0.074$ (stat) ± 0.030 (syst).

Contents

List of Figures	xiv
List of Tables	xviii
1 <i>CP</i> violation in the Standard Model	1
1.1 The Standard Model	3
1.2 Parity, charge conjugation, and time reversal	5
1.3 <i>CP</i> violation and cosmology	6
1.4 Discovery of <i>CP</i> violation	8
1.4.1 Experimental confirmation of <i>CP</i> violation	9
1.4.2 Theoretical model for <i>CP</i> violation	10
1.5 The CKM matrix	11
1.5.1 Higgs mechanism origin	11
1.5.2 Parameter counting	13
1.5.3 CKM parameterization	14
1.5.4 Unitarity triangle	15
1.6 Manifestations of <i>CP</i> violation	17
1.6.1 <i>CP</i> violation in decay	18
1.6.2 Mixing of neutral mesons	19
1.6.3 <i>CP</i> violation in mixing	22
1.6.4 Time evolution of neutral mesons	22
1.6.5 Mixing phenomenology in the B^0 system	23
1.6.6 <i>CP</i> violation in mixing and decay	26
1.7 The golden decay $B^0 \rightarrow J/\psi K_S^0$	29
1.7.1 Evaluating $\lambda_{J/\psi K_S^0}$	29
1.8 Measuring <i>CP</i> violation at <i>BABAR</i>	33
1.8.1 Coherent B meson production at the $\Upsilon(4S)$	33
1.8.2 Experimental challenges	35
1.9 Constraints on the unitarity triangle	37
1.10 Previous measurements of $\sin 2\beta$	41

2	The <i>BABAR</i> detector	43
2.1	PEP-II	43
2.2	<i>BABAR</i> detector overview	50
2.3	Silicon vertex tracker	53
2.3.1	SVT geometry	53
2.3.2	Silicon sensors	56
2.3.3	Front end electronics	57
2.3.4	Alignment	58
2.3.5	Performance	60
2.4	Drift chamber (DCH)	61
2.4.1	DCH design	62
2.4.2	DCH performance	64
2.5	Detector of internally reflected Cherenkov light (DIRC)	66
2.5.1	DIRC geometry	67
2.5.2	DIRC performance	68
2.6	Electromagnetic calorimeter (EMC)	69
2.6.1	EMC layout	69
2.6.2	EMC performance	71
2.7	Instrumented flux return (IFR)	75
2.7.1	IFR overview	75
2.7.2	IFR performance	76
3	Analysis overview	79
3.1	Analysis outline	82
3.2	Additional <i>CP</i> modes	82
4	Reconstruction of <i>B</i> mesons	85
4.1	Track and neutral reconstruction	86
4.2	Particle identification	87
4.2.1	Charged lepton identification	88
4.2.2	Kaon identification	90
4.2.3	Event selection	92
4.3	Reconstruction of decay daughters	94
4.3.1	Selection of π^0 mesons	95
4.3.2	Selection of K_S^0 mesons	95
4.3.3	Selection of ρ , a_1^+ , and K^{*0} mesons	96
4.3.4	Charmonium meson selection	96
4.3.5	Charmed meson selection	102
4.4	<i>B</i> meson reconstruction	104
4.4.1	Helicity definition	106
4.4.2	Thrust definition	108

4.5	Reconstructing decays to CP eigenstates	108
4.5.1	Peaking backgrounds for the CP sample	109
4.6	Reconstructing decays to flavor-eigenstates	112
4.6.1	Peaking backgrounds for the B_{flav} sample	113
4.7	Reconstructing charged B decay control samples	115
5	Flavor tagging	117
5.1	Importance of tagging	117
5.2	Sources of B flavor information	119
5.2.1	Lepton tags	119
5.2.2	Kaon tags	121
5.2.3	Soft pion tags	123
5.3	Tagging algorithm	124
5.4	Performance of the tagging algorithm	126
6	Time difference measurement	129
6.1	Reconstruction of B_{rec} vertex	129
6.2	Reconstruction of B_{tag} vertex and Δz	130
6.3	Converting Δz to Δt	133
6.4	Resolution function	135
6.5	Vertexing checks	139
6.5.1	Comparison of CP and flavor-eigenstate samples	139
6.5.2	Vertex resolution in the vertical direction	141
6.6	Vertex resolution in continuum events	143
7	Fit method	147
7.1	Maximum-likelihood fit	148
7.2	Signal description	149
7.3	Background modeling	151
7.3.1	Likelihood function for CP eigenstates	151
7.3.2	Likelihood function for flavor-eigenstates	154
7.4	Free parameters of the likelihood fit	155
7.5	External parameters of likelihood fit	157
7.6	Validation studies	158
7.6.1	Study of simulated signal decays	158
7.6.2	Study of simulated signal and background decays	159
7.6.3	Determining the maximum-likelihood bias	160
8	Fit results	163
8.1	Data sample	163
8.2	Maximum-likelihood fit results	166

8.2.1	Goodness of fit	169
8.2.2	Flavor tagging results	172
8.2.3	$J/\psi K_L^0$ and $J/\psi K^{*0}$ results	174
8.3	Cross checks	175
8.3.1	CP decay mode	175
8.3.2	Flavor tagging category	176
8.3.3	B^0 and \bar{B}^0 flavor tags	176
8.3.4	J/ψ reconstruction mode	179
8.3.5	Run period	182
8.3.6	Control samples	184
8.4	Fit for $ \lambda_{f_{CP}} $	185
9	Systematic uncertainties	189
9.1	Signal parameters	190
9.1.1	Shared average signal dilutions	190
9.1.2	Shared signal resolution function parameters	191
9.1.3	Signal resolution function model	192
9.1.4	Resolution function for right and wrong tagged events	193
9.2	Background parameters	194
9.2.1	CP content of the background	195
9.2.2	Lifetime of CP background	195
9.2.3	Fraction of peaking background	195
9.2.4	Signal probability determination	196
9.2.5	m_{ES} endpoint	196
9.2.6	Background resolution function	197
9.2.7	Mixing component of background B_{flav} lifetime	197
9.3	External parameters	197
9.4	Detector effects	199
9.4.1	Beam spot position	199
9.4.2	SVT alignment	199
9.4.3	Uncertainty on z scale	200
9.5	Monte Carlo correction	200
9.6	Doubly-CKM-suppressed $b \rightarrow u$ transitions	201
9.7	Total systematic uncertainty	205
9.8	Additional validation studies	205
10	Conclusion	209
10.1	Interpretation	211
10.2	Future measurements	211
A	Spectroscopy of charmonium	215

B <i>BABAR</i> author list	219
Bibliography	229

List of Figures

1.1	Asymmetry in angular distribution of polarized ^{60}Co beta decay.	9
1.2	Feynman diagrams of $K^0 \rightarrow \mu^+ \mu^-$.	11
1.3	The unitarity triangle.	17
1.4	$B^0-\bar{B}^0$ mixing diagrams.	25
1.5	Decay diagrams for $B^0 \rightarrow J/\psi K_s^0$.	30
1.6	Distribution of Δt for B^0 and \bar{B}^0 CP events.	35
1.7	Constraints on unitarity triangle apex.	40
2.1	Scan of Υ resonances measured by CLEO.	44
2.2	Schematic representation of PEP-II.	46
2.3	Integrated luminosity delivered by PEP-II and recorded by the <i>BABAR</i> detector between 1999-2002.	47
2.4	Interaction region.	48
2.5	<i>BABAR</i> detector.	52
2.6	Transverse schematic of SVT.	54
2.7	Longitudinal schematic of SVT.	55
2.8	Schematic block diagram of SVT.	56
2.9	A simplified representation of an inner-layer SVT wafer.	57
2.10	Schematic diagram of the ATOM chip.	58
2.11	Comparison of local SVT alignment.	60
2.12	Z hit resolution of the SVT.	61
2.13	Side view of the <i>BABAR</i> drift chamber.	62
2.14	Schematic layout of the first four layers of DCH drift cells.	64
2.15	DCH reconstruction efficiency.	65
2.16	DCH p_T resolution.	66
2.17	Schematic of DIRC geometry.	68
2.18	DIRC efficiency and misidentification probability of charged kaons.	69
2.19	A longitudinal cross-section of the EMC (top half).	71
2.20	Invariant two photon mass in $B\bar{B}$ events.	72

2.21	Electron efficiency and pion misidentification probability using the EMC.	74
2.22	Overview of the IFR	76
2.23	IFR muon efficiency and pion misidentification probability.	78
3.1	Distribution of Δt for mixed and unmixed events.	80
4.1	Distributions of electron selection criteria variables.	89
4.2	Distribution of muon selection criteria variables.	91
4.3	Distributions of DIRC Cherenkov angle as function of momentum for kaons and pions.	92
4.4	Distribution of R_2 for Monte Carlo $B\bar{B}$ and continuum events.	94
4.5	Mass distribution for K_S^0 candidates.	97
4.6	Mass distribution for J/ψ candidates.	99
4.7	Mass distribution for $\psi(2S)$ candidates.	100
4.8	Mass distribution for χ_{c1} candidates.	101
4.9	Mass distribution for η_c candidates.	101
4.10	Distribution of D^0 and D^+ mass pulls.	103
4.11	Distribution of $m(D^0\pi^+) - m(D^0)$ and $m(D^0\pi^0) - m(D^0)$ in data.	104
4.12	Schematic representation of helicity angles for the decay $B^0 \rightarrow J/\psi K_S^0$	107
4.13	Distribution of $\cos\theta_\ell$ for signal and sideband $B^0 \rightarrow J/\psi K_S^0$ and $B^+ \rightarrow J/\psi K^+$ candidates in data.	107
4.14	Distribution of m_{ES} for CP modes in data.	110
4.15	Distribution of peaking background in m_{ES} using inclusive $B^0 \rightarrow J/\psi X$ Monte Carlo.	111
4.16	Distribution of m_{ES} for all B^0 flavor-eigenstate modes in data.	113
4.17	Distribution of m_{ES} for B^- control sample decay modes in data.	115
5.1	Illustration of B decay to primary and secondary leptons.	120
5.2	Distribution of lepton momentum in center-of-mass frame used for flavor tagging.	121
5.3	Illustration of B decay to right and wrong sign kaons.	122
5.4	Distribution of charged kaon momentum in the c.m. frame and multiplicity per event.	123
5.5	Schematic representation of flavor tagging algorithm.	126
6.1	Schematic representation of $\Upsilon(4S) \rightarrow B\bar{B}$ decay in yz plane.	131
6.2	Residual Δz distribution for $J/\psi K_S^0$ simulation.	132
6.3	Correlation between $\sigma_{\Delta t}$ and the RMS and mean offset of the residual Δt distribution from simulation.	136
6.4	Illustration of the sign of the residual Δz distribution mean.	136

6.5	Illustration of correlation between offset in the Δz residual mean and the polar angle of charm meson flight.	137
6.6	Comparison of $\sigma_{\Delta t}$ between data and Monte Carlo simulation for open charm and charmonium final states.	139
6.7	Comparison of the various properties of the B_{tag} vertex in a subset of the full data set for the CP and flavor-eigenstate samples.	140
6.8	Comparison of $\sigma_{\Delta z}$ for B_{CP} and flavor-eigenstate data samples.	142
6.9	Schematic representation of the B_{tag} and B_{rec} decays in the xy plain relative to the beamspot.	143
6.10	Comparison of Δy and $\Delta y/y$ distributions in data and Monte Carlo simulation for CP and flavor-eigenstate samples.	144
6.11	Comparison of per-event error in data and Monte Carlo simulation for continuum control sample.	145
7.1	Schematic representation of parabolic log-likelihood.	149
7.2	Residual $\sin 2\beta$ distribution using event sized samples of simulated B_{CP} decays.	162
8.1	Distribution of m_{ES} for CP events passing vertexing requirements for each tagging category.	166
8.2	Distribution of m_{ES} for flavor-eigenstate events passing vertexing requirements for each tagging category.	167
8.3	Distribution of B^0 and \bar{B}^0 tagged events as a function of Δt and Δt asymmetry for CP sample.	169
8.4	The raw asymmetry in the number of B^0 and \bar{B}^0 tags in the CP sample binned by Δt	170
8.5	Distribution of error on $\sin 2\beta$ from fits to 1000 toy experiments for each CP decay mode.	172
8.6	Distribution of log-likelihood from fits to 1000 toy experiments for each CP decay mode.	173
8.7	Distribution of events as a function of Δt for B^0 and \bar{B}^0 tagged for each CP decay mode.	177
8.8	Raw Δt asymmetry for each CP decay mode.	178
8.9	Δt distributions of B^0 and \bar{B}^0 tagged events and raw asymmetry for $\eta_c K_s^0$	179
8.10	Comparison of $\sin 2\beta$ found in each CP decay mode to value found in combined CP sample.	180
8.11	Distribution of events as a function of Δt for each flavor tagging category in the CP sample.	181
8.12	Raw Δt asymmetry for each tagging category.	182
8.13	Comparison of $\sin 2\beta$ in subsets of the full CP data sample.	184

8.14	Comparison of $\sin 2\beta$ in various control samples.	186
9.1	Dependence of $\sin 2\beta$ on $\tau(B^0)$ and Δm_d	198
9.2	Dilutions as a function of $\sigma_{\Delta t}$ from simulated B_{CP} decays.	202
9.3	Bias in simulated and toy Monte Carlo from the linear $\sigma_{\Delta t}$ dilution dependence.	203
9.4	The CKM favored and suppressed Feynman diagrams for the final state $D^-\pi^+$	203
9.5	Variation in $\sin 2\beta$ compared to the nominal fit for various alternative vertexing, tagging, and reconstruction configurations.	207
10.1	Comparison of $\sin 2\beta$ measurements with the current world-average.	210
10.2	Comparison of the solutions for β in the $(\bar{\rho}, \bar{\eta})$ plane with other constraints on the apex of the unitarity triangle.	212
10.3	Statistical error on $\sin 2\beta$ from each <i>BABAR</i> measurement.	213
A.1	Discovery of the J/ψ meson at SLAC.	216
A.2	The observed spectroscopy of charmonium ($c\bar{c}$) mesons.	218

List of Tables

2.1	Production cross-sections of e^+e^- interactions at the $\Upsilon(4S)$ resonance.	45
2.2	Typical and design beam parameters of the PEP-II storage rings.	46
2.3	<i>BABAR</i> detector parameters.	52
2.4	Properties of DCH gas mixture.	63
2.5	Properties of CsI(Tl).	70
4.1	Branching fractions for the decay $B^0 \rightarrow J/\psi K_s^0$	85
4.2	Summary of electron identification criteria.	90
4.3	Summary of muon identification criteria.	90
4.4	Branching fractions and decay modes of relevant charmonium mesons.	98
4.5	Particle identification and invariant mass requirements for J/ψ and $\psi(2S) \rightarrow \ell^+\ell^-$ candidates.	98
4.6	Branching fractions and decay modes of D^0 and D^+ charm mesons.	102
4.7	Branching fractions for B^0 decays to charmonium CP -eigenstates.	109
4.8	Event yields for the CP sample.	109
4.9	Peaking background fractions for the CP sample.	112
4.10	Branching fractions for B^0 decays to flavor-eigenstates.	112
4.11	Event yields for the B_{flav} sample.	114
4.12	Event yields for the B^- control sample.	116
5.1	Input taggers used for flavor tagging algorithm.	125
5.2	Category definition used by tagging algorithm.	127
5.3	Category merging scheme for tagging algorithm.	127
5.4	Performance of tagging algorithm after category merging.	127
7.1	Breakdown of free parameters in $\sin 2\beta$ maximum-likelihood fit.	155
7.2	Average mistag fractions of B^+ control sample.	157
7.3	Fit results for the high statistics B_{flav} simulated Monte Carlo sample.	159

7.4	Results of fits for $\sin 2\beta$ in high statistics simulated Monte Carlo of CP eigenstate decays.	160
7.5	Results of $\sin 2\beta$ fits using a simulated sample of inclusive $B^0 \rightarrow J/\psi X$ decays.	160
8.1	Event yields by tagging category for signal CP events after vertexing requirements.	164
8.2	Event yields by tagging category for signal flavor-eigenstate sample after vertexing requirements.	164
8.3	Signal yield and purity of CP events by tagging category.	165
8.4	Signal yield and purity of flavor-eigenstate events by tagging category.	166
8.5	Maximum-likelihood fit results for the CP data sample.	168
8.6	Goodness of fit results from toy Monte Carlo.	171
8.7	Flavor tagging performance in data.	174
8.8	Values of $\sin 2\beta$ found for each CP decay mode.	176
8.9	Value of $\sin 2\beta$ for each flavor tagging category for the CP sample.	177
8.10	Value of $\sin 2\beta$ for B^0 and \bar{B}^0 tagged events.	179
8.11	Value of $\sin 2\beta$ for $J/\psi \rightarrow e^+e^-$ and $J/\psi \rightarrow \mu^+ \mu^-$	181
8.12	Definition and luminosity of different data taking periods.	183
8.13	Value of $\sin 2\beta$ in various run-blocks.	183
8.14	Value of $\sin 2\beta$ in control samples.	185
9.1	Systematic uncertainty due to fixed width and bias of the outlier Gaussian.	192
9.2	Systematic uncertainty from the signal probability determination.	196
9.3	Systematic uncertainty from the m_{ES} endpoint value of the ARGUS fit.	197
9.4	Variation in $\sin 2\beta$ and its error when Δm_d and (or) $\tau(B^0)$ are free parameters in the likelihood fit.	198
9.5	Slope of dilution as a function of $\sigma_{\Delta t}$ from simulated B_{CP} decays.	201
9.6	Summary of contributions to the systematic uncertainty on $\sin 2\beta$	206
A.1	Properties of charmonium mesons.	218

Chapter 1

CP violation in the Standard Model

For every one billion particles of antimatter there were one billion and one particles of matter. And when the mutual annihilation was complete, one billionth remained – and that’s our present universe.

Albert Einstein

The Standard Model (SM) [1] of particle physics successfully accommodates all current experimental results. However, due partly to the large number of ad hoc inputs the theory requires, it is widely believed that the SM will be relegated to a low energy approximation of a more comprehensive theory in the near future. Consequently, many experiments now aim to probe the Standard Model’s less well constrained parameters in the hopes of uncovering unexpected results that will illuminate the path to new physics.

Charge-parity (*CP*) symmetry violation is one area where experiment has only recently begun to rigorously test the theory. As will be shown, the Standard Model Lagrangian is not required to be invariant under the *CP* transformation. The existence of at least three quark generations in the SM allows for a non-zero phase in the Cabibbo-Kobayashi-Moskawa (CKM) matrix [2] that relates the quark eigenstates in the weak basis to the mass eigenstates. This

irremovable phase in the CKM matrix is the only SM source of CP violating effects¹. While CP violation was discovered in the kaon system [4, 5], it remains to be proven that the CP violating mechanism of the Standard Model accounts for the CP violating effects seen in nature. It may be possible to determine this in the B meson system by making enough theoretically clean CP violating (along with complementary CP conserving) observations. This thesis reports on the most anticipated first observation of CP violation in the B meson system made by the *BABAR* collaboration at the Stanford Linear Accelerator Center (SLAC).

This chapter describes the mechanism of CP violation in the Standard Model as it applies to the B meson system and how its effects may be measured. In Sec. 1.1 we introduce the elementary particles and interactions of the Standard Model, assuming some prior familiarity. We define the discrete symmetry operators representing parity, charge conjugation, and time reversal and discuss some of their properties in Sec. 1.2. Sec. 1.3 presents the relationship between CP violation and the observed baryon asymmetry of the universe. In Sec. 1.4, we describe the experimental discovery of CP violation that occurred well before a theoretical foundation existed to explain it.

At this point the focus shifts to understanding the theory as it developed in a historical manner. In Sec. 1.5, we flesh out fully the details of the already introduced CKM mechanism and describe the unitarity triangle, which is useful in determining the amount of CP violation that can be measured in the B meson system. Following this, in Sec. 1.6, we present the three ways that CP violation may be manifested in the SM. This section concludes with the form of a time-dependent CP violating asymmetry between the difference in proper decay-times of neutral B mesons that decay to CP eigenstates. This asymmetry, for CP eigenstates consisting of a charmonium and K_s^0 meson, will be the main focus of this thesis as it allows the determination of one angle in

¹We ignore non-perturbative corrections to the SM tree-level Lagrangian that are expected to induce a second possible source of CP violation [3].

the unitarity triangle called β .

The theoretical interest of a final CP eigenstate that consists of a charmonium and K_s^0 meson is explained in Sec. 1.7 and the experimental issues which make the asymmetry's measurement non-trivial are given in Sec. 1.8. Pre-existing constraints on the apex of the unitarity triangle, and hence the angle β , are reviewed in Sec. 1.9. Finally, the results of other collaborations' efforts to measure β are presented in Sec. 1.10.

1.1 The Standard Model

Quarks ² and leptons are the fundamental particles of the Standard Model which comprise all known matter. Termed fermions, they have half integer values of spin measured in units of Planck's constant \hbar . Nature has been found to exhibit three forces, named the strong, electroweak and gravitational, which dictate the manner in which these particles interact. The forces mediate the interactions of the quarks and leptons through the exchange of gauge bosons (particles with integer values of spin). Quarks and leptons are distinguished based on their coupling to the strong force: quarks have color charge, meaning they interact strongly, while leptons do not. There is experimental evidence for the existence of 6 quarks and 6 leptons (as well as their anti-particles) each divided into three generations:

$$\begin{pmatrix} u \\ d \end{pmatrix} \quad \begin{pmatrix} c \\ s \end{pmatrix} \quad \begin{pmatrix} t \\ b \end{pmatrix} \tag{1.1.1}$$

$$\begin{pmatrix} \nu_e \\ e^- \end{pmatrix} \quad \begin{pmatrix} \nu_\mu \\ \mu^- \end{pmatrix} \quad \begin{pmatrix} \nu_\tau \\ \tau^- \end{pmatrix} \tag{1.1.2}$$

Of these particles, the top quark (t) and tau neutrino (ν_τ) were the most recently detected, both by Fermilab experiments [8, 9].

²Gell-Mann [6] and Zweig [7] independently proposed the existence of quarks in 1964.

In the quark sector, the doublets of each generation have identical properties except for mass which increases from a few MeV/c^2 for the up quark to $174 \text{ GeV}/c^2$ for the top quark. This trend holds for the charged lower entry of each lepton doublet as well, where the mass ranges from $0.511 \text{ MeV}/c^2$ for the e^- to $1.78 \text{ GeV}/c^2$ for the τ^- . Recent experimental evidence confirming neutrino mixing implies non-zero neutrino masses [10]. Analyses of the low energy beta decay of tritium atoms limits the electron neutrino mass to less than 3 eV [11]. The Standard Model provides no explanation for the orders of magnitude mass differences between generations.

One can give a complete characterization of the quarks and leptons by specifying their quantum numbers: effectively listing which particles will respond to which force. The electric charge of the upper entry in each quark doublet of 1.1.1 is $+(2/3)e$ and the charge of the lower entry is $-(1/3)e$ where $-e$ is the electron charge. The electric charge of the lower entry in each lepton doublet of 1.1.2 is $-e$ while the 3 neutrinos have zero electric charge. The left-handed chiral projection of each fermion pair transforms as a weak isospin $SU(2)$ ³ doublet with the upper (lower) entry having a component of $+1(-1)$ along the quantized axis. The right-handed fermions transform as weak isospin singlets⁴.

As already stated, gauge bosons act as the transmitters of forces between quarks and leptons. Gravitons, which have yet to be experimentally observed, couple to massive quarks and leptons. The strength of the gravitational force between elementary particles is orders of magnitude weaker than any of the other forces to be discussed. A relativistic quantum field theory of gravity has not yet been successfully formulated.

Eight gluons, each carrying two units of color charge, couple quarks through the strong force. As gluons have non-zero color charge, they also couple to themselves, a generic feature of non-abelian field theories. At short distances

³Some familiarity with group theory is assumed.

⁴Right-handed neutrinos have not been observed but non-zero neutrino masses indicate they should exist. if they are Dirac particles.

the coupling strength approaches zero, allowing the theory to be described perturbatively [12]. This free behavior of the quarks at short distances is commonly called asymptotic freedom. At large distances the coupling strength becomes too large for perturbation theory to be valid. The photon carries the electromagnetic interaction, coupling to a charged quark or lepton with a strength proportional to the electric charge. Electromagnetic and strong interactions conserve quark flavor.

Finally, all quarks and leptons interact weakly through W^+ , W^- , and Z^0 boson exchange. For leptons, this coupling strength is proportional to the Fermi constant (G_F). While weak neutral currents also conserve quark flavor, weak charged currents couple quarks of different flavors, as well as different generations. The relative strength of these flavor changing quark couplings are described by the elements of the CKM matrix. After reviewing the history of CP violation, we will return to a discussion of the CKM matrix in Sec. 1.5.

Isolated quarks have not been observed in nature, but colorless bound states of a quark-antiquark pair called mesons and three quarks called baryons (both of which are termed hadrons) do exist. We shall often use the term B meson in this thesis to refer to a particle which contains a b and d quark. For reference, a B^0 is composed of a $\bar{b}d$ pair, a \bar{B}^0 of a $b\bar{d}$ pair, a B^+ of a $\bar{b}u$ pair, and a B^- of a $b\bar{u}$ pair. When discussing the meson with quark content $b\bar{s}$, the common notation B_s will be used.

1.2 Parity, charge conjugation, and time reversal

In order to understand CP violation in the Standard Model, we must necessarily begin with a precise definition of the parity, charge conjugation and time reversal operators. Such operators have historically been interesting to study because of Noether's theorem [13] that links conserved quantities to sym-

metries, transformations that do not alter the equations of motion of a given system.

Parity, denoted P , is a discrete unitary ($P^{-1} = P^\dagger$) space-time transformation which reverses the momentum of a particle, flipping the handedness of the coordinate system used to describe space. A particle's four vector (t, \vec{x}) transforms under P to four vector $(t, -\vec{x})$. Since spin may be thought of as a quantum mechanical analog of angular momentum, given by $\vec{r} \times \vec{p}$, one sees that spin remains invariant under P as both the momentum and position change sign. The projection of spin along the particle's direction of motion, termed helicity, will also change sign. By definition, we require P acting twice on a particle to leave it invariant, implying $P = P^{-1}$ and that the eigenvalues of P are ± 1 .

Charge conjugation, denoted C , is a unitary non-spacetime discrete transformation which transforms particles into anti-particles. C reverses the charge of all internal quantum numbers (not just electric charge), leaving momentum and spin unchanged. The C operator also leaves a particle invariant when applied twice, yielding $C = C^{-1} = C^\dagger$. The combined operation CP changes a particle to its anti-particle, reversing its momentum and helicity.

A final discrete space-time transformation we are concerned with is time reversal, T . An anti-unitary operator, T transforms $(t, \vec{x}) \rightarrow (-t, \vec{x})$ interchanging the forward and backward light cones and flipping the particle's spin. Any Lorentz-invariant quantum field theory with a Hermitian Hamiltonian must have the combination CPT as an exact symmetry [14].

1.3 CP violation and cosmology

We have stated that one reason we are interested in studying CP violation is to determine whether CP violating effects can be explained within the context of the SM. In addition, there is an important cosmological motivation for understanding CP violation related to the observed preponderance of matter over

antimatter in the universe [15]. No primordial antimatter has been observed in the universe. The evidence for a matter dominated universe consists of null searches for light antinuclei near the vicinity of the earth [16], observations of cosmic rays that only contain antimatter consistent with secondary production from collisions with interstellar matter, and the lack of an anomaly in the background γ ray spectrum that would have been enhanced by the annihilation of matter and antimatter galaxies. These constraints have led to the conclusion that on scales larger than 100 Mpc (1Mpc $\sim 3 \cdot 10^{19}$ km) to 1 Gpc the universe consists only of matter [17].

In 1967, Sakharov pointed out that this cosmological asymmetry could arise dynamically during the evolution of the universe if three conditions are satisfied: the existence of a baryon number violating mechanism, C and CP violation, and a departure from thermal equilibrium in order to produce a net baryon number [18]. It is natural to wonder whether the CP violation required to explain this asymmetry can be provided by the CKM mechanism of the SM. While an explanation of the argument is beyond the scope of this thesis, it seems most theorists believe [19] that sources of CP violation beyond the SM are required to produce the observed baryon number violation ⁵. Further, it appears that this question is not even relevant since it has been shown that the third condition of a departure from thermal equilibrium cannot be fulfilled within the SM [21].

Consequently, examinations of CP violation in the B meson system will not directly shed light on the matter asymmetry of the universe. However, theories that can explain this asymmetry must include additional sources of CP violation [19]. These new sources are strongly constrained by current experimental results from CP violation in the kaon system and from the absence of flavor changing neutral currents. Therefore, determining the pattern of CP violation in the neutral B system may be extremely useful in excluding classes

⁵Models in which the CKM mechanism does receive a large enhancement at high temperatures (see Ref. [20]) are usually regarded as unconvincing.

of SM extensions and indirectly lead to insights concerning the nature of the cosmological matter asymmetry.

1.4 Discovery of CP violation

Following Fermi's (incomplete) ansatz of vector-vector weak current coupling in nuclear beta decay [22], most theoretical particle physicists believed C , P , and T were conserved by all the Standard Model forces. However, after surveying the evidence in 1956, Lee and Yang pointed out that experiments had not yet tested parity invariance of weak decays [23]. Motivated by this work, Wu *et. al* conducted an experiment where the spin of ^{60}Co nuclei were aligned with the direction of an externally applied magnetic field [24]. They observed that electrons from the decay $^{60}\text{Co} \rightarrow ^{60}\text{Ni}^* + e^- + \bar{\nu}_e$ were preferentially emitted in the direction opposite to that of the external magnetic field (see Fig. 1.1a). This observation can be explained if the weak decay couples a helicity -1 electron with a helicity $+1$ antineutrino as shown in Fig. 1.1b. If parity were conserved, one would observe both negative and positive helicity electrons emitted in this decay process. Consequently, the Wu result indicated that parity is violated in weak interactions. Further, according to Lee and Yang's work, the large value of the observed asymmetry suggested that charge conjugation was also violated [23].

Subsequent experiments have revealed that parity and charge conjugation are maximally violated in weak decays. This follows directly from the vector-axial vector ($V - A$) structure of the weak current. However, a $V - A$ current that connects two quark fields transforms under CP to its hermitian conjugate (taking the coupling constant to be real). Consequently, after parity and charge conjugation invariance were separately shown to be violated in weak interactions, most physicists still assumed that CP was an exact symmetry [25].

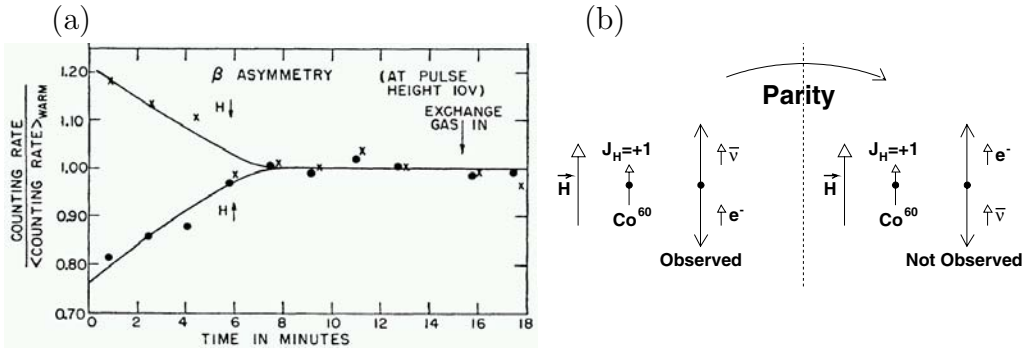


Figure 1.1: (a) Asymmetry in the angular distribution of electrons from polarized ${}^{60}\text{Co}$ decay. The electrons are preferentially emitted in the direction opposite to the applied magnetic field (\vec{H}) along which the ${}^{60}\text{Co}$ nuclei are polarized. As the experimental apparatus warms, the polarization becomes random and the asymmetry vanishes; (b) The results can be explained if the weak decay couples negative helicity electrons with positive helicity antineutrinos. The parity transformed version of the experiment is not observed.

1.4.1 Experimental confirmation of CP violation

Cronin, Fitch, Christenson, and Turlay falsified the assumption of CP symmetry in 1964 by detecting the decay of the long lived neutral kaon, termed the K_L^0 (the short lived kaon meson is called the K_S^0), to two charged pions. In the absence of orbital angular momentum, the 2π and 3π final states of neutral kaon decays have P of $+1$ and -1 , C of $+1$ and $+1$, and consequently CP of $+1$ and -1 respectively. Following the phase convention,

$$CP|K^0\rangle = |\bar{K}^0\rangle, \quad (1.4.1)$$

it was thought that the neutral kaon mass eigenstates were also eigenstates of CP :

$$\begin{aligned} |K_S^0\rangle &= \sqrt{\frac{1}{2}}(|K^0\rangle + |\bar{K}^0\rangle) \quad [CP = +1] \\ |K_L^0\rangle &= \sqrt{\frac{1}{2}}(|K^0\rangle - |\bar{K}^0\rangle) \quad [CP = -1] \end{aligned} \quad (1.4.2)$$

However, observing K_L^0 decays to 2π ($CP = +1$) final states with an probability of $\approx 10^{-3}$, the experimenters demonstrated that nature violates CP conservation at a very small level. Cronin and Fitch subsequently received the Nobel

Prize for this work in 1980. In his Nobel Prize lecture, Fitch interestingly pointed out that there were “no precursive indications, either theoretical or experimental” for their discovery [26].

1.4.2 Theoretical model for CP violation

In the same year of Cronin and Fitch’s remarkable observation, Cabibbo began laying the theoretical foundation required for understanding CP violation [27]. He proposed that charged current interactions couple the u quark to the rotated quark state d' , where

$$d' = d \cos \theta_c + s \sin \theta_c \quad (1.4.3)$$

and θ_c is referred to as the Cabibbo angle. This framework explains the suppression of $\Delta S = 1$ leptonic kaon decays ($K^+ \rightarrow \mu^+ \nu_\mu$) relative to $\Delta S = 0$ leptonic pion decays ($\pi^+ \rightarrow \mu^+ \nu_\mu$); the decays have the same Feynman diagram after making the quark substitution $s \rightarrow d$. The sine of the Cabibbo angle has been measured to be 0.22.

A three quark model (u, d , and s) coupling via Cabibbo mixing contains significant contributions from flavor changing neutral currents ($s \rightarrow d$ transitions). This implies a sizable branching fraction for the decay $K_L^0 \rightarrow \mu^+ \mu^-$. The failure to observe this decay led Glashow, Iliopoulos, and Maiani (GIM) to propose the existence of the c quark before its experimental discovery [28]. Building upon the mechanism of Cabibbo to include $c \rightarrow s'$ coupling, with

$$\begin{pmatrix} d' \\ s' \end{pmatrix} = \begin{pmatrix} \cos \theta & \sin \theta \\ -\sin \theta & \cos \theta \end{pmatrix} \begin{pmatrix} d \\ s \end{pmatrix} \quad (1.4.4)$$

the decay $K_L^0 \rightarrow \mu^+ \mu^-$ can proceed through two second order diagrams. The diagrams are identical except for the substitution of a c quark for the virtual u quark connecting the \bar{s} and d of the K_L^0 as shown in Fig. 1.2 Neglecting the mass difference of the u and c quarks, the diagrams destructively interfere, with the relative minus sign coming from the $-\sin \theta$ matrix element of 1.4.4, yielding an overall null rate for the decay.

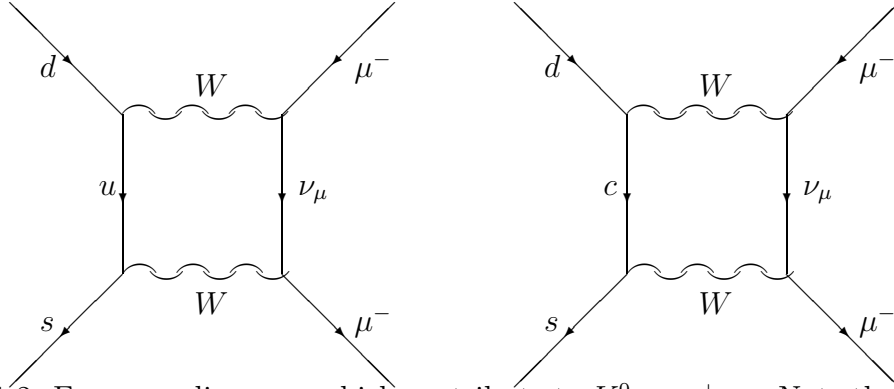


Figure 1.2: Feynman diagrams which contribute to $K^0 \rightarrow \mu^+ \mu^-$. Note that the left and right diagrams are identical except for the quark substitution $u \leftrightarrow c$.

1.5 The CKM matrix

In 1973, Kobayashi and Maskawa expanded the GIM mechanism of 1.4.4 to include a third quark generation ⁶ in the commonly referred to CKM matrix:

$$\begin{pmatrix} d' \\ s' \\ b' \end{pmatrix} = \begin{pmatrix} V_{ud} & V_{us} & V_{ub} \\ V_{cd} & V_{cs} & V_{cb} \\ V_{td} & V_{ts} & V_{tb} \end{pmatrix} \begin{pmatrix} d \\ s \\ b \end{pmatrix}. \quad (1.5.1)$$

The matrix describes the coupling strength of weak charged quark currents. In this section, we attempt to explain the origin of the CKM matrix in the SM in terms of its fundamental connection to fermion masses. Then we show that the CKM matrix has exactly one phase in a 3 quark generation universe. Finally, we illustrate the manner in which this phase leads to CP violation in the SM.

1.5.1 Higgs mechanism origin

In the SM, fermionic masses are generated by Yukawa couplings between left-handed fermion $SU(2)$ doublets, right-handed singlets, and the Higgs dou-

⁶In fact, the expansion involved an arbitrary number of quark generations, but we restrict our study to the experimentally established three families of the SM here.

blet [29]:

$$\mathcal{L}_Y = - \sum_{i,j} \left[\Gamma_{ij} \begin{pmatrix} \bar{p}_L^j & \bar{n}_L^j \end{pmatrix} \begin{pmatrix} \phi^+ \\ \phi^0 \end{pmatrix} n_R^i + \Delta_{ij} \begin{pmatrix} \bar{p}_L^j & \bar{n}_L^j \end{pmatrix} \begin{pmatrix} \phi^{0\dagger} \\ -\phi^- \end{pmatrix} p_R^i + h.c. \right] \quad (1.5.2)$$

where $p(n)$ are the positively (negatively) charged quark fields, Γ and Δ are arbitrary complex matrices, ϕ^0 and ϕ^+ are the neutral and charged components of the Higgs doublet respectively, i and j run over the three quark generations, and L and R denote chiralities of -1 and $+1$ respectively. Charged current interactions mediated by W bosons are given by:

$$\mathcal{L}_{cc} = \frac{g}{\sqrt{2}} \sum_{i,j} \left[W_\mu^+ \bar{p}_L^i \gamma^\mu n_L^i + W_\mu^- \bar{n}_L^i \gamma^\mu p_L^i \right] \quad (1.5.3)$$

Expanding the Higgs doublet around its vacuum expectation value v , with quantum fluctuations given by a Higgs field $H(x)$,

$$\phi = \begin{pmatrix} \phi^+ \\ \phi^0 \end{pmatrix} = \frac{1}{\sqrt{2}} \begin{pmatrix} 0 \\ v + H(x) \end{pmatrix}, \quad (1.5.4)$$

we find that the mass terms of 1.5.2 become

$$\mathcal{L}_{mass} = - \sum_{i,j} \left[\Gamma_{ij} \bar{n}_L^j n_R^i + \Delta_{ij} \bar{p}_L^j p_R^i + h.c. \right] \frac{v}{\sqrt{2}} \quad (1.5.5)$$

The Yukawa coupling matrices, Γ and Δ , may be diagonalized by a unitary transformation to the quark mass eigenstate basis (the physical basis) which transforms the quark states according to:

$$\begin{aligned} p_L^i &= U_u^{ij} u_L^j \\ n_L^i &= U_d^{ij} d_L^j \end{aligned} \quad (1.5.6)$$

This transformation leads us to rewrite the charged boson current of 1.5.3 in the quark mass basis as

$$\mathcal{L}_{cc} = \frac{g}{\sqrt{2}} \left[W_\mu^+ \bar{u}_L^i \gamma^\mu \left(U_u^\dagger U_d \right)_{ij} d_L^j + W_\mu^- \bar{d}_L^i \gamma^\mu \left(U_u^\dagger U_d \right)_{ij}^\dagger u_L^j \right] \quad (1.5.7)$$

Consequently, flavor-changing weak interactions relate the u_L^i quarks with a unitary transformation of the d_L^i quarks where the rotation is given by the CKM matrix of 1.5.1,

$$V = U_u^\dagger U_d \tag{1.5.8}$$

Defined as a product of unitary matrices, the CKM matrix is unitary by construction. This framework elucidates the close connection between CKM elements and the generation of fermionic masses in the SM.

1.5.2 Parameter counting

To understand CP violation in the SM, it is necessary to determine how many physical parameters this complex CKM matrix requires. In general, an $n \times n$ complex matrix has $2n^2$ real parameters. Unitarity provides n constraints from the normalization of each column and

$$2 \binom{n}{2} = n(n-1) \tag{1.5.9}$$

constraints from the orthogonality of the columns. This leaves $2n^2 - n - n(n-1) = n^2$ real parameters. However, we are still free to attach an arbitrary phase, $q_L^i \rightarrow \exp[i\alpha^i] q_L^i$, to each of the quark fields, thereby reducing the number of phases in the CKM matrix. Examining the first term of 1.5.7 we see that the freedom to rephase the $(d_L \ s_L \ b_L)$ quark fields allows us to make one row of V real. Similarly, the freedom to rephase the $(u_L \ c_L \ t_L)$ fields, allows us to make a column of V real. In general, then, we can remove $2n - 1$ phases of V in this manner (one of our column and one of our row elements must be the same). This leaves us with

$$N_{param} = n^2 - (2n - 1) = (n - 1)^2 \tag{1.5.10}$$

physical parameters of V . An $n \times n$ matrix which is orthogonal has $N_{real} = n(n-1)/2$ real parameters, sometimes referred to as Euler rotation angles.

Consequently, an n generation CKM matrix has

$$\begin{aligned}
 N_{phases} &= N_{param} - N_{real} \\
 &= (n-1)^2 - n(n-1)/2 \\
 N_{phases} &= (n-1)(n-2)/2
 \end{aligned}$$

phases. Thus, in a 2 generation SM, V has no complex phase while it has exactly one phase in a 3 generation SM. We will now explain the manner in which this phase causes CP violation.

Let's consider a flavor changing process in which a quark with negative electric charge radiates a W^- and a positively charged quark is created, $d_j \rightarrow W^- u_i$. According to 1.5.7, this coupling is proportional to V_{ij} . Of interest is whether the Lagrangian remains invariant when we consider this process after acting with the CP operator. It can be shown [30] that this process transforms under CP to $\bar{d}_j \rightarrow W^+ \bar{u}_i$, with the coupling constant, V_{ij} , remaining unchanged. In order for the SM Lagrangian to be invariant under CP , this CP conjugated term must be contained in Eq. 1.5.7 and should correspond to the term representing the *physically* CP conjugate process. However, we find that the physically CP conjugate process is given by the second term of 1.5.7 and is proportional to V_{ij}^* . Consequently, the SM Lagrangian is only CP invariant if the CKM matrix is real. As has just been shown, a three generation CKM matrix does not generally satisfy this requirement. More generally, we see that a Lagrangian containing coupling terms with complex coefficients that have a relative phase different from zero or π will not be CP invariant.

1.5.3 CKM parameterization

Parameterizing the CKM matrix by incorporating the constraints of three generation unitarity and experimental observations proves useful in comparing the relative strengths of different weak decays. As has been shown, rephasing the quark fields allows us to remove the phase from five of the CKM elements.

It then seems natural to parameterize the remaining elements in terms of three Euler angles and one phase that cannot be eliminated by any additional rephasings.

In 1983, Wolfenstein introduced an approximate parameterization of the CKM matrix [31] in terms of an expansion in the sine of the Cabibbo angle, $\lambda = \sin \theta_c$, which still remains useful. His novelty was incorporating the experimental evidence that $|V_{cb}| \sim |V_{us}|^2$ which is not obvious *a priori*, as one might naively guess that any single generation transition should be of the same order. Wolfenstein's parameterization

$$V = \begin{pmatrix} 1 - \lambda^2/2 & \lambda & A\lambda^3(\rho - i\eta) \\ -\lambda & 1 - \lambda^2/2 & A\lambda^2 \\ A\lambda^3(1 - \rho - i\eta) & -A\lambda^2 & 1 \end{pmatrix} + \mathcal{O}(\lambda^4), \quad (1.5.11)$$

where A is a constant of order unity, preserves unitarity to order λ^3 . The experimental evidence that $|V_{ub}|/|V_{cb}| \sim \lambda/2$ implies that ρ and η should be less than one. In this expansion, V_{ub} and V_{td} carry the complex phase. The usefulness of this parameterization becomes apparent when we introduce the unitarity triangle in the next section.

1.5.4 Unitarity triangle

Consider the orthogonality condition imposed on the first and third columns of the CKM matrix:

$$V_{ud}V_{ub}^* + V_{cd}V_{cb}^* + V_{td}V_{tb}^* = 0 \quad (1.5.12)$$

We note that each term in the sum is of order λ^3 . This equation, first emphasized by Bjorken and Chau and Keung, can be interpreted as representing a triangle in the complex plane as shown in the top of Figure 1.3 [32]. As all the sides have comparable lengths, the angles of this triangle should be approximately $\pi/3$ radians each. Other triangles one may obtain by this same procedure have equal area but two angles near zero and one angle near π as

one side of the triangle is much larger than the others. To leading order in the Wolfenstein parameterization,

$$\frac{V_{ud}V_{ub}^*}{|V_{cd}V_{cb}|} = \rho + i\eta \quad (1.5.13)$$

$$\frac{V_{cd}V_{cb}^*}{|V_{cd}V_{cb}|} = -1 \quad (1.5.14)$$

$$\frac{V_{td}V_{tb}^*}{|V_{cd}V_{cb}|} = 1 - \rho - i\eta \quad (1.5.15)$$

This result motivated the labeling of the vertices of the triangle shown in Figure 1.3. We note that while the overall orientation of the triangle is arbitrary, the lengths of its sides and the angles between them remain unchanged after a rephasing of the CKM matrix. The inner angles of the triangle are defined by ⁷

$$\begin{aligned} \alpha &\equiv \arg\left(-\frac{V_{td}V_{tb}^*}{V_{ud}V_{ub}^*}\right) \\ \beta &\equiv \arg\left(-\frac{V_{cd}V_{cb}^*}{V_{td}V_{tb}^*}\right) \\ \gamma &\equiv \arg\left(-\frac{V_{ud}V_{ub}^*}{V_{cd}V_{cb}^*}\right) \end{aligned} \quad (1.5.16)$$

Using this definition and the result $z_2/z_1 = |z_2/z_1| \exp[i(\theta_2 - \theta_1)]$, where $z_i = |z_i| \exp(i\theta_i)$, we can write

$$\sin 2\beta = \text{Im} \left(\frac{V_{cb}^* V_{cd} V_{tb} V_{td}^*}{V_{cb} V_{cd}^* V_{tb}^* V_{td}} \right) \quad (1.5.17)$$

which will be useful in our later discussions. As a phase invariant quantity, the angle β is a physically meaningful parameter which, as we will show, can be measured using neutral B decays to charmonium final states. First we will discuss the various ways in which CP violation is manifested in the SM.

⁷These angles are also commonly labeled ϕ_1, ϕ_2 , and ϕ_3 in the literature.

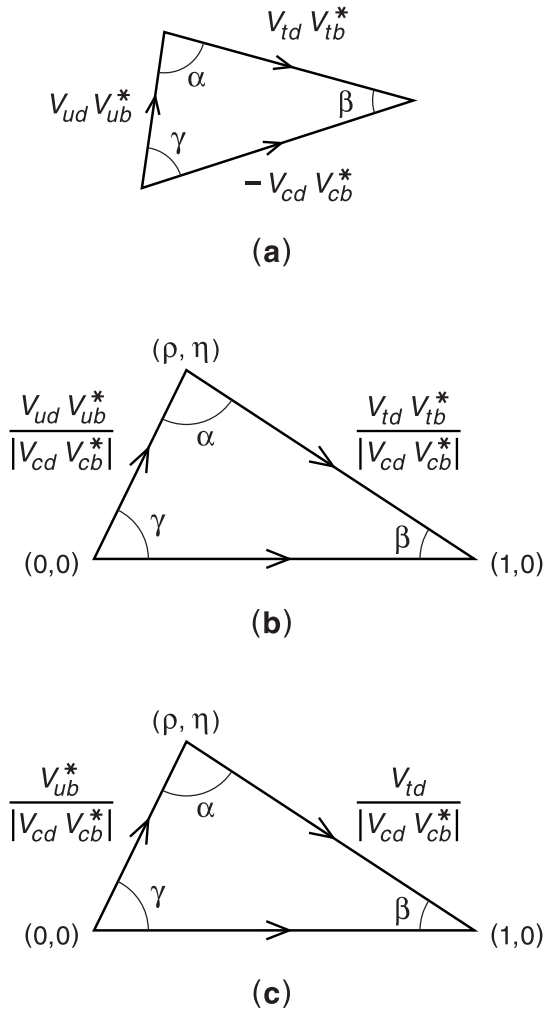


Figure 1.3: The CKM unitarity triangle: (a) the orthogonality condition of the first and third columns of the CKM matrix may be represented in the complex plane as a closed triangle as shown, whose overall orientation is arbitrary; (b) we have rescaled the lengths of each side by $|V_{cd}V_{cb}^*|$ and adopted a phase convention in which $V_{cd}V_{cb}^*$ is real and negative; (c) we have relabeled the sides using the approximation $V_{ud} = V_{tb} = 1$. Figure courtesy of Jeff Richman's Les Houches lectures [38].

1.6 Manifestations of CP violation

We have shown that in the SM with three generations the CKM matrix has an irreducible phase which necessarily leads to CP violation. There are three

ways this phase factor can be manifested: CP violation in direct decay, CP violation in mixing, and CP violation in the interference between decay and mixing. For this paper, we are most concerned with understanding this last type of CP violation. However, as it incorporates elements of the first two types, we will briefly describe the SM constraints which permit observation of all three types. As will be shown, the essential ingredient common to all of these is quantum mechanical interference between at least two amplitudes for a particle transition. We will focus our discussion on the decay and mixing processes of pseudoscalar P^0 and CP conjugate \bar{P}^0 mesons. We assume that neither is an eigenstate of CP . The following sections parallel work from additional sources [29, 38, 39].

1.6.1 CP violation in decay

First, we consider the condition necessary to generate CP violation in decay by comparing the decay rate $\Gamma(P^0 \rightarrow f)$ with $\Gamma(\bar{P}^0 \rightarrow \bar{f})$. The CP transformation of the states $|P^0\rangle$, $|\bar{P}^0\rangle$, and $|f\rangle$ is arbitrarily defined to be

$$CP|P^0\rangle = e^{i\zeta_P}|\bar{P}^0\rangle \quad (1.6.1)$$

$$CP|\bar{P}^0\rangle = e^{-i\zeta_P}|P^0\rangle \quad (1.6.2)$$

$$CP|f\rangle = e^{i\zeta_f}|\bar{f}\rangle \quad (1.6.3)$$

We denote the transition matrix T and assume that CP is conserved in the transition, $[T, CP] = 0$. Then we find

$$\langle f|T|P^0\rangle = \langle f|(CP)^\dagger(CP)T(CP)^\dagger(CP)|P^0\rangle \quad (1.6.4)$$

$$\langle f|T|P^0\rangle = e^{i(\zeta_P - \zeta_f)}\langle \bar{f}|T|\bar{P}^0\rangle \quad (1.6.5)$$

Defining the amplitude A as $A \equiv A(P^0 \rightarrow f) = \langle f|T|P^0\rangle$ and $\bar{A} \equiv A(\bar{P}^0 \rightarrow \bar{f}) = \langle \bar{f}|T|\bar{P}^0\rangle$, we find that a phase independent requirement of CP invariance in decay is

$$\left| \frac{\bar{A}}{A} \right| = 1 \quad (1.6.6)$$

There are three types of phases which one encounters in transition amplitudes that are traditionally referred to as weak, strong, and spurious phases. A weak phase is defined to be one which changes signs when one moves from the transition amplitude for a given process to the amplitude for the CP conjugate process, relating it to the product of CKM matrix elements. A strong phase is one which has the same sign in the two processes. Strong phases originate from final-state interaction scatterings from on-shell states. Having no physical relevance, spurious phases are global conventional relative phases between an amplitude and its CP conjugate amplitude resulting from the assumed CP transformation of the field operators as shown in Eq. 1.6.3.

We now assume that the amplitude A is the sum of amplitudes A_j corresponding, for example, to different Feynman diagrams for the process. We also assume that each amplitude contains a strong and weak phase $e^{i\delta_j}$ and $e^{i\phi_j}$ respectively:

$$A = \sum_j |a_j| e^{i\delta_j} e^{i\phi_j} \quad (1.6.7)$$

Then according to our previous discussion, we may write

$$\frac{\bar{A}}{A} = \left| \frac{\sum_j |a_j| e^{i(\delta_j - \phi_j)}}{\sum_j |a_j| e^{i(\delta_j + \phi_j)}} \right|, \quad (1.6.8)$$

which can alternatively be expressed as

$$|\bar{A}|^2 - |A|^2 = 2 \sum_{i,j} |a_i| |a_j| \sin(\phi_i - \phi_j) \sin(\delta_i - \delta_j). \quad (1.6.9)$$

Thus, one sees that it is necessary to have interfering amplitudes with both non-zero strong and weak relative phase differences in order to observe CP violation in direct decay.

1.6.2 Mixing of neutral mesons

Before discussing CP violation in mixing, it is necessary to review the SM formalism regarding the oscillations of neutral mesons. We continue to use the

notation P^0 and \bar{P}^0 to refer to a generic pseudo-scalar meson (possibly a K^0 , D^0 , B^0 , or B_s) and its anti-particle. Neglecting the weak force, the P^0 and \bar{P}^0 mesons would be stable and have the same mass. Decays to real and virtual final states and mixing between the P^0 and \bar{P}^0 are governed by the weak force. Generally, we can represent any state in the system by

$$a(t)|P^0\rangle + b(t)|\bar{P}^0\rangle + \sum_n c_n|n\rangle \quad (1.6.10)$$

However, we use an approximation first derived by Wigner and Weisskopf [33] in which we write the time evolution of the wave function without explicitly displaying the decays to the states $|n\rangle$ as

$$i\frac{d}{dt}\begin{pmatrix} \psi_1 \\ \psi_2 \end{pmatrix} = \begin{pmatrix} T_{11} & T_{12} \\ T_{21} & T_{22} \end{pmatrix} \begin{pmatrix} \psi_1 \\ \psi_2 \end{pmatrix} \quad (1.6.11)$$

In this approximation the Hamiltonian matrix \mathbf{T} is not Hermitian. We represent this matrix as

$$\mathbf{T} = \mathbf{M} - \frac{i}{2}\mathbf{\Gamma} \quad (1.6.12)$$

where \mathbf{M} and $\mathbf{\Gamma}$ are hermitian matrices governing the mass and lifetime of the P^0 and \bar{P}^0 respectively. The elements of these matrices are determined using second-order perturbation theory to be

$$M_{ij} = m_0\delta_{ij} + \langle i|H_w|j\rangle + \sum_n \mathcal{P} \frac{\langle i|H_w|n\rangle\langle n|H_w|j\rangle}{m_0 - E_n} \quad (1.6.13)$$

$$\Gamma_{ij} = 2\pi \sum_n \delta(m_0 - E_n)\langle i|H_w|n\rangle\langle n|H_w|j\rangle \quad (1.6.14)$$

where H_w contains the weak interactions inducing mixing and decay and \mathcal{P} indicates that we are to take the principal value of the sum over intermediate states to avoid the singularities where $m_0 = E_n$. Note, from these definitions and the matrix structure of 1.6.11, that indices i and j run over 1 and 2 where $1 \equiv P^0$ and $2 \equiv \bar{P}^0$. The off-diagonal elements of \mathbf{M} are determined by transitions through off-shell virtual intermediate states (second-order weak transitions in the SM) whereby $P^0 \leftrightarrow \bar{P}^0$ and $\bar{P}^0 \leftrightarrow P^0$. Note that the $\langle i|H_w|j\rangle$

transition amplitudes are zero in the SM since there are no first order $\Delta\text{Flavor} = 2$ processes (where an f quark is destroyed and an \bar{f} quark is created). The off-diagonal elements of Γ are given by on-shell transitions through real physical states to which both P^0 and \bar{P}^0 decay. CPT invariance requires $M_{11} = M_{22}$ and $\Gamma_{11} = \Gamma_{22}$ [29] which agrees with our intuition that P^0 and \bar{P}^0 have the same mass and lifetime in the flavor basis. This enables us to write the Hamiltonian as

$$T = \begin{pmatrix} M & M_{12} \\ M_{12}^* & M \end{pmatrix} - \frac{i}{2} \begin{pmatrix} \Gamma & \Gamma_{12} \\ \Gamma_{12}^* & \Gamma \end{pmatrix} \quad (1.6.15)$$

To determine the time evolution of the P^0 \bar{P}^0 system we first solve for the eigenvalues of the Hamiltonian and find

$$\begin{aligned} \mu_{\pm} &= T_{11} \pm (T_{12}T_{21})^{1/2} \\ &= \left(M \pm \text{Re}(T_{12}T_{21})^{1/2} \right) - \frac{i}{2} \left(\Gamma \mp 2\text{Im}(T_{12}T_{21})^{1/2} \right) \\ &= M_{\pm} - \frac{i}{2} \Gamma_{\pm} \end{aligned} \quad (1.6.16)$$

where we have defined M_{\pm} and Γ_{\pm} by the bracketed expressions in the second equation. We label the physical mass eigenstates with a subscript $+$ and $-$ to refer to the heavy and light one respectively, which follows the standard convention in the B system (in the K system it is customary to distinguish between the states by their lifetimes). Choosing a relative phase convention, we write the mass eigenstates as

$$\begin{aligned} |P_+\rangle &= N \left(p|P^0\rangle + q|\bar{P}^0\rangle \right) \\ |P_-\rangle &= N \left(p|P^0\rangle - q|\bar{P}^0\rangle \right) \end{aligned} \quad (1.6.17)$$

where $N = 1/\sqrt{|p|^2 + |q|^2}$. At this point we drop the overall normalization since it does not play any role in the following discussion. The mass and width difference between our neutral mesons is given by

$$\begin{aligned} \Delta m &\equiv M_- - M_+ = m_H - m_L \\ \Delta\Gamma &\equiv \Gamma_- - \Gamma_+ = \Gamma_H - \Gamma_L \end{aligned} \quad (1.6.18)$$

where Δm is positive by definition (the sign of $\Delta\Gamma$ needs to be determined from experiment). Solving for the eigenvector components, we find

$$\alpha \equiv \frac{q}{p} = \left(\frac{T_{21}}{T_{12}} \right)^{1/2} = \left(\frac{M_{12}^* - \frac{i}{2}\Gamma_{12}^*}{M_{12} - \frac{i}{2}\Gamma_{12}} \right)^{1/2} \quad (1.6.19)$$

1.6.3 CP violation in mixing

We shall shortly employ these results to describe the time evolution of the $P^0 \bar{P}^0$ system, but first we examine the condition necessary for the system to violate CP conservation by mixing. We define normalized states of definite CP by

$$|P_{CP=\pm}\rangle = \frac{1}{\sqrt{2}} \left(|P^0\rangle \pm e^{i\zeta} |\bar{P}^0\rangle \right) \quad (1.6.20)$$

where the kets $|P_{CP=\pm}\rangle$ are eigenstates of the CP transformation given by 1.6.3 corresponding to ± 1 eigenvalues. The CP operator commutes with the Hamiltonian only if CP is conserved. This implies that the mass eigenstates are also eigenstates of CP . By inspection with the definition of the mass eigenstates given in Eq. 1.6.17, we observe that the mass eigenstates will only be eigenstates of CP if α is a pure phase. Thus, the condition that CP be violated in mixing is equivalent to

$$|\alpha| = \left| \frac{q}{p} \right| \neq 1 \quad (1.6.21)$$

One can use Eq. 1.6.19 to show that this condition requires M_{12} and Γ_{12} to be collinear in the complex plane in order for CP to be conserved, a surprisingly simple condition given the potential number of real and virtual states available.

1.6.4 Time evolution of neutral mesons

We would now like to determine the time evolution of the $P^0 \bar{P}^0$ system. Recalling the form of the propagator in quantum mechanics, we write the evolution of the mass eigenstates as

$$|P_{\pm}(t)\rangle = P_{\pm}(0)e^{-i\mu_{\pm}t}|P_{\pm}\rangle \quad (1.6.22)$$

where $P_{\pm}(0)$ are the amplitudes at time zero. We'd like to determine the time evolution of the flavor eigenstates in terms of the flavor basis for reasons which will become clear shortly. After some algebraic manipulation, inverting Eq. 1.6.17 and eliminating the mass eigenstates, we find

$$\begin{aligned} |P^0(t)\rangle &= f_+(t)|P^0\rangle + \alpha f_-(t)|\bar{P}^0\rangle \\ |\bar{P}^0(t)\rangle &= \frac{1}{\alpha}f_-(t)|P^0\rangle + f_+(t)|\bar{P}^0\rangle \end{aligned} \quad (1.6.23)$$

where

$$f_{\pm} = e^{-iM_+t}e^{-\Gamma_+t/2} \pm e^{-iM_-t}e^{-\Gamma_-t/2} \quad (1.6.24)$$

and we assumed that our initial state was either pure P^0 or \bar{P}^0 . From this expression, we may calculate time dependent mixing probabilities. We find that the oscillation probability, or the probability to have a \bar{P}^0 at time t given a P^0 at time zero is

$$\text{Prob}(P^0 \rightarrow \bar{P}^0) = \frac{1}{4}|\alpha|^2 \left[e^{-\Gamma_+t} + e^{-\Gamma_-t} - 2e^{-\Gamma t} \cos(\Delta mt) \right] \quad (1.6.25)$$

where $\Gamma = (1/2)(\Gamma_+ + \Gamma_-)$. The expression for the probability of a \bar{P}^0 to oscillate to a P^0 may be found by letting $\alpha \rightarrow \alpha^{-1}$ in the above expression. The probability to have a P^0 at time t given a P^0 at time zero, or the probability *not* to have mixed, is given by

$$\text{Prob}(P^0 \rightarrow P^0) = \frac{1}{4}|\alpha|^2 \left[e^{-\Gamma_+t} + e^{-\Gamma_-t} + 2e^{-\Gamma t} \cos(\Delta mt) \right] \quad (1.6.26)$$

This unmixed probability is the same for a \bar{P}^0 and P^0 because of *CPT* symmetry.

1.6.5 Mixing phenomenology in the B^0 system

Thus far we have been completely generic in our discussion of the P^0 meson. However, for the purposes of this thesis we are interested in the simplifications that arise when we take the P^0 to be a B^0 meson, which is also referred to

as the B_d^0 or B_d meson. In the B_d system, it is expected that the lifetime difference is negligible relative to the meson lifetime,

$$\frac{\Delta\Gamma}{\Gamma} \sim \mathcal{O}(1\%) \quad (1.6.27)$$

Recall that the difference in width is generated by decays to real states that both the B^0 and \bar{B}^0 can reach. The branching fractions of these decays should be dominated by SM tree diagrams [34] which are not larger than 10^{-3} . Additionally, the amplitudes for these processes will interfere causing some cancellation in the sum. Consequently, $\Delta\Gamma$ and Γ_{12} are expected to be very small allowing us to simplify our previous results by setting $\Gamma_{\pm} = \Gamma$ and $\Delta\Gamma = 0$. Experimental measurements have found [11] that

$$\Delta m/\Gamma = 0.755 \pm 0.015 \quad (1.6.28)$$

indicating that model independently we may expect $\Gamma_{12} \ll M_{12}$ [34]. To set the scale for equations which will follow, we note that the B^0 mixing frequency has been measured to be

$$\Delta m = (0.489 \pm 0.008)\hbar \text{ ps}^{-1} \quad (1.6.29)$$

Furthermore, within the SM, we may calculate M_{12} and Γ_{12} as a cross-check to verify these approximations. The off-shell mixing amplitudes given by second order W -exchange box diagrams which contribute to M_{12} , shown in Fig. 1.4, are dominated in the SM by virtual top quarks running through the loops [35]:

$$M_{12} = \frac{G_F^2}{12\pi^2} m_B m_W^2 \eta_B B_B f_B^2 (V_{tb} V_{td}^*)^2 S_0(x_t) \quad (1.6.30)$$

where $x_t = m_t^2/m_W^2$, $\eta_B = 0.55$ is a QCD correction, $B_B f_B^2$ parameterizes the hadronic matrix element, and S_0 is a kinematic factor given approximately by [36]

$$S_0 = 2.4 \left(\frac{m_t}{170\text{GeV}} \right)^{1.52} \quad (1.6.31)$$

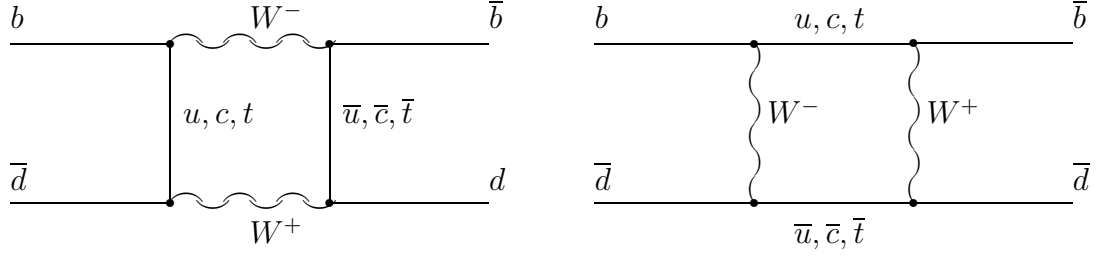


Figure 1.4: $B^0 \bar{B}^0$ mixing diagrams.

Using a calculation of Γ_{12} [37], we find that

$$\left| \frac{\Gamma_{12}}{M_{12}} \right| = \mathcal{O}(m_b^2/m_t^2) \ll 1 \quad (1.6.32)$$

as expected.

These results have important implications for the observation of CP violation in mixing in the B_d system. We recall that the condition for this type of CP violation is that $|\alpha| \neq 1$. Using the condition in Eq 1.6.32 and our definition of α from 1.6.19, we find

$$\alpha = \left(\frac{M_{12}^* - \frac{i}{2}\Gamma_{12}^*}{M_{12} - \frac{i}{2}\Gamma_{12}} \right)^{1/2} \approx \left(\frac{M_{12}^*}{M_{12}} \right)^{1/2} \quad (1.6.33)$$

which means that $|\alpha| = 1$ holds to $\mathcal{O}(m_c^2/m_t^2)$ [35]. Therefore, one does not expect to observe CP violation in mixing in the B_d system. The world averaged measurement of this quantity agrees, finding zero CP violating effects in mixing in the B_d system with a precision of less than 0.5% [11]. We also find, using the calculation of M_{12} given in 1.6.30,

$$\alpha = \frac{V_{tb}^* V_{td}}{V_{tb} V_{td}^*} = e^{-2i\phi_M} \quad (1.6.34)$$

where we have defined $2\phi_M$ as the CKM phase of the $B^0 \bar{B}^0$ mixing diagram shown in Fig. 1.4. Using the approximations derived in this section ($|\alpha| = 1$ and $\Gamma_{\pm} = \Gamma$), we may write the time-dependent formula for the mixing probabilities given by 1.6.25 and 1.6.26 in the B_d system as

$$\text{Prob(mixed)} = \frac{1}{2} e^{-\Gamma t} [1 - \cos(\Delta m t)] \quad (1.6.35)$$

$$\text{Prob(unmixed)} = \frac{1}{2} e^{-\Gamma t} [1 + \cos(\Delta m t)] \quad (1.6.36)$$

1.6.6 CP violation in mixing and decay

We may now use results from the previous sections to describe CP violation in the interference between mixing and decay, the type most relevant for this thesis. We shall focus on the time-evolution of the decays of B^0 and \bar{B}^0 mesons into common final CP eigenstates. We begin by rewriting the time dependence of our flavor states in the B_d system using the approximations found in section 1.6.5:

$$|B^0(t)\rangle = e^{-iMt}e^{-\Gamma t/2} \left[\cos(\Delta mt/2)|B^0\rangle + i\alpha \sin(\Delta mt/2)|\bar{B}^0\rangle \right] \quad (1.6.37)$$

$$|\bar{B}^0(t)\rangle = e^{-iMt}e^{-\Gamma t/2} \left[(i/\alpha) \sin(\Delta mt/2)|B^0\rangle + \cos(\Delta mt/2)|\bar{B}^0\rangle \right] \quad (1.6.38)$$

where we have used $M = (1/2)(M_+ + M_-)$. We define the amplitudes for a B^0 and \bar{B}^0 to a decay to the same final CP eigenstate f_{CP} as

$$A_{f_{CP}} \equiv \langle f_{CP}|B^0\rangle, \quad \bar{A}_{f_{CP}} \equiv \langle f_{CP}|\bar{B}^0\rangle \quad (1.6.39)$$

where the CP eigenvalue of f_{CP} is given by $\eta_{f_{CP}} = \pm 1$. We also define the phase invariant quantity $\lambda_{f_{CP}}$ as

$$\lambda_{f_{CP}} \equiv \alpha \frac{\bar{A}_{f_{CP}}}{A_{f_{CP}}} \quad (1.6.40)$$

Under a rephasing of the quark fields α , $\bar{A}_{f_{CP}}$, and $A_{f_{CP}}$ will change phases. However, it is straightforward to show that this rephasing cancels in the ratio.

With these definitions, we find that the amplitudes (Amp) of the B^0 and \bar{B}^0 decays to f_{CP} are given by

$$\begin{aligned} Amp(B^0(t) \rightarrow f_{CP}) &= e^{-iMt}e^{-\Gamma t/2} \left[A_{f_{CP}} \cos\left(\frac{\Delta mt}{2}\right) + i\alpha \bar{A}_{f_{CP}} \sin\left(\frac{\Delta mt}{2}\right) \right] \\ Amp(\bar{B}^0(t) \rightarrow f_{CP}) &= e^{-iMt}e^{-\Gamma t/2} \left[i\alpha A_{f_{CP}} \sin\left(\frac{\Delta mt}{2}\right) + \bar{A}_{f_{CP}} \cos\left(\frac{\Delta mt}{2}\right) \right] \end{aligned}$$

After some trigonometric substitutions and simplification using our above definitions, the time-dependent probability for an initial B^0 or \bar{B}^0 to decay to a

CP eigenstate is found to be ⁸

$$\begin{aligned}\Gamma(B^0(t) \rightarrow f_{CP}) &= |A_{f_{CP}}|^2 e^{-\Gamma t} \times \left[\frac{1 + |\lambda_{f_{CP}}|^2}{2} \right. \\ &\quad \left. + \frac{1 - |\lambda_{f_{CP}}|^2}{2} \cos(\Delta m t) - \Im \lambda_{f_{CP}} \sin(\Delta m t) \right] \\ \Gamma(\bar{B}^0(t) \rightarrow f_{CP}) &= |A_{f_{CP}}|^2 e^{-\Gamma t} \times \left[\frac{1 + |\lambda_{f_{CP}}|^2}{2} \right. \\ &\quad \left. - \frac{1 - |\lambda_{f_{CP}}|^2}{2} \cos(\Delta m t) + \Im \lambda_{f_{CP}} \sin(\Delta m t) \right] \end{aligned} \quad (1.6.41)$$

where again we have used $|\alpha| = 1$. A time-dependent CP asymmetry may be defined as ⁹

$$\mathcal{A}_{CP}(t) \equiv \frac{\Gamma(\bar{B}^0(t) \rightarrow f_{CP}) - \Gamma(B^0(t) \rightarrow f_{CP})}{\Gamma(\bar{B}^0(t) \rightarrow f_{CP}) + \Gamma(B^0(t) \rightarrow f_{CP})} \quad (1.6.42)$$

Substituting our previous expressions for the decay probabilities, we find

$$\mathcal{A}_{CP}(t) = -\frac{1 - |\lambda_{f_{CP}}|^2}{1 + |\lambda_{f_{CP}}|^2} \cos(\Delta m t) + \frac{2\Im \lambda_{f_{CP}}}{1 + |\lambda_{f_{CP}}|^2} \sin(\Delta m t) \quad (1.6.43)$$

We see that CP violation in interference between mixing and decay can be written as the sum of a cosine and sine term, where the coefficient of the cosine term is a function of $|\lambda_{f_{CP}}|$ and the coefficient of the sine term is a function of $\Im(\lambda_{f_{CP}})/|\lambda_{f_{CP}}|$. It is often written in the literature that a non-zero coefficient of the cosine terms probes direct CP violating effects (note that the coefficient vanishes when $|\lambda_{f_{CP}}| = 1$). Since we have already found in the B_d system that

$$|\lambda_{f_{CP}}| = |\alpha| \cdot \left| \frac{\bar{A}_{f_{CP}}}{A_{f_{CP}}} \right| = \left| \frac{\bar{A}_{f_{CP}}}{A_{f_{CP}}} \right| \quad (1.6.44)$$

one sees then that this statement merely reflects the condition that $|A_{f_{CP}}| \neq |\bar{A}_{f_{CP}}|$ which was shown to be the condition for direct CP violation in section 1.6.1.

⁸We follow the convention of using Γ to represent the amplitude for a decay process even though we are also using it to represent the inverse lifetime of the B^0 . Context should make the symbol meaning evident.

⁹Please note that the literature has not converged on a convention for the sign of this asymmetry.

Also, it was shown, if there is only one weak phase which contributes to the B^0 and \bar{B}^0 decay to the final state (either because there is only one amplitude or because all the amplitudes carry the same phase), that $|A_{f_{CP}}| = |\bar{A}_{f_{CP}}|$ and $|\lambda_{f_{CP}}| = 1$. In this case, the time-dependent asymmetry simplifies to

$$\mathcal{A}_{CP}(t) = \Im \lambda_{f_{CP}} \sin(\Delta mt) \quad (1.6.45)$$

In order to evaluate the phase of $\lambda_{f_{CP}}$, we recall from Eq 1.6.34 that α contributes the weak mixing phase difference, $e^{-2i\phi_M}$. Then, for this special case where only one weak phase (defined as $e^{i\phi_D}$) contributes to the decay to the final CP eigenstate, it can be demonstrated [34] that

$$\frac{\bar{A}_{f_{CP}}}{A_{f_{CP}}} = \eta_{f_{CP}} e^{-2i\phi_D} \quad (1.6.46)$$

We combine these results, finding

$$\lambda_{f_{CP}} = \alpha \frac{\bar{A}_{f_{CP}}}{A_{f_{CP}}} = \eta_{f_{CP}} e^{-2i(\phi_D + \phi_M)} \quad (1.6.47)$$

Thus, $\lambda_{f_{CP}}$ depends only on the sum of the *weak* mixing and decay phases which are directly dependent on CKM matrix elements. Both of these phases rotate under a rephasing of the quark fields but their sum still remains invariant. It is rather fortuitous that all hadronic elements and strong phases have vanished, allowing the time-dependent asymmetry to depend solely on the CKM parameters we had hoped to measure. Remember that the cancellation occurred because of the non-intuitive constraint we imposed on direct CP violation in Eq 1.6.9: namely that there must be *both* strong and weak relative phase differences in order for direct CP violation to be manifested in nature. The relative weak phase difference when only one weak phase contributes is trivially zero and even though strong decay phase differences may exist, the hadronic uncertainties associated with these phases are not relevant to the CP asymmetry. Combining these results, the time-dependent CP asymmetry becomes

$$\mathcal{A}_{CP}(t) = -\eta_{f_{CP}} \sin(2(\phi_M + \phi_D)) \sin(\Delta mt) \quad (1.6.48)$$

1.7 The golden decay $B^0 \rightarrow J/\psi K_S^0$

The decay $B^0 \rightarrow J/\psi K_S^0$ is often called “golden” because of its usefulness, both theoretical and experimental, in measuring CP violation in the interference between mixing and decay. The decay has a large branching fraction ($\sim 10^{-4}$), relative to other B^0 decays to CP eigenstates, with a clear signature and small backgrounds. We will quantify these statements in Chapter 4. Meanwhile, we will elucidate the value of this mode from a theoretical perspective.

1.7.1 Evaluating $\lambda_{J/\psi K_S^0}$

We developed a rather succinct expression (1.6.48) for CP violation in interference in the preceding sections which was predicated on the assumption that only one amplitude contributed to the decay to the final state. We first check the validity of this assumption for the golden mode $B^0 \rightarrow J/\psi K_S^0$. The Feynman diagrams for this decay are illustrated in Fig. 1.5. The color suppressed tree decay is shown on the left and the gluonic penguin decays on the right. The quark content of the tree decay is given by a $b \rightarrow c\bar{c}s$ transition. The term color suppression refers to the fact that the W^- must decay to a $\bar{c}s$ pair which carry the correct color for hadronizing into separate mesons (the s with the spectator d quark and the \bar{c} with the c quark from the b decay) with zero net color. We are interested in understanding the amount each diagram contributes to the final decay amplitude.

The CKM phase associated with the tree diagram is given by $V_{cb}V_{cs}^*$. There are three terms which contribute to the penguin amplitude depending on whether a u , c , or t quark is running through the loop. We write the sum of the amplitudes (including the tree as)

$$A(c\bar{c}s) = V_{cb}V_{cs}^*(T_{c\bar{c}s} + P_s^c) + V_{tb}V_{ts}^*P_s^t + V_{ub}V_{us}^*P_s^u \quad (1.7.1)$$

where $T_{c\bar{c}s}$ denotes the tree amplitude and P_s^q represent a penguin amplitude with a $q = u, c, t$ in the loop. We use the orthogonality constraint from the

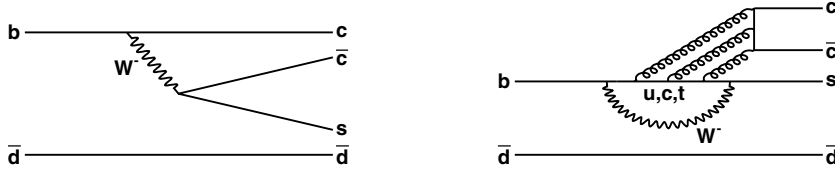


Figure 1.5: Feynman diagrams for the (left) color suppressed tree and (right) gluonic penguin decays for $B^0 \rightarrow J/\psi K_s^0$. Appendix A explains why the J/ψ couples to three gluons but not one or two.

second and third columns of the CKM matrix,

$$V_{cb}V_{cs}^* + V_{tb}V_{ts}^* + V_{ub}V_{us}^* = 0 \quad (1.7.2)$$

to eliminate $V_{cb}V_{cs}^*$ from the last equation. Then Eq. 1.7.1 becomes

$$A(c\bar{c}s) = V_{cb}V_{cs}^*(T_{c\bar{c}s} + P_s^c - P_s^t) + V_{ub}V_{us}^*(P_s^u - P_s^t) \quad (1.7.3)$$

We see that there are two weak phases which contribute to the decay $B^0 \rightarrow J/\psi K_s^0$. Using the Wolfenstein parameterization¹⁰ given in 1.5.11, we find that the magnitude of the ratio of the CKM factors associated with the pure penguin to penguin plus tree amplitudes is

$$\left| \frac{V_{ub}V_{us}^*}{V_{cb}V_{cs}^*} \right| = \left| \frac{A\lambda^4(\rho - i\eta)}{A\lambda^2} \right| = \lambda^2 \sqrt{\rho^2 + \eta^2} \sim \lambda^2 \quad (1.7.4)$$

where we have neglected terms $\mathcal{O}(\lambda^4)$.

Further, while the calculation of penguin amplitudes is problematic, it has been shown that the differences of penguin amplitudes are finite and well-defined [30]. The ratio of the contribution from the difference between a top and light quark penguin to the contribution from a tree diagram is of order

$$R_{PT} = \frac{P^t - P^{light}}{T} \sim \frac{\alpha_s}{12\pi} \ln \frac{m_t^2}{m_b^2} \sim \mathcal{O}(0.03) \quad (1.7.5)$$

¹⁰Remember that here $\lambda = \sin \theta_c$. It has nothing to do with $\lambda_{f_{CP}}$ discussed previously.

Consequently, we find that the second term of Eq. 1.7.3 is suppressed relative to the first by $R_{PT}\lambda^2$. This implies then that the decay $B^0 \rightarrow J/\psi K_S^0$ has effectively one decay amplitude ($V_{cb}V_{cs}^*$), meaning that the time-dependent asymmetry derived in 1.6.48 is free of hadronic uncertainties to $\mathcal{O}(10^{-3})$. As will now be shown, this decay allows for the theoretically cleanest measurement of a CKM parameter to date [30].

As we have justified the expression for $\lambda_{f_{CP}}$ given by Eq. 1.6.47, we now calculate $\lambda_{f_{CP}}$ for the CP eigenstate $J/\psi K_S^0$. This means we need to determine the CP eigenvalue of the final state, the mixing amplitude, and decay amplitude. Most of this work has already been done.

We first determine the CP eigenvalue of the state. Since the B^0 is a scalar particle, the J/ψ is a vector particle (with spin = 1), and the K_S^0 is a scalar, there must exist one unit of orbital angular momentum between the J/ψ and K_S^0 to conserve angular momentum in the decay. This adds a multiplicative factor of (-1) when determining the parity eigenvalue of the final state since $P = (-1)^L$, where L is the orbital angular momentum. Ignoring the small amount CP violation of the kaon system, the K_S^0 is an eigenstate of positive CP as is the J/ψ . Thus the CP eigenvalue of the final state is found to be

$$\eta_{J/\psi K_S^0} = (-1) CP(K_S^0) CP(J/\psi) = -1 \quad (1.7.6)$$

We have already found that the mixing phase of the B_d system, is given by

$$e^{-2i\phi_M} = \frac{M_{12}^*}{M_{12}} = \frac{V_{td}V_{tb}^*}{V_{td}^*V_{tb}} \quad (1.7.7)$$

Further, we have just shown that the single dominant decay amplitude contributes a phase factor

$$e^{-2i\phi_D} = \frac{V_{cb}V_{cs}^*}{V_{cb}^*V_{cs}} \quad (1.7.8)$$

There exists a complication that has been overlooked so far in this calculation. We originally stated that we were concerned with decays to a final CP eigenstate that were common to both the B^0 and \bar{B}^0 . However, the B^0 decays to $J/\psi K^0$ while the \bar{B}^0 decays to $J/\psi \bar{K}^0$. The resolution comes from the fact

that there is mixing in the neutral kaon system just as in the B system so that decays through both a K^0 and \bar{K}^0 can lead to a K_S^0 in the final state. Incorporating this fact will add the mixing phase from the kaon system to our calculation of the weak decay phase. To be precise,

$$\frac{\bar{A}_{J/\psi K_S^0}}{A_{J/\psi K_S^0}} = \frac{\langle K_S^0 | \bar{K}^0 \rangle \langle J/\psi \bar{K}^0 | T | \bar{B}^0 \rangle}{\langle K_S^0 | K^0 \rangle \langle J/\psi K^0 | T | B^0 \rangle} = \frac{\langle K_S^0 | \bar{K}^0 \rangle}{\langle K_S^0 | K^0 \rangle} \frac{V_{cb} V_{cs}^*}{V_{cb}^* V_{cs}} \quad (1.7.9)$$

Writing the analog of Eq. 1.6.17 for the neutral kaon system as

$$\langle K_S^0 | = p^* \langle K^0 | + q^* \langle \bar{K}^0 | \quad (1.7.10)$$

our ratio of decay amplitudes becomes

$$\frac{\bar{A}_{J/\psi K_S^0}}{A_{J/\psi K_S^0}} = \left(\frac{q^*}{p^*} \right)_K \frac{V_{cb} V_{cs}^*}{V_{cb}^* V_{cs}} \quad (1.7.11)$$

The CKM elements which dominant K^0 \bar{K}^0 mixing have been found to be $V_{cs}^* V_{cd}$ [35]. This calculation is not trivial as there is competition from the CKM suppressed term $V_{ts}^* V_{td}$ since it receives a kinematic enhancement. Recall that in the calculation of the mixing phase in the B system that each loop term carried a CKM phase of the same order so the top enhancement clearly dominated.

We combine these results to find:

$$\lambda_{J/\psi K_S^0} = \eta_{J/\psi K_S^0} e^{-2i\phi_M} e^{-2i\phi_D} \left(\frac{q^*}{p^*} \right)_K \quad (1.7.12)$$

$$= (-1) \left(\frac{V_{td} V_{tb}^*}{V_{td}^* V_{tb}} \right) \left(\frac{V_{cb} V_{cs}^*}{V_{cb}^* V_{cs}} \right) \left(\frac{V_{cs} V_{cd}^*}{V_{cs}^* V_{cd}} \right) \quad (1.7.13)$$

$$= - \left(\frac{V_{td} V_{tb}^* V_{cb} V_{cd}^*}{V_{td}^* V_{tb} V_{cb}^* V_{cd}} \right) \quad (1.7.14)$$

$$\lambda_{J/\psi K_S^0} = -e^{-2i\beta} \quad (1.7.15)$$

where we have used the definition of β from 1.5.16. In order to find the time-dependent asymmetry we note $\Im(\lambda_{J/\psi K_S^0}) = \sin 2\beta$ yielding

$$\mathcal{A}_{CP}(t) = \sin 2\beta \sin(\Delta m t) \quad (1.7.16)$$

For completeness, we also show the time-dependence of the B^0 and \bar{B}^0 decays to $J/\psi K_S^0$:

$$\Gamma_{B^0 \rightarrow J/\psi K_S^0}(t) = |A_{J/\psi K_S^0}|^2 e^{-\Gamma t} [1 - \sin 2\beta \sin(\Delta m t)] \quad (1.7.17)$$

$$\Gamma_{\bar{B}^0 \rightarrow J/\psi K_S^0}(t) = |A_{J/\psi K_S^0}|^2 e^{-\Gamma t} [1 + \sin 2\beta \sin(\Delta m t)] \quad (1.7.18)$$

where t is measured in the rest frame of the B and the meson was in the state $|B^0\rangle$ or $|\bar{B}^0\rangle$ respectively at time zero.

1.8 Measuring CP violation at *BABAR*

The discussion thus far has avoided addressing the non-trivial experimental issues concerning creating copious amounts of B mesons, detecting their decay products, and measuring their proper decay times in order to measure CP violation. These issues are addressed in the following sections leading to a slight refinement of some results already obtained. More detailed accounts of the experimental setup will follow in subsequent chapters.

1.8.1 Coherent B meson production at the $\Upsilon(4S)$

The PEP-II asymmetric-energy B Factory [40] at SLAC operates by colliding electrons and positrons at a center of mass energy near the $\Upsilon(4S)$ mass. The $\Upsilon(4S)$ is a bound $b\bar{b}$ vector meson whose mass lies above the threshold for decaying into B mesons. The $\Upsilon(4S)$ decays to $B^0 \bar{B}^0$ pairs and $B^+ B^-$ pairs about 50% of the time each. Since the $\Upsilon(4S)$ is produced through coupling to a virtual photon ($C = -1$), and since the electromagnetic interaction conserves C , the wave function of the $B^0 \bar{B}^0$ pair must also be an eigenstate of C with eigenvalue -1 . We write the total wave-function in the rest frame of the $\Upsilon(4S)$ as,

$$|\Psi(t_1, t_2)_{C=-1}\rangle = \frac{1}{\sqrt{2}} \left[|B^0(t_1); \vec{k}\rangle \otimes |\bar{B}^0(t_2); -\vec{k}\rangle - |\bar{B}^0(t_1); \vec{k}\rangle \otimes |B^0(t_2); -\vec{k}\rangle \right] \quad (1.8.1)$$

where \vec{k} ($-\vec{k}$) is the three-momentum of the right (left) moving meson. We substitute previous expressions from 1.6.38 for the time-dependence of $|B^0(t)\rangle$ and $|\bar{B}^0(t)\rangle$ and find [38]

$$\begin{aligned} |\Psi(t_1, t_2)_{C=-1}\rangle &= \frac{1}{\sqrt{2}} e^{-iM(t_1+t_2)} e^{-\Gamma(t_1+t_2)/2} \\ &\times \left[\cos(\Delta m(t_1 - t_2)/2) \left(|B^0; \vec{k}\rangle \otimes |\bar{B}^0; -\vec{k}\rangle - |B^0; \vec{k}\rangle \otimes |\bar{B}^0; -\vec{k}\rangle \right) \right. \\ &\left. - i \sin(\Delta m(t_1 - t_2)/2) \left(\frac{1}{\alpha} |B^0; \vec{k}\rangle \otimes |B^0; -\vec{k}\rangle - \alpha |\bar{B}^0; \vec{k}\rangle \otimes |\bar{B}^0; -\vec{k}\rangle \right) \right] \end{aligned}$$

Up until the time one of the mesons decays, $t_1 = t_2$ and the previous equation contains only a $|B^0; \vec{k}\rangle |\bar{B}^0; -\vec{k}\rangle$ or $|\bar{B}^0; \vec{k}\rangle |B^0; -\vec{k}\rangle$. The notation is somewhat cumbersome but the point is that the B s are evolving coherently. At any given instant before either decay, if one B is known to be a B^0 then the other B must be a \bar{B}^0 at that instant. Consequently if at time $t_{tag} = t_1$ one B decays to some final state which uniquely identifies its flavor as a B^0 , the other meson is known to be a \bar{B}^0 and will evolve forward in time as $|\bar{B}^0(t_2 - t_{tag})\rangle$. We connect this fact to our prior work by considering the probability of the B^0 decaying at time t_{CP} to an eigenstate of CP while the \bar{B}^0 decays at time t_{tag} to a state which uniquely identifies its flavor (thus the amplitude for the B^0 to decay to this state is zero). This yields

$$\begin{aligned} P(t_{CP}, t_{tag}) &= N e^{-\Gamma(t_{CP}+t_{tag})} |A_{CP}|^2 |A_{tag}|^2 \left\{ 1 + |\lambda_{f_{CP}}|^2 \right. \\ &\left. + (1 - |\lambda_{f_{CP}}|^2) \cos[\Delta m(t_{CP} - t_{tag})] - 2\Im(\lambda_{f_{CP}}) \sin[\Delta m(t_{CP} - t_{tag})] \right\} \end{aligned} \quad (1.8.2)$$

This is basically the same time-dependent behavior that was found in Eq. 1.6.41. Choosing the \bar{B}^0 to decay to a CP eigenstate and the B^0 to decay to a state which tags its flavor flips the sign of both the cosine and sine coefficient in the previous equation. Then, the generalization of the time-dependence for an event where one meson's flavor is tagged and the other decays to the CP eigenstate $J/\psi K_s^0$ is given by

$$f_{\pm} = \frac{\Gamma}{4} e^{-\Gamma|\Delta t|} \{ 1 \pm \sin 2\beta \sin(\Delta m \Delta t) \} \quad (1.8.3)$$

where $\Delta t = t_{CP} - t_{tag}$ and the + or - label indicates whether the tagging meson was a B^0 or \bar{B}^0 respectively. Fig. 1.6 shows the difference in time distributions for B^0 and \bar{B}^0 tags using a value of 0.75 for $\sin 2\beta$. The time-dependent asymmetry becomes

$$\mathcal{A}_{CP}(\Delta t) = \sin 2\beta \sin(\Delta m \Delta t) \quad (1.8.4)$$

We notice that the asymmetry is now a function of the difference of the proper time decays of the two mesons. If one was unable to measure the time of the tag, t_{tag} , relative to the time of the decay, t_{CP} , the asymmetry would vanish because the integral of 1.8.4 over the range $[-\infty, \infty]$ is null. Thus, in order to obtain information about the parameter $\sin 2\beta$ we must be able to resolve the time difference between the two B meson decays.

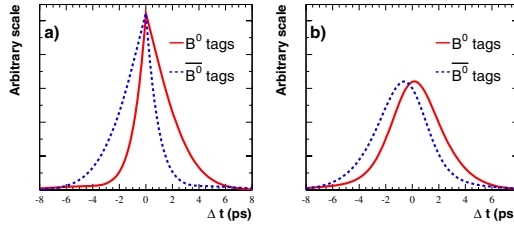


Figure 1.6: Distribution of Δt for B^0 (solid) and \bar{B}^0 (dashed) tagged CP events using an input value of 0.75 for $\sin 2\beta$ with a) perfect tagging and Δt resolution, and b) typical mistag rates and Δt resolution. Note that the asymmetry of the B^0 and \bar{B}^0 distributions with respect to $\Delta t = 0$ results from CP violation in the interference between decay and mixing.

1.8.2 Experimental challenges

In the preceding section, we mentioned three aspects necessary to observe CP violating effects in an $\Upsilon(4S)$ detector environment: (1) the production of large quantities of $B^0 \bar{B}^0$ pairs; (2) the ability to tag the flavor of a neutral meson (B_{tag}) when it decays; and (3) the ability to measure the proper decay time difference between the B_{tag} and a meson which decays to a CP eigenstate

(B_{CP}). To produce the large quantities of mesons needed, B-factory machines make luminosity (number of colliding beam particles per cross-sectional area per second) their highest priority. The specifics of how the PEP-II accelerator optimizes its beam parameters to achieve this goal will be detailed in Chapter 2. The second and third conditions have important experimental consequences that we will expand upon.

Recall that a B^0 meson has a $\bar{b}d$ quark content while a \bar{B}^0 has a $b\bar{d}$ quark content. The different flavors of this initial heavy b quark lead to different final states accessible to the B^0 and \bar{B}^0 . Semi-leptonic decays, for example, proceed through the emission of a W^- (W^+) by the $b(\bar{b})$ resulting in a negatively (positively) charged high energy lepton in the final state. Detection of this lepton allows one to determine the flavor of the decaying meson. The additional handles one uses to tag, such as the charge of kaons and the charge of pions from D^* decays, will be discussed further in Chapter 5.

The tagging algorithm has a non-negligible probability of determining the B_{tag} flavor incorrectly which we term the mistag rate w . The Δt probability distribution function of CP events given by Eq. 1.8.3 changes as a result:

$$\begin{aligned} f_{\pm} &= \frac{\Gamma}{4} e^{-\Gamma|\Delta t|} \{1 \pm (1-w) \sin 2\beta \sin(\Delta m \Delta t) \mp w \sin 2\beta \sin(\Delta m \Delta t)\} \\ &= \frac{\Gamma}{4} e^{-\Gamma|\Delta t|} \{1 \pm (1-2w) \sin 2\beta \sin(\Delta m \Delta t)\} \end{aligned} \quad (1.8.5)$$

Defining the dilution ¹¹ factor, $\mathcal{D} = (1-2w)$, the measured time-dependent asymmetry becomes

$$\mathcal{A}_{CP}(t) = \mathcal{D} \sin 2\beta \sin(\Delta m_d \Delta t) \quad (1.8.6)$$

The dilution also plays an important role in terms of the measurement's precision as will also be explained in Chapter 5.

We have shown that one must measure the proper decay-time difference, Δt , in order to measure CP violation. As the sum of masses of two B mesons

¹¹The term dilution is somewhat counter-intuitive as the best tagging algorithm has a dilution of one and the worst a dilution of zero.

approximately equals the $\Upsilon(4S)$ mass, the B s from the $\Upsilon(4S)$ decay have momenta in the $\Upsilon(4S)$ frame which is only $\sim 350 \text{ MeV}/c$ (implying $\gamma\beta \sim 0.07$). Therefore, if the $\Upsilon(4S)$ and detector rest frames are the same, the mean separation between the two B meson vertices will be about $60 \mu\text{m}$, a distance too small to be resolved with today's detectors.

To circumvent this problem of the B mesons decaying too near each other in the detector frame, one builds asymmetric e^+e^- colliders where one of the beams carries significantly larger energy than the other. At PEP-II, the $\Upsilon(4S)$ is produced moving along with the beam direction (z axis) with an average Lorentz boost $\langle\gamma\beta\rangle = 0.55$. Therefore, the proper decay-time difference Δt is, to an excellent approximation, proportional to the distance Δz between the two B^0 -decay vertices along the axis of the boost,

$$\Delta t \approx \frac{\Delta z}{c\langle\gamma\beta\rangle} \quad (1.8.7)$$

The average separation of the two B decay vertices is then $\Delta z = \Delta t\langle\gamma\beta\rangle c\tau_{B^0} \sim 260 \mu\text{m}$ while the RMS Δz resolution of the detector is about $180 \mu\text{m}$. Consequently, we are able to resolve the difference in the z vertex separation of the mesons which allows the CP asymmetry to be measured. Additionally, the finite resolution of the detector plays an important role in measuring this quantity. The methods by which this resolution is determined will be explained in Chapter 6. Figure 1.6 shows the effects of typical mistags and Δt detector resolution on the Δt distribution for tagged CP events.

1.9 Constraints on the unitarity triangle

Our main goal is to understand whether the KM mechanism can adequately describe CP violation in the B system where it has not yet been tested. From Fig. 1.3, we see that a measurement of $\sin 2\beta$ constrains the apex of the unitarity triangle whose area represents the size of the CP violating interference terms. There are other constraints on the apex of this triangle which result from both

CP conserving and CP violating processes. We detail those constraints now so that we may subsequently evaluate how well they agree with the measured value of $\sin 2\beta$ that we report in this thesis. This then accomplishes our goal of determining the consistency of the KM mechanism with CP violation in the B system.

The Wolfenstein parameterization of the CKM matrix given in Eq. 1.5.11 labels the four free CKM parameters A , λ , ρ , and η . We first note that the CKM elements of the upper left-hand 2×2 sector which govern first and second generation flavor transitions have been measured using tree level semileptonic decays to a precision of $\leq 7\%$. Specifically, measurements of semi-leptonic neutral and charged kaon decays yield

$$\lambda = |V_{us}| = 0.2196 \pm 0.0026. \quad (1.9.1)$$

One sees by inspection of the parameterization that $A = |V_{cb}|/|V_{us}|^2$. Heavy quark effective theory [41] provides a mostly model-independent treatment of semileptonic B decays to charmed mesons which has been used to calculate

$$|V_{cb}| = (41.2 \pm 2.0) \times 10^{-3}, \quad (1.9.2)$$

which in conjunction with Eq.1.9.1 determines A . Thus, semi-leptonic decays of B mesons and kaons have provided measurements of both A and λ .

Further inspection of Eq. 1.5.11 reveals that a measurement of $|V_{ub}|$ constrains the apex of the triangle by

$$\left(\frac{V_{ub}^*}{V_{cd}V_{cb}} \right) = \sqrt{\rho^2 + \eta^2} \quad (1.9.3)$$

Since $|V_{cd}| \sim \lambda$ by unitarity and $|V_{cb}|$ is known (Eq. 1.9.2), we see that a measurement of $|V_{ub}|$ determines a circle in the (ρ, η) plane centered at $(0, 0)$. Inclusive measurements of the lepton energy spectrum in $b \rightarrow ul\bar{\nu}$ decays above the endpoint of the $b \rightarrow cl\bar{\nu}$ lepton energy spectrum have been used along with exclusive semi-leptonic decays to determine

$$|V_{ub}| = (3.6 \pm 0.7) \times 10^{-3} \quad (1.9.4)$$

The large error on this parameter reflects its strong reliance on theoretical models to predict the endpoint of the lepton energy spectrum. The B Factories hope to reduce this error to the 10% level within the next few years.

The $B^0 \bar{B}^0$ oscillation frequency (Eq. 1.6.30) provides a constraint on $|V_{tb}V_{td}^*|$ with the largest uncertainty coming from lattice QCD calculations of the contribution from the B^0 decay and bag constants, $B_B f_B^2 = (1.30 \pm 0.12)(198 \pm 30 \text{ MeV})^2$. It is found that

$$|V_{tb}V_{td}^*| = 0.0079 \pm 0.0015 \quad (1.9.5)$$

Using the Wolfenstein parameterization, we find $|V_{tb}V_{td}^*| = A^2 \lambda^6 [(1 - \rho)^2 + \eta^2]$. A measurement of Δm_d then provides a constraint in the (ρ, η) plane in the form of a circle centered at $(1, 0)$ (the circle is really an annulus when the errors are taken into account).

A measurement of the oscillation frequency in the B_s system (Δm_s) provides a similar constraint. In fact, this will be one of the most anticipated measurements to be made by the CDF collaboration in RunII [42] as the uncertainty in $|V_{td}|$ is greatly reduced when one takes the ratio of mixing frequencies,

$$\frac{\Delta m_s}{\Delta m_d} = \frac{M_{B_s} B_{B_s} f_{B_s}^2 |V_{tb}^* V_{ts}|}{M_{B_d} B_{B_d} f_{B_d}^2 |V_{tb}^* V_{td}|} \quad (1.9.6)$$

because the lattice calculation of the ratio of bag and decay constants is much more reliable than the absolute calculation of their individual values. Until then, the current limit on B_s mixing of $\Delta m_s > 13.1 \text{ ps}^{-1}$ provides a circular constraint in the (ρ, η) plane.

An additional constraint exists from the CP violating complex parameter ϵ_K in the kaon system. One may show that $\mathcal{R}e(\epsilon_K)$ is a manifestation of CP violation in mixing while $\mathcal{I}m(\epsilon_K)$ is a manifestation of CP violation in the interference between decays with and without mixing [30]. A measurement of ϵ_K along with the value of $|V_{cb}|$, constrain the vertex of the unitarity triangle to lie on a hyperbola [43].

The constraints discussed on the vertex of the unitarity triangle from Δm_d , Δm_s , $|V_{ub}/V_{cb}|$, and ϵ_K , are displayed in Fig. 1.7 which was created by the CKMfitter package [44]. The figure depicts the constraints in the $(\bar{\rho}, \bar{\eta})$ plane where the expansion in λ has been extended out to greater accuracy by

$$\begin{aligned}\bar{\rho} &= \rho(1 - \lambda^2/2) \\ \bar{\eta} &= \eta(1 - \lambda^2/2)\end{aligned}$$

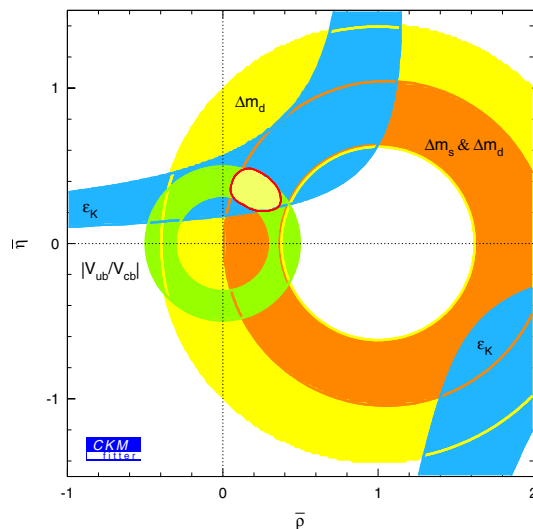


Figure 1.7: Constraints on the apex of the unitarity triangle from measurements of ϵ_K , Δm_d and Δm_s , and $|V_{ub}/V_{cb}|$.

The combination of all constraints prefers a solution for the apex which lies in the first quadrant. We note that a given measurement of $\sin 2\beta$ determines β up to a four-fold ambiguity. If one finds $\sin 2\beta = \Omega$, then we define $\chi \equiv \sin^{-1}(\Omega)$ and the allowed solutions for β are given by

$$\beta = \frac{\chi}{2}, \frac{\chi}{2} + \pi, \frac{\pi - \chi}{2}, \frac{3\pi - \chi}{2} \quad (1.9.7)$$

Further, it is fairly straightforward to show [45] that a measurement of $\sin 2\beta$ constrains the coordinates of the apex of the unitarity triangle by the equation

$$\sin 2\beta = \frac{2\bar{\eta}(1 - \bar{\rho})}{\bar{\eta}^2 + (1 - \bar{\rho})^2} \quad (1.9.8)$$

1.10 Previous measurements of $\sin 2\beta$

Measurements of $\sin 2\beta$ have been made previously by various collaborations. The first measurement was done by the OPAL collaboration at LEP in 1998 using a sample of 4.4 million hadronic Z^0 decays [46]. Reconstructing 24 signal $B^0 \rightarrow J/\psi K_s^0$ decays with a purity of 60%, they measured

$$\sin 2\beta_{OPAL} = 3.2_{-2.0}^{+1.8} \pm 0.5 \quad (1.10.1)$$

where the first error is statistical and the second is systematic. The large errors limit the usefulness of their result in resolving the apex of the unitarity triangle.

A second measurement was made by the ALEPH collaboration at LEP1 in 2000 using 4 million hadronic Z^0 decays [47]. Using 23 signal candidates with an estimated purity of 71% they found

$$\sin 2\beta_{ALEPH} = 0.84_{-1.04}^{+0.82} \pm 0.16 \quad (1.10.2)$$

The CDF collaboration at Fermilab reported results of their measurement also in 2000 which used 110 pb^{-1} of proton-antiproton collisions at a center of mass energy of 1.8 TeV [48]. They reconstruct a sample of $\sim 400 B^0 \rightarrow J/\psi K_s^0$ decays where $J/\psi \rightarrow \mu^+ \mu^-$ and $K_s^0 \rightarrow \pi^+ \pi^-$. They divide their sample into two groups based on whether the muon tracks from the J/ψ have information from the silicon detector. They employ different tagging algorithms for these two sets, measuring

$$\sin 2\beta_{CDF} = 0.79 \pm 0.39 \pm 0.16 \quad (1.10.3)$$

In 1999, the KEKB [49] and PEP-II B Factories began operation, each with the foremost goal of making a more precise measurement of $\sin 2\beta$ than had previously been achieved. Since then, both collaborations have met that goal nearly synchronously, updating their result every six months to a year with each new measurement superseding the previous one. This thesis reports on the latest result from *BABAR* [50] which used a data set of about 88 million

B decays to several CP eigenstates. A comparison with the most result from Belle [51] (and with all previous results) will be presented in Chapter 8.

Chapter 2

The *BABAR* detector

The data used in the analysis presented in this thesis consist of about 88 million $\Upsilon(4S) \rightarrow B\bar{B}$ decays collected between 1999-2002 with the *BABAR* detector at the PEP-II asymmetric-energy *B* Factory at SLAC. In this chapter, we present an overview of the PEP-II collider and *BABAR* detector. We attempt to highlight the physics goals that motivated the construction and the performance requirements of each subdetector. Emphasis will be given to the elements of the subdetectors which are essential to the measurement of $\sin 2\beta$. More in depth descriptions of PEP-II and the *BABAR* detector are given in Refs. [40, 52].

2.1 PEP-II

PEP-II, an upgrade of an e^+e^- storage facility constructed at SLAC around 1980 called the Positron-Electron Project (PEP), was designed specifically to meet the physics demands of measuring CP violation in the *B* system as outlined in Sec. 1.8. These demands, which require the production of approximately 100 million $B\bar{B}$ mesons and the ability to measure the separation between the decay vertices of the mesons, translate into constructing a high luminosity asymmetric energy e^+e^- collider operating at the resonance of the

$\Upsilon(4S)$ meson. Constraining the center of mass (c.m.) energy to the peak of the $\Upsilon(4S)$ resonance (10.58 GeV) leads to the hadronization of $b\bar{b}$ pairs into an $\Upsilon(4S)$. The $b\bar{b}$ pairs are created from the energy released by the annihilation of the electron and positron. The $\Upsilon(4S)$, in turn, decays nearly exclusively to pairs of B mesons. Fig. 2.1 shows a scan of the Υ resonances measured with the CLEO detector at CESR [53]. Coupling this B meson production mechanism with a luminosity of $3 \times 10^{33} \text{ cm}^{-2}\text{s}^{-1}$ satisfies the large data sample requirement on a timescale of a few years. The e^+ and e^- beams have energies of 3.1 and 9.0 GeV respectively, causing the $\Upsilon(4S)$ to be boosted by $\gamma\beta = 0.55$ in the lab frame. A boost of this value separates the average vertices of the two B mesons by $\sim 260 \mu\text{m}$ in the lab, a resolvable distance with current detector technology.

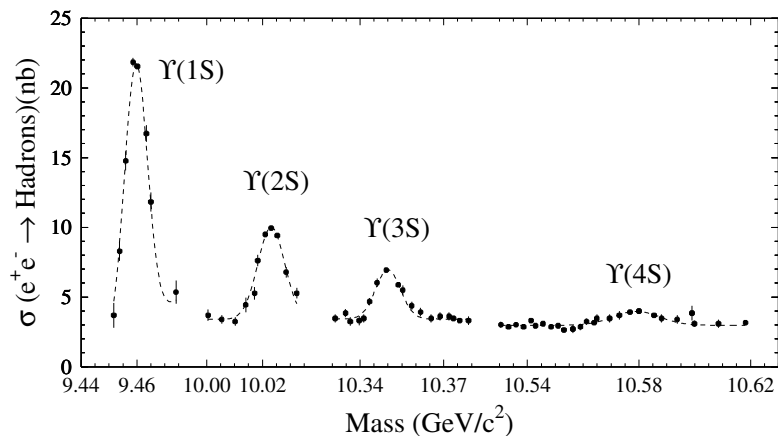


Figure 2.1: Scan of the hadronic cross section as a function of center of mass energy near the Υ mass made by the CLEO detector. Note the broad peak of the $\Upsilon(4S)$ which has the shortest lifetime since it sits above the kinematic limit for $B\bar{B}$ production. There are discontinuities in the horizontal axis scale.

While the beam energies are usually tuned to yield a center of mass energy equal to the peak of the $\Upsilon(4S)$ resonance, about 12% of the time they are adjusted so that the c.m. energy is 40 MeV lower. This allow studies of backgrounds where lighter quark anti-quark pairs ($u\bar{u}$, $d\bar{d}$, $s\bar{s}$, or $c\bar{c}$) are produced

from the energy released in the e^+e^- annihilation. These are called continuum events. Table 2.1 lists the $q\bar{q}$ production cross-sections from e^+e^- interactions at a c.m. energy equal to the peak of the $\Upsilon(4S)$ resonance. Continuum background events may be distinguished from the signal $B\bar{B}$ events based on the event shape as will be described in Chapter 4. Production of $b\bar{b}$ pairs accounts for about 24% of the $q\bar{q}$ production.

$e^+e^- \rightarrow$	cross-section (nb)
$b\bar{b}$	1.05
$c\bar{c}$	1.30
$u\bar{u}$	0.35
$s\bar{s}$	1.39
$d\bar{d}$	0.35
$\tau^+ \tau^-$	0.94
$\mu^+ \mu^-$	1.16
e^+e^-	~ 40

Table 2.1: Fermion anti-fermion production cross-sections at a c.m. energy equal to the $\Upsilon(4S)$ mass.

PEP-II consists of two independent storage rings, a Low Energy Ring (LER) of positrons which sits above a High Energy Ring (HER) circulating electrons, in a 2.2km circular tunnel. The rings receive the beams from a two mile long linear accelerator (linac). A schematic representation of the linac and the storage rings is shown in Fig. 2.2. Electrons are initially ejected from a semiconductor by polarized laser light and are then accelerated down the linac using microwave electromagnetic wave pulses produced by klystrons. After reaching an energy of ~ 1 GeV the electron beam is sent through a damping ring for focusing before being reinserted in the linac. A portion of the electrons are diverted from the linac and directed onto a tungsten target. This collision produces e^+e^- pairs whose positrons are extracted with magnets and sent to the beginning of the linac, to be accelerated in the same manner as the electrons, before being stored in the LER. The storage rings achieve high luminosity

by using large beam currents (1 – 2 Amperes) separated into many bunches. Table 2.2 lists some of the design and typical beam parameters of the storage rings. PEP-II has been able to exceed its design luminosity using fewer bunches than had been anticipated. The integrated luminosity delivered by PEP-II and recorded by the *BABAR* detector between 1999-2002 is shown in Fig. 2.3.

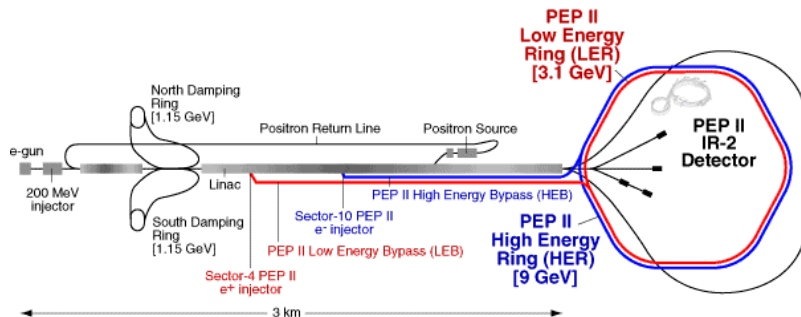


Figure 2.2: Schematic representation of SLAC linac which delivers electron and positron beams to the HER and LER.

Parameters	Design	Typical
Energy HER/LER (GeV)	9.0/3.1	9.0/3.1
Current HER/LER (A)	0.75/2.15	0.7/1.3
# of bunches	1658	553-829
Bunch spacing (ns)	4.2	6.3-10.5
σ_{Lx} (μm)	110	120
σ_{Ly} (μm)	3.3	5.6
σ_{Lz} (mm)	9	9
Luminosity ($10^{33} \text{ cm}^{-2}\text{s}^{-1}$)	3	3
Luminosity (pb^{-1}/d)	135	150

Table 2.2: Design and typical operation beam parameters of the PEP-II storage rings. HER and LER refer to the high energy electron and low energy positron rings respectively as explained in the text. The RMS size of the horizontal, vertical, and longitudinal luminous region are denoted σ_{Lx} , σ_{Ly} , and σ_{Lz} .

After circulating in the storage rings, the beams collide head-on at the interaction point (IP) before they are separated magnetically in the horizontal plane by a pair of dipole magnets (B1) located at ± 21 cm on either side of

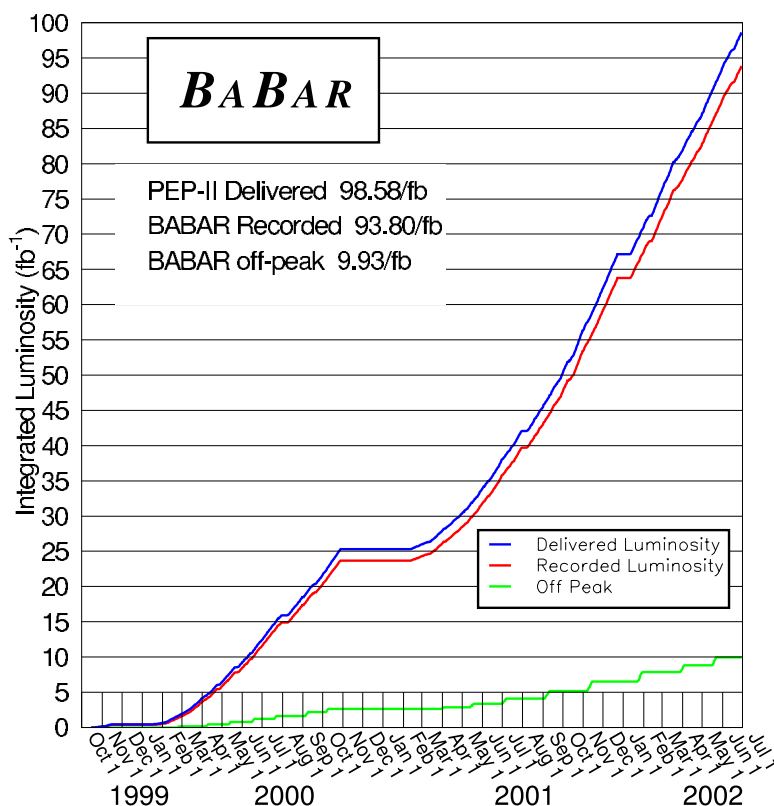


Figure 2.3: Integrated luminosity delivered by PEP-II (red curve) and recorded by the *BABAR* detector (blue curve) between 1999-2002 for data taken on the peak of the $\Upsilon(4S)$ resonance. The luminosity of data taken about 40 MeV below the peak is also shown (green curve).

the IP, followed by a series of offset quadrupole magnets used for strong focusing as shown in Fig. 2.4. The B1 dipoles are permanent magnets composed of samarium-cobalt, while the Q2, Q4, and Q5 quadrupoles are standard iron magnets. The interaction region is surrounded by a water-cooled beryllium beam pipe with an outer radius of 2.8 cm, which contributes about 1.06% of a radiation length at normal incidence (including the water layer). The beam pipe is wrapped with 150 μm of tantalum foil on either side of the IP, beyond $z = 10.1$ cm and $z = -7.9$ cm¹. The pair of Q1 magnets, B1 magnets, and the

¹ $z = 0$ is the nominal interaction point along the beam direction.

beam pipe are assembled into a rigid structure, along with the silicon vertex detector that will be discussed shortly, called the support tube. It has a diameter of roughly 43 cm, and contributes about 0.5% of a radiation length at normal incidence.

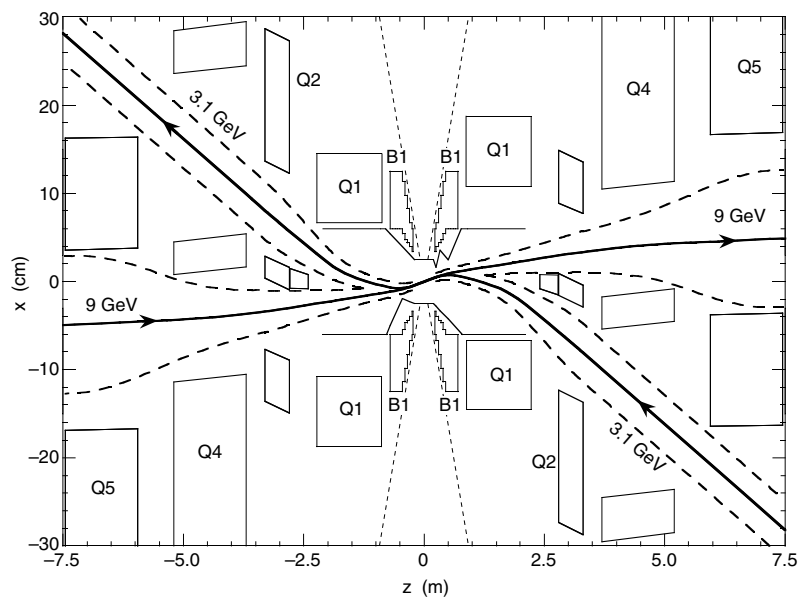


Figure 2.4: The interaction region plan view. Note the difference in the length scale of the two axes. The beams collide head-on, and are separated magnetically before the next collision by the B1 dipole magnets. The focusing of the beams is achieved by using the quadrupole magnets, Q1, Q2, Q4, and Q5. The dashed lines indicate the 300 mrad detector acceptance cutoff.

The large beam currents and number of closely-spaced bunches that make it possible for PEP-II to achieve its high luminosity have important consequences for the machine-induced backgrounds, as well as for the detector and interaction region layout. The detector geometry will be presented in Sec. 2.2. The primary accelerator backgrounds come from synchrotron radiation near the IP, interactions between the beam particles and residual gas molecules in the rings, and electromagnetic interactions generated by beam-beam collisions. The B1 separation dipoles reduce parasitic crossings at the expense of producing a large flux of synchrotron photons which must be absorbed by masks.

Beam particles may leave the ring if they lose sufficient energy through beam-gas bremsstrahlung or Coulomb scatter at a large angle from residual beam gas molecules. As the separation dipoles will bend energy-degraded particles with a larger curvature than the beam particles, most *BABAR* detector systems experience occupancy peaks and potential radiation damage from the LER and HER in the horizontal plane. Bremsstrahlung photons also contribute to radiation damage in the horizontal plane.

A trigger system is used to enhance the collection of interesting physics events with respect to background or common processes which occur much more frequently (Bhabha events). The trigger system operates as a conditioned sequence of two independent stages. The first level trigger (L1), with an output rate ≤ 2 kHz is implemented in hardware using data from the drift chamber, electromagnetic calorimeter, and neutral hadron detector. The second level trigger (L3) output rate is limited to 120Hz, using software algorithms to select events of interest that have passed L1. The L1 and L3 terminology is historical since the original trigger design included an intermediate decision processing stage L2. The L1 and L3 systems have met their design goal of 99% triggering efficiency for $B\bar{B}$ events at a luminosity of $3 \times 10^{33} \text{ cm}^{-2}\text{s}^{-1}$.

In Chapter 4, we discuss the event selection of neutral B mesons. Two important variables that will be used for this selection rely on a knowledge of the center of mass beam energy. The mean energies of the two beams are calculated from the total magnetic bending strength and the average deviations of the accelerating frequencies from their central values. The systematic uncertainty in the PEP-II calculation of the absolute beam energies is estimated to be 5 – 10 MeV. The RMS energy spreads of the LER and HER beams are 2.3 and 5.5 MeV, respectively, resulting in a 2.6 MeV spread in the total beam energy in the $\Upsilon(4S)$ frame.

Additionally, knowing the size and position of the luminous beam region (beam spot) will play an important role in the determination of the B meson vertex separation. As it is too small to be measured directly, the vertical size

is inferred from the measured luminosity, horizontal size, and beam currents. The vertical size varies by about $1 - 2 \mu\text{m}$. The transverse size and position are determined by analyzing the distribution of the distance of closest approach to the z -axis of the tracks in well measured two-track events as a function of azimuthal angle. The uncertainties in the average beam position are of the order of a few μm in the transverse plane and $100 \mu\text{m}$ along the beam axis. Variations between runs in the beam position are comparable to these uncertainties, indicating stability over the period of a run. Further, the results of an offline analysis which measures the primary vertices in multi-hadron events agree with the beam spot sizes measured by PEP-II. The horizontal, vertical, and longitudinal RMS size of the luminous region is typically $120 \mu\text{m}$, $5 \mu\text{m}$, and 9 mm respectively.

2.2 *BABAR* detector overview

The *BABAR* detector was designed to achieve the physics goals stated at the beginning of this chapter and to accommodate a high luminosity machine. These goals dictate the following requirements:

- a large acceptance down to small polar angles relative to the boost direction, implying an asymmetric detector construction;
- charged particle transverse momentum (p_t) reconstruction in the range $\sim 60 \text{ MeV} < p_t < \sim 4 \text{ GeV}$;
- excellent vertex resolution in directions parallel and transverse to the beam axis;
- efficient electron and muon identification with low misidentification probabilities for hadrons. This feature is essential for the reconstruction of charmonium ($c\bar{c}$) mesons and for flavor tagging;

- the ability to accurately discriminate between hadrons, specifically $K, \pi,$ and $p,$ over a wide momentum range for flavor tagging and for the reconstruction of exclusive final states like $B^0 \rightarrow K^+\pi^-$ and $B^0 \rightarrow \pi^+\pi^-;$
- good angular and energy resolution of photons from π^0 and radiative decays down to 20 MeV in energy;
- the capability to identify neutral hadrons.

The detector saw its first collisions in May of 1999. Figure 2.5 shows a longitudinal section through the detector center. The detector center is offset by 37 cm relative to the IP in the direction of the boost (the HER direction) to maximize acceptance. The detector consists of five major components: a silicon vertex tracker, a drift chamber, a particle identification detector, an electromagnetic calorimeter, and a neutral hadron and muon detector. The first three of these are surrounded by a superconducting coil designed to provide a 1.5 T axial magnetic field. The z -axis coincides with the principal axis of the drift chamber which is rotated by about 20 mrad relative to the beam axis. Detector acceptance extends from $-0.92 < \cos \theta < 0.94$ in the lab where $\theta = 0$ points along the boost direction.

The silicon vertex tracker (SVT) provides precise measurements of the angles and positions of charged tracks just outside the beam pipe. Additionally, the SVT functions as the lone tracker for low transverse momenta charged particles. The drift chamber (DCH) measures the momentum of charged particles and their energy loss due to ionization, which is used for particle identification purposes. The detector of internally reflected Cherenkov light (DIRC) identifies pions and kaons with momenta between 0.5 and 4.5 MeV/ c . The electromagnetic calorimeter (EMC), composed of thallium doped cesium iodide (CsI(TL)) crystals, detects electromagnetic showers and provides good photon identification and electron identification for electrons with energy greater than 0.5 GeV. The instrumented flux return (IFR) is designed to identify muons and neutral

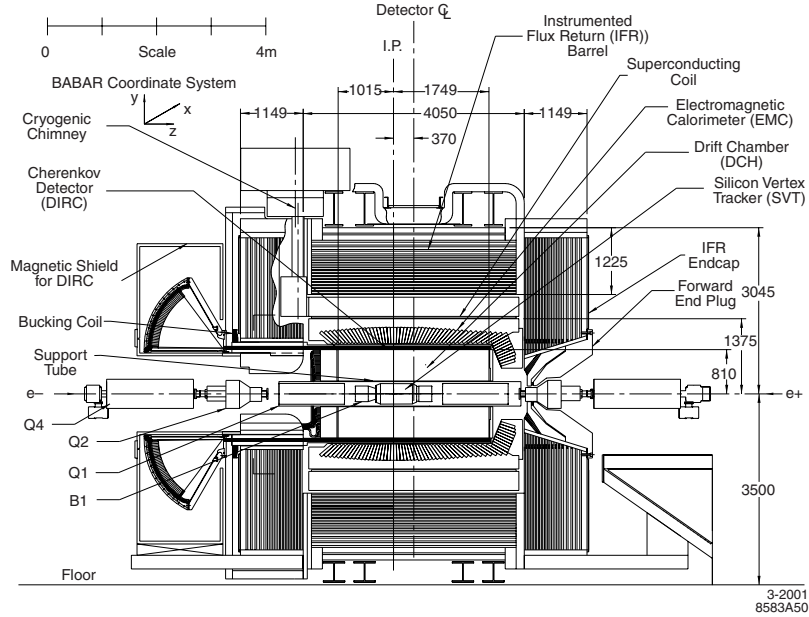


Figure 2.5: *BABAR* detector longitudinal section

hadrons (K_L^0 primarily). Some important design parameters of the detector are displayed in Table 2.3.

Parameter	Value
Tracking coverage($/4\pi$)	0.92
$\sigma(p_T)(\%)(1 \text{ GeV pions at } 90^\circ)$	0.36
$\sigma(z_0)(\mu\text{m})(1 \text{ GeV pions at } 90^\circ)$	52
Calorimetry coverage($/4\pi$)	0.90
X_0 before calorimeter(at 90°)	0.25
$\sigma(E)/E(\%)(1 \text{ GeV } \gamma \text{ at all angles})$	1.8
γ efficiency within acceptance (at 100 MeV)	0.92
Charged Hadron ID coverage($/4\pi$)	0.84

Table 2.3: Parameters of the *BABAR* detector. Acceptance coverages are given in the c.m. system.

We now present a more in-depth description of each subdetector. Since the measurement of $\sin 2\beta$ given in this thesis depends directly on the resolution of the distance between the two B decay vertices, which is determined primarily

by the SVT, we describe the SVT in more detail than the other subdetectors.

2.3 Silicon vertex tracker

The SVT was designed to provide precise reconstruction of charged particle trajectories and decay vertices near the interaction region. Since time-dependent CP asymmetries depend on a measurement of the separation of the B decay vertices when the mesons are produced coherently, the SVT is a crucial component of the *BABAR* experiment. The mean spatial resolution on the decay vertex along the z -axis of a fully reconstructed B^0 meson must be better than $80\ \mu\text{m}$ to avoid significant impact on the asymmetry measurement [54]. Additionally, the SVT must be capable of providing standalone tracking for charged particles with transverse momentum less than $120\ \text{MeV}/c$, the minimum that can be measured efficiently in the DCH alone. As multiple scattering is the dominant factor affecting tracking precision at momenta below about $1\ \text{GeV}/c$, it is critical to minimize the amount of material tracks will traverse.

The constraints imposed by these physics requirements led to building the SVT out of double-sided AC coupled silicon strip sensors in a five layer radial geometry. The spatial resolution for tracks perpendicular to the plane of the sensors is $10 - 15\ \mu\text{m}$ in the three inner layers and about $40\ \mu\text{m}$ in the two outer layers, which achieves the B vertex resolution listed above. The inner three layers measure track impact parameters while the outer two layers are required for pattern recognition to accomplish low p_t tracking.

2.3.1 SVT geometry

The double-sided silicon strip sensors are organized into modules. There are 6 straight modules in each of the inner three layers. There are 16 and 18 modules in layers four and five respectively that are arch-shaped. Figs. 2.6 and 2.7 show a transverse and longitudinal schematic view of the SVT. The

arch design minimizes the amount of silicon needed to cover the solid angle and avoids large angles between the incident tracks and the silicon wafers. The strips on opposite sides of each sensor are oriented orthogonally with the strips that measure the ϕ coordinate of a track (ϕ strips) running parallel to the beam and the strips that measure a track's z coordinate (z strips) running transverse to the beam axis.

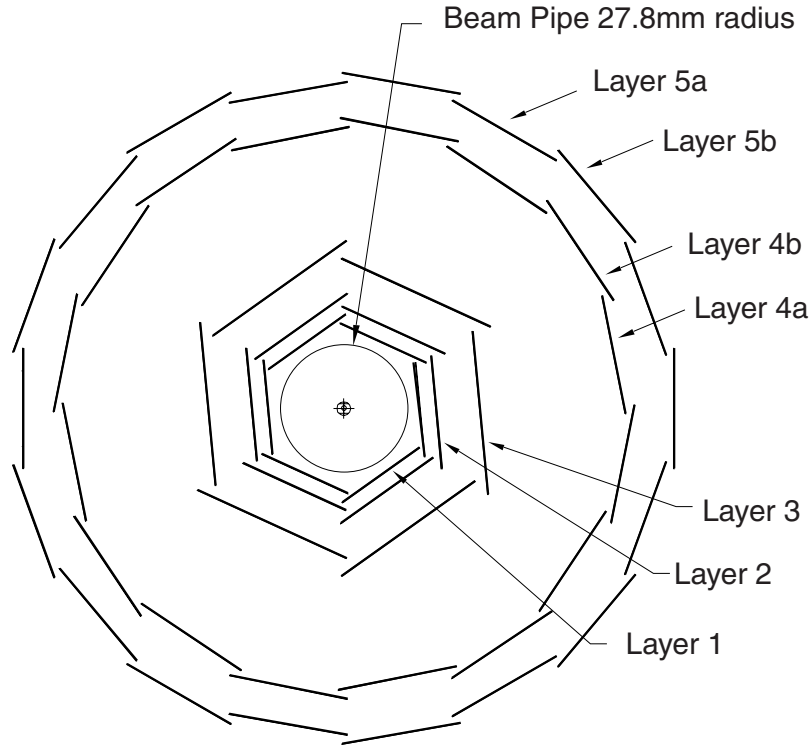


Figure 2.6: Schematic transverse view of SVT

A different sensor shape is required for the planar section of the modules in each layer of the SVT. The modules are electrically separated into forward and backward halves termed half-modules. The ϕ strips of sensors in the same half-module are electrically connected with wire bonds to form a single readout strip 140 mm (240 mm) long in the inner (outer) layers. There is a one-to-one correspondence between z strips and readout channels for the inner three layers, but in the outer two layers two z strips on different sensors are electrically con-

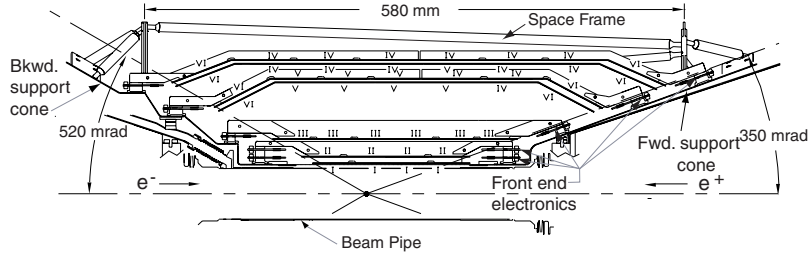


Figure 2.7: Schematic longitudinal view of SVT. The roman numerals label the different types of sensors.

nected (ganged) to one channel. The z strips are 50 or 100 mm long depending on whether one or two sensors are ganged.

The inner modules are tilted by 5° in ϕ which is useful for determining internal alignment since adjacent modules overlap. The arch geometry of the outer modules prevents tilting but gaps are avoided by dividing layers 4 and 5 into two sub-layers (a and b) mounted at slightly different radii. The total active silicon area is 0.96 m^2 covering 92% of the c.m. system solid angle.

A block diagram of SVT components is shown in Fig. 2.8. The major detector components are the silicon sensors, the *fanout* circuits, the *Front End Electronics* (FEE), and the data transmission system. The signals from the sensor strips arrive at the readout electronics by way of fanout circuits composed of conducting traces on a $50 \mu\text{m}$ Upilex (a Kapton-like material) substrate. The readout electronics are mounted outside the active detector volume to reduce multiple scattering. The fanout circuit and sensor unit is referred to as a Detector Fanout Assembly (DFA). The DFAs are wire bonded to thick film double-sided hybrid circuits called *High Density Interconnects* (HDIs) which hold the sensor ATOM (*A Time-Over Threshold Machine*) chips [55].

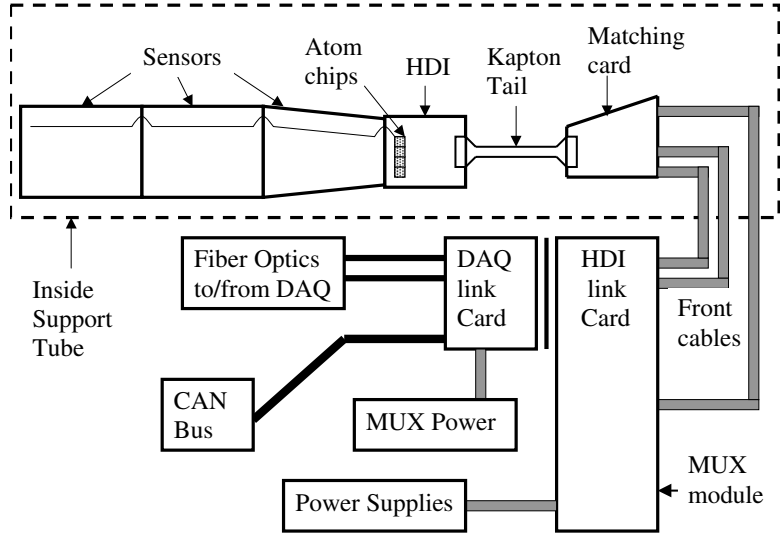


Figure 2.8: Schematic block diagram showing the different components of the SVT.

2.3.2 Silicon sensors

The silicon sensors are made of $300\ \mu\text{m}$ thick double-sided silicon strip devices. Since a minimum ionizing particle (MIP) typically loses $3.8\ \text{MeV}/\text{cm}$ to excitation of the surrounding medium, and the average energy required to create an electron-hole pair in silicon is $\sim 3.6\ \text{eV}$, the wafers yield large signals of $\sim 24,000$ electron-hole pairs per MIP. They are built on n-type substrates with p^+ strips and n^+ strips on the two opposite sides (there are individual p-stops to insulate the n^+ strips). The operating bias voltage is typically 10V above the depletion voltage which ranges from $25\text{-}55\text{V}$. The strips are biased on both sides with polysilicon resistors ($4\text{-}20\ \text{M}\Omega$). The strips are AC-coupled to electronics via integrated decoupling capacitors whose capacitance varies above a minimum value of $14\ \text{pF}/\text{cm}$. To achieve the necessary spatial resolution while reducing the number of readout channels, most of the modules have a *floating strip* (a strip which is not read-out) between two readout strips. The physical strip pitch is $50\ \mu\text{m}$ in most layers while the readout pitch is $50\ (100)\ \mu\text{m}$ on

the $\phi(z)$ side in the inner layers, increasing to 100 (200) μm in layers four and five. Leakage currents were measured to be 50 nA/cm² on average at 10V above depletion. A simplified schematic representation of a wafer is shown in Fig. 2.9.

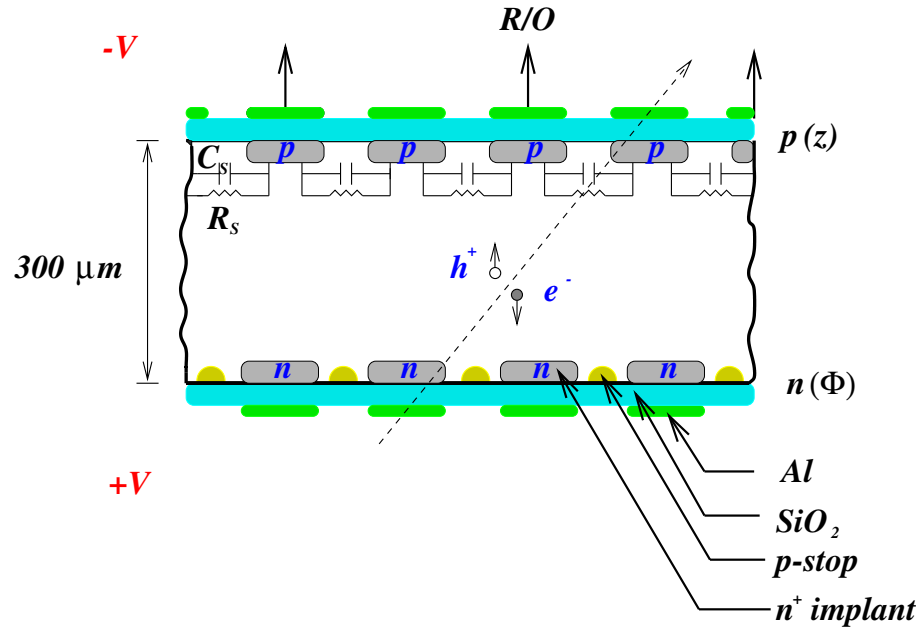


Figure 2.9: A simplified representation of an inner-layer SVT wafer. The implants are capacitively coupled to the aluminum readout strips. The p^+ -stops on the $n(\phi)$ side serve to isolate the n^+ implants. Figure courtesy of Natalia Kuznetzova.

2.3.3 Front end electronics

As previously described, the ATOM chips are mounted on the HDIs outside of the active detector volume. This chip is depicted schematically in Fig. 2.10. The chip contains 128 channels each of which consists of a charge-sensitive preamplifier followed by a shaper. The output of the shaper signal is sent to a programmable-threshold comparator which counts the width of the pulse (*Time over Threshold*, ToT). The ToT is a quasi-logarithmic function of the collected charge. This output is stored in a circular buffer at 30 MHz until requested

by the Level 1 (L1) trigger at which point the ToT, time of the hit sensor, and strip address are formatted, serialized, and delivered. Each channel also contains a test charge injection circuit used for calibration. Since the average noise behavior of the ATOM varies between $\sim 800 - 1600$ electrons depending on the capacitance of the strips, the signal to noise ratio for a MIP is larger than 1 σ .

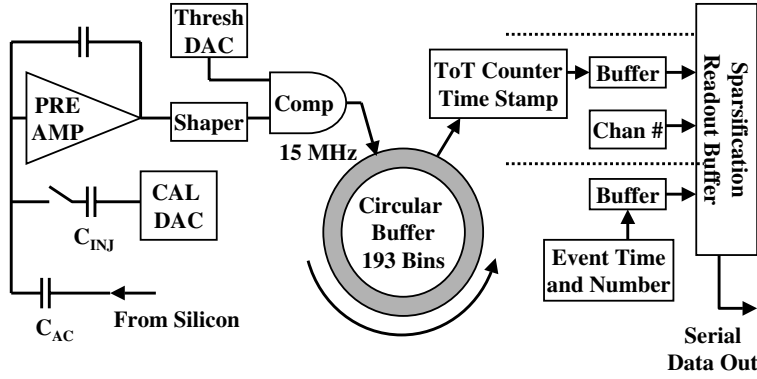


Figure 2.10: Schematic diagram of the ATOM front end integrated circuit. There are 128 channels on each chip. The ATOM chip is described in detail in Ref. [55].

2.3.4 Alignment

There are two stages to the alignment of the SVT. In the first, the relative positions of the 340 silicon sensors are determined. This is called "local" alignment. Following this, the SVT is aligned as a whole within the global coordinate system defined by the DCH. The separation of the process into these stages results from the stability in time of the local positions compared to the global one. Additionally, as the local alignment procedure is considerably more complex, the global alignment can be updated on a run-by-run basis while the local alignment constants can be changed as needed. Uncertainty in the local alignment leads to a systematic error in the determination of $\sin 2\beta$ that will

be discussed in Chapter 9.

Primarily tracks from $e^+e^- \rightarrow \mu^+ \mu^-$ (dimuon) and cosmic rays events, which may be collected in a few days of normal running conditions, are used for the local alignment procedure. In the dimuon events, each track is fit with a Kalman filtering technique [56] that utilizes the known beam momentum as a constraint. The cosmic events are used to eliminate any systematic distortion due to imprecision in the knowledge of the beam momenta. The track parameters are determined without using any information from the DCH. An optical survey with a measurement precision of $4 \mu\text{m}$ was performed during the assembly of the SVT. This survey is used only to constrain sensors relative to each other within the same module. With the optical information and the hit residuals from the muon tracks, a χ^2 for each sensor is iteratively minimized with respect to the sensor's six local parameters. The procedure yields an internally consistent local alignment by employing the combination of constraints from the overlapping region of the silicon sensors, the muon Kalman fits, the cosmic rays, and the optical survey.

The second step in the alignment process determines the relative position of the now rigid body SVT with respect to the DCH. Tracks with sufficient SVT and DCH hits are fit once using the information from only one of the two detectors. Three translation and three rotation parameters are determined by minimizing the difference between the track parameters obtained from both fits. This alignment is performed every few hours and the constants obtained are used to reconstruct the data in the subsequent run, a procedure known as *rolling calibrations*.

Fig. 2.11 compares the optical alignment made during the SVT assembly in February 1999 and a local alignment (made without the use of the optical constraints) using data taken during January 2000. The second set of plots shows the difference in alignment sets for data taken in January 2000 as compared to March 2000. In general, the stability of the inner three layers is very good.

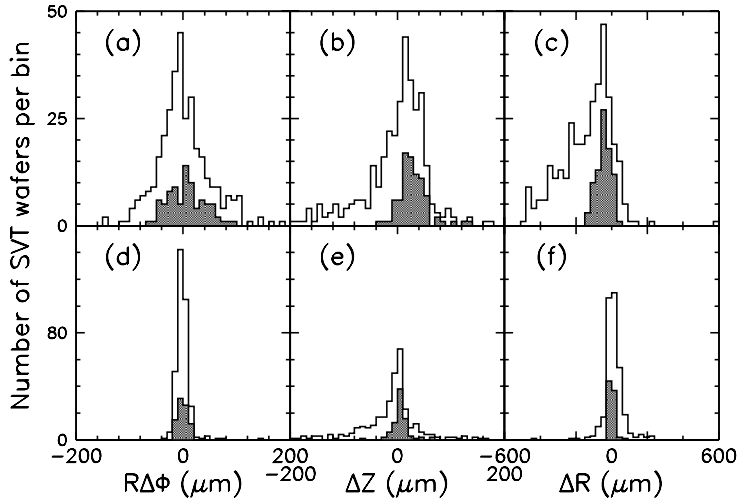


Figure 2.11: Comparison of a local alignment of the SVT sensors using data from January 2000 with the optical survey made during assembly in 1999 in the (a) $r\Delta\phi$, (b) Δz , and (c) Δr coordinates. Plots (d), (e), and (f) show the difference between two local alignments as explained in the text for the $r\Delta\phi$, Δz , and Δr coordinates, respectively. In all plots, the shaded regions correspond to the sensors in the first three layers, which are seen to be relatively stable over time.

2.3.5 Performance

The efficiency of the SVT in adding hits to tracks is calculated for each half-module by comparing the number of associated hits to the number of tracks crossing the module. Excluding defective readout sections (9 out of 208), a combined hardware and software efficiency of 97% is measured. The spatial resolution, with which we are most concerned, is determined using high momentum tracks in two prong events by measuring the distance in the plane of the sensor between the track trajectory and the hit. Subtracting the uncertainty in the track trajectory from the residuals allows one to obtain the hit resolution. Fig. 2.12 shows the SVT hit resolution for z side hits as a function of track incident angle for each SVT layer. The measured resolutions are in agreement with those necessary to determine the vertex separation of B meson decays as listed in Sec. 2.3.

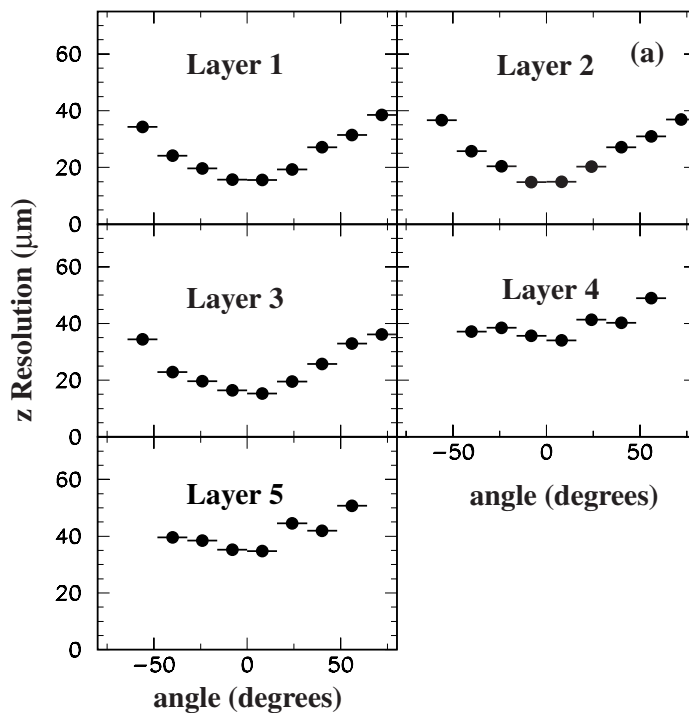


Figure 2.12: SVT hit resolution in the z coordinate in microns plotted against the track incident angle in degrees for each layer of the SVT. Note that a resolution of $10 - 15 \mu\text{m}$ is achieved in the inner layers, a precision necessary to measure B decay vertices to $80 \mu\text{m}$.

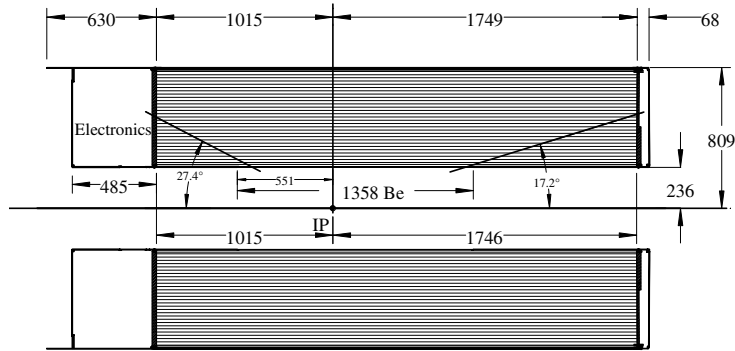
2.4 Drift chamber (DCH)

The main purpose of the DCH is to provide efficient detection of charged particles and to measure their momenta and angles with high precision. At lower momenta, these measurements dominate the errors on the extrapolation of the tracks to the subdetectors lying outside the DCH. Track parameter uncertainties at the DIRC add to the uncertainty in the measurement of the Cherenkov angle. The DCH must supply information for the charged particle trigger with a maximum time jitter of $0.5 \mu\text{s}$. Additionally, the DCH must measure the ionization loss (dE/dx) of charged tracks in order to yield infor-

mation on particle identification (PID). In the extreme forward and backward regions (outside the DIRC's acceptance), the DCH is the sole detector used for determining particle identification. The DCH is described in detail in Ref. [57].

2.4.1 DCH design

A schematic longitudinal cross section of the DCH and its dimensions are shown in Fig. 2.13. The DCH is a cylinder 280 cm in length with an inner radius of 23.6 cm, an outer radius of 80.9 cm, and 2.4 cm thick aluminum endplates. It extends beyond the backward endplate by 48.5 cm to house the readout electronics, HV distribution, cables, and an RF shield. The DCH is shifted forward relative to the IP in the direction of the boost so that particles emitted at polar angles of 17.2° traverse at least half of the layers before encountering the front endplate.



BaBar Drift Chamber

AMB 97-10-15

Figure 2.13: Side view of the *BABAR* drift chamber. The dimensions are in mm.

The DCH has 40 layers of small hexagonal cells to provide up to 40 spatial and ionization loss measurements for charged particles with transverse momentum greater than $180 \text{ MeV}/c$. Longitudinal position information is obtained by placing the wires in 24 of the 40 layers at small angles with respect to the

z -axis. The DCH utilizes low-mass aluminum field wires and a 80:20 gas mixture of helium:isobutane which together present 0.2% of a radiation length of material. Properties of the gas mixture are shown in Table 2.4.

Parameter	Values
Mixture He : C ₄ H ₁₀	80:20
Radiation Length	807 m
Primary Ions	21.2/cm
Drift Velocity	22 $\mu\text{m}/\text{ns}$
Lorentz Angle	32°
dE/dx Resolution	6.9%

Table 2.4: Properties of helium-isobutane gas mixture at atmospheric pressure and 20°C. The drift velocity is given for operation without magnetic field, while the Lorentz angle is stated for a 1.5 T magnetic field.

The 40 cylindrical layers of cells are grouped into ten superlayers of four each, with the same wire orientation and equal numbers of cells in each layer within the superlayer. Sequential layers are displaced by half a cell length. The stereo angles of the superlayers alternate between axial (A) and stereo (U,V) pairs, in the order AUVAUVAUVA, as shown in Fig. 2.14. The stereo angles vary between ± 45 mrad and ± 76 mrad. The drift cells are hexagonal in shape which produces an approximate circular symmetry over a large portion of the cell in terms of drift times. Each cell consists of one tungsten-rhenium sense wire 20 μm in diameter tensioned with a 30 gram weight surrounded by six field wires. The field wires are held at ground potential and the sense wires at a normal operating potential of 1960 V leading to an avalanche gain of approximately 5×10^4 .

The drift chamber electronics is designed to detect the leading edge of the signal from charge arriving at a sense wire and digitize the drift time with 1 ns resolution leading to a position resolution of 140 μm averaged over the cells. A measurement of dE/dx requires integrating the total charge in the pulse. These goals are accomplished using a 4-bit TDC for time measurement, a slow

shaper, and a 6-bit 15 MHz FADC to digitize the the total deposited charge.

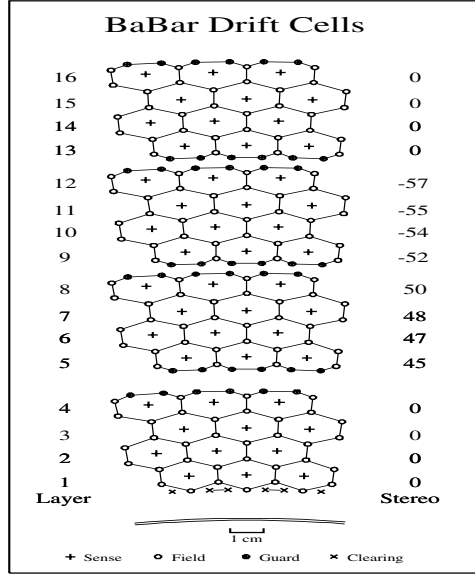


Figure 2.14: Schematic layout of drift cells for the four innermost superlayers. Lines have been added between field wires to aid in visualization of the cell boundaries. The numbers on the right side give the stereo angles (mrad) of sense wires in each layer.

2.4.2 DCH performance

The absolute DCH track reconstruction efficiency is determined as the ratio of the number of reconstructed DCH tracks to the number of tracks reconstructed by the SVT, after requiring that the SVT tracks fall within the DCH acceptance. Studies have been performed for different samples of multi-hadron events. Fig. 2.15 shows the reconstruction efficiency as a function of transverse momentum and polar angle for data taken at operating voltages of 1900 and 1960V for one such study. The measurement errors are dominated by the uncertainty in the correction for fake tracks in the SVT.

As discussed, while the position and angle measurements near the IP are dominated by the SVT measurements, the DCH contributes primarily to the

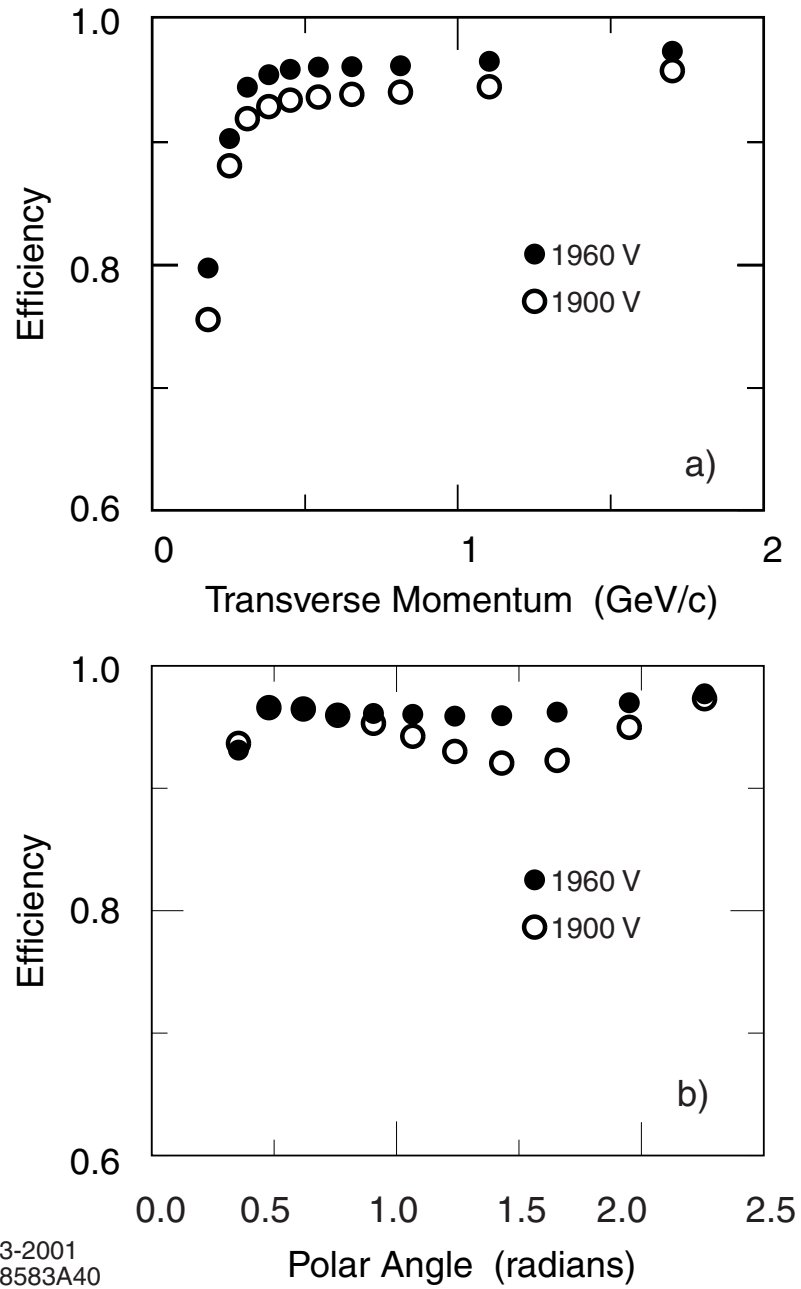


Figure 2.15: The track reconstruction efficiency in the DCH as a function of a) transverse momentum and b) polar angle for operating voltages of 1900 and 1960V. Both voltages were used for recording the data that is used in this analysis.

p_T measurement. Fig. 2.16 shows the resolution in the transverse momentum derived from cosmic ray muons. The data are well represented by a linear function,

$$\sigma(p_T)/p_T = (0.13 \pm 0.01)\% \times p_T + (0.45 \pm 0.03)\% \quad (2.4.1)$$

where the transverse momentum p_T is measured in GeV/c .

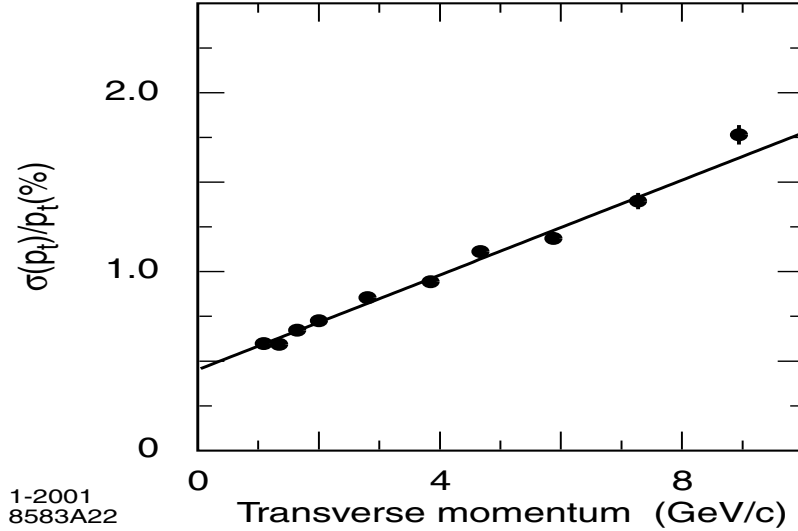


Figure 2.16: Resolution in the transverse momentum p_T determined from cosmic ray muons.

2.5 Detector of internally reflected Cherenkov light (DIRC)

The DIRC is a novel ring-imaging Cherenkov detector designed to efficiently identify kaons used for tagging the flavor of B mesons (from the cascade decay $b \rightarrow c \rightarrow s$) where kaon momenta extend up to about $2 \text{ GeV}/c$. Additionally, the DIRC must help distinguish between the two-body decays $B^0 \rightarrow \pi^+\pi^-$ and $B^0 \rightarrow K^+\pi^-$ which necessitates separating kaons from pions up to $4 \text{ GeV}/c$ at large polar angles in the laboratory frame. The DIRC is described in detail in Ref. [58].

2.5.1 DIRC geometry

Charged particles that traverse a radiator with a velocity greater than the velocity of light in the radiator emit photon radiation at an angle characteristic of their velocity, termed the Cherenkov angle. The DIRC relies on the preservation of the Cherenkov angle of photon radiation by total internal reflection from a flat surface. Fig. 2.17 shows a schematic of the DIRC geometry. The DIRC radiator consists of 144 long straight bars of synthetic quartz with rectangular sections, arranged in a 12-sided barrel structure. The bars are 4.9 m in length with a transverse area of 6 cm². The Cherenkov angle θ_c of the radiation is related to the velocity v of a charged particle by $\cos \theta_c = 1/(nvc)$, where c is the speed of light and n is the mean index of refraction of fused silica ($n = 1.473$). To avoid instrumenting both ends of the bars with photon detectors, a mirror is placed at the forward end to reflect incident photons to the backward, instrumented end.

Once photons arrive at the backward end, most of them emerge into a purified water-filled expansion region (whose volume is about six cubic meters) called the *standoff box* (SOB). The refractive index of the water matches reasonably well that of the bars which minimizes total internal reflection at the water-quartz interface. Cherenkov photons are detected in the visible and the near-UV range by a close-packed array of linear focused 2.82 cm diameter photomultiplier tubes (PMTs). A fused silica wedge at the exit of the quartz bar reflects photons at large angles relative to the bar axis which reduces the area requiring instrumentation. There are about 11,000 PMTs at the rear of the SOB that are nearly 1.2 m away from the end of the bars. The expected Cherenkov light pattern at the PMT surface is a conic section, where the cone opening angle is θ_c modified by refraction at the exit from the fused silica wedge.

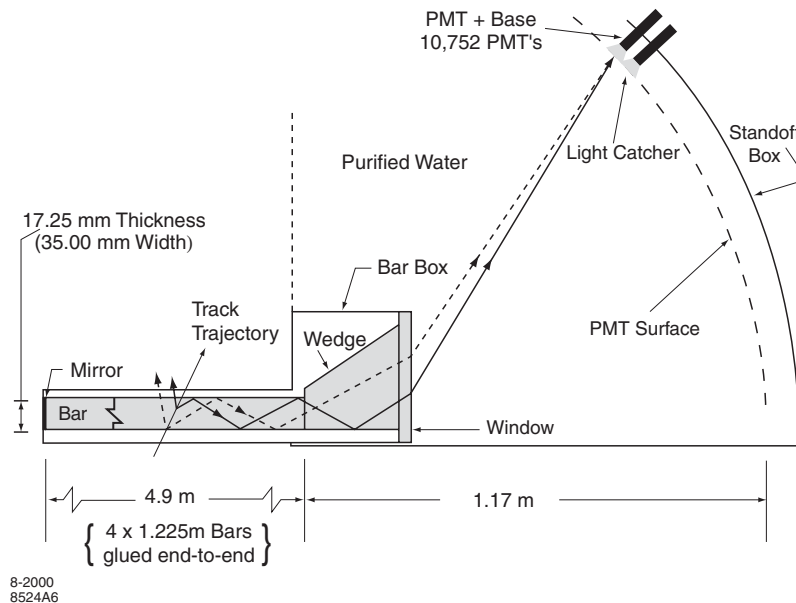


Figure 2.17: Schematics of the DIRC fused silica radiator bar and imaging region.

2.5.2 DIRC performance

The resolution on the track Cherenkov angle (σ_{θ_c}) scales like

$$\sigma_{\theta_c} = \sigma_\gamma / \sqrt{N_\gamma} \quad (2.5.1)$$

where σ_γ is the single photon Cherenkov angle resolution and N_γ is the number of photons detected. The single photon angular resolution has been determined to be 10.2 mrad using a sample of dimuon events where the mean number of photons in these events at normal incidence is about 30. This leads to a 2.5 mrad track Cherenkov angle resolution for the dimuon events which can be extrapolated, using the difference between the expected Cherenkov angles of charged pions and kaons, to a pion-kaon separation power of 4.2σ at a momentum of $3 \text{ GeV}/c$. The efficiency for correctly identifying a charged kaon that traverses the DIRC and the probability to wrongly identify a pion as a kaon are determined using $D^0 \rightarrow K^- \pi^+$ decays selected from inclusive D^* production and are shown in Fig. 2.18 for a particular choice of selection criteria. The

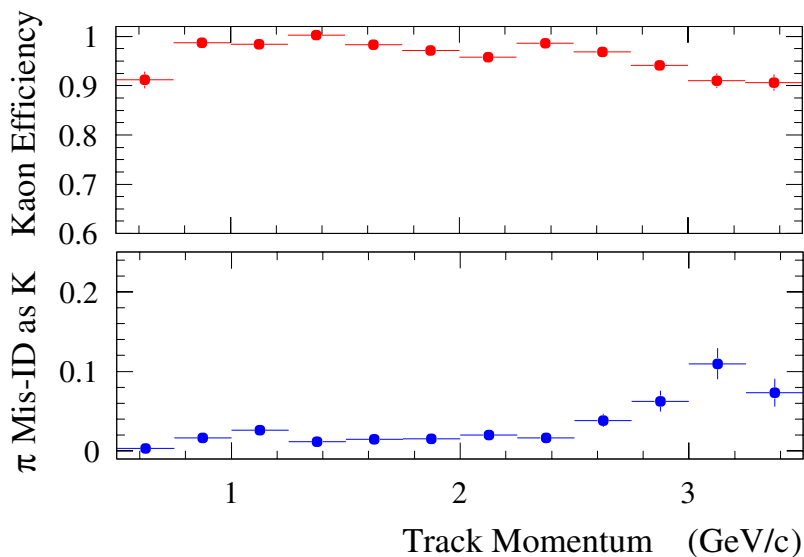


Figure 2.18: Efficiency and misidentification probability for the selection of charged kaons as a function of track momentum.

mean kaon selection efficiency and pion misidentification are $96.2 \pm 0.2\%$ (stat.) and $2.1 \pm 0.1\%$ (stat.) respectively.

2.6 Electromagnetic calorimeter (EMC)

To detect photons from π^0 and η decays as well as those from other electromagnetic and radiative processes, the EMC must efficiently measure the energy and position of electromagnetic showers over the range from 20 MeV to 9 GeV. The EMC also identifies electrons that are used for flavor tagging from semi-leptonic B decays and electrons from $J/\psi \rightarrow e^+e^-$ decays. The EMC is described in detail in Ref. [59].

2.6.1 EMC layout

The physics requirements listed above led to the construction of a calorimeter using a finely segmented array of thallium-iodide doped cesium iodide (CsI(Tl)) crystals which are read out with silicon photodiodes matched to the

spectrum of the scintillation light. The crystal properties are displayed in Table 2.5. The minimum measurable energy of the crystals is around 20 MeV limited mostly by beam and event-related background and the amount of material in front of the calorimeter.

Parameter	Values
Radiation Length	1.85 cm
Molière Radius	3.8 cm
Density	4.53 g/cm ³
Light Yield	50,000 γ / MeV
Light Yield Temp. Coeff.	0.28%/°C
Peak Emission λ_{max}	565 nm
Refractive Index (λ_{max})	1.80
Signal Decay Time	680 ns (64%) 3.34 μ s (36%)

Table 2.5: Properties of CsI(Tl)

The EMC consists of a cylindrical barrel section with inner and outer radii 91 and 136 cm respectively and a forward endcap as shown in Fig. 2.19. Its laboratory coverage extends in polar angle from 15.8° to 141.8°. The barrel is composed of 5760 CsI(Tl)crystals arranged azimuthally in 48 rings with 120 crystals each while the endcap holds 820 crystals grouped in eight rings tilted at an angle of 22.7° from vertical. The crystals are grouped into modules made from thick carbon fiber composite, supported from the rear, and mounted in an aluminum support cylinder fixed to the coil cryostat. The barrel and outer five rings contribute less than 0.6 radiation length of material in front of the crystals.

The trapezoidal crystals, which extend in length from 29.6 cm in the backward to 32.4 cm in the forward direction, act both as a total-absorption scintillating medium and as a light guide to collect light at the photodiodes that are mounted on the rear surface. The diode output signal is amplified, digitized, buffered and sent to the Level 1 trigger system. The average light yield per

crystal is about 7300 photoelectrons/ MeV with a mean electronic noise of 900 electrons. This noise is negligible compared to that from the beam background which is typically a factor of three higher. The energy scale of the individual crystals is calibrated at low energies using a 6.13 MeV photon source and at high energies using photons from radiative Bhabha events. Corrections for energy loss due to leakage and absorption are performed as a function of polar angle and measured energy deposited.

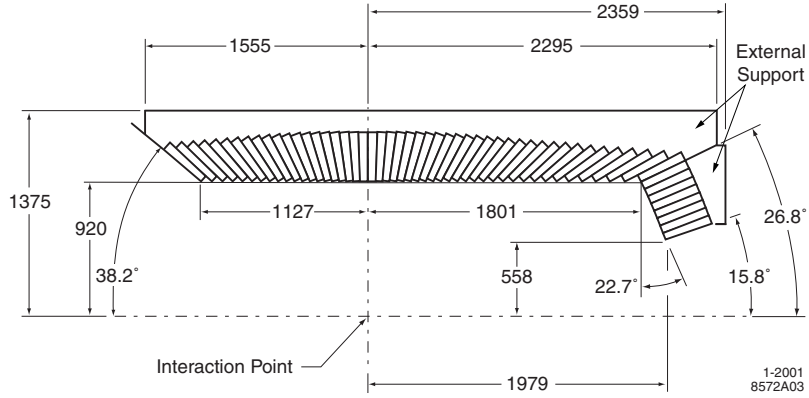


Figure 2.19: A longitudinal cross-section of the EMC (top half) indicating the arrangement of the 56 crystal rings. All dimensions are in mm.

2.6.2 EMC performance

Using a variety of physics sources, a fit to the energy dependence of the EMC results in the following form:

$$\frac{\sigma_E}{E} = \frac{(2.32 \pm 0.30)\%}{E^{1/4}} \oplus (1.85 \pm 0.12)\% \quad (2.6.1)$$

where the energy is measured in GeV. The energy dependent term is mostly due to fluctuations in photon statistics but is influenced by the electronic noise of the photon detector and the number of real photons from beam-generated backgrounds. The constant term dominates at higher energy and arises from non-uniformity in light collection, from leakage or absorption, and from calibration uncertainties. The two-photon invariant mass from $B\bar{B}$ decays is shown

in Fig. 2.20 where the energy of the photons and π^0 are required to be greater than 30 and 300 MeV respectively. The fit yields a resolution of $6.9 \text{ MeV}/c^2$ for the reconstruction of the π^0 mass.

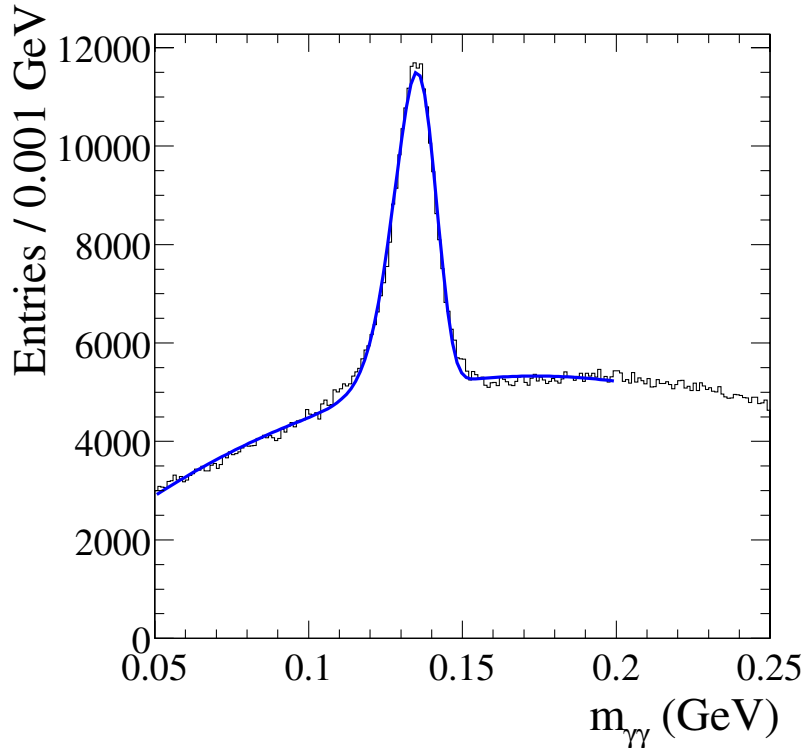


Figure 2.20: Invariant mass of two photons in $B\bar{B}$ events. The energies of the photons and π^0 must be greater than 30 and 300 MeV respectively. The solid line is a fit to the data.

The EMC is also primarily responsible for electron identification, which will be discussed in further detail in Chapter 4 as it pertains to J/ψ reconstruction. The separation between electrons and charged hadrons is primarily based on the shower energy, lateral and azimuthal shape of the shower [60, 61], and track momentum. The most important variable is the ratio of shower energy to track momentum (E/p) which should be peaked at one for an electron and around 0.1 – 0.3 for a hadron. Fig. 2.21 shows the efficiency for electron identification and pion misidentification as a function of momentum for two sets of selec-

tion criteria. The electron identification efficiency is measured using radiative Bhabha and $e^+e^- \rightarrow e^+e^-e^+e^-$ events and the pion misidentification probability is measured for selected charged pions from K_s^0 decays and three prong τ decays. A restrictive selection results in a mean efficiency of 94.8% in the momentum range $0.5 \text{ GeV}/c < p < 2.0 \text{ GeV}/c$ with a mean pion misidentification probability of 0.3%.

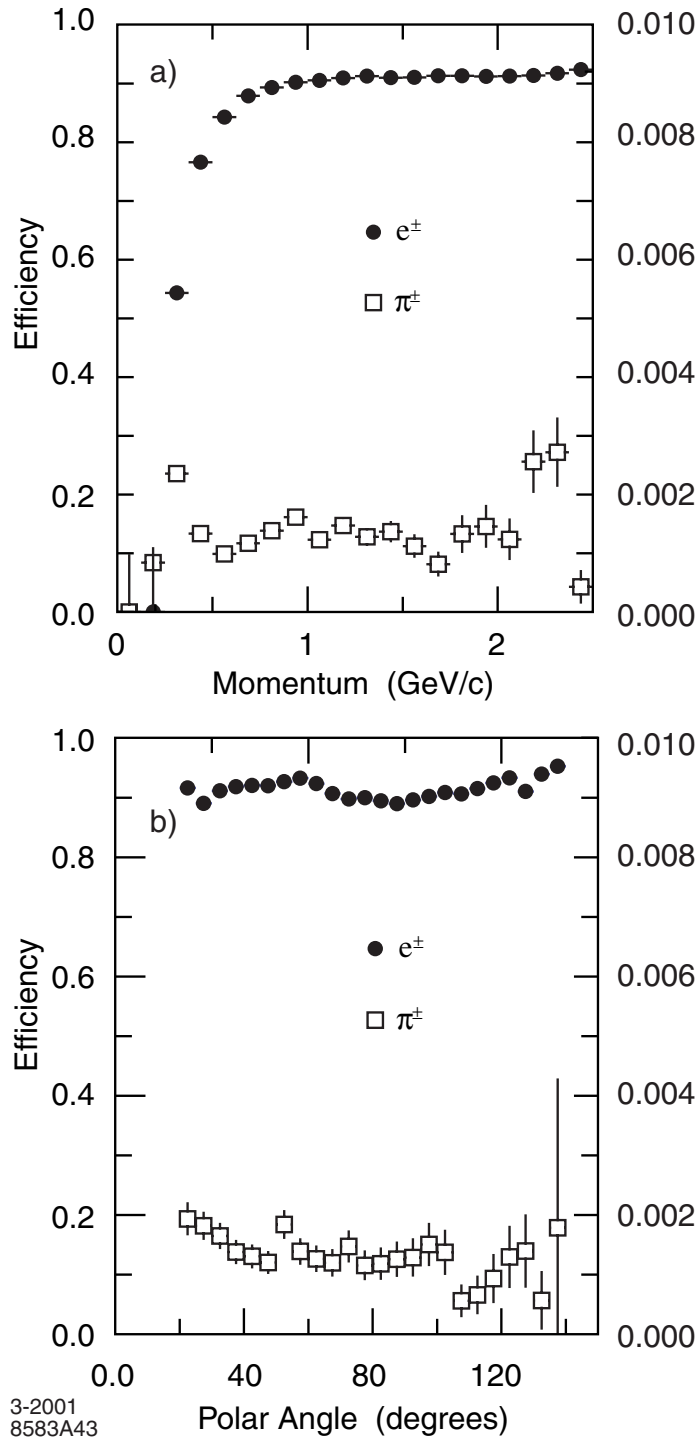


Figure 2.21: Electron efficiency (left vertical scale) and pion misidentification probability (right vertical scale) as a function of laboratory a) particle momentum and b) polar angle.

2.7 Instrumented flux return (IFR)

The IFR is required to identify muons with high efficiency and purity, and to detect neutral hadrons (primarily K_L^0) over a wide range of momenta and angles. Muon detection is important for tagging the flavor of semi-leptonic B decays and for the reconstruction of $J/\psi \rightarrow \mu^+ \mu^-$ decays. The performance of the IFR is described in detail in Ref. [62].

2.7.1 IFR overview

The steel flux return of the magnet serves as a muon filter and neutral hadron absorber for the IFR. The steel is finely segmented and instrumented with active detector resistive plate chambers (RPCs) [63] which readout two coordinates. The IFR consists of a central barrel region and two end doors as shown in Fig. 2.22. The steel is segmented into 18 plates, increasing from a thickness of 2 cm at the inner nine plates to 10 cm at the outermost plate. The steel plates are separated by a gap which is 3.5 cm in the inner layers of the barrel and 3.2 cm elsewhere. There are 19 RPC layers in the barrel and 18 in the endcaps. Additionally, there are two layers of cylindrical RPCs between the EMC and the magnet cryostat to detect particles exiting the EMC. The steel in the barrel region comprises about 4 interaction lengths of material for a muon.

RPCs detect streamers induced by ionizing particles via capacitive readout strips. They consist of two bakelite (phenolic polymer) sheets which are 2 mm thick and are separated by a 2 mm gap filled with a non-flammable gas mixture containing about 56.7% Argon, 38.8% Freon 134A ($C_2H_2F_4$), and 4.5% isobutane. A potential difference of ~ 8 kV is maintained between the sheets so that an ionizing particle crossing the gas gap produces a quenched discharge. The signals are read out capacitively, on both sides of the gap, by external electrodes made of aluminum strips on a mylar substrate.

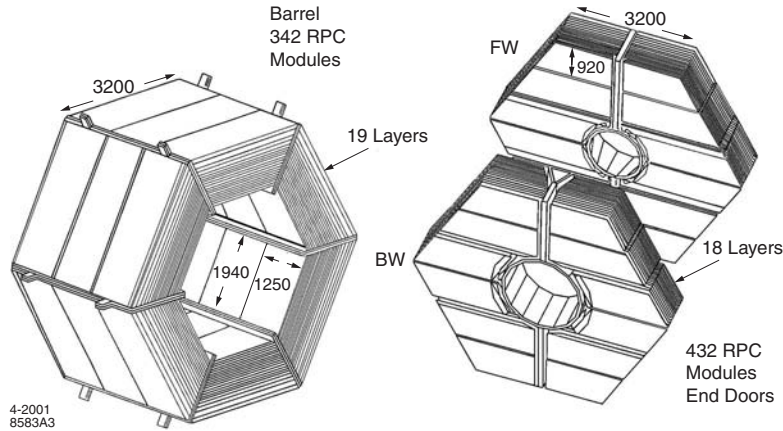


Figure 2.22: .

Barrel sectors and forward (FW) and backward (BW) end doors of the IFR. The shape of the RPC modules and their dimensions in mm are indicated.

2.7.2 IFR performance

Muon identification relies primarily on the IFR though other detectors contribute complementary information. Charged particle muon candidates reconstructed by the SVT and DCH are required to meet the criteria for minimum ionizing particles in the EMC. Reconstructed tracks are extrapolated to the IFR detector volume taking into account the non-uniform magnetic field, multiple scattering, and average energy loss. IFR clusters are formed from nearby hits in a given layer and hits in different layers using two algorithms. For each cluster, we calculate the following in order to select muons: the total number of interaction lengths from the IP to the last RPC layer; the difference between this measured number of traversed interaction lengths and the number expected for a muon of the same momentum and angle; the average number and the RMS of the distribution of RPC strips per layer; the χ^2 for the geometric match between the projected track and the cluster centroids in different RPC layers; and the χ^2 of a polynomial fit to the two-dimensional IFR clusters.

The muon detection performance has been measured on samples of muons

from $\mu\mu ee$ and $\mu\mu\gamma$ final states as well as pions from three-prong τ decays and $K_s^0 \rightarrow \pi^+ \pi^-$ decays. These control samples are selected using kinematic variables uncorrelated with those used for muon selection. Fig.2.23 shows the muon efficiency and pion misidentification probability for these samples as a function of momentum and polar angle for loose selection criteria. We find an average muon detection efficiency of about 90% in the momentum range of $1.5 < p < 3.0 \text{ GeV}/c$ with a pion fake rate of about 6 – 8%, where 2% comes from muons which decay in flight.

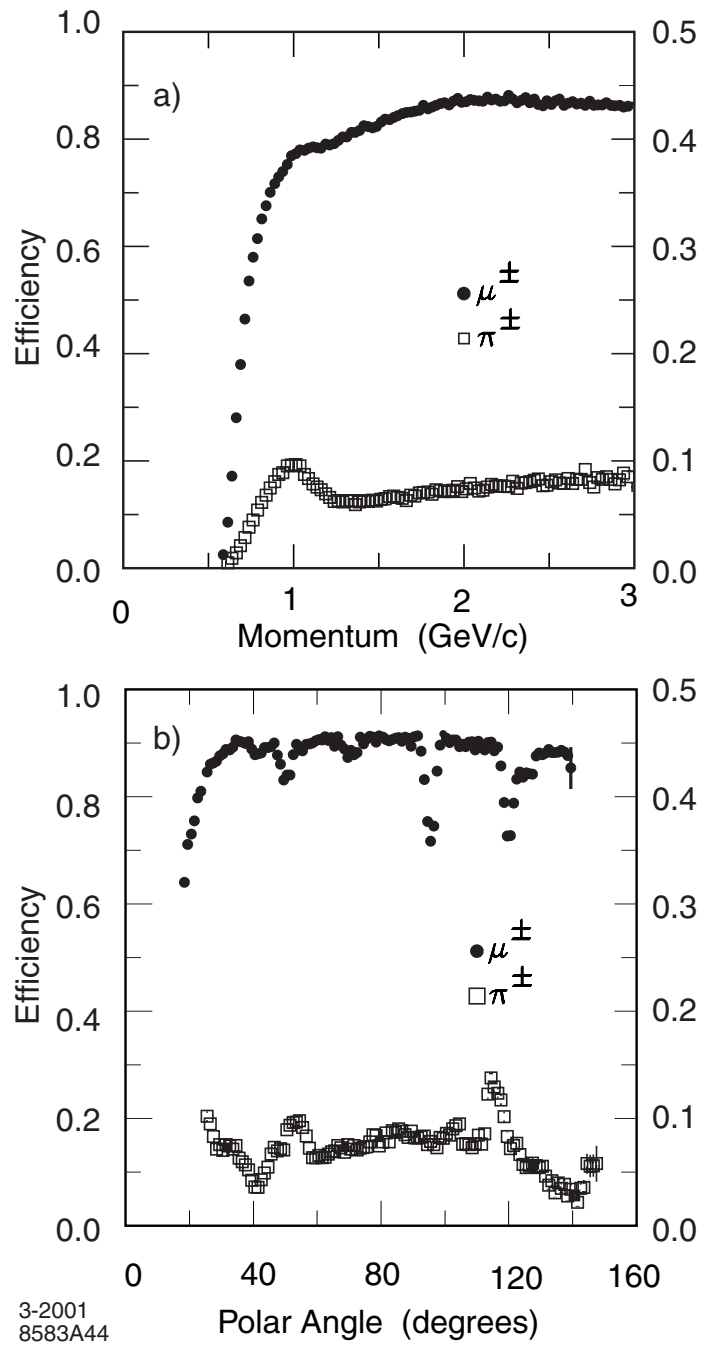


Figure 2.23: Muon efficiency (left scale) and pion misidentification probability (right scale) as a function of laboratory a) track momentum and b) polar angle (for $1.5 < p < 3.0$ GeV/c), using loose selection criteria.

Chapter 3

Analysis overview

Due to the complexity of this measurement, we present a brief overview of the analysis technique that will be detailed in Chapters 4 through 8. This chapter serves as a road map to guide the reader through the analysis. Some of the details that have already been covered will be summarized again for completeness.

In Sec. 1.6.5 it was shown that the probability for $B^0-\bar{B}^0$ mixing is a function of Δm_d and the proper time difference Δt between the two B decays. Neglecting any background contributions, the probability distribution functions (PDFs) for the mixed ($-$) and unmixed ($+$) events, \mathcal{H}_\pm , can be expressed as the convolution of the underlying oscillatory physics distribution

$$h_\pm = \frac{\Gamma}{4} e^{-\Gamma|\Delta t|} [1 \pm \mathcal{D} \cos(\Delta m_d \Delta t)], \quad (3.0.1)$$

with a time-difference resolution function $\mathcal{R}(\delta_t = \Delta t - \Delta t_{true}; \hat{a})$ to give

$$\mathcal{H}_\pm(\Delta t; \Gamma, \Delta m_d, \mathcal{D}, \hat{a}) = h_\pm(\Delta t_{true}; \Gamma, \Delta m_d, \mathcal{D}) \otimes \mathcal{R}(\delta_t; \hat{a}), \quad (3.0.2)$$

where Δt and Δt_{true} are the measured and true time differences, \hat{a} are parameters of the resolution function, and \mathcal{D} is the dilution that was defined in Sec. 1.8.2. Fig. 3.1 illustrates the impact of typical mistag and Δt resolution effects on the distribution of Δt for mixed and unmixed events.

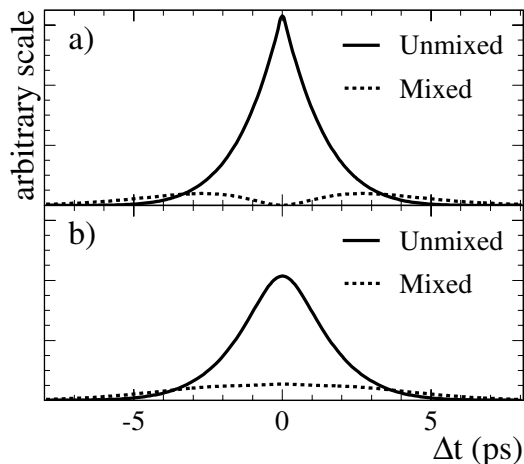


Figure 3.1: Distribution of Δt for mixed and unmixed events with a) perfect flavor tagging and Δt resolution and b) typical mistag rates and Δt detector resolution.

The mixing frequency, dilutions (there may be more than one depending on the number of flavor tagging categories), and resolution function parameters can be measured in events where one neutral B meson is fully reconstructed in a flavor-eigenstate and the flavor of the other B is tagged by its decay products, since this information is sufficient to classify the event as mixed or unmixed. In this analysis, we reconstruct B mesons in the flavor-eigenstates $B^0 \rightarrow D^{(*)-}\pi^+$, $D^{(*)-}\rho^+$, $D^{(*)-}a_1^+$, and $J/\psi K^{*0}(K^+\pi^-)$. If, for example, we reconstruct a B^0 in the final state $D^{(*)-}\pi^+$ and the flavor of the other meson in the event is found to be a \bar{B}^0 (B^0) when it decays, then the event is classified as unmixed (mixed). The events with B mesons reconstructed in flavor-eigenstates will be used to determine the dilution and resolution function parameters, which are needed to measure $\sin 2\beta$.

This is accomplished by constructing a likelihood-function, by summing \mathcal{H}_\pm over all mixed and unmixed events in a given uniquely assigned tagging category i and summing over all tagging categories, given by

$$\ln \mathcal{L}_{\text{mix}} = \sum_i^{\text{tagging}} \left[\sum_{\text{unmixed}} \ln \mathcal{H}_+(\Delta t; \Gamma, \Delta m_d, w_i, \hat{a}_i) + \right.$$

$$\sum_{\text{mixed}} \ln \mathcal{H}_-(\Delta t; \Gamma, \Delta m_d, w_i, \hat{a}_i) \Big] \quad (3.0.3)$$

The characteristics of likelihood-functions will be explained in detail in Chapter 7. Maximizing Eqn. 3.0.3 allows us to determine the mistag rates w_i and the resolution function parameters \hat{a}_i of each flavor tagging category ¹.

The probability distribution functions that were derived in Sec. 1.8 for the Δt distributions of tagged events where a neutral B meson decays to a CP eigenstate,

$$f_{\pm} = \frac{\Gamma}{4} e^{-\Gamma|\Delta t|} [1 \pm \mathcal{D} \sin 2\beta \sin(\Delta m \Delta t)] \quad (3.0.4)$$

where the $+(-)$ label indicates that the tagging meson was a B^0 (\bar{B}^0), must also be convolved with a time resolution function $\mathcal{R}(\Delta t, \hat{a})$ to take into account the detector resolution. This results in a new probability distribution function \mathcal{F}_{\pm} given by

$$\mathcal{F}_{\pm}(\Delta t; \Gamma, \Delta m_d, w, \sin 2\beta, \hat{a}) = f_{\pm}(\Delta t_{\text{true}}; \Gamma, \Delta m_d, w, \sin 2\beta) \otimes \mathcal{R}(\delta_t; \hat{a}), \quad (3.0.5)$$

where the resolution function $\mathcal{R}(\delta_t; \hat{a})$ is the same as in 3.0.2.

We can use a similar method as that described for measuring the mistag rates and resolution function parameters of the flavor-eigenstate sample in order to determine $\sin 2\beta$. This is done using the tagged B_{CP} sample by maximizing the log-likelihood function

$$\ln \mathcal{L}_{CP} = \sum_i^{\text{tagging}} \left[\sum_{B^0 \text{tag}} \ln \mathcal{F}_+(\Delta t; \Gamma, \Delta m_d, w_i, \sin 2\beta, \hat{a}_i) + \sum_{\bar{B}^0 \text{tag}} \ln \mathcal{F}_-(\Delta t; \Gamma, \Delta m_d, w_i, \sin 2\beta, \hat{a}_i) \right] \quad (3.0.6)$$

where the outer summation is over tagging categories i and the inner summations are over the B^0 and \bar{B}^0 tags within a given uniquely-assigned tagging category. In practice, the fit for $\sin 2\beta$ is performed on the combined flavor-eigenstate and CP samples with a log-likelihood given by the sum of Eqn 3.0.3

¹We could also determine Δm_d with this procedure but that is not the goal of this analysis.

and 3.0.6. In this way we can simultaneously determine the mistag rates, resolution function parameters, and $\sin 2\beta$. The likelihood contains additional terms described in Chapter 7 to account for backgrounds.

3.1 Analysis outline

The components of the $\sin 2\beta$ analysis are presented in the following chapters. In Chapter 4, we describe the reconstruction of neutral B decays to CP modes $J/\psi K_S^0$, $\psi(2S)K_S^0$, $\chi_{c1}K_S^0$, and $\eta_c K_S^0$, as well as the reconstruction of neutral B decays to the flavor-eigenstates listed above, and the reconstruction of charged B decays to $J/\psi K^+$, $\psi(2S)K^+$, $\chi_{c1}K^+$, and $\bar{D}^{(*)0}\pi^+$ final states that are used as a control sample.

Chapter 5 discusses how the flavor of the tagging meson is determined. The method used to measure the distance Δz between the two neutral B meson vertices along the $\Upsilon(4S)$ boost axis and its conversion to Δt is described in Chapter 6.

In Chapter 7 we construct a likelihood function that describes the time evolution of signal and background events in the presence of mixing and CP asymmetries. The results of the $\sin 2\beta$ measurement and systematic uncertainties are given in Chapters 8 and 9, respectively. Finally, we discuss the consequences of the measurement and prospects for improvements in Chapter 10.

3.2 Additional CP modes

Reconstruction of B meson decays to the $CP = +1$ eigenstate $J/\psi K_L^0$ and the mixed CP state $J/\psi K^{*0}$ ($K^{*0} \rightarrow K_S^0 \pi^0$) are also used to measure $\sin 2\beta$. The CP eigenstate of $J/\psi K_L^0$ is opposite that of $J/\psi K_S^0$ since the K_L^0 has a CP eigenvalue of -1 while the K_S^0 has an eigenvalue of $+1$ (see Eqn. 1.4.2). This means that the amplitude of the time-dependent CP -violating asymmetry (Eqn. 1.6.48) for this mode is flipped relative to the $\eta_{CP} = -1$ decays.

Thus, comparing the measured value of $\sin 2\beta$ from $J/\psi K_S^0$ and $J/\psi K_L^0$ decays is an excellent cross-check of the analysis procedure. Additionally, of course, adding the fully reconstructed $J/\psi K_L^0$ decays allows us to make a more precise measurement.

Conservation of angular momentum dictates that the final state of a B^0 decay (in the B^0 rest frame) must have zero total angular momentum. The vector-vector final state $J/\psi K^{*0}$ may have a total spin of 0,1, or 2 using the known rules of quantum mechanics for adding two spin 1 particles. Consequently, the orbital angular momentum L of the state must be 0,1, or 2 in order that the state have zero total angular momentum. The presence of even ($L = 0, 2$) and odd ($L = 1$) orbital angular momentum in the $B^0 \rightarrow J/\psi K^{*0}$ final state means that there are CP -even and CP -odd contributions to the decay rate (since the parity of the final state goes like $(-1)^L$). When the angular information in the decay is ignored, the measured CP asymmetry in $J/\psi K^{*0}$ is reduced by a factor $1 - 2R_\perp$ where R_\perp is the fraction of the $L = 1$ component.

We measure $\sin 2\beta$ using B^0 decays to $J/\psi K_L^0$ and $J/\psi K^{*0}$ ($K^{*0} \rightarrow K_S^0 \pi^0$). Results of these measurements will be presented in Chapter 8 for completeness, but they will not be discussed in detail in contrast to the $\eta_{CP} = -1$ final states. Reconstruction and background complexities distinguish the $J/\psi K_L^0$ and $J/\psi K^{*0}$ final states from the other CP eigenstates.

Chapter 4

Reconstruction of B mesons

This chapter describes the reconstruction of events that contain a neutral B meson decay to a charmonium¹ and K_s^0 meson where the CP eigenvalue of the final state is -1 . The reconstructed charmonium states include J/ψ , χ_{c1} , $\psi(2S)$, and η_c mesons. Appendix A contains a description of the spectroscopy of these $c\bar{c}$ states. The relevant branching fractions for the most abundant of these modes, $B^0 \rightarrow J/\psi K_s^0$, are shown in Table 4.1. With an $\sim 80 \text{ fb}^{-1}$ data set and a reconstruction efficiency of 45%, one expects the total yield (sum of B^0 and \bar{B}^0 decays) for this mode to be about 1300 events.

Decay	Branching Fraction
$\Upsilon(4S) \rightarrow B^0 \bar{B}^0$	$\sim 50\%$
$B^0 \rightarrow J/\psi K_s^0$	$(4.5 \pm 0.6) \times 10^{-4}$
$J/\psi \rightarrow l^+ l^-$	$(11.81 \pm 0.14)\%$
$K_s^0 \rightarrow \pi^+ \pi^-$	$(68.61 \pm 0.28)\%$
Total	$(3.6 \pm 0.5) \times 10^{-5}$

Table 4.1: Branching fractions for the decay $B^0 \rightarrow J/\psi K_s^0$

In addition to the CP sample, neutral B mesons that decay to flavor eigenstates are reconstructed. The final hadronic states in this sample consist of B^0

¹The word charmonium denotes a bound state of $c\bar{c}$ quarks.

$\rightarrow D^{(*)-}\pi^+, D^{(*)-}\rho^+, D^{(*)-}a_1^+$, and $J/\psi K^{*0}(K^+\pi^-)$. The term flavor-eigenstate implies that the final state tags the flavor of the B meson when it decays (i.e., only a B^0 decays to $D^{(*)-}\pi^+$ and only a \bar{B}^0 decays to $D^{(*)+}\pi^-$ ²). The flavor-eigenstate sample (B_{flav}) is used to determine the mistag rates and resolution function parameters as will be explained in Chapters 5 and 6. Additionally, validation studies are performed with a control sample of B^+ mesons which decay to the final states $J/\psi K^+, \psi(2S)K^+, \chi_{c1}K^+, \eta_c K^+$, and $\bar{D}^{(*)0}\pi^+$.

In Sec. 4.1, the basic track and neutral reconstruction algorithms are defined. The subdetector information used to identify electrons, muons, and kaons is described in Sec. 4.2. This information provides the background for Sec. 4.3 where we detail the reconstruction of B meson decay daughters. In Sec. 4.4, we discuss the techniques used to select signal B meson candidates while reducing background contributions. This leads to a presentation of the yields for the neutral B^0 charmonium CP sample in Sec. 4.5, the neutral B^0 flavor-eigenstate sample in Sec. 4.6, and the charged B^+ control sample in Sec. 4.7.

4.1 Track and neutral reconstruction

Charged particle track reconstruction begins in the DCH using the same fast pattern recognition algorithm employed by the Level-3 trigger. This algorithm identifies and links superlayer-based track segments from particles with transverse momentum greater than about 500 MeV that originate near the IP. Additional algorithms attempt to find tracks of lower momentum that do not pass through the entire radius of the DCH or near the IP. At the end of this process, the tracks are refit with a Kalman-filter fitter [56] that takes into account the distribution of detector material and the non-uniformities in the magnetic field. The resulting tracks are projected into the SVT where silicon-strip hits consistent with the extrapolated track are added. Remaining SVT

²This statement is only true to first order. We discuss corrections from second order effects in detail in Sec. 9.6.

hits are passed to complementary standalone track finding algorithms. Finally, an attempt is made to combine tracks that have been found by only one of the two tracking systems due to a large angle scattering in the beam pipe. Efficiencies of the tracking reconstruction were discussed in Sec. 2.3 and 2.4. The efficiency for finding tracks in $B\bar{B}$ events with transverse momenta greater than 200 MeV/ c is about 95%.

Reconstruction of neutral particles begins in the EMC by identifying crystals that have at least 10 MeV of deposited energy. Neighboring crystals with energy greater than 1 MeV are added to form what is termed a *cluster*. Clusters are divided into “bumps” based on the number of local maxima they contain, where local maxima are defined as candidate crystals that have a fractional energy deposition greater than each of their neighbors. This division of clusters is necessary to resolve overlapping photon candidates (e.g., from high-energy π^0 decays). If none of the charged tracks projected to the inner face of the calorimeter intersect the crystals of a bump, the bump is assumed to have been formed from the electromagnetic shower of a neutral photon. The energy resolution and performance of the EMC was characterized in Sec. 2.6.

4.2 Particle identification

Some information concerning particle identification has already been covered in Sec. 2.5, 2.6, and 2.7. Particles are distinguished using measurements of energy loss (dE/dx) in the SVT layers and DCH, momentum in the DCH, the number of Cherenkov photons emitted and the Cherenkov angle in the DIRC, electromagnetic energy deposited in the EMC, and penetration length in the IFR. These quantities are used to define different selection categories as well as likelihood ratios derived from them, and from neural network algorithms that combine the likelihoods from different subdetectors.

4.2.1 Charged lepton identification

Electrons and muons are primarily used to reconstruct J/ψ mesons and for flavor tagging. Electron candidates are identified by the ratio of the energy they deposit in the EMC to their momentum, E/p . The measured dE/dx in the DCH must also be consistent with the electron hypothesis. Information about the lateral energy moment (LAT) [60] and the Zernike moments A_{mn} [61] of the particle's associated electromagnetic shower also distinguishes electrons. LAT is a measure of the radial energy profile of the shower while the Zernike moment A_{42} measures the asymmetry about the shower's maximum. Fig. 4.1 shows plots of E/p , LAT, A_{42} , and dE/dx measured in the DCH for electrons in data from control samples. Additionally, the agreement between the observed and expected Cherenkov angle in the IFR is used to select the highest purity sample. Table 4.2 lists the selection criteria used to define four categories (**VeryLoose**, **Loose**, **Right**, **VeryTight**) of electron candidates. Candidates whose measured dE/dx satisfies the **VeryTight** requirement but that do not have an associated EMC cluster are retained as **noCal** electrons. This last category is intended to identify electrons that are outside the EMC acceptance, especially those that travel in the direction opposite the boost where there is no endcap.

Muon candidates are identified by the measured number of hadron interaction lengths (n_λ) traversed through the IFR, and the difference (Δn_λ) between n_λ and the predicted penetration depth for a muon of the same momentum and polar angle. Contamination from hadronic showers is rejected using the average number of hits (\bar{n}_{hits}) and the variance ($\sigma_{\bar{n}_{hits}}$) of hits in each RPC layer, the χ^2 for the geometric match between the track extrapolation to the IFR and the RPC hits (χ_{trk}^2), and the χ^2 of a polynomial fit to the RPC hits (χ_{fit}^2). Muons within the EMC acceptance are also required to deposit energy (E_{EMC}) consistent with a MIP. Fig. 4.2 shows distributions of (n_λ), Δn_λ , (χ_{trk}^2), and E_{EMC} for muons from data control samples. Table 4.3 lists the selection

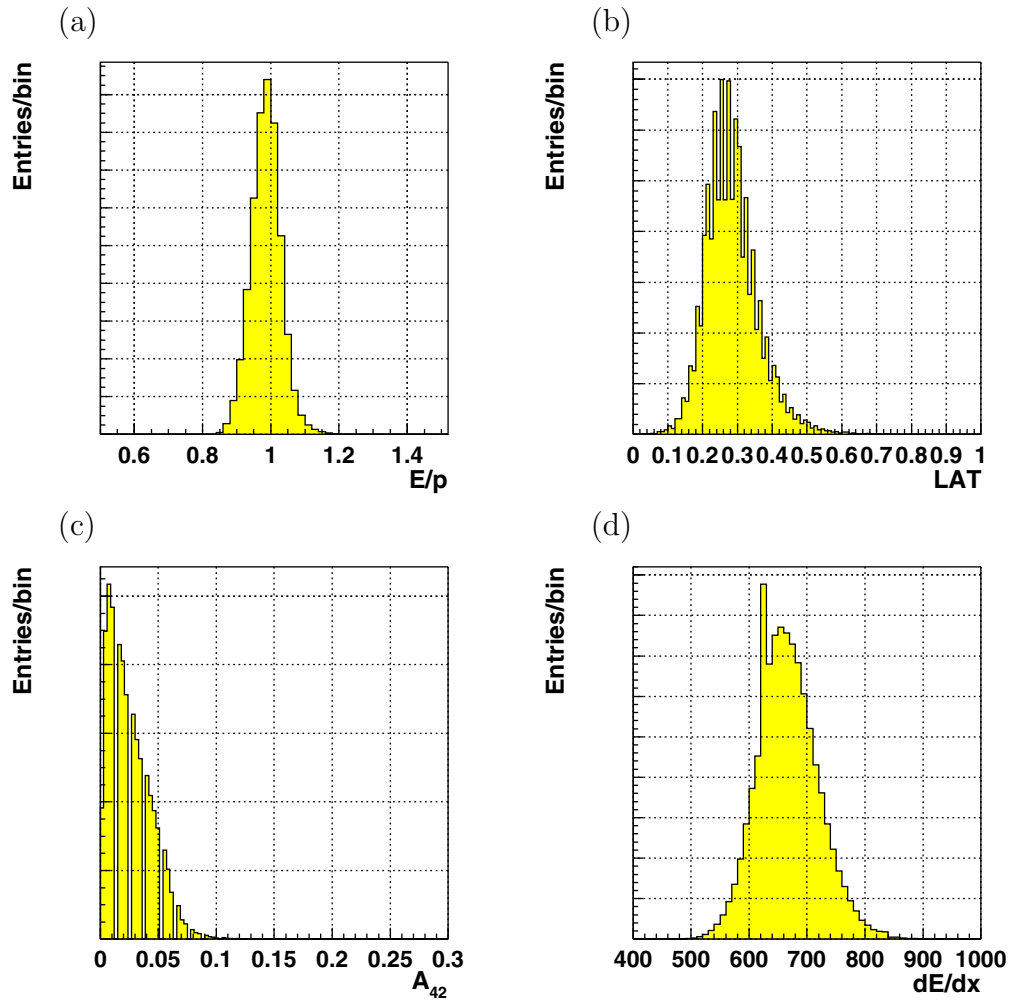


Figure 4.1: Distributions of (a) E/p , (b) LAT, (c) A_{42} , and (d) dE/dx measured in the DCH for electrons in data from control samples. The empty bins in the A_{42} distribution are an artifact of the chosen bin size. Note that the units of dE/dx in (d) are arbitrary.

criteria used to define four categories of muon candidates.

Typical electron and muon efficiencies and pion misidentification probabilities were given in Sec. 2.6.2 and 2.7.2. The `Loose` selection criteria yields electrons (muons) with an efficiency of 97% (86%) and a pion fake rate of 5% (7%) for candidates with momentum greater than $1 \text{ GeV}/c$.

Category	dE/dx	E/p	LAT	A_{42}	$\Delta\theta_c$
VeryLoose	$[-3\sigma, 7\sigma]$	> 0.50	-	-	-
Loose	$[-3\sigma, 7\sigma]$	> 0.65	-	-	-
Tight	$[-3\sigma, 7\sigma]$	$[0.75, 1.3]$	$[0.0, 0.6]$	-	-
VeryTight	$[-2.2\sigma, 4\sigma]$	$[0.89, 1.2]$	$[0.1, 0.6]$	< 0.11	$[-3\sigma, 3\sigma]$

Table 4.2: Summary of electron identification criteria. The difference between the mean dE/dx and the expectation for an electron is required to lie within the interval specified in terms of the expected dE/dx resolution σ . LAT and A_{42} refer to the longitudinal and azimuthal EMC shower shapes respectively and $\Delta\theta_c$ refers to the difference between the measured and expected Cherenkov angle. Distributions of the selection variables are shown in Fig. 4.1. For reference, the mean of the dE/dx plot in Fig. 4.1d is 650 with a resolution of 50 in arbitrary units.

Category	n_λ	Δn_λ	\bar{n}_{hits}	$\sigma_{n_{hits}}$	χ_{trk}^2/n_{lyr}	χ_{fit}^2/n_{lyr}	E_{EMC} [GeV]
VeryLoose	> 2.0	< 2.5	< 10	< 6	-	-	< 0.5
Loose	> 2.0	< 2.0	< 10	< 6	< 7	< 4	< 0.5
Tight	> 2.2	< 1.0	< 8	< 4	< 5	< 3	$[0.05, 0.4]$
VeryTight	> 2.2	< 0.8	< 8	< 4	< 5	< 3	$[0.05, 0.4]$

Table 4.3: Summary of muon identification criteria. The variable definitions are provided in the text and distributions of selected variables are shown in Fig. 4.2.

4.2.2 Kaon identification

Kaon candidates are distinguished from pions and protons using measurements of dE/dx in the SVT and DCH, the number of Cherenkov photons emitted in the DIRC, and the Cherenkov angle in the DIRC. Pion, kaon, and proton likelihoods \mathcal{L}_π , \mathcal{L}_K , and \mathcal{L}_p are computed using the difference between the measured and expected truncated-mean dE/dx in the DCH assuming Gaussian distributions for the given candidate hypothesis. A likelihood is computed in the DIRC for each particle type using the expected number of Cherenkov photons and the difference between the measured and expected Cherenkov angle for the given mass hypothesis. Fig. 4.3 shows the Cherenkov angle as a

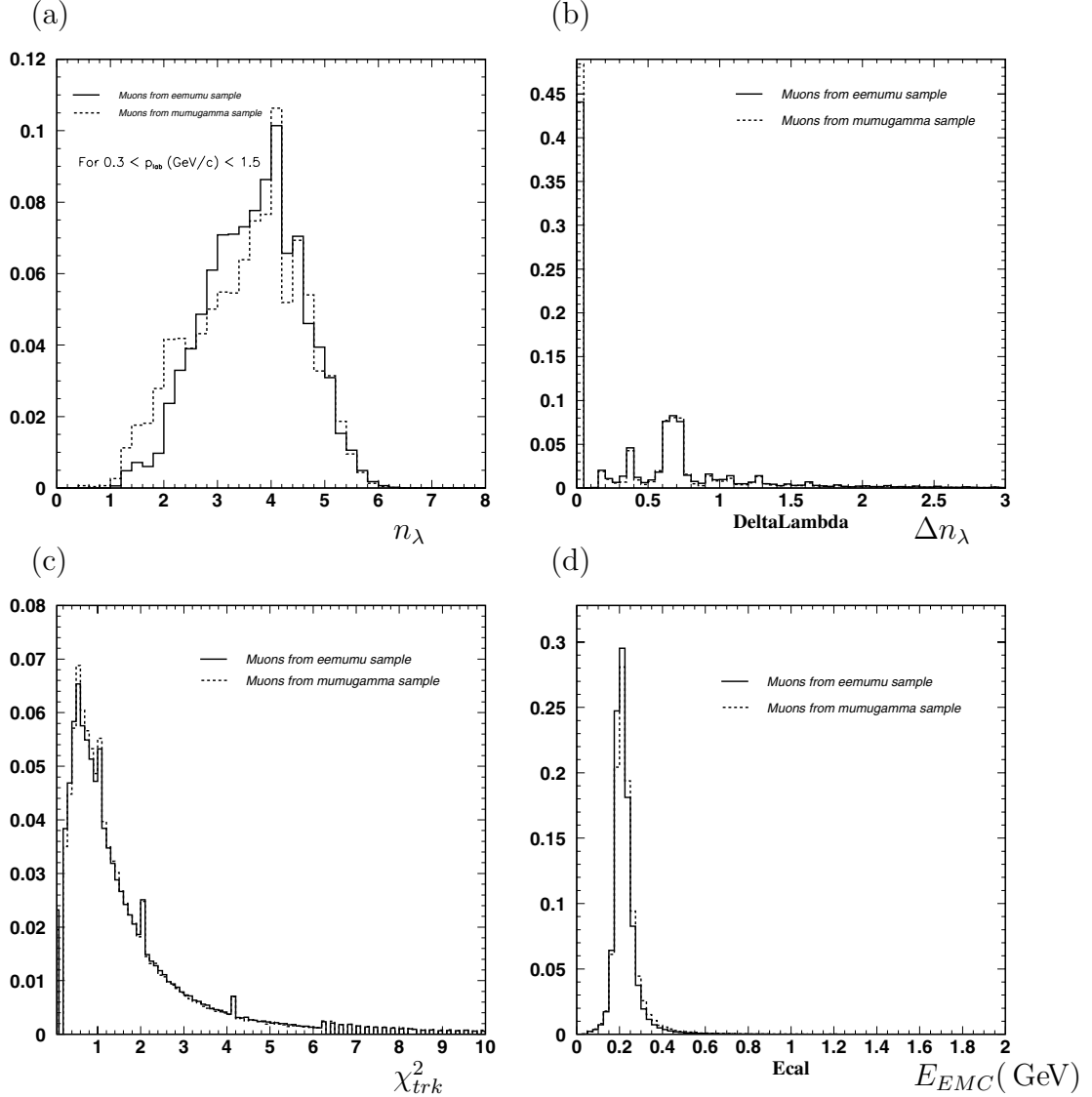


Figure 4.2: Distributions of (a) n_λ , (b) Δn_λ , (c) χ_{trk}^2 , and (d) E_{EMC} for muons from a data control sample of $e^+e^- \rightarrow e^+e^- \mu^+ \mu^-$ (dashed histogram) and $\rightarrow \mu^+ \mu^- \gamma$ (solid histogram).

function of momentum for tracks from a $D^{*+} \rightarrow D^0(\rightarrow K^- \pi^+) \pi^+$ data control sample where the pions and kaons have been kinematically identified.

The exclusive reconstruction of B meson decays does not generally require explicit kaon identification. For some modes, a `VeryLoose` kaon selection based on likelihood ratios is used to reduce backgrounds. The likelihood is con-

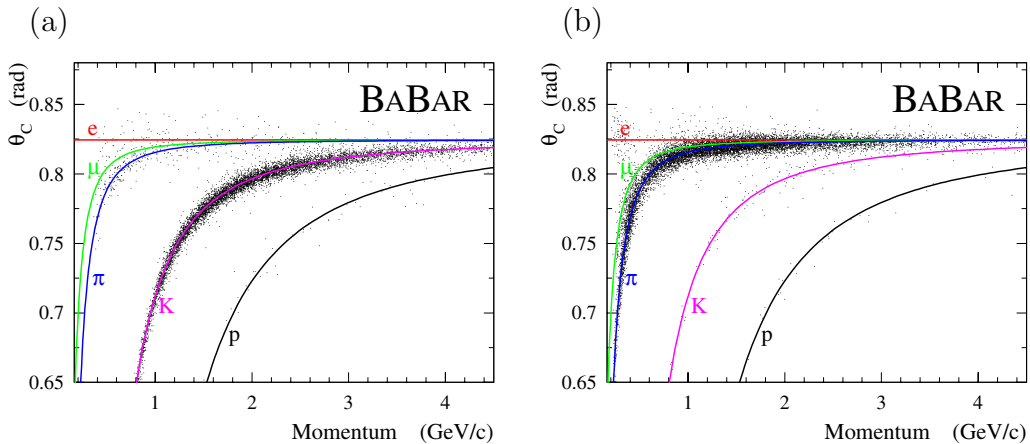


Figure 4.3: Distributions of DIRC Cherenkov angle as a function of momentum for kinematically identified (a) kaons and (b) pions from a data control sample of inclusive $D^{*+} \rightarrow D^0(\rightarrow K^-\pi^+)\pi^+$ decays.

constructed from different subdetector likelihoods depending on the momentum of the kaon candidate. Kaon candidates are rejected if the likelihood ratios satisfy $\mathcal{L}_K/\mathcal{L}_\pi < r$, where $r = 0.1$ for $p < 0.5 \text{ GeV}/c$ and $r = 1$ for $p \geq 0.5 \text{ GeV}/c$. Tracks without PID are assumed to be kaons. This `VeryLoose` requirement has a roughly constant selection efficiency of 95% and a pion misidentification rate of at most 15% for tracks in the transverse momentum range 1 to 2.5 GeV/c .

4.2.3 Event selection

Since many of the recorded events that pass the L3 trigger do not originate from e^+e^- collisions (they may be from beam-gas or beam-wall interactions), we impose loose selection criteria that nearly all $B\bar{B}$ events will pass. We require at least three reconstructed tracks in the polar range $0.41 < \theta_{lab} < 2.54$ rad. The tracks must be within 1.5 cm in the plane transverse to the beam direction (transverse plane) and 10 cm in z of the nominal beamspot and must be reconstructed by the DCH. For each event, a primary vertex is formed from a vertex fit to all charged tracks in the fiducial volume. Tracks which contribute

a large χ^2 to the fit are removed until the probability of the χ^2 is greater than 1% or until only two tracks remain. This method achieves a resolution of about $70\ \mu\text{m}$ in x and y for hadronic events. The primary vertex must be within $0.5\ \text{cm}$ of the average beamspot positions in the transverse plane and $6\ \text{cm}$ longitudinally.

Neutrals are defined to be electromagnetic bumps in the calorimeter in the polar range $0.410 < \theta_{lab} < 2.409$ rad which are not associated to a charged track, have an energy greater than $30\ \text{MeV}$, and a $\text{LAT} < 1.1$. The total energy of the event in the fiducial region for charged tracks and neutrals must be greater than $4.5\ \text{GeV}$.

Additionally, to reduce continuum background from $q\bar{q}$ events, the normalized second Fox-Wolfram moment [64] R_2 of the the event, calculated using charged tracks and neutrals, must be less than 0.5. The l^{th} Fox-Wolfram moment (FW_l) is the momentum-weighted sum of Legendre polynomial of the l^{th} order computed from the cosine of the angle between all pairs of tracks as:

$$FW_l = \frac{\sum_{i,j} |p_i||p_j|P_l(\cos\theta_{ij})}{E_{tot}^2} \quad (4.2.1)$$

where i and j run over all tracks and neutrals, p is the momentum of the track or neutral, P_l is the l^{th} order Legendre polynomial, θ is the angle between the two candidates, and E_{tot} is the total energy of the tracks and neutrals in the event. The ratio R_2 is defined to be FW_2/FW_0 . Since the momentum of the B mesons is only $\sim 350\ \text{MeV}/c$ in the $\Upsilon(4S)$ frame, the distribution of tracks from the two B decays is isotropic. The tracks from continuum events, on the other hand, tend to be collinear in this frame as the jets originate back to back with significant momentum (compared to the B momentum in this frame). The ratio R_2 provides good separation power between the jet-like continuum and spherical $B\bar{B}$ events as shown in Fig 4.4 for Monte Carlo.

The selection of multihadron events described in the preceding paragraphs is $95 \pm 1\%$ efficient for $B\bar{B}$ decays as estimated from a Monte Carlo simulation.

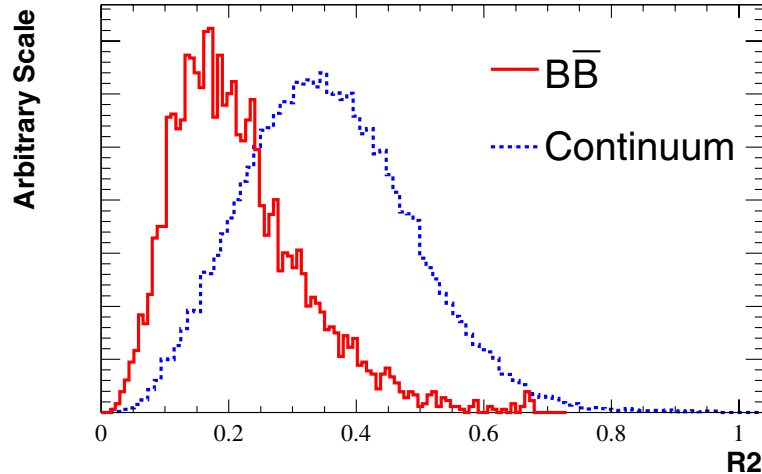


Figure 4.4: Distribution of R_2 , calculated using all fiducial tracks and neutrals, for Monte Carlo $B\bar{B}$ (solid) and continuum (dashed) events normalized to unit area. The separation power of R_2 is evident. $B\bar{B}$ events are selected requiring $R_2 < 0.5$.

4.3 Reconstruction of decay daughters

Vertex and kinematic fitting is used to improve four-momenta and position measurements of composite candidates, as well as to measure the time difference between the decay of the neutral B mesons. For example, the determination of the B^0 decay vertex can be improved by constraining the line-of-flight of the K_s^0 to intersect the charmonium vertex. Also, the energy resolution of the B^0 may be improved by constraining the charmonium and K_s^0 mesons to their known masses. Generalized procedures which use the Lagrange-multiplier technique [65] have been implemented. Possible constraints include a common decay vertex, mass, energy, momentum, beam energy, beam-spot position, and line-of-flight. Since some of these constraints require non-linear fits, the iterative procedure is defined to converge when successive steps yield a change in the χ^2 which is less than 0.01 within a maximum of six iterations.

We reconstruct neutral B mesons which decay to a charmonium meson and a K_s^0 in order to measure $\sin 2\beta$. The K_s^0 is reconstructed in its decay $K_s^0 \rightarrow$

$\pi^+ \pi^-$ for all charmonium mesons and also in its decay $K_s^0 \rightarrow \pi^0 \pi^0$ for the mode $J/\psi K_s^0$. The following subsections describe the π^0 , K_s^0 , and charmonium reconstruction methods.

4.3.1 Selection of π^0 mesons

Neutral pion candidates are formed from pairs of photon candidates with energy greater than 30 MeV which are assumed to originate from the primary vertex. The photon pair must have an invariant mass within $\pm 20 \text{ MeV}/c^2$ (2.5σ , see Fig. 2.20) of the nominal π^0 mass and a summed energy greater than 200 MeV. Candidates are fit with a kinematic and π^0 mass constraint. Efficiencies for this selection for photon pairs within the EMC acceptance range from 55 to 65% for π^0 energies in the range 0.3 to 2.5 GeV, typical for B decays.

4.3.2 Selection of K_s^0 mesons

We reconstruct K_s^0 candidates as $\pi^+ \pi^-$ and $\pi^0 \pi^0$ which have respective branching fractions of $68.6 \pm 0.3\%$ and $31.4 \pm 0.3\%$. For candidates reconstructed as $\pi^+ \pi^-$, the invariant $\pi^+ \pi^-$ mass determined at the vertex of the two tracks must be between 489 and 507 MeV/c^2 ($\sim 3\sigma$). Since the reconstruction of a B meson when it decays to $J/\psi K_s^0$ is extremely clean (very low background), we loosen this restriction³ by requiring that the invariant $\pi^+ \pi^-$ mass is between 473 and 523 MeV/c^2 . The three dimensional flight length of the K_s^0 candidate with respect to the vertex of the charmonium candidate must be greater than 1 mm. Fig. 4.5 shows a plot of the mass distribution for $K_s^0 \rightarrow \pi^+ \pi^-$ candidates in a subset of the full data sample.

We form $K_s^0 \rightarrow \pi^0 \pi^0 \rightarrow 4\gamma$ candidates by combining pairs of π^0 candidates, requiring the mass of each candidate be within 100 to 155 MeV/c^2 ($-5\sigma, +3\sigma$) and the photons from each candidate not to overlap in the EMC. For a K_s^0

³This allows the recovery of 7% of this signal which would otherwise be lost due to poorly reconstructed low momentum charged pions.

candidate with an energy greater than 800 MeV and a mass between 300 and 700 MeV/ c^2 at the event's primary vertex, we perform a mass constrained fit to each photon pair constraining it to the nominal π^0 mass. The fit is iterated assuming different decay points along the K_s^0 flight path, as defined by the J/ψ decay vertex and the initial K_s^0 momentum vector direction. The point where the product of the fit χ^2 probabilities for the two π^0 pairs is maximized is taken to be the K_s^0 decay vertex. The distance from the J/ψ vertex to the K_s^0 decay vertex must be between -10 and +40 cm (the negative distance takes into account the vertex resolution). The K_s^0 mass determined at the K_s^0 decay vertex must be between 470 and 536 MeV/ c^2 . Fig. 4.5 shows a plot of the mass distribution for $K_s^0 \rightarrow \pi^0 \pi^0$ candidates in a subset of the full data sample.

4.3.3 Selection of ρ , a_1^+ , and K^{*0} mesons

For $\rho^- \rightarrow \pi^- \pi^0$ decays, the $\pi^- \pi^0$ mass is required to be within ± 150 MeV/ c^2 of the nominal ρ^- mass. The π^0 from the ρ^- decay must have an energy greater than 300 MeV. The invariant mass of the $K^+ \pi^-$ from K^{*0} decays must be within 100 MeV/ c^2 of the nominal K^{*0} mass. The three charged pions used to reconstruct the mode $a_1^+ \rightarrow \pi^+ \pi^- \pi^+$ must have a mass between 1.0 and 1.6 GeV/ c^2 . Also, the χ^2 probability of a vertex fit of the a_1^+ candidate must be greater than 0.1%. The widths of the ρ , a_1^+ , and K^{*0} are 149, 250–600, and 51 MeV/ c^2 respectively.

4.3.4 Charmonium meson selection

This section describes the selection criteria for charmonium mesons that are used to reconstruct B meson candidates in the B_{CP} and control samples. The decay modes and branching fractions of the charmonium mesons used in this analysis are given in Table 4.4. Candidate J/ψ and $\psi(2S)$ mesons are reconstructed in their decays to e^+e^- and $\mu^+\mu^-$ pairs; $\psi(2S)$ mesons are also reconstructed as $J/\psi \pi^+ \pi^-$. Candidate χ_{c1} mesons are reconstructed as $J/\psi \gamma$

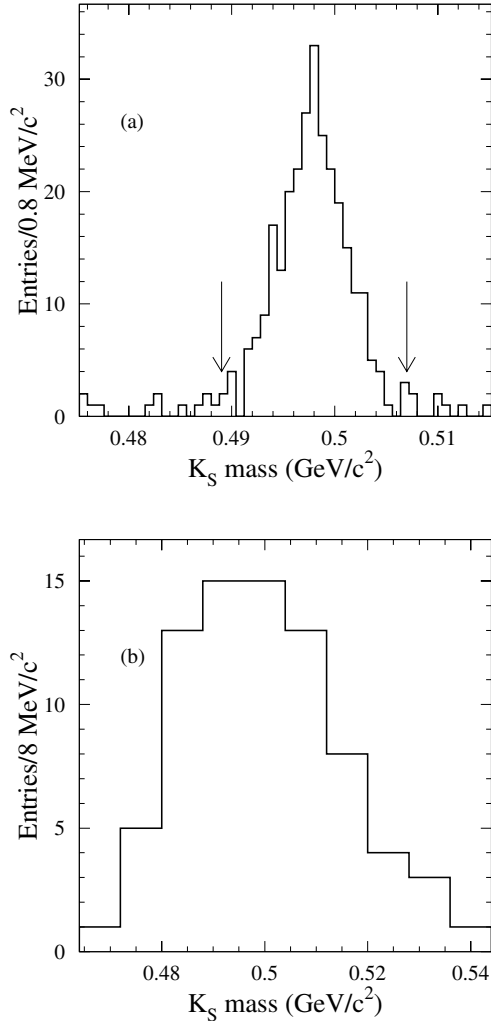


Figure 4.5: K_S^0 mass distribution observed in $B^0 \rightarrow J/\psi K_S^0$ candidates passing the selection cuts for (a) $K_S^0 \rightarrow \pi^+ \pi^-$ and (b) $K_S^0 \rightarrow \pi^0 \pi^0$.

and η_c mesons are reconstructed in hadronic decays to $K\bar{K}\pi$ final states. The particle identification and invariant mass requirements of the lepton pairs is displayed in Table 4.5. The requirements vary by decay mode because of the different amount of background in each mode.

In the e^+e^- decays of the J/ψ and $\psi(2S)$, an attempt is made to recover bremsstrahlung photons which may have originated in the detector material

Meson	Mass(MeV/ c^2)	Decay Mode	Branching fraction (%)
η_c	2979.7 ± 1.5	$K\bar{K}\pi$	5.5 ± 1.7
J/ψ	3096.9 ± 0.04	e^+e^-	5.93 ± 0.10
		$\mu^+\mu^-$	5.88 ± 0.10
χ_{c1}	3510.51 ± 0.12	$J/\psi\gamma$	31.6 ± 3.2
$\psi(2S)$	3685.96 ± 0.09	$J/\psi\pi^+\pi^-$	30.5 ± 1.6
		e^+e^-	0.73 ± 0.04
		$\mu^+\mu^-$	0.70 ± 0.09

Table 4.4: Branching fractions and decay modes of charmonium mesons used in this analysis

B channel	e^+e^- candidates			$\mu^+\mu^-$ candidates		
	Minimal	Restrictive	$m(e^+e^-)$	Minimal	Restrictive	$m(\mu^+\mu^-)$
$J/\psi K_S^0$	None	Tight or NoCal	[2.95,3.14]	MIP	Loose	[3.06,3.14]
$\psi(2S)K_S^0(\ell^+\ell^-)$	VeryLoose	Tight	[3.436,3.736]	VeryLoose	Loose	[3.06,3.14]
$\psi(2S)K_S^0(\pi^+\pi^-)$	VeryLoose	Tight	[2.95,3.14]	VeryLoose	Loose	[3.06,3.14]
$\chi_{c1}K_S^0$	Loose	Tight	[2.95,3.14]	VeryLoose	Loose	[3.06,3.14]

Table 4.5: Particle identification and invariant mass requirements for J/ψ and $\psi(2S) \rightarrow \ell^+\ell^-$ candidates. Both daughters must pass the minimal PID criteria while only one must pass the restrictive criteria. Electron and muon identification requirements are listed in Sec. 4.2. Mass ranges are listed in units of GeV/c^2 and MIP refers to a minimum-ionizing particle.

or as final state radiation (termed internal Bremsstrahlung) following the J/ψ decay. The photon emission causes the magnitude of the measured momentum of the e^\pm track to be less than its actual value, reducing the reconstruction efficiency of the charmonium meson. Photons are typically emitted along the direction of the parent e^\pm track: the mean separation angle is of the order m_e^2/E_e , which is less than 5 mrad for an electron energy greater than 1 GeV. The EMC bump of the bremsstrahlung photon and parent e^\pm are well separated in the ϕ direction, however, because the charged track is bent by the 1.5 T magnetic field. Monte Carlo studies have shown that $\sim 90\%$ of the radiated photon bumps in the EMC lie within 35 mrad in polar angle and 50 mrad in azimuth of the initial e^\pm track direction evaluated at the primary vertex.

The photon bremsstrahlung candidates must have energy greater than 30 MeV, LAT between 10^{-4} and 0.80, and $A_{42} < 0.25$. The four-momentum of an identified bremsstrahlung photon candidate measured in the EMC is added to the four-momentum of the associated electron or positron track. Recovering the bremsstrahlung photons increases the efficiency for reconstructing J/ψ and $\psi(2S)$ decays to e^+e^- by about 30%. Fig. 4.6 shows the mass distribution in data of J/ψ candidates.

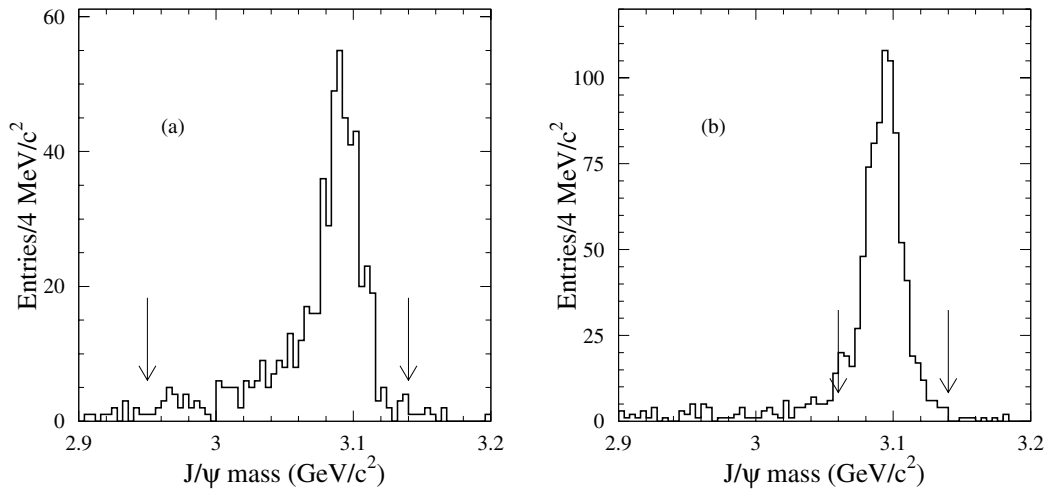


Figure 4.6: Invariant mass distribution for (a) $J/\psi \rightarrow e^+e^-$ and (b) $J/\psi \rightarrow \mu^+\mu^-$ candidates in $B^0 \rightarrow J/\psi K_s^0$ and $B^+ \rightarrow J/\psi K^+$ events passing the selection criteria. The arrows indicate the mass interval used to select the J/ψ candidates. Note the asymmetric tail below the J/ψ mass for e^+e^- candidates that results from energy loss due to bremsstrahlung.

To reconstruct the $\psi(2S)$ in its $J/\psi\pi^+\pi^-$ decay mode, J/ψ candidates are constrained to their nominal mass and combined with pairs of oppositely charged tracks whose invariant mass lies between 400 and 600 MeV/c^2 . The candidate must also satisfy $574 < m(J/\psi\pi^+\pi^-) - m(J/\psi) < 604 \text{ MeV}/c^2$. Fig. 4.7 show the mass distribution in data of $\psi(2S)$ candidates.

χ_{c1} candidates are reconstructed in the $J/\psi \gamma$ decay mode, which accounts for about 32% of χ_{c1} decays. The photons must lie within the EMC fiducial vol-

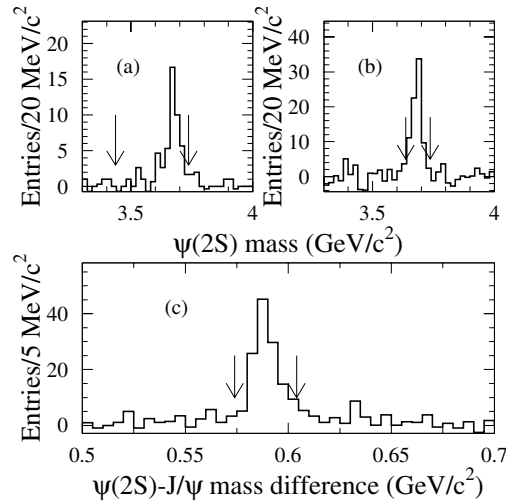


Figure 4.7: Invariant $\psi(2S)$ mass distribution observed in data in $B^0 \rightarrow \psi(2S)K_s^0$ and $B^+ \rightarrow \psi(2S)K^+$ candidates passing selection criteria, for (a) $\psi(2S) \rightarrow e^+e^-$, (b) $\psi(2S) \rightarrow \mu^+\mu^-$, and (c) the $\psi(2S) - J/\psi$ mass difference for $\psi(2S) \rightarrow J/\psi\pi^+\pi^-$. The intervals used to select $\psi(2S)$ candidates are indicated by the arrows.

ume and have an energy greater than 150 MeV. Photons that form an invariant mass between 120 and 150 MeV/c^2 with any other photon whose energy is at least 70 MeV are rejected in order to remove those candidates that originated in the decay of a π^0 . The χ_{c1} invariant mass must be between 3.477 and 3.547 GeV/c^2 . Fig. 4.8 shows the mass distribution of $\chi_{c1} - J/\psi$ candidates in data.

The η_c candidates are reconstructed in the $K_s^0K^+\pi^-$ and $K^+K^-\pi^0$ final states. The charged kaon candidates must satisfy kaon identification criteria based on the Cherenkov angle measured in the DIRC or dE/dx measured in the DCH. The $K_s^0 \rightarrow \pi^+\pi^-$ candidate and π^0 candidate from the η_c decay must have reconstructed masses within 12.5 and 15 MeV/c^2 respectively of their nominal masses. The η_c candidates which have $2.90 > m(KK\pi) < 3.15 \text{ GeV}/c^2$ are combined with K_s^0 candidates that have an invariant mass within 10 MeV/c^2 of the nominal K_s^0 mass. The η_c invariant mass window contains events from the hadronic decays of the J/ψ to the same final states. Since the underlying quark

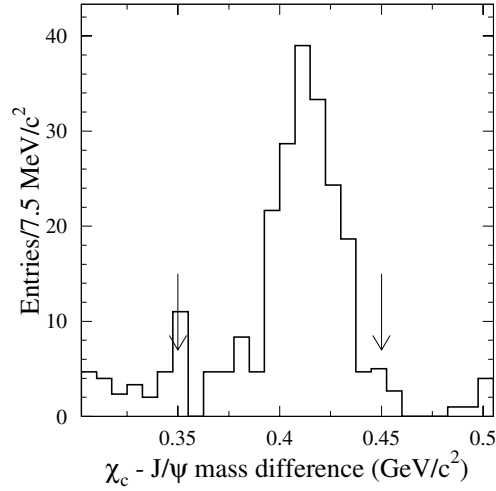


Figure 4.8: Invariant mass distribution in data for $\chi_{c1} - J/\psi$ observed in $B^0 \rightarrow \chi_{c1} K_s^0$ and $B^+ \rightarrow \chi_{c1} K^+$ candidates passing the event selection. The mass difference interval used to select χ_{c1} candidates is indicated by the arrows.

process is the same and because the $B^0 \rightarrow \eta_c K_s^0$ and $B^0 \rightarrow J/\psi K_s^0$ decays have the same $CP = -1$, the J/ψ events are included in the final sample, contributing $(15 \pm 2)\%$ to the total η_c yield. Fig. 4.9 shows a fit to the η_c mass distribution in data.

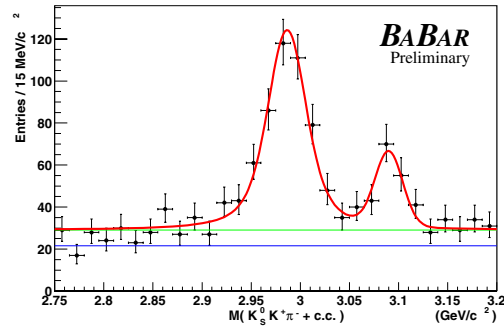


Figure 4.9: η_c mass distribution observed in $B^0 \rightarrow \eta_c K_s^0$ candidates passing the selection cuts with a fit superimposed. The selection includes the contribution from hadronic decays of the J/ψ , shown as the peak at $3.097 \text{ GeV}/c^2$.

4.3.5 Charmed meson selection

We reconstruct D^0 mesons in the decay channels $K^-\pi^+$, $K^-\pi^+\pi^0$, and $K^-\pi^+\pi^-\pi^+$ and D^- candidates in the channels $K^+\pi^-\pi^-$ and $K_s^0\pi^-$. The branching fractions for these decays is shown in Table 4.6. Charged and neutral kaons must have a momentum greater than 200 MeV/ c . We require D^0 and D^- candidates to be within $\pm 3\sigma$ of their nominal masses, where the resolution σ is calculated for each event from the measured track parameters. The distributions of the difference between measured and nominal D^0 and D^- masses normalized by the measured resolution, shown in Fig. 4.10, have an RMS of 1.1-1.2 when fit with a Gaussian, indicating that the resolution is slightly worse than expected. For $D^0 \rightarrow K^-\pi^+\pi^0$, we only reconstruct the dominant resonant mode $D^0 \rightarrow K^-\rho^+$ followed by $\rho^+ \rightarrow \pi^+\pi^0$. The absolute value of the cosine of the angle between the π^+ and the D^0 in the ρ^+ rest frame must be greater than 0.4. Additionally, all D^0 and D^- candidates must have a momentum greater than 1.3 GeV/ c^2 in the $\Upsilon(4S)$ rest frame and a χ^2 probability for the geometric vertex fit greater than 0.1%. After satisfying these requirements, the charmed mesons are mass constrained to their nominal values.

Meson	Mass(MeV/ c^2)	Decay Mode	Branching fraction (%)
D^0	1864.5 ± 0.5	$K^-\pi^+\pi^0$	10.2 ± 0.9
		$K^-\pi^+\pi^+\pi^-$	7.5 ± 0.3
		$K^-\pi^+$	3.8 ± 0.1
D^+	1869.5 ± 0.5	$K^-\pi^+\pi^+$	9.1 ± 0.6
		$K_s^0\pi^+$	1.4 ± 0.1

Table 4.6: Branching fractions and decay modes D^0 and D^+ charm mesons used in this analysis

We form D^{*+} candidates in the decay $D^{*+} \rightarrow D^0\pi^+$ by combining a D^0 with a "soft pion" whose momentum is greater than 70 MeV/ c . The soft pion is constrained to originate from the beamspot when the D^{*+} vertex is computed. Since the B mesons have a non-negligible transverse flight length, the effective

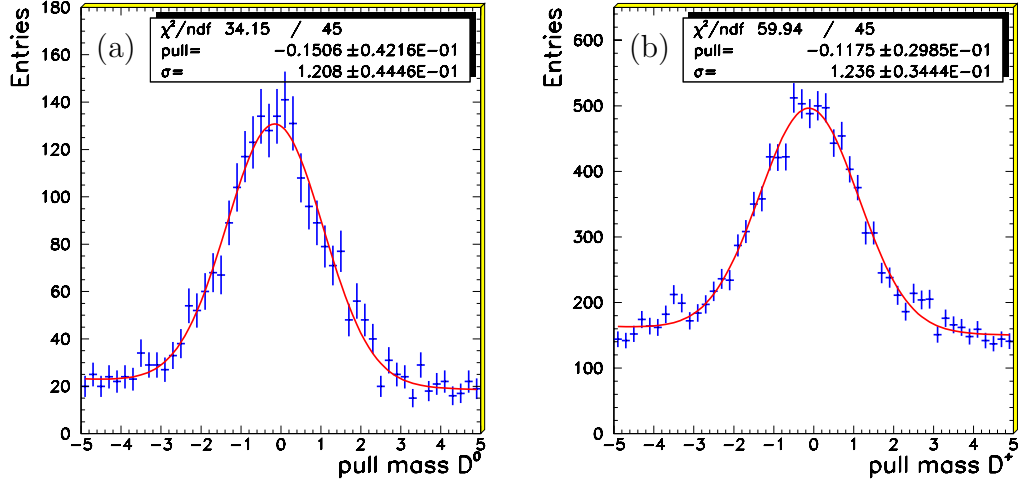


Figure 4.10: Distribution of (a) D^0 and (b) D^+ mass pulls for selected candidates. The mass pull is defined to be the difference between the measured mass and its nominal value divided by the measured error on the mass. A fit to a Gaussian distribution is overlaid on the data (points with error bars).

vertical size of the beam-spot is enlarged from its measured value to $40 \mu\text{m}$. D^{*+} candidates must have $|m(D^0\pi^+) - m(D^0)|$ within $3.3 \text{ MeV}/c^2$ of the nominal value for the $D^0 \rightarrow K^-\pi^+\pi^0$ mode and within $2.4 \text{ MeV}/c^2$ for all other modes. This corresponds to about ± 2.5 times the resolution of this variable. Fig 4.11a shows the distribution of $m(D^0\pi^+) - m(D^0)$ for data and simulated Monte Carlo.

We form D^{*0} candidates by combining a D^0 with a π^0 with momentum less than $450 \text{ MeV}/c$ in the $\Upsilon(4S)$ frame. D^{*0} candidates must have $|m(D^0\pi^0) - m(D^0)|$ within $4.2 \text{ MeV}/c^2$ ($\pm 3\sigma$) of the nominal value. Fig. 4.11b shows the distribution of $m(D^0\pi^0) - m(D^0)$ for data overlaid with a fit that uses a Gaussian distribution to model the signal component.

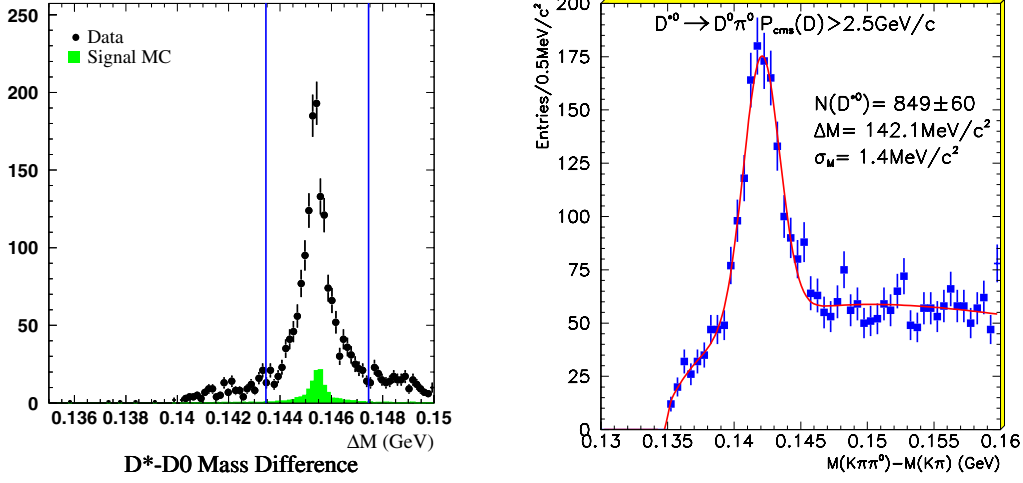


Figure 4.11: Distribution of (a) $m(D^0\pi^+) - m(D^0)$ and (b) $m(D^0\pi^0) - m(D^0)$ in data. The vertical lines in (a) indicate the selection criteria and the solid histogram shows the distribution in simulated Monte Carlo not normalized to the data sample. The data (points with error bars) in (b) are overlaid with a fit that models the signal component with a Gaussian distribution.

4.4 B meson reconstruction

We reconstruct B candidates in all modes using a pair of nearly uncorrelated kinematic variables, the difference ΔE between the energy of the B candidate and the beam energy in the c.m. frame, and the beam-energy substituted mass (m_{ES}). We define m_{ES} as

$$m_{\text{ES}} = \sqrt{\left(\frac{\frac{1}{2}s + \vec{\mathbf{p}}_{\mathbf{B}} \cdot \vec{\mathbf{p}}_{\mathbf{i}}}{E_i}\right)^2 - p_{\mathbf{B}}^2} \quad (4.4.1)$$

where s is the square of the c.m. energy, E_i and $\vec{\mathbf{p}}_{\mathbf{i}}$ are the total energy and the three momentum of the initial state in the laboratory frame, and $\vec{\mathbf{p}}_{\mathbf{B}}$ is the three momentum of the B candidate in the same frame. In the c.m. frame, this formula simplifies to

$$m_{\text{ES}} = \sqrt{E_{\text{beam}}^2 - p^{*2}} \quad (4.4.2)$$

where E_{beam} is the energy of the beam and p^* is the measured momentum of the B meson in the c.m. frame. For signal events, we expect $m_{\text{ES}} = m_B$, where m_B is the known B mass, and $\Delta E = 0$. For the purpose of determining event yields and purities, a signal region is defined in the $(m_{\text{ES}}, \Delta E)$ plane as $5.27 < m_{\text{ES}} < 5.29 \text{ GeV}/c^2$ and $|\Delta E| < 3\sigma(\Delta E)$, where $\sigma(\Delta E)$ is the resolution on ΔE . Also, a so-called sideband region is defined as $5.20 < m_{\text{ES}} < 5.26 \text{ GeV}/c^2$ and $|\Delta E| < 3\sigma(\Delta E)$. The resolution on ΔE is mode dependent and varies between about 10 MeV and 40 MeV in data, with larger values typically from modes with one or more π^0 , like $J/\psi K_s^0 (\pi^0 \pi^0)$. When more than one B candidate is reconstructed in the same event with $m_{\text{ES}} > 5.20 \text{ GeV}/c^2$, we choose the one with the smallest value of $|\Delta E|$.

Two types of background in the sample of B^0 candidates are distinguished. The first background, called combinatorial background, arises from random combinations of charged tracks and neutral showers from both B mesons in $B\bar{B}$ events or from continuum events. This background is distributed evenly in m_{ES} and does not show any enhancement near the B mass. The second background, called peaking background, consists of events where the B is reconstructed with all of its correct decay products except for usually one lower momentum track which came from the other B . Peaking backgrounds show a structure similar to the signal shape in the m_{ES} distribution with a resolution typically 10% larger.

Signal yields and purities are obtained by fitting the m_{ES} distribution of B candidates with a Gaussian distribution $\mathcal{S}(m_{\text{ES}})$ for the signal and an empirical phase space distribution [66] (henceforth referred to as the ARGUS distribution) $\mathcal{A}(m_{\text{ES}})$ for the combinatorial background. The functional form of $\mathcal{A}(m_{\text{ES}})$ is given by

$$\mathcal{A}(m_{\text{ES}}; m_0, \zeta) = A_B m_{\text{ES}} \sqrt{1 - x_{ES}^2} e^{\zeta(1 - x_{ES}^2)}, \quad (4.4.3)$$

with $x_{ES} \equiv m_{\text{ES}}/m_0 < 1$, where m_0 represents the kinematic upper limit which is held fixed at the c.m. beam energy $E_b^* = 5.291 \text{ GeV}$, and ζ and A_B are free parameters. The measured value of m_{ES} along with the Gaussian and ARGUS

fit parameters will be used to assign per-event signal probabilities that will be described in more detail in Chapter 7. The purity is defined to be the ratio of the integral of the Gaussian signal component of the m_{ES} distribution above $5.27 \text{ GeV}/c^2$ to the sum of this integral and the integral of events in the ARGUS component in the same m_{ES} range. The signal probability, p , is defined to be

$$p(m_{\text{ES}}) = \frac{\mathcal{S}(m_{\text{ES}})}{\mathcal{S}(m_{\text{ES}}) + \mathcal{A}(m_{\text{ES}})} \quad (4.4.4)$$

4.4.1 Helicity definition

For J/ψ and $\psi(2S)$ decays to $\ell^+\ell^-$ pairs, we use the helicity angle θ_ℓ to further reduce the contribution from continuum background. We define θ_ℓ as the angle in the charmonium rest frame between the ℓ^- and the charmonium direction in the B candidate rest frame. Fig. 4.12 gives a schematic representation of this angle for the decay $B^0 \rightarrow J/\psi K_s^0$. Since the B is a pseudoscalar, the charmonium and K_s^0 meson cannot have a net spin projection along their decay axis direction in the B rest frame in order to conserve angular momentum. This means that the J/ψ or $\psi(2S)$ has its spin transverse to its direction of motion (referred to as longitudinal polarization) since there can be no cancellation with the spin zero K_s^0 meson. It can be shown [38] that the amplitude for the decay of a particle with spin J and projection M along an arbitrary z axis to particles 1 and 2 of helicity λ_1 and λ_2 is proportional to the function $d_{M,\lambda_1-\lambda_2}^J(\theta)$, where θ is the polar angle between the momentum of particle 2 with respect to the spin quantization axis. The probability for longitudinally polarized J/ψ or $\psi(2S)$ vector meson to decay to two spin (1/2) leptons that have opposite helicity is then proportional to the square of $d_{0,1}^1$, or $\sin^2 \theta_\ell$. This angle is very useful in rejecting background since the distribution of $\cos \theta_\ell$ is peaked at ± 1 for background and at zero for signal modes. Fig. 4.13 makes this evident, displaying the distribution of $\cos \theta_\ell$ observed in data for $B^0 \rightarrow J/\psi K_s^0$ and $B^+ \rightarrow J/\psi K^+$ candidates in the signal and sideband region.

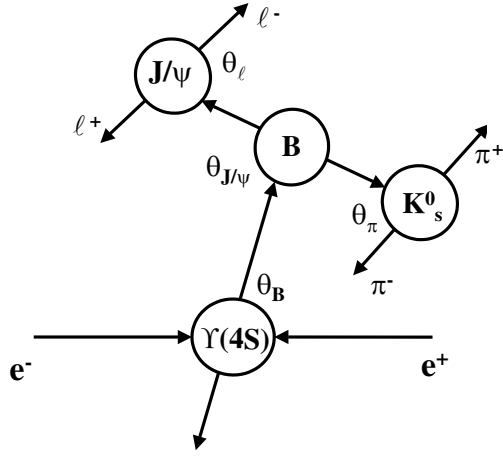


Figure 4.12: Helicity angle definitions for the decay $\Upsilon(4S) \rightarrow B\bar{B} \rightarrow J/\psi(\ell^+\ell^-)K_s^0$ as explained in the text. For the $J/\psi \rightarrow \ell^+\ell^-$ decay shown, the probability is proportional to $\sin^2\theta_\ell$.

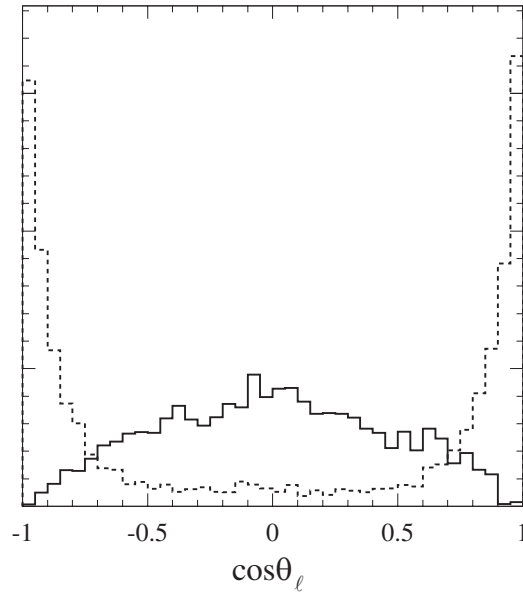


Figure 4.13: Distributions of $\cos\theta_\ell$ observed in data for $B^0 \rightarrow J/\psi K_s^0$ and $B^+ \rightarrow J/\psi K^+$ candidates. The dashed histogram shows candidates in the sideband region and the solid histogram shows candidates in the signal region, after subtracting the appropriately scaled contribution from the sideband. Both histograms have been normalized to unit area.

4.4.2 Thrust definition

Suppression of continuum background for events containing $\psi(2S) \rightarrow J/\psi \pi^+ \pi^-$ and χ_{c1} decays, where the helicity angle is not applicable, is also provided by restricting the thrust angle θ_{th} , defined as the angle between the thrust axis of the particles that form the reconstructed B candidate (B_{rec}) and the thrust axis of the remaining tracks and neutral clusters, computed in the c.m. frame. The thrust axis of a collection of particles is the direction about which the transverse momenta of the particles is a minimum. The distribution of $\cos(\theta_{th})$ for $B\bar{B}$ events is flat, again due to the small momenta of the B mesons in the $\Upsilon(4S)$ frame, while $|\cos(\theta_{th})|$ is peaked at 1 for continuum events which are composed of roughly collinear jets of light quarks.

4.5 Reconstructing decays to CP eigenstates

The branching fractions for the B^0 decays to CP eigenstates that are used in this analysis are shown in Table 4.7. The B_{CP} sample is formed by combining charmonium meson candidates with K_s^0 candidates. Both the charmonium and K_s^0 candidate are mass constrained to their known masses (except for the η_c candidates because of their natural finite width). For J/ψ candidates reconstructed as e^+e^- ($\mu^+\mu^-$) in the $B^0 \rightarrow J/\psi K_s^0$ mode, we require $|\cos \theta_\ell| < 0.8$ (0.9). For $\psi(2S)K_s^0$ candidates, $|\cos \theta_\ell|$ of the $\psi(2S)$ must be less than 0.9 for both leptonic modes. For the $J/\psi \pi^+ \pi^-$ decay of the $\psi(2S)$ and for $\chi_{c1}K_s^0$ candidates, we require $|\cos \theta_{th}| < 0.9$. The background rejection methods used for $\eta_c K_s^0$ candidate selection are more complicated and are described in detail in Ref. [67]. Fig. 4.14 shows the m_{ES} distributions from the full data set for the CP modes after a 3σ (ΔE) cut has been applied. Signal event yields and purities, determined from a fit to the m_{ES} distributions as explained in Sec. 4.4, are shown in Table 4.8. The quoted yields and purity contain contributions from peaking background.

Decay	Branching fraction (10^{-4})
$B^0 \rightarrow J/\psi K_S^0$	4.4 ± 0.3
$B^0 \rightarrow \psi(2S)K_S^0$	2.8 ± 0.8
$B^0 \rightarrow \chi_{c1}K_S^0$	$2.0^{+0.6}_{-0.5}$
$B^0 \rightarrow \eta_c K_S^0$	5.5^{+3}_{-3}

Table 4.7: Branching fractions for B^0 decays to charmonium CP -eigenstates.

Final State	Signal	Purity (%)	$\sigma(m_{ES})$	
$J/\psi K_S^0$ ($K_S^0 \rightarrow \pi^+ \pi^-$)	e^+e^- $\mu^+\mu^-$	683 ± 28 746 ± 28	93 98	2.69 ± 0.10 2.62 ± 0.08
$J/\psi K_S^0$ ($K_S^0 \rightarrow \pi^0 \pi^0$)	e^+e^- $\mu^+\mu^-$	112 ± 12 142 ± 13	83 91	2.87 ± 0.30 3.30 ± 0.26
$\psi(2S)K_S^0$	e^+e^-	106 ± 15	83	2.88 ± 0.43
	$\mu^+\mu^-$	106 ± 11	93	2.55 ± 0.22
$\chi_{c1}K_S^0$	e^+e^-	56 ± 8	95	3.15 ± 0.39
	$\mu^+\mu^-$	55 ± 8	94	2.61 ± 0.35
$\eta_c K_S^0$	$K^+K^-\pi^0$	174 ± 17	70	2.62 ± 0.27
Total		2153 ± 50	92	2.73 ± 0.06

Table 4.8: Event yields, purity, and resolution on m_{ES} for the CP sample before any tagging or vertexing requirements. The yields and purity are obtained from a fit to the m_{ES} distribution after selection on ΔE . Purities are quoted for $m_{ES} > 5.27 \text{ GeV}/c^2$. We also fit for the mean of the Gaussian component but we omit those results here since the mean is found to be consistent with the B^0 mass for all modes.

4.5.1 Peaking backgrounds for the CP sample

The fraction of peaking background has been estimated with a sample of $B^0 \rightarrow J/\psi X$ Monte Carlo events for all final states except $\eta_c K_S^0$. Since peaking background looks like signal in the m_{ES} distribution, it is not accounted for by the ARGUS background component of the m_{ES} fit. For each CP mode (excluding $\eta_c K_S^0$), we perform two fits to the m_{ES} distribution of the Monte Carlo events: first for all events, and second, removing the signal CP events. In the second fit, the sigma and mean of the Gaussian signal component are

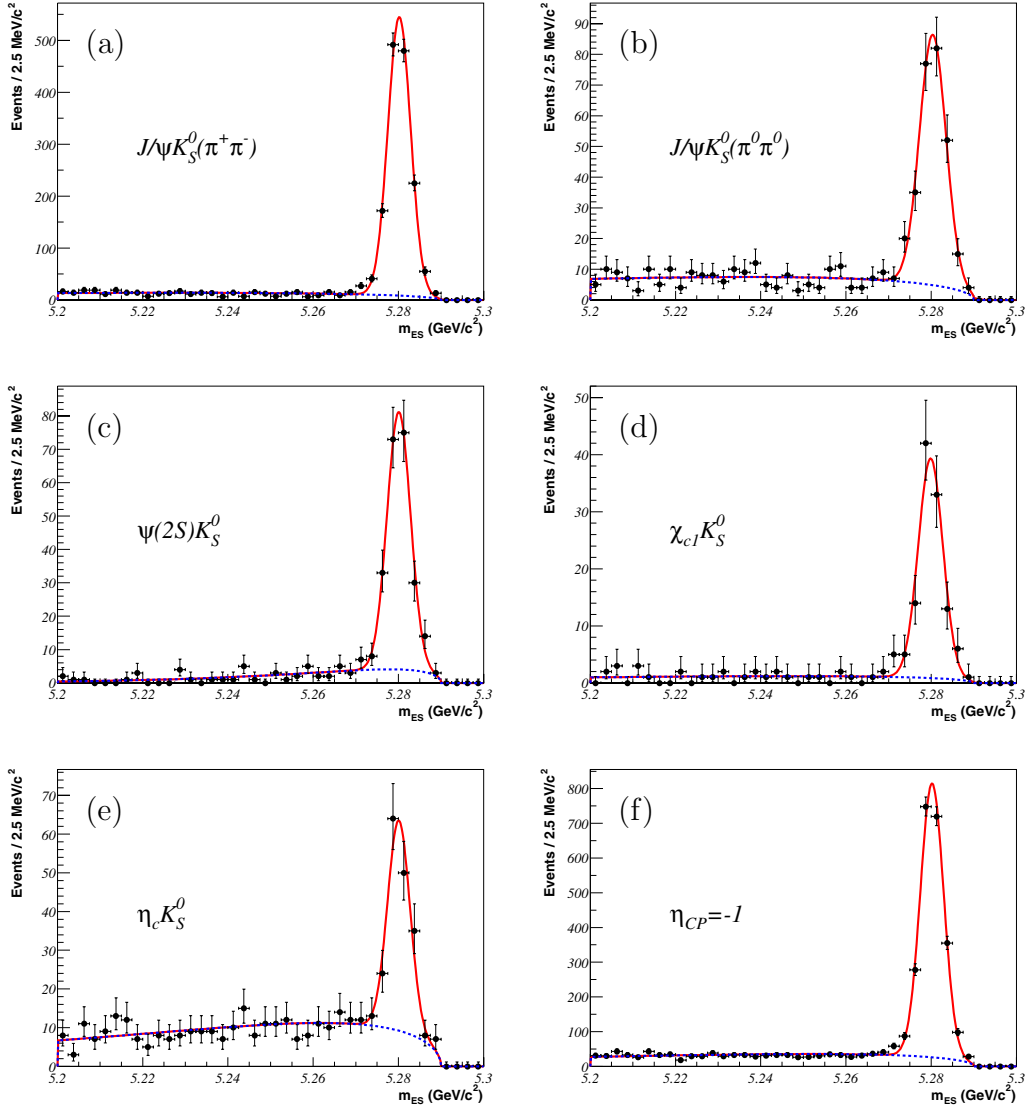


Figure 4.14: Distribution of m_{ES} for neutral B^0 CP eigenstates reconstructed as (a) $J/\psi K_S^0 (\pi^+ \pi^-)$, (b) $B^0 \rightarrow J/\psi K_S^0 (\pi^0 \pi^0)$, (c) $\psi(2S) K_S^0$, (d) $\chi_{c1} K_S^0$, (e) $\eta_c K_S^0$, and (f) all modes with a CP eigenvalue of -1 . Overlaid on each plot is the result of a fit to a Gaussian distribution for the signal and an ARGUS distribution for the background.

fixed to the values determined from the first fit. The ratio of the Gaussian areas from the fits determines the peaking background fraction. Table 4.9 and

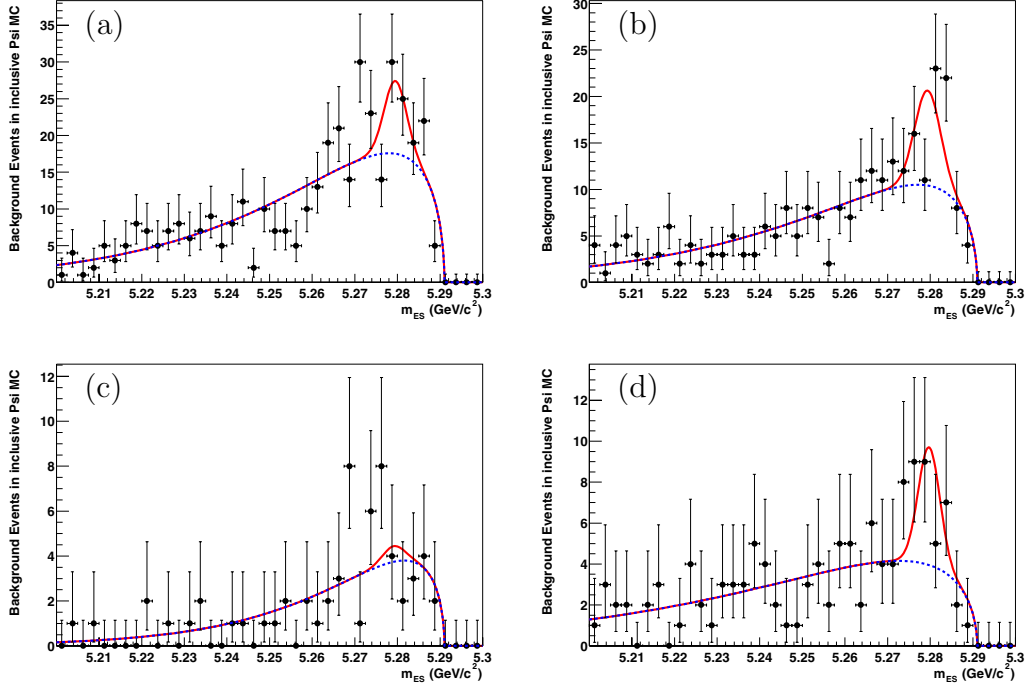


Figure 4.15: Fits to m_{ES} distribution of inclusive $B^0 \rightarrow J/\psi X$ Monte Carlo to determine peaking background fractions for (a) $J/\psi K_S^0 (\pi^+ \pi^-)$, (b) $J/\psi K_S^0 (\pi^0 \pi^0)$, (c) $\psi(2S)K_S^0$, and (d) $\chi_{c1}K_S^0$.

Fig. 4.15 show the results of these fits. For $\eta_c K_S^0$, the peaking background is determined from a joint fit to the m_{ES} and η_c mass distribution as described in [67]. The fraction is determined with the assumptions that the majority of the background comes from B mesons which decay to the same final state particles but not through an η_c resonance, and that the distribution of this background is flat in the η_c mass distribution. These assumptions were verified on a high statistics Monte Carlo sample. The peaking background fraction is determined to be $(13.9 \pm 3.6)\%$ for $\eta_c K_S^0$. The fraction of peaking background is a direct input used to determine $\sin 2\beta$ as will be explained in Chapter 7.

Final State	Fraction of peaking background (%)
$J/\psi K_S^0 (K_S^0 \rightarrow \pi^+ \pi^-)$	0.28 ± 0.11
$J/\psi K_S^0 (K_S^0 \rightarrow \pi^0 \pi^0)$	1.76 ± 0.57
$\psi(2S)K_S^0$	1.17 ± 3.10
$\chi_{c1}K_S^0$	3.54 ± 1.44
$\eta_c K_S^0$	13.1 ± 5.9

Table 4.9: Peaking background fractions for the CP sample. The errors are the statistical errors from the m_{ES} fits.

Decay	Branching fraction (10^{-3})
$B^0 \rightarrow D^- \pi^+$	3.0 ± 0.4
$B^0 \rightarrow D^- \rho^+$	7.8 ± 1.4
$B^0 \rightarrow D^- a_1^+$	6.0 ± 3.3
$B^0 \rightarrow D^{*-} \pi^+$	2.76 ± 0.21
$B^0 \rightarrow D^{*-} \rho^+$	7.3 ± 1.5
$B^0 \rightarrow D^{*-} a_1^+$	1.30 ± 0.27
$B^0 \rightarrow J/\psi K^{*0}$	1.31 ± 0.09

Table 4.10: Branching fractions for B^0 decays to flavor-eigenstates used in this analysis.

4.6 Reconstructing decays to flavor-eigenstates

Candidates in the B_{flav} sample of neutral flavor-eigenstate B mesons are formed by combining a D^{*-} or D^- with a π^+, ρ^+ , or a_1^+ , or by combining a J/ψ candidate with a $K^{*0} (\rightarrow K^+ \pi^-)$. The branching fractions for these decays are shown in Table 4.10. The charged pion in the decay $B^0 \rightarrow D^{(*)-} \pi^+$ and $B^0 \rightarrow D^{(*)-} \rho^+$ must have a momentum greater than 200 MeV/ c^2 . For the decay mode $B^0 \rightarrow D^{(*)-} a_1^+$, the charged pions must have momentum larger than 150 MeV/ c^2 . For most decay modes, it is possible to achieve signal purities of at least 90% using **VeryLoose** (or no) kaon particle identification. However, for the modes $B^- \rightarrow D^- a_1^+$ and $B^- \rightarrow D^- \rho^+$, the **VeryTight** kaon PID selection is required to reduce large combinatorial backgrounds.

For final states with a D^* and 2 (3) pions we require $|\cos \theta_{th}| < 0.9(0.8)$

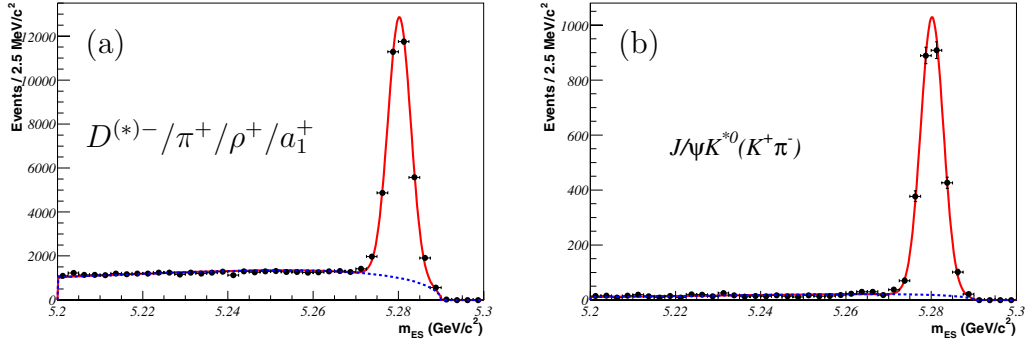


Figure 4.16: Distribution of m_{ES} for B^0 flavor-eigenstate candidates to (a) open charm and (b) charmonium final states. Overlaid in both cases is the result of a fit with a Gaussian distribution for the signal and an Argus function for the background.

for the $D^0 \rightarrow K^-\pi^+$ and $K^-\pi^+\pi^0$ modes and 0.8 (0.7) for $D^0 \rightarrow K^-\pi^+\pi^+\pi^-$ and $D^0 \rightarrow K_s^0\pi^+\pi^-$. Modes which contain a D^- and a $\pi^+, \rho^+,$ or a_1^+ in the final state must have $|\cos\theta_{th}| < 0.9, 0.8,$ or 0.7 respectively.

The distribution of m_{ES} for all the hadronic B^0 flavor-eigenstates after a $3\sigma \Delta E$ cut has been applied is shown in Fig. 4.16 The purities and yields are given in Table 4.11.

4.6.1 Peaking backgrounds for the B_{flav} sample

The signal yields for the B_{flav} sample shown in Table 4.11 contain a small fraction of peaking background from other charged and neutral B decay modes. Typically, the peaking background results from the replacement of one low momentum pion which originated in the decay of the B_{flav} meson by another low momentum pion which originated in the decay of the other B meson. The decay Δt distribution of the neutral peaking background events will have the same structure as the signal since the vertex (and hence Δt) will primarily be determined by the higher momentum tracks in the decay which have been correctly identified. For peaking background events with charged B mesons,

Final State	Signal	Purity (%)	$\sigma(m_{\text{ES}})$
$B^0 \rightarrow D^{*-} \pi^+$	7333 ± 143	92	2.69 ± 0.06
$B^0 \rightarrow D^{*-} \rho^+$	4668 ± 199	85	3.11 ± 0.13
$B^0 \rightarrow D^{*-} a_1^+$	3471 ± 150	79	2.69 ± 0.10
$B^0 \rightarrow D^- \pi^+$	8222 ± 205	82	2.62 ± 0.06
$B^0 \rightarrow D^- \rho^+$	4669 ± 201	77	3.00 ± 0.12
$B^0 \rightarrow D^- a_1^+$	2643 ± 156	66	2.58 ± 0.14
$B^0 \rightarrow J/\psi K^{*0}(K^+ \pi^-)$	2689 ± 54	95	2.65 ± 0.04
Total	34404 ± 215	82	2.67 ± 0.02

Table 4.11: Event yields, purity and resolution on m_{ES} for the flavor-eigenstate sample before any tagging or vertexing requirements. The yields and purity are obtained from a fit to the m_{ES} distribution after selection on ΔE . Purities are quoted for $m_{\text{ES}} > 5.27 \text{ GeV}/c^2$. We also fit for the mean of the Gaussian component but we omit those results here since the mean is found to be consistent with the B^0 mass for all modes

however, the time structure will no longer be the same as the signal because the neutral and charged B mesons have different lifetimes. Further, charge conservation prohibits mixing in the charged B peaking background events which is not true for the peaking background from neutral decays. Consequently, the fraction of peaking background coming from charged B decays is estimated with a sample of $\Upsilon(4S) \rightarrow B^+ B^-$ Monte Carlo events where the B^- are forced to decay into the final states $D^{(*)0} \pi^- / \rho^- / a_1^-$ (since these modes are the dominant contribution to the peaking background). We then reconstruct the events in this sample the same way that the signal B_{flav} events are reconstructed. Fitting the m_{ES} distribution with a Gaussian function whose mean and width are fixed by the B^0 signal parameters, we find a peaking background fraction of $(1.3 \pm 0.3_{-0.5}^{+0.2})\%$. The Δt structure of the peaking background in the Monte Carlo is found to be consistent with the lifetime of the B^- as expected.

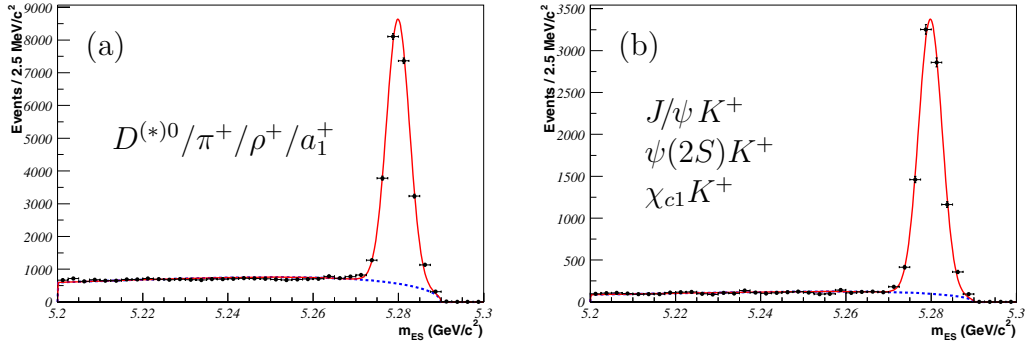


Figure 4.17: Distribution of m_{ES} for B^- control sample candidates to (a) open charm and (b) charmonium final states. Overlaid in both cases is the result of a fit with a Gaussian distribution for the signal and an Argus function for the background.

4.7 Reconstructing charged B decay control samples

We reconstruct B^- candidates as a control sample for the $\sin 2\beta$ analysis and to validate the flavor-tagging algorithms. The B^- control sample is formed by combining a D^{*0} , D^0 , J/ψ , $\psi(2S)$, or χ_{c1} candidate with a π^+ or K^+ . We require $|\cos\theta_{th}| < 0.9$ for $D^0 \rightarrow K^-\pi^+$, 0.7 for $D^0 \rightarrow K_S^0\pi^+\pi^-$, and 0.8 for other D^0 decay modes to reduce continuum background. There is no PID requirement on the charged kaon or pion from the B^- decay, but the pion must have momentum greater than 150 MeV/c in the laboratory. The distributions of m_{ES} for the charmonium and open charm B^- decay modes after a $3\sigma \Delta E$ cut has been applied are shown in Fig. 4.17. The purities and yields are given in Table 4.12.

Final State	Signal	Purity (%)	$\sigma(m_{\text{ES}})$
$B^- \rightarrow D^0 \pi^-$	15647 ± 282	83	2.69 ± 0.05
$B^- \rightarrow D^{*0} \pi^-$	6198 ± 183	89	3.10 ± 0.09
$J/\psi K^+$	5666 ± 78	95	2.52 ± 0.04
$\psi(2S)K^+$	865 ± 31	94	2.65 ± 0.16
$\chi_{c1}K^+$	553 ± 25	95	2.81 ± 0.21

Table 4.12: Event yields, purity and resolution on m_{ES} for the B^- control sample before any tagging or vertexing requirements. The yields and purity are obtained from a fit to the m_{ES} distribution after selection on ΔE . Purities are quoted for $m_{\text{ES}} > 5.27 \text{ GeV}/c^2$.

Chapter 5

Flavor tagging

In order to measure the time-dependent asymmetry of neutral B decays to CP eigenstates in $\Upsilon(4S) \rightarrow B\bar{B}$ events, it is necessary to determine the flavor of the other B meson that we refer to as the B_{tag} . This is accomplished by examining the decay products of the B_{tag} , which are obviously correlated with its flavor. In an ideal world we would like to develop a tagging algorithm that is capable of identifying the flavor of any B decay without making a mistake. We quantify our algorithm, then, by its tagging efficiency ϵ , defined as the fraction of events with a reconstructed B that are tagged, and by its mistag rate w , which measures the probability that the algorithm gives the wrong answer for the flavor of the B_{tag} .

5.1 Importance of tagging

To understand the statistical impact of the efficiency and mistag rate of the tagging algorithm on our ability to measure $\sin 2\beta$, let's consider a general asymmetry where we tag N^a events of type a and N^b of type b . The measured (true) asymmetry $A_m(A_t)$ is defined as

$$A_i = \frac{N_i^a - N_i^b}{N_i^a + N_i^b}, \quad (5.1.1)$$

where i represents either measured (m) or true (t) quantities. We relate A_m to A_t by noting that the measured number of events of each type can be written as

$$\begin{aligned} N_m^a &= \epsilon[N_t^a(1-w) + N_t^b w] \\ N_m^b &= \epsilon[N_t^a w + N_t^b(1-w)], \end{aligned}$$

where ϵ is the efficiency to tag events, and w is the probability of incorrectly tagging an event. We assume for simplicity that ϵ and w are the same for events in both categories. We then find that

$$\frac{N_m^a - N_m^b}{N_m^a + N_m^b} = (1-2w) \frac{N_t^a - N_t^b}{N_t^a + N_t^b}. \quad (5.1.2)$$

Defining the dilution, \mathcal{D} , to be $1-2w$, we can relate the measured and true asymmetry by

$$A_m = \mathcal{D}A_t, \quad (5.1.3)$$

Assuming that the error on N_m^a (N_m^b) goes like $\sqrt{N_m^a}$ ($\sqrt{N_m^b}$), one finds from Eqn. 5.1.1 that the error on the measured asymmetry is given by

$$\sigma(A_m) = \sqrt{\frac{1 - A_m^2}{N_m}}, \quad (5.1.4)$$

where $N_m = N_m^a + N_m^b$. Then the error on the true asymmetry is given by

$$\sigma(A_t) = \frac{\sigma(A_m)}{\mathcal{D}} = \sqrt{\frac{1 - A_m^2}{N_t \epsilon \mathcal{D}^2}}, \quad (5.1.5)$$

where $N_t = N_t^a + N_t^b = N_m/\epsilon$. In the experiment, N_t is just the number of events collected before tagging has been applied (i.e., for our purposes this corresponds to the number of fully reconstructed B decays to CP eigenstates).

We are accustomed to the error on a measured quantity scaling like $1/\sqrt{N}$. For an asymmetry measurement, however, we see that this scaling is modified to $1/\sqrt{N\epsilon\mathcal{D}^2}$. In other words, in order to measure $\sin 2\beta$ with the smallest error given some number of fully reconstructed B mesons which decay to CP eigenstates, we need to maximize the product of the tagging efficiency and the square of the dilution. This product, termed the Q factor, is the figure of merit for the tagging algorithm to be discussed.

5.2 Sources of B flavor information

All sources of flavor tagging information arise from correlations between the charge of the initial bottom quark in the B_{tag} and its decay products. Decays of the B_{tag} to leptons, kaons, and low momentum pions from D^* decays (“soft pions”) provide the most useful information in determining the flavor of the parent B meson.

5.2.1 Lepton tags

Electrons and muons are produced in $B\bar{B}$ events from semileptonic B decays, semileptonic $D^{(*)}$ decays, decays of charmonium mesons, kaon and pion decays, and photon conversions. Semileptonic decays of B mesons are the most important for lepton tagging. A neutral B^0 meson (composed of a $\bar{b}d$ quark pair) decays semileptonically by the transition $\bar{b} \rightarrow \bar{c}W^+(\rightarrow \ell^+\nu_\ell)$. The virtual W^+ turns into either a $e^+\nu_e$ or $\mu^+\nu_\mu$ pair about 21% of the time. The positive charge of the lepton tags the flavor of the parent meson as being a B^0 (negatively charged leptons tag \bar{B}^0 mesons). These primary leptons are called direct or right-sign leptons. Leptons may also originate from cascade processes where the \bar{c} quark decays to an \bar{s} by emitting a W^- which gives a negatively charged lepton, $\bar{b} \rightarrow \bar{c}W^+ \rightarrow \bar{s}W^-(\rightarrow \ell^-\nu_\mu)$. Fig. 5.1 illustrates the decays which result in primary and secondary lepton production. The leptons from cascade decays (secondary leptons) have a much softer momentum spectrum than primary leptons. Another source of wrong flavor assignment results from hadrons being misidentified as leptons which can be reduced by requiring well identified leptons using particle identification information.

Three kinematic variables are used in our tagging algorithm to distinguish primary and secondary leptons. The c.m. momentum (p^*) of the candidate track is the most powerful discriminating variable. Fig 5.2 shows p^* for electrons and muons in data, after background subtraction based on the m_{ES} sideband events, compared to simulation. The primary lepton spectrum extends to

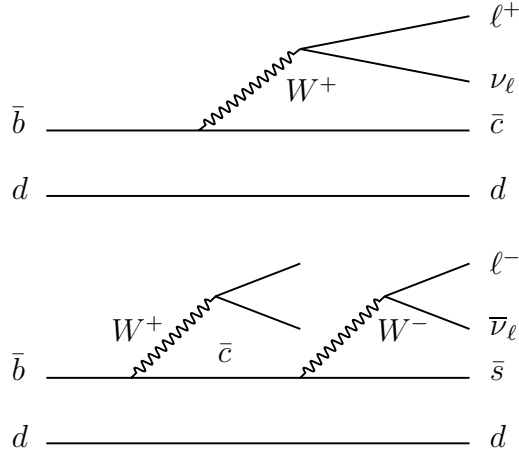


Figure 5.1: Illustration of B^0 decay to primary (top) and secondary (bottom) leptons used for flavor tagging. Positively charged primary leptons tag B^0 mesons.

much higher momenta as expected. The second discriminating variable, E_{90}^W , is defined as the energy in the hemisphere defined by the direction of the virtual W^\pm in the assumed semileptonic B decay. This energy is calculated in the $\Upsilon(4S)$ frame assuming the B_{tag} is at rest. The W^\pm direction is inferred from the sum of the lepton candidate and the neutrino momentum, which we take to be the missing momentum using all charged tracks in the B_{tag} . This variable peaks at zero for primary leptons from semileptonic B decays since the virtual W^\pm travels opposite the hadronic B decay products. Also, primary lepton selection is based on the cosine of the angle between the lepton candidate's momentum and the missing momentum in the event ($\cos\theta_{miss}$) due to the presence of a neutrino. The distribution of $\cos\theta_{miss}$ depends on the probability distribution for different kinematic configurations of the specific three-body semileptonic B decay, but tends to peak at -1 for primary leptons whereas the background has a flatter distribution.

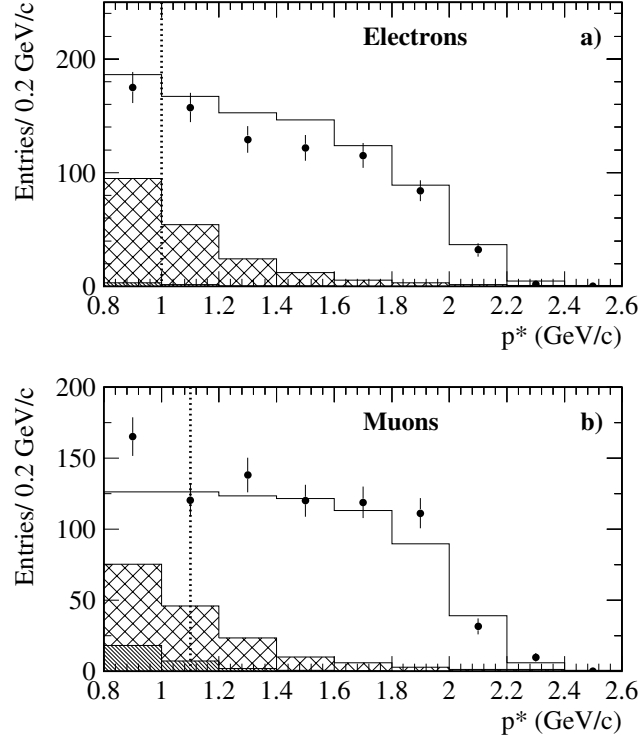


Figure 5.2: Distribution of c.m. momenta for (a) electrons and (b) muons in data which are shown as points. The open histogram shows primary leptons, the cross-hatched histogram cascade leptons, and the diagonally hatched histogram fake leptons, all from Monte Carlo simulation.

5.2.2 Kaon tags

The principal sources of charged kaons from b -quark decays are [68]:

$$b \rightarrow cW^-; c \rightarrow W^+s, s \Rightarrow K^- \quad (a)$$

$$b \rightarrow XW^-; W^- \rightarrow \bar{c}s, s \Rightarrow K^- \text{ and/or } \bar{c} \rightarrow W^+\bar{s}, \bar{s} \Rightarrow K^+ \quad (b)$$

$$b \rightarrow cW^-; W^- \rightarrow \bar{u}s, s \Rightarrow K^- \text{ and/or } c \rightarrow XW^+, W^+ \rightarrow u\bar{s}, \bar{s} \Rightarrow K^+ \quad (c)$$

$$b \rightarrow Xs\bar{s}; s \Rightarrow K^- \text{ and/or } \bar{s} \Rightarrow K^+ \quad (d)$$

$$b \rightarrow sq\bar{q} \text{ (penguin)}; s \Rightarrow K^- \quad (e)$$

The kaon from the dominant process (a) is referred to as the right sign kaon (a K^- indicates a \bar{B}^0 tag). We see that processes (b), (c), and (d) yield both right sign and wrong sign kaons, usually with a second strange particle in the

event. Doubly Cabibbo-suppressed (see Sec. 9.6) and penguin process (e) give small contributions. Fig. 5.3 illustrates a B decay to both right and wrong sign kaons. Events containing more than one kaon with the same charge occur since the processes listed are not mutually exclusive. Wrong-sign kaons contribute to the mistag rate. The multiplicities for right and wrong sign kaons from B decays have been measured by the ARGUS collaboration [69]:

$$n(B^0 \rightarrow K^+ X) = 0.58 \pm 0.01 \pm 0.08$$

$$n(B^0 \rightarrow K^- X) = 0.13 \pm 0.01 \pm 0.05$$

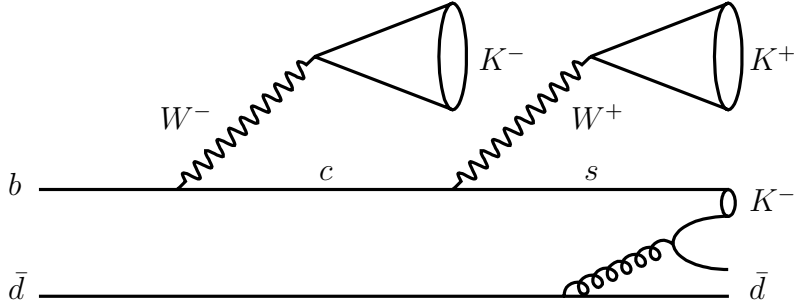


Figure 5.3: Illustration of \bar{B}^0 decay to right and wrong sign kaons. Negatively charged kaons tag \bar{B}^0 mesons.

Since most kaons produced in B^0 decays are right sign kaons, the presence of a single charged kaon provides a powerful tag. However, we were unable to identify a kinematic variable that could distinguish between right and wrong sign kaons. Consequently, a tagging algorithm based only on a single kaon charge can only use pid information (to reduce the contamination from pions faking kaons) and will be subject to an irreducible mistag rate from wrong sign kaon production.

Since a significant fraction of B decays contain more than one charged kaon, we use a tagging algorithm that relies on information from the charges

of the three best identified kaon candidates in an event ¹. In many events, neutral kaons are produced as well, weakening the tagging information carried by the charged kaons. The c.m. momentum spectrum for charged kaons and the distribution of charged kaon multiplicity are shown in Fig. 5.4 for data compared to simulation.

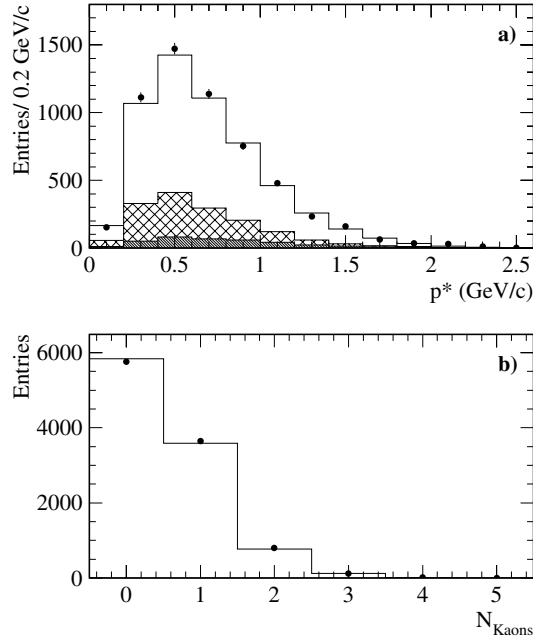


Figure 5.4: Distribution of (a) c.m. momenta for charged kaons and (b) multiplicity of charged kaons per event in data which are shown as points. The histograms are from simulation. In (a), the diagonally-hatched histogram is from fake kaons, the cross-hatched histogram is from wrong sign kaons, and the open histogram is from right sign kaons.

5.2.3 Soft pion tags

Charged slow pions originating from $D^{*\pm}$ decays are another source of flavor tagging information which, compared to lepton or kaon tags, have the opposite

¹The term best is used to indicate the kaon with the largest *SingleKaonTag* value that is described in Sec. 5.3.

charge (a negatively charged soft pion tags a B^0). The term soft refers to the fact that the charged D^* is barely massive enough to decay to a D^0 and pion; the momentum of the charged pion and D^0 in the $D^{*\pm}$ frame is only $39 \text{ MeV}/c$. Because the slow pion and D^0 are nearly at rest in the $D^{*\pm}$ frame, the boost of the $D^{*\pm}$ in the B rest frame causes the opening angle between the slow pion and D^0 in this frame to be very small. Since the B is nearly at rest in the c.m. frame, this production mechanism gives rise to an angular correlation between the soft pion and thrust axis of the B decay products.

Consequently, the tagging algorithm uses three discriminating variables to identify slow pions: the momentum of the slow pion in the c.m. frame, the cosine between the soft pion and the thrust axis (computed using charged and neutral particles) in the c.m. frame, and kaon pid information. The kaon pid information is used to reject the small contribution from low momentum kaons.

5.3 Tagging algorithm

Several flavor tagging algorithms have been developed at *BABAR*. They are all based on exploiting the sources of tagging information described in the previous section. A multivariate tagging algorithm [70] that uses categories based on the physics of the B_{tag} decay was used for this analysis.

In each event containing a fully reconstructed B meson (B_{rec}), the charged tracks and neutral clusters associated with the B_{rec} are removed. The remaining tracks which have been found to originate near the primary vertex and neutral clusters with energy greater than 50 MeV are used for tagging. Electron (muon) candidates are selected from tracks which pass the **VeryTight** (**Tight**) pid selection criteria listed in Sec. 4.2. Kaon candidates must satisfy the **VeryLoose** criteria. A list of tracks is also created from tracks that fail the electron and muon selection, called the Nonlepton list.

There are two major stages in the tagging algorithm. The first stage consists of seven neural networks which are each designed to distinguish B^0 and \bar{B}^0

Input Tagger	Track List	Discriminating Variables
<i>ElectronTag</i>	Electron List	$p^*, E_{90}^W, \cos \theta_{miss}$
<i>MuonTag</i>	MuonList	$p^*, E_{90}^W, \cos \theta_{miss}$
<i>KinematicLeptonTag</i>	Nonlepton List	$p^*, E_{90}^W, \cos \theta_{miss}$
<i>SingleKaonTag</i>	Charged Tracks	kaon pid variables
<i>KaonTag</i> (3 best kaons)	Single Kaon Tag	best three kaon tags
<i>SlowPionTag</i>	Charged tracks	$p^*, \cos \theta_{thrust} $, kaon pid
<i>KaonSlowPionTag</i>	Kaon Tag, Pion Tag	kaon tag, pion tag, $\cos \theta_{K\pi}$
<i>Maximum p^* Tag</i>	Charged tracks	p^*

Table 5.1: Input tagger names, lists, and discriminating variables used in the first stage of the flavor tagging algorithm.

meson decays using different physical sources of tagging information. We refer to each neural network in this stage as an "input tagger". The input taggers are trained using extensive Monte Carlo simulations of $B\bar{B}$ events. Each input tagger outputs a continuous tag value between ± 1 with an output of $+1(-1)$ indicating a higher probability of the meson being a B^0 (\bar{B}^0). The properties of the input taggers are shown in Table 5.1. In the second stage of the tagging algorithm, a final neural network combines the outputs of the input taggers taking into account correlations between different sources of flavor information. The final neural network also outputs a tag value (tag_f) between ± 1 and provides an estimate of the mistag probability for each event. The structure of the algorithm is illustrated schematically in Fig. 5.5.

Using both the tag value returned by each input tagger and the final neural net tag value, the algorithm assigns events to hierarchical, mutually exclusive tagging categories. Each event is placed in the most powerful tagging category whose requirements it fulfills. The method ensures that the categories are directly related to the physical processes involved in the B_{tag} decay. This is beneficial compared to an algorithm without categories or one that defines categories based only the final output of a neural net tagger because correlations may exist between *one* tagging category and some variable in the analysis

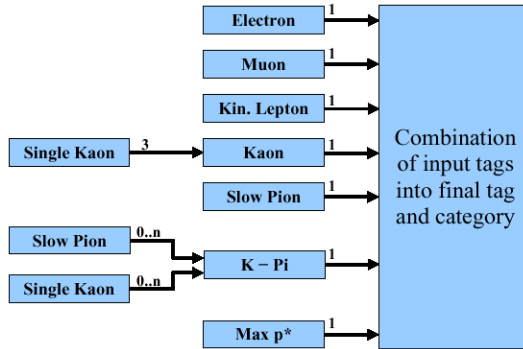


Figure 5.5: Schematic representation of flavor tagging algorithm.

(the event-by-event measured error on Δt , for example) that are both used to determine $\sin 2\beta$. The use of categories, then, allows for these correlations to be explicitly parameterized where they otherwise might not have been observed. This will become clearer in Chapter 7 when we detail the method used to determine $\sin 2\beta$.

Table 5.2 defines the tagging categories based on the value returned by the input taggers and the final neural net tag. These categories may be merged for simplification without significant loss in tagging power. The scheme used to merge these detailed categories into 4 final categories named `Lepton`, `Kaon-I`, `Kaon-II`, and `Inclusive` is shown in Table 5.3. We note that the `Inclusive` category is the only one without a well defined physics content (it only makes a requirement on the final neural tag).

5.4 Performance of the tagging algorithm

The performance of the tagging algorithm has been evaluated on a high statistics sample of Monte Carlo simulated $B\bar{B}$ decays where one B meson decays is forced to decay to $\pi^+ \pi^-$ and the other B meson decays generically. The results are shown in Table 5.4. The difference between the efficiency, mistag rate, and Q factor for B^0 and \bar{B}^0 mesons are called $\Delta\epsilon$, Δw , and ΔQ

Category	Cuts on input tags	Cut on $ tag_f $
Electron-kaon	$ ElectronTag > 0.7$ & $ KaonTag > 0.2$	$ tag_f > 0.8$
Muon-kaon	$ MuonTag > 0.7$ & $ KaonTag > 0.2$	$ tag_f > 0.8$
Electron	$ ElectronTag > 0.7$	$ tag_f > 0.8$
Muon	$ MuonTag > 0.7$	$ tag_f > 0.8$
Kaon-slow pion	$ KaonSlowPionTag > 0.1$	$ tag_f > 0.8$
Kaon I	$ KaonTag > 0.2$	$ tag_f > 0.7$
Slow pion	$ SlowPionTag > 0.1$	$ tag_f > 0.5$
Kaon II	$ KaonTag > 0.2$	$ tag_f > 0.4$
Other	none	$ tag_f > 0.2$

Table 5.2: Category definition used by tagging algorithm.

Merged category	Categories merged together
Lepton	Electron-Kaon, Muon-Kaon, Electron, Muon
Kaon-I	Kaon-Slow Pion, Kaon I
Kaon-II	Slow Pion, Kaon II
Inclusive	Other

Table 5.3: Category merging scheme for tagging algorithm.

respectively.

Category	$\epsilon(\%)$	$\Delta\epsilon(\%)$	$w(\%)$	$\Delta w(\%)$	$Q(\%)$	$\Delta Q(\%)$
Lepton	10.0 ± 0.1	0.5 ± 0.2	2.8 ± 0.1	-0.7 ± 0.3	9.0 ± 0.1	0.7 ± 0.2
Kaon-I	17.6 ± 0.1	-0.4 ± 0.2	9.2 ± 0.2	-0.9 ± 0.4	11.7 ± 0.1	0.2 ± 0.3
Kaon-II	19.9 ± 0.1	0.5 ± 0.2	21.2 ± 0.3	-3.0 ± 0.5	6.6 ± 0.1	1.5 ± 0.3
Inclusive	20.1 ± 0.1	-0.2 ± 0.2	30.9 ± 0.3	-2.3 ± 0.6	2.9 ± 0.1	0.7 ± 0.2
Total	67.7 ± 0.2	0.5 ± 0.5			30.2 ± 0.2	3.2 ± 0.5

Table 5.4: Performance of tagging algorithm on simulated $B\bar{B}$ events after category merging. The differences between the efficiency, mistag rate, and Q factor for B^0 and \bar{B}^0 decays is written as $\Delta\epsilon$, Δw , and ΔQ respectively.

We make the following observations concerning the tagging performance on Monte Carlo:

- The total efficiency for tagging a B meson is roughly 2/3;

- The **Kaon-I** category provides the most powerful flavor tag. This is not unexpected due to the multiplicity of right sign kaons in B decays;
- The **Lepton** category has the lowest mistag rate;
- The mistag rate difference Δw for the **Kaon-II** and **Inclusive** categories are significantly different from zero. This may be related to the differences in interaction cross sections for positively and negatively charged kaons and pions with the detector material;
- The product of the tagging efficiency and the dilution squared is about 30%. This represents the effective tagging efficiency of the algorithm.

We note that the algorithm was trained using simulated events and we have evaluated its performance using simulated events as well. One might worry that differences between $B\bar{B}$ decays in data and Monte Carlo simulation could bias the tagging performance in the data. However, the mistag rates and efficiencies for each category will be measured on the data using the B_{flav} sample. This procedure will be explained in detail in Chapter 7. For now, we point out that while training the algorithm on Monte Carlo may make its performance sub-optimal, it will not bias the results of the $\sin 2\beta$ analysis since the relevant flavor tagging parameters will be measured using data.

Chapter 6

Time difference measurement

In Sec. 1.8, we constructed a CP violating asymmetry proportional to $\sin 2\beta$ that is a function of the proper decay time difference Δt between a neutral B meson reconstructed as a CP eigenstate (B_{rec}) and a neutral B meson whose decay products tag its flavor (B_{tag}). Further, since the asymmetry was shown to vanish when integrated over $\Delta t \equiv t_{rec} - t_{tag}$ from $[-\infty, +\infty]$, we must be able to resolve Δt in order to measure $\sin 2\beta$. This chapter explains how Δt is determined from the measured separation between the vertex of the B_{rec} and the vertex of the B_{tag} along the z axis. The resolution on the separation is dominated by the resolution on the B_{tag} vertex.

6.1 Reconstruction of B_{rec} vertex

The B_{rec} vertex is reconstructed using the charged tracks belonging to the B_{rec} candidate. Tracks from long lived B_{rec} daughter candidates, like K_S^0 and D mesons that travel in the detector before decaying, are first fit to a separate vertex. Then the resulting momentum and position of the composite candidate are used in the fit to the B_{rec} vertex. Though charmonium daughters are mass constrained before creating the B_{rec} candidate, this constraint is removed when determining the B_{rec} position to avoid potential bias. The RMS resolution on

the z vertex position of the B_{rec} in Monte Carlo simulation is about $65 \mu\text{m}$ for more than 99% of the B candidates.

6.2 Reconstruction of B_{tag} vertex and Δz

The B_{tag} decay vertex is determined using the tracks in the event that were not used to construct the B_{rec} candidate. To avoid biasing the B_{tag} vertex position, tracks from the decay of long-lived K_S^0 and Λ candidates are replaced by the composite candidate momentum and tracks consistent with photon conversions ($\gamma \rightarrow e^+e^-$) in the detector material are excluded.

An additional constraint is employed which increases the efficiency of the B_{tag} vertex algorithm. Momentum conservation of the $\Upsilon(4S)$ decay requires that

$$\vec{p}_{B_{tag}} = \vec{p}_{\Upsilon(4S)} - \vec{p}_{B_{rec}}. \quad (6.2.1)$$

Using the measured vertex position and momentum of the B_{rec} along with their associated errors, we can construct a vector from the B_{rec} vertex which intersects the beam spot where the $\Upsilon(4S)$ decayed. Then, since we know the average momentum of the $\Upsilon(4S)$ ($\vec{p}_{\Upsilon(4S)}$), we can construct a vector representing the B_{tag} that should intersect its decay vertex. This constraint, referred to as the pseudo-track constraint, is illustrated schematically in Fig. 6.1. The efficiency of the algorithm is improved using this constraint since it allows a determination of the B_{tag} vertex even when there is only one charged track used to make the B_{tag} candidate (determining the vertex of one track without any additional constraints is not possible).

With the charged tracks described, and the estimated momentum provided by this constraint, a geometrical fit to a single vertex is performed to determine the B_{tag} vertex position. The fit proceeds iteratively, removing in each attempt the track with the largest vertex χ^2 contribution greater than 6, until converging or failing. Removal of the bad χ^2 tracks reduces contamination from

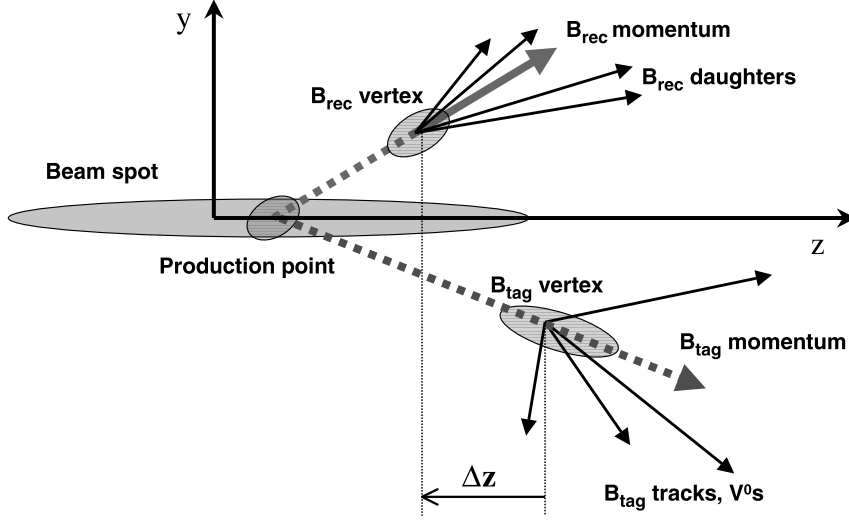


Figure 6.1: Schematic view of the geometry in the yz plane for a $\Upsilon(4S) \rightarrow B\bar{B}$ decay. The momentum direction of the B_{tag} can be estimated using the measured vertex and momentum of the B_{rec} , the beam spot position in the xy plane, and the $\Upsilon(4S)$ average boost. Note that the scale in the y direction has been magnified significantly compared to that in the z direction.

charged and neutral D mesons that have a $c\tau$ of $315\ \mu\text{m}$ and $123\ \mu\text{m}$ respectively. The significant flight length of these mesons pulls (i.e., biases) the B_{tag} vertex position in the direction of their decay products. This effect causes the resolution on the B_{tag} vertex to be significantly worse than the resolution on the B_{rec} vertex, where the tracks originating directly from the B_{rec} decay are known and are generally of higher momentum.

We fit the residual Δz distribution (measured Δz minus true Δz) to the sum of three Gaussian distributions as shown in Fig. 6.2 for simulated $B^0 \rightarrow J/\psi K_S^0$ decays. The width of the sum of the narrowest (core) and second-narrowest (tail) Gaussian is about $190\ \mu\text{m}$. The narrowest Gaussian is found to have a width of $100\ \mu\text{m}$ and contain 70% of the total area. The Gaussian with the largest width (outlier) contains only 1% of the area. Performances of the algorithm on simulation are only provided here as a benchmark. Evaluations using data will be presented shortly.

The assumed positions of the SVT silicon wafers determines the absolute

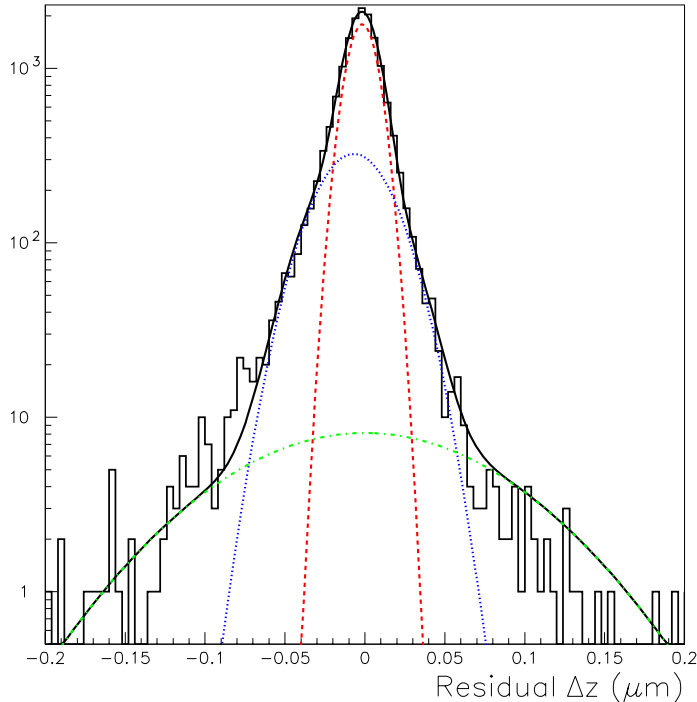


Figure 6.2: Residual Δz distribution (measured Δz minus true Δz) for $B^0 \rightarrow J/\psi K_s^0$ Monte Carlo simulation. Overlaid is a fit to the sum of three Gaussian distributions; the contribution of each Gaussian is indicated by the dashed curves. The width of the narrowest Gaussian, which contains 70% of the total area, is about $100 \mu\text{m}$.

scale of the Δz measurement. As was discussed in Sec. 2.3, these positions were measured using an optical survey before the SVT was installed. The uncertainty in the measured value of $\sin 2\beta$ resulting from our limited knowledge of the internal alignment of the SVT is discussed in Sec. 9.4.2. We also check the absolute z scale using interactions of charged particles at the known positions of distinct mechanical features located about 18 cm apart at each end of the beampipe. We measure the positions of track vertices originating at least 2 cm from the primary vertex that contain an identified proton, which result from e^\pm -nucleon interactions in the material. The measured distance along the z axis

between the mechanical features agrees with the known distances to a precision of 0.2%.

6.3 Converting Δz to Δt

To measure the time-dependent asymmetry we must convert the measurement of the vertex separation Δz to the proper decay time difference Δt . The accuracy of this conversion is largely dominated by the experimental resolution on the Δz measurement. Neglecting the boost of the B mesons in the $\Upsilon(4S)$ frame, we find

$$\Delta z = \gamma\beta c\Delta t \tag{6.3.1}$$

where $\gamma\beta = 0.55$ is the $\Upsilon(4S)$ boost factor and c is the speed of light. The $\Upsilon(4S)$ boost, calculated directly from the beam energies and monitored every 5 seconds, has an uncertainty of 0.1%. While treating the mesons at rest in the $\Upsilon(4S)$ system contributes much less uncertainty in the conversion than the experimental resolution, it has been shown to introduce a 0.4% bias in measurements of B lifetimes [71]. Additionally, this approximation ignores the 20 mrad rotation in the xz plane between the *BABAR* detector coordinate axes and the boost direction.

The effects of the rotation and B meson boost in the $\Upsilon(4S)$ frame may be partially corrected for by using the measured momentum direction of the fully reconstructed B_{rec} candidate. The proper time of the B_{rec} decay as measured in its rest frame (at position $\vec{x} = 0$) is denoted t_{rec} . From special relativity we know that the time interval for this decay measured in the $\Upsilon(4S)$ frame increases to $\gamma_{rec}^* t_{rec}$ where γ_{rec}^* is the boost factor of the B_{rec} in the $\Upsilon(4S)$ frame. The position of the decay in the $\Upsilon(4S)$ frame is then given by $\vec{\beta}_{rec}^* c\gamma_{rec}^* t_{rec}$ where $\vec{\beta}_{rec}^*$ is the velocity of the B_{rec} in the $\Upsilon(4S)$ frame. The projection of the distance along the boost axis is $\beta_{rec}^* c\gamma_{rec}^* t_{rec} \cos\theta_{rec}^*$ where $\cos\theta_{rec}^*$ is the polar angle between the boost direction and the B_{rec} direction in the $\Upsilon(4S)$ frame.

Boosting this distance to the lab frame we find

$$z_{rec} = \gamma\beta c [\gamma_{rec}^* t_{rec}] + \gamma [\beta_{rec}^* c \gamma_{rec}^* t_{rec} \cos \theta_{rec}^*] \quad (6.3.2)$$

Keeping track of an extra minus sign we pick up for one term of the B_{tag} since its momentum points opposite to the B_{rec} in the $\Upsilon(4S)$ frame, we can now write the conversion more accurately as

$$\Delta z = \gamma\beta c [\gamma_{rec}^* \Delta t] + \gamma [\beta_{rec}^* c \gamma_{rec}^* \cos \theta_{rec}^* (t_{rec} + t_{tag})]. \quad (6.3.3)$$

The difference between Eqn 6.3.1 and Eqn 6.3.3 is very small since $\beta_{rec}^* = 0.064$ and $\gamma_{rec}^* = 1.002$. Unfortunately we still need an estimate for the sum of the proper decay times $t_{rec} + t_{tag}$ in the second term of Eqn 6.3.3. The obvious approach $\langle t_{rec} + t_{tag} \rangle = 2\tau_B$ is not sensitive to the variation of $t_{rec} + t_{tag}$ with Δt . We take this effect into account by averaging over the Δt range [72], yielding

$$\langle t_{rec} + t_{tag} \rangle |_{\Delta t} = \tau_B + \Delta t \quad (6.3.4)$$

Consequently, we approximate the conversion between the measured z vertex separation and the proper decay time difference as

$$\Delta z = \gamma\beta c [\gamma_{rec}^* \Delta t] + \gamma [\beta_{rec}^* c \gamma_{rec}^* \cos \theta_{rec}^* (\Delta t + \tau_B)]. \quad (6.3.5)$$

The event-by-event difference between Δt calculated using Eqn 6.3.5 and Eqn 6.3.1 has an RMS of 0.20 ps (which is about 13% of τ_{B^0}). Eqn 6.3.5 improves the Δt resolution by about 5%.

Events which do not pass some loose requirements made on the measured value of Δt are rejected. These requirements are:

- The Δz vertex fit must converge;
- The error on Δt determined from the fit must be less than 2.5 ps;
- $|\Delta t|$ must be less than 20 ps.

These requirements are about 97% efficient in data and Monte Carlo simulation independent of the B_{rec} decay mode. Also, no correlation between the efficiency and the true value of Δt is found in the simulation.

6.4 Resolution function

As discussed in Chapter 3, due to the finite resolution of the SVT, the measured value of Δt must be convolved with a resolution function which accurately reflects the detector's measurement imprecision. The resolution function is represented in terms of $\delta_t = \Delta t - \Delta t_{true}$ by a sum of three Gaussian distributions (referred to as the core, tail, and outlier components) with distinct means and widths:

$$\mathcal{R}(\delta_t; \hat{a}) = \frac{1}{\sqrt{2\pi}} \left[\frac{f_1}{S_1\sigma_{\Delta t}} \exp\left(-\frac{(\delta_t - k_1\sigma_{\Delta t})^2}{2(S_1\sigma_{\Delta t})^2}\right) + \frac{1 - f_1 - f_3}{S_2\sigma_{\Delta t}} \exp\left(-\frac{(\delta_t - k_2\sigma_{\Delta t})^2}{2(S_2\sigma_{\Delta t})^2}\right) + \frac{f_3}{\sigma_3} \exp\left(-\frac{\delta_t^2}{2\sigma_3^2}\right) \right] \quad (6.4.1)$$

where \hat{a} is used to represent the parameters that the resolution function depends on, f_1 and f_3 are the fractions of the core and outlier Gaussian respectively, and the additional variables are described below. The widths of the core and tail Gaussians are given by the product of the event-by-event measured error $\sigma_{\Delta t}$, derived from the Δz vertex fit, with scale factors S_1 and S_2 respectively. The scale factors accommodate an overall underestimate or overestimate of the errors for all events. This model assumes then that the width of the residual distribution (in other words the RMS of the δ_t distribution) is proportional to $\sigma_{\Delta t}$. This assumption is verified in Monte Carlo simulation as shown in Fig. 6.3a where the RMS of the residual Δt distribution is plotted as a function of $\sigma_{\Delta t}$.

The mean of the core and tail Gaussian distributions may be different from zero to account for a bias in the B_{tag} vertex position due to tracks that originate in the decay of long lived charm mesons. In the resolution function, these mean offsets are scaled by the per-event error measurement $\sigma_{\Delta t}$ to account for an observed correlation shown in Fig. 6.3b between the mean of the δ_t distribution and $\sigma_{\Delta t}$ in Monte Carlo simulation. We see from this figure that the mean offset is shifted to negative values of Δt .

To understand the sign of this offset, we consider the distribution of the measured and true value of Δz (which are both signed quantities where $\Delta z =$

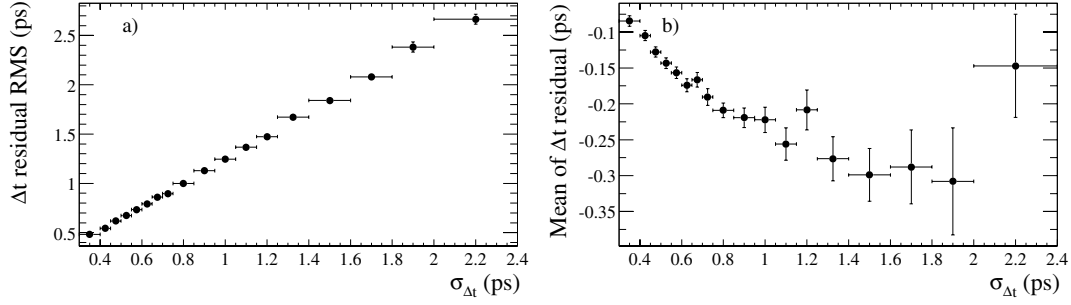


Figure 6.3: Correlation between the event-by-event error on Δt ($\sigma_{\Delta t}$) and a) the RMS and b) the mean of the $\Delta t = \Delta t - \Delta t_{true}$ distribution from Monte Carlo simulation

$z_{rec} - z_{tag}$). In most cases, the tracking resolution is not good enough to separate primary tracks that originate directly in the B_{tag} decay and secondary tracks that originate from the decay of a long-lived charm meson. Since the B mesons are boosted primarily in the $+z$ direction, the position of the secondary decay vertex is located at more positive values of z than the position of the primary B_{tag} vertex. This explains why the position of the B_{tag} vertex is biased toward positive z values. However, the B_{tag} vertex can be located with roughly equal probability on either side of the B_{rec} vertex. Fig. 6.4 illustrates why the sign of the residual distribution is biased to negative values regardless of whether the B_{tag} decays at a z position more or less positive than the B_{rec} vertex position.

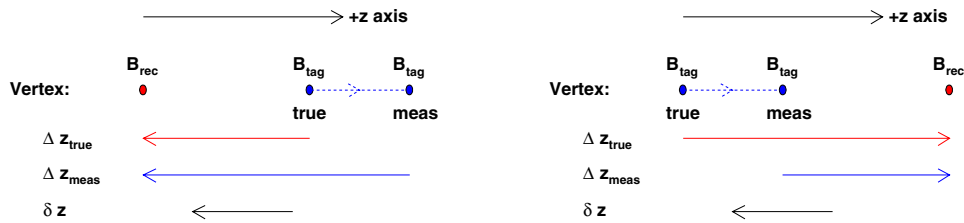


Figure 6.4: Illustration of the true B_{rec} , true B_{tag} , and measured B_{tag} vertices. The measured B_{tag} vertex is normally biased to more positive value of z because the charm mesons fly along the direction of the boost. Since the measured value of Δz (Δz_{meas}) and the true value (Δz_{true}) are signed quantities, the mean of the residual Δz distribution $\delta_z = \Delta z_{meas} - \Delta z_{true}$ is biased to negative values.

We also understand the origin of the correlation between the mean offset of the residual and the per-event error. This results from the fact that the vertex error ellipse for the charm meson is oriented with its major axis along the charm flight direction. This means that the charm flight direction and the error on the measured B_{tag} vertex are correlated. Charm mesons which fly at polar angles near $\pi/2$ in the laboratory frame will have the best z resolution and will introduce the least bias in measuring the B_{tag} vertex position, while charm mesons which fly along the z axis will introduce a larger bias in this position measurement. The dependence on the offset in the mean of the Δz residual as a function of the charm meson polar angle is illustrated in Fig. 6.5.

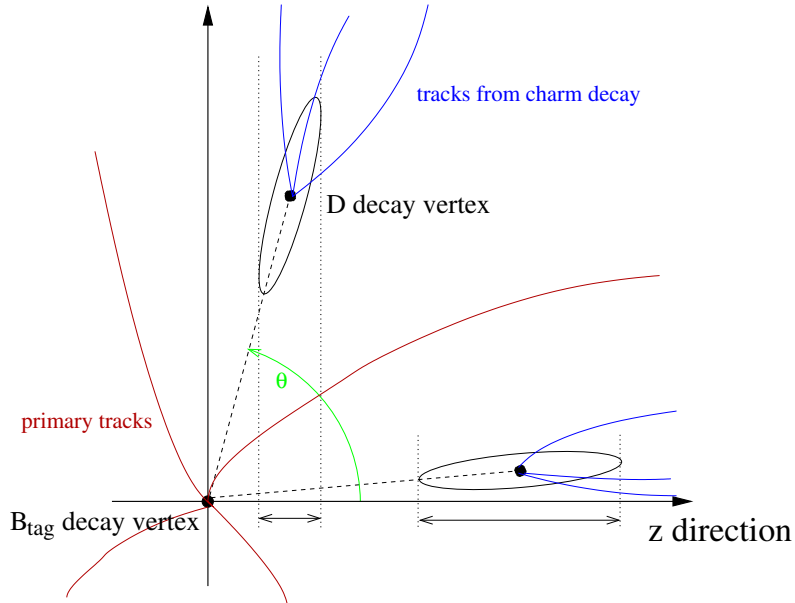


Figure 6.5: Illustration of the effect that leads to a correlation of $\sigma_{\Delta z}$ and the offset in the mean of the Δz residual. The figure show primary tracks originating from the B_{tag} decay and secondary tracks from a charm meson distributed uniformly in a cone about the charm meson direction. There are two flight directions shown for the charm meson which result in significantly different projections of its z vertex position error along the z axis. These projections correlate the offset in the Δz residual distribution with the event-by-event error measured on the B meson vertex separation $\sigma_{\Delta z}$.

We expect differences in the resolution of the B_{tag} vertex based on the

flavor tagging category of the B_{tag} . For example, B mesons tagged with a high momentum primary lepton will be less subject to bias in the determination of the vertex position from residual charm meson decays than B mesons tagged using the charge of a well identified kaon (where there is high probability of charm pulling the vertex). Monte Carlo simulation confirms this expectation. Consequently, the mean of the core Gaussian is allowed to be different for each tagging category. One common mean is used for the tail component. The third Gaussian accounts for the less than 1% of events with incorrectly reconstructed vertices. Its width (σ_3) is fixed to 8 ps and it has no offset. The scale factor of the tail (S_2) is also fixed to 3 to reduce correlations between the Gaussian parameters. Consequently, the resolution function has 8 free parameters: two fractions (f_1 and f_3), a core scale factor S_1 , a core mean for each tagging category ($k_1 \times 4$), and a tail mean (k_2).

Since the modeling of the resolution function depends on $\sigma_{\Delta t}$ accurately representing the error of the Δt measurement, we hope that the distribution of $\sigma_{\Delta t}$ looks similar in data and Monte Carlo simulation. Fig. 6.6 shows good agreement for this distribution in data and simulation for a combination of $\eta_{CP} = -1$ charmonium modes and for the flavor-eigenstate sample. Since the resolution on Δt is dominated by the measurement of the B_{tag} vertex position, no significant differences are expected between the Δt resolution function for the flavor-eigenstate and the CP -eigenstate sample. Therefore, identical resolution functions are used for all modes.

The resolution function parameters will be obtained in data from the likelihood fit to the Δt distribution of the flavor-eigenstate and CP samples. Since there are about 15 times more fully reconstructed B mesons in the flavor-eigenstate sample (the yields for both samples were given in Sec. 4.5 and 4.6), the resolution function parameters will mostly be determined by these events.

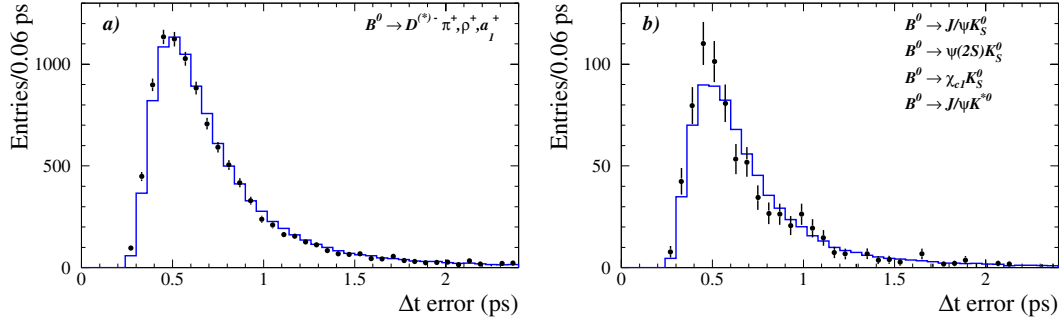


Figure 6.6: Comparison of $\sigma_{\Delta t}$ between data and Monte Carlo simulation for a) a sample of neutral B decays to flavor-eigenstates and b) a sample of neutral B decays to CP -eigenstates. The histogram corresponds to the simulation and the points with error bars to data. The Monte Carlo distribution has been normalized to the same area as the data and the data has been background subtracted using events from the m_{ES} sideband.

6.5 Vertexing checks

Two fundamental assumptions of the analysis, as explained in the last section, are that the per-event vertex errors provide a good measure of the relative uncertainty on the Δz measurement for each event, and that resolution function parameters should be the same for the flavor-eigenstate and CP samples. This sections describe several methods which attempt to validate these assumptions.

6.5.1 Comparison of CP and flavor-eigenstate samples

In Fig. 6.7, we compare various properties of the flavor-eigenstate sample with the combined $\eta_{CP} = -1$ and $J/\psi K^{*0}$ samples. The $J/\psi K^{*0}$ sample is included with the $\eta_{CP} = -1$ sample here (as opposed to its normal inclusion with the flavor-eigenstate sample) to improve the statistics of the CP sample and because the topology of the reconstructed side of the event is clearly very similar. The variables investigated include the χ^2 probability for the vertex fits, the number of tracks used in the B_{tag} vertex, the momentum in the $\Upsilon(4S)$ frame, and polar angle in the laboratory frame of tracks used in the B_{tag} ver-

tex. We find good agreement between the distributions for all the variables considered.

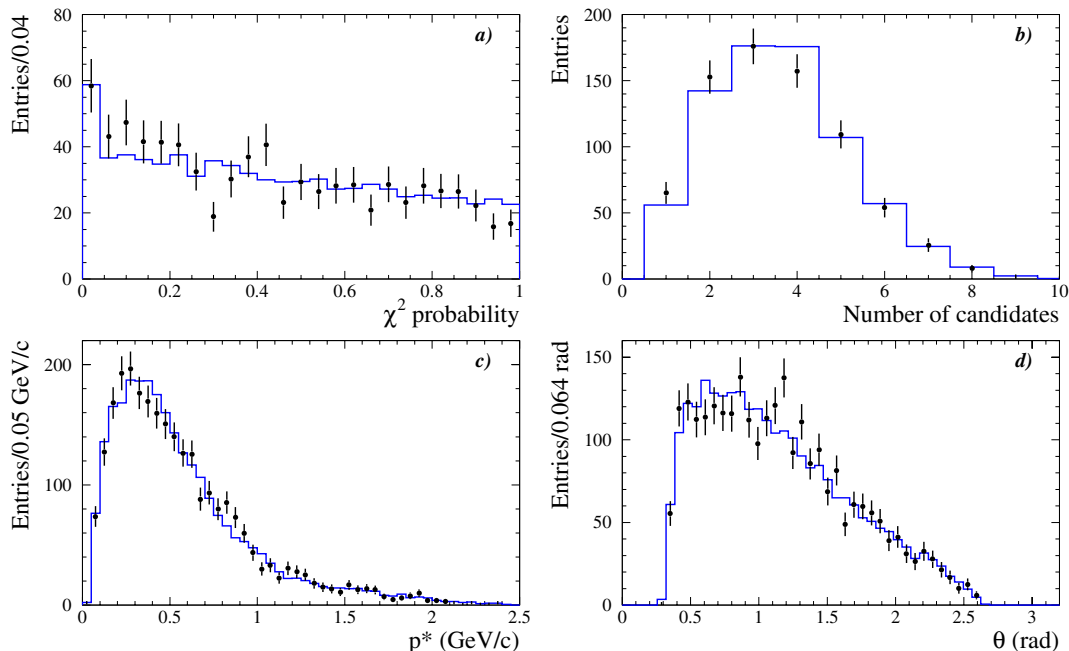


Figure 6.7: Comparison in data of (a) the probability of the χ^2 of the B_{tag} vertex fit, (b) the number of tracks used in the determination of the B_{tag} vertex position, (c) the momentum in the $\Upsilon(4S)$ frame, and (d) polar angle in the laboratory frame for tracks in the B_{tag} vertex, for the η_{CP} and $J/\psi K^{*0}$ (points with error bars) and flavor-eigenstate (histogram) samples. All distributions have been background subtracted using events from the m_{ES} sideband. The flavor-eigenstate sample has been normalized to the same area as the distributions from the combined η_{CP} and $J/\psi K^{*0}$ CP samples. There is good agreement for all variables compared.

Comparisons between the different CP modes in data and simulation also show no significant differences in variables which influence the Δz resolution. However, a small difference in the Δz resolution is seen when comparing the CP sample to the flavor-eigenstate sample in data and Monte Carlo simulation. The CP sample has slightly better Δz resolution which can be seen by comparing the distributions in Fig 6.6a and 6.6b, or more directly in Fig. 6.8. Simulation finds that the most probable value for $\sigma_{\Delta t}$ is about 0.017 ps (3%)

worse for the B_{flav} sample. This results from the fact that the average momentum of tracks used to determine the B_{rec} vertex is larger in the B_{CP} sample than the B_{flav} sample because the average number of tracks in the B_{CP} decay is less. This effect does not introduce a systematic error into the likelihood fit since the resolution function incorporates the event-by-event error $\sigma_{\Delta t}$ on the vertex resolution explicitly. In fact, Monte Carlo simulation verifies that the pull distributions for Δt (residual Δt divided by the measured error $\sigma_{\Delta t}$) are nearly Gaussian with unit width for both the B_{CP} and B_{tag} samples. A width significantly greater (less) than 1 for either would indicate that the per-event error was an underestimate (overestimate). Any remaining effects due to potential differences in the scale factors for the B_{CP} and B_{tag} samples are included as a systematic uncertainty (see Sec. 9.1.2).

6.5.2 Vertex resolution in the vertical direction

The small spread of the beamspot (about $10 \mu\text{m}$) in the vertical (y) direction allows us to make meaningful comparisons of the resolution for the CP and flavor-eigenstate samples by measuring the distance Δy between the B_{rec} or B_{tag} and the nominal beamspot position in the y direction. The larger size of the beamspot in the x and z directions make comparisons in those dimensions meaningless because the x and z resolutions are dominated by the spread in the width of the beamspot. We can also determine the accuracy of the per-event errors $\sigma(\Delta y)$ with this procedure.

The average beam-spot position in y is determined with a precision of less than a few microns using two-track events for each data run, where each run consists of about one hour of recorded data. We note that Δy has a non-negligible contribution due to the lifetime of the B and its transverse momentum. The RMS of the distribution of the B flight length in the y direction is about $25 \mu\text{m}$. Fig. 6.9 illustrates the geometry of the B_{tag} and B_{rec} decays in the xy plane relative to the beamspot. The RMS of the Δy distribution,

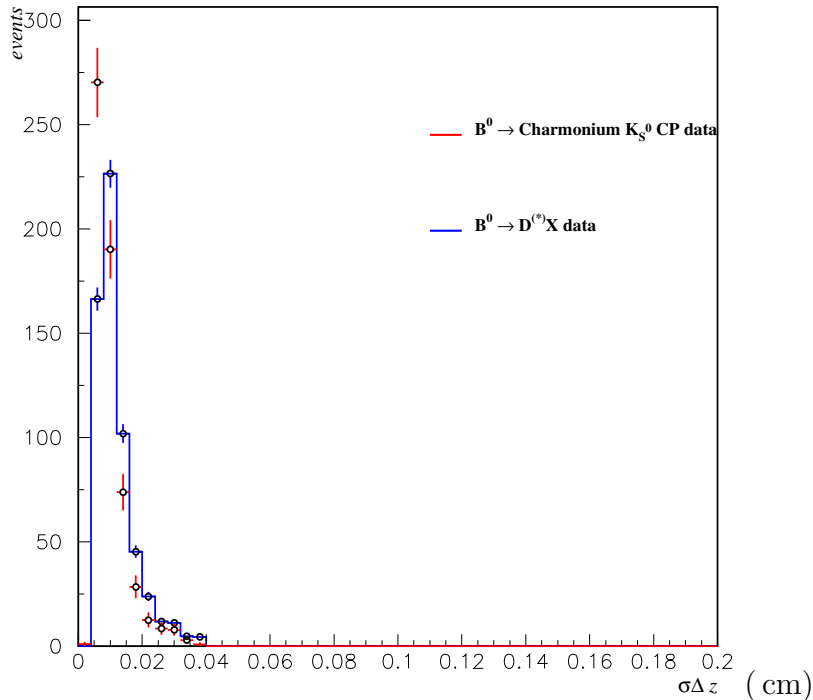


Figure 6.8: Comparison of $\sigma_{\Delta z}$ for $\eta_{CP} = -1$ (points with error bars) and flavor-eigenstate (histogram) sample in data. The distributions have been background-subtracted with events from the m_{ES} sideband. The flavor-eigenstate has been normalized to the number of events in the CP sample. The average per-event error is slightly less for the CP sample.

then, results from a convolution of the intrinsic beamspot resolution and the B flight distance in the y direction. This distribution also allows us to check that the pseudo-track constraint of the vertexing algorithm, which was described in Sec. 6.2, yields sensible results.

The distance in y between the B_{tag} vertex and beam spot is used to measure the B_{tag} vertex resolution and bias in y . Fig. 6.10 shows the distribution of Δy and $\Delta y/\sigma(\Delta y)$ for the B_{tag} vertex for the flavor-eigenstate and CP samples, in data and Monte Carlo simulation. The RMS of the Δy distribution is about $35 \mu\text{m}$ as expected. The RMS of the $\Delta y/\sigma(\Delta y)$ distribution is 1.3 and 1.4

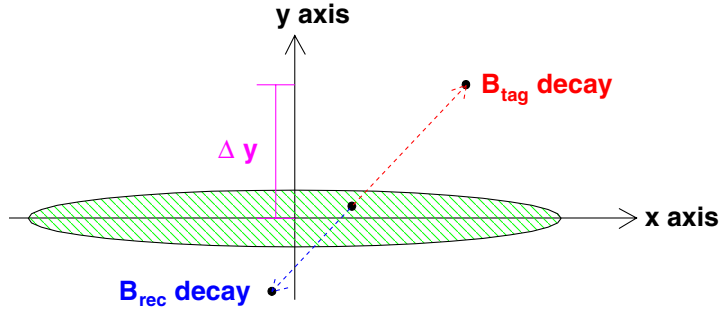


Figure 6.9: Schematic illustration of the B_{tag} and B_{rec} decay in the xy plane relative to the beamspot. The small spread in the beamspot in the y direction allows us to make useful vertexing checks by measuring the distance between the nominal beamspot and the B_{tag} decay vertex.

for Monte Carlo simulation and data, respectively. No statistically significant biases are observed. Similar results are obtained for the B_{rec} vertex. The resolution on the y vertex positions of the B_{rec} and B_{tag} are found to be in good agreement in the data for the CP and flavor-eigenstate samples. The resolution is typically 5-10% worse in data than simulation.

6.6 Vertex resolution in continuum events

We use continuum events to cross-check the reliability of the Δz vertexing algorithm and quantify differences between results obtained with Monte Carlo simulation and data. We randomly split charged tracks from off-resonance data events into two lists requiring each list to have at least four tracks. We vertex both lists separately using the same algorithm used to determine the Δz vertex separation of the two B mesons described above, but we remove the pseudo-track constraint. Since all tracks from both lists should originate from a common vertex (ignoring the fact that some charm mesons will fly a few hundred microns before decaying, an effect most pronounced in $c\bar{c}$ events), we expect the separation between the vertex of each list to be zero. Additionally,

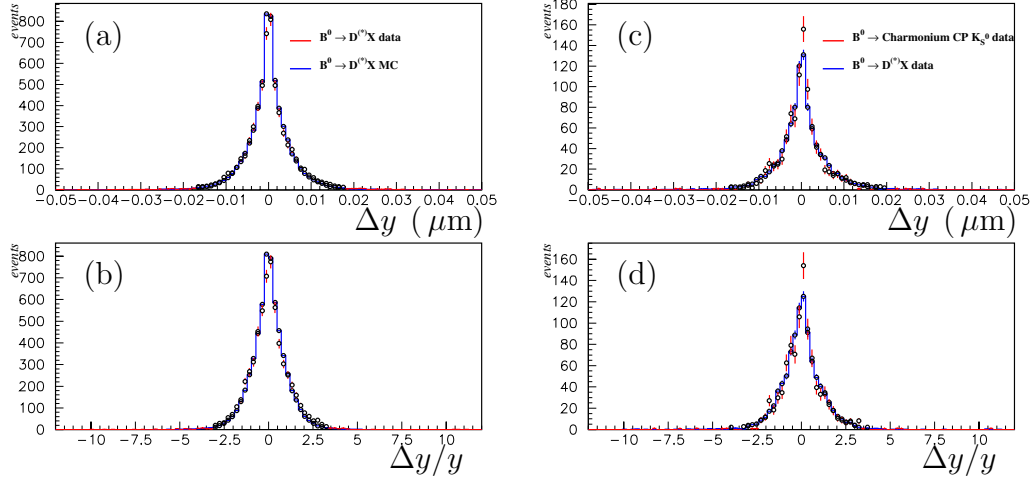


Figure 6.10: Comparison of (a) Δy and (b) $\Delta y/y$ for flavor-eigenstate data (points with error bars) and Monte Carlo simulation (histogram). The distribution of the simulation has been normalized to the number of events in the data distribution. A comparison of (c) Δy and (d) $\Delta y/y$ is also made for CP eigenstate data (points with error bars) and flavor-eigenstate data (histograms). The flavor-eigenstate distribution is normalized to the number of events in the CP sample in (c) and (d). The RMS of the Δy distribution is about $35 \mu\text{m}$ in both cases and the RMS of $\Delta y/y$ is about 1.4 (1.3) for data (simulation).

the resolution on each vertex should be similar to the resolution of the B_{tag} vertex. Consequently, this check allows us to measure the difference between vertex resolution in data and simulation and a potential bias in the vertex algorithm. Figure 6.11 shows that there is reasonably good agreement in data and simulation for the distribution of the per-event error of the vertex of one of the lists. Figure 6.11 also compares the vertex separation Δz between the vertex of each list and the separation divided by the quadrature error of the vertices $\Delta z/\sigma(\Delta z)$ between data and Monte Carlo simulation. We find that the RMS of the Δz and $\Delta z/\sigma(\Delta z)$ are about 15% larger in data than in simulation which agrees with the results for Δy shown above.

A second control sample consists of reconstructed high momentum D^{*+} candidates in the decay modes $D^{*+} \rightarrow D^0 \pi^+$; $D^0 \rightarrow K^- \pi^+$, $K^- \pi^+ \pi^0$, and

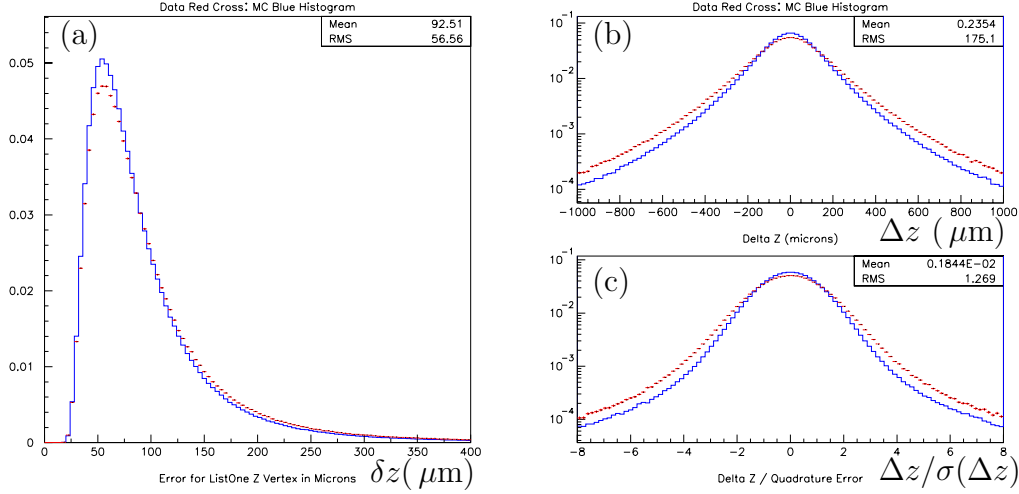


Figure 6.11: Comparison of (a) the per-event error δz returned on the vertex position of one of the charged track lists, (b) the separation Δz between the vertex of each list, and (c) the separation between each vertex divided by the quadrature error $\Delta z/\sigma(\Delta z)$ of the two vertices in data (dashed histogram) and Monte Carlo simulation (solid histogram) for continuum control sample.

$K^-\pi^+\pi^+\pi^-$. The remainder of the charged tracks (fragmentation particles and recoil charm decay products) are also vertexed with the standard B_{tag} vertex algorithm. Monte Carlo simulation indicates that the resolution on the D^{*+} vertex is about $90 \mu\text{m}$, very similar to the resolution on the B_{rec} vertex. After fitting the distance between the D^{*+} vertex and the vertex formed from the rest of the tracks in the event to the sum of three Gaussians, we find a resolution of $140 \mu\text{m}$ for 97% of the events, compared to $150 \mu\text{m}$ for 99% of the $B\bar{B}$ events. The distribution of this distance divided by its error is also fit to the sum of three Gaussians. These studies find that the bias in the resolution function due to charm decay products that is observed in data is well reproduced by the Monte Carlo simulation. We find that the resolution measured in data is about 10% worse than that predicted by the simulation, which agrees with our previous results.

Chapter 7

Fit method

As was discussed in Chapter 3, $\sin 2\beta$ is determined from the flavor tagged B_{CP} sample by maximizing $\ln \mathcal{L}_{CP}$. The likelihood is constructed from probability density functions f_{\pm} (Eqn. 3.0.4) that describe the time evolution of tagged B_{CP} mesons. The coefficient of the time-dependent sine term of these functions is proportional to $\mathcal{D} \sin 2\beta$. In order to extract $\sin 2\beta$ from a fit then, the value of \mathcal{D} must be fixed or come from a separate source which does not depend on $\sin 2\beta$ (since $\sin 2\beta$ and \mathcal{D} are completely anti-correlated in f_{\pm}). Similarly, one also needs to know the resolution function parameters \hat{a} . If we assume that the dilutions and resolution function parameters do not depend on the decay mode of the fully reconstructed B meson, as we argued in the preceding two chapters, then we can determine these parameters using the much larger flavor eigenstate sample. This results from the fact that the dilutions and resolution function parameters also appear in the mixing likelihood $\ln \mathcal{L}_{\text{mix}}$ (Eqn 3.0.3). We could fit for $\sin 2\beta$ with \mathcal{D} and \hat{a} fixed to the values we obtain by maximizing $\ln \mathcal{L}_{\text{mix}}$. However, this procedure ignores the (small) correlations introduced between these parameters and $\sin 2\beta$ in the B_{CP} sample. Therefore, we fit the tagged mixing and CP samples simultaneously, maximizing the sum $\ln \mathcal{L}_{\text{mix}} + \ln \mathcal{L}_{CP}$.

7.1 Maximum-likelihood fit

We now digress in order to define what is meant by a maximum-likelihood fit. This discussion follows one given in Ref. [73]. Consider a set of N measurements t_1, t_2, \dots, t_N where one knows that the measured values are distributed according to a probability density function $f(t; a)$ that depends on an unknown parameter a . The probability of obtaining the given measured set of data is the product of the individual probabilities obtained for each event. This product is termed the likelihood $\mathcal{L}(t_1, t_2, \dots, t_n; a)$ and is defined as

$$\mathcal{L}(t_1, t_2, \dots, t_n; a) = f(t_1; a)f(t_2; a)\dots f(t_N; a) = \prod_i^N f(t_i; a) \quad (7.1.1)$$

An estimate for the value of the true parameter \hat{a} is determined by maximizing the likelihood of Eqn 7.1.1. Essentially, one finds the value of a that makes the probability of the measured data set t_1, t_2, \dots, t_N as large as possible. In practice, it is typically easier to maximize the natural logarithm of \mathcal{L} (since the natural log is a monotonically increasing function the maximum of a function with dependent parameter a and the natural log of the function will occur at the same value of a). Consequently, one tries to find the maximum ¹ of

$$\sum_i^N \ln f(t_i, a). \quad (7.1.2)$$

The Maximum-Likelihood Theorem states that in the limit of large data sets, $N \rightarrow \infty$, the maximum value of $\ln \mathcal{L}(t_i; a)$ occurs at the true value \hat{a} of the parameter one wants to estimate and that there is no other method of estimation that is more accurate [74].

It can also be shown that for large N , $\mathcal{L}(t_i; a)$ approaches a Gaussian distribution. Denoting the most probable value of a as a^* (this is the value of a where the likelihood is maximized), we can write

$$\mathcal{L}(t_i; a) \propto \exp \left[-\frac{(a - a^*)^2}{2\sigma^2} \right] \quad (7.1.3)$$

¹We actually find the minimum of $-\ln \mathcal{L}$ but this is a trivial difference.

where σ is the RMS spread of a about a^* . Therefore, by plotting $\ln \mathcal{L}$, the $n\sigma$ error of the estimator occurs at the value of a where the log-likelihood has fallen by $0.5n^2$ from its maximum. This is illustrated schematically in Fig. 7.1. This feature of the maximum likelihood method is extremely useful.

We have assumed for simplicity that there is only one unknown parameter a , but the formalism naturally generalizes when one needs to estimate the best values for a set of parameters a_1, a_2, \dots, a_n . In this case, we solve the n simultaneous equations

$$\frac{\partial \ln \mathcal{L}}{\partial a_j} = 0 \quad \text{for all } j = 1, \dots, n$$

In the large N limit, the likelihood is a multidimensional Gaussian.

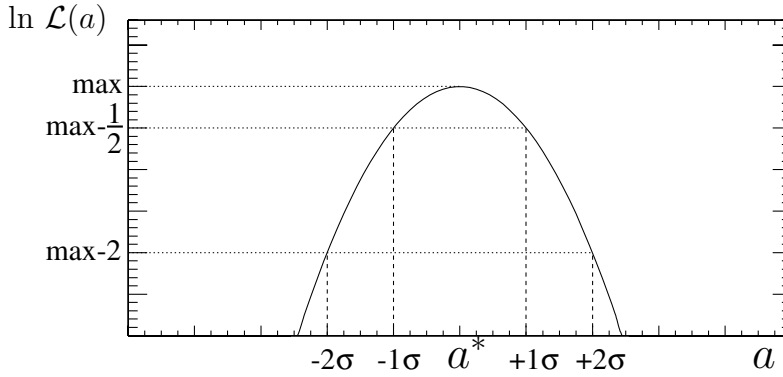


Figure 7.1: Schematic representation of a parabolic log-likelihood $\ln \mathcal{L}(a)$ that is a function of an unknown parameter a . The likelihood is maximized at $a = a^*$ and the $n\sigma$ estimates of a^* can be read from the plot by finding where the likelihood has fallen by $0.5n^2$ from its maximum value.

7.2 Signal description

It has been shown that the probability distribution function for the decay time difference of the tagged B_{CP} sample is given by

$$f_{\pm} = \frac{\Gamma}{4} e^{-\Gamma|\Delta t|} [1 \pm \mathcal{D} \sin 2\beta \sin(\Delta m \Delta t)] \quad (7.2.1)$$

where the $+(-)$ label indicates that the tagging meson was a B^0 (\bar{B}^0). In this formulation, we have assumed that the mistag rates (and hence dilutions) for B^0 and \bar{B}^0 mesons are the same. This may not be a valid assumption since the detector has different responses to positive and negative pions and kaons due to differences in total and charge-exchange cross sections. To account for potential differences in mistag rates, we allow for separate mistag rates w for B^0 and \bar{w} for \bar{B}^0 mesons with the conventions

$$\begin{aligned}\langle w \rangle &= \frac{1}{2}(w + \bar{w}); & \Delta w &= (w - \bar{w}) \\ \mathcal{D} &= 1 - 2w; & \bar{\mathcal{D}} &= 1 - 2\bar{w} \\ \langle \mathcal{D} \rangle &= \frac{1}{2}(\mathcal{D} + \bar{\mathcal{D}}); & \Delta \mathcal{D} &= (\mathcal{D} - \bar{\mathcal{D}})\end{aligned}$$

This modifies Eqn 7.2.1 to

$$\begin{aligned}f'_+ &\propto f_+(1 - w) + f_- \bar{w} \\ f'_- &\propto f_-(1 - \bar{w}) + f_+ w \\ f'_\pm &\propto 1 \mp w \pm \bar{w} \pm \alpha(1 - w - \bar{w}) \\ f'_\pm &\propto 1 \pm \frac{1}{2}\Delta \mathcal{D} \pm \langle \mathcal{D} \rangle \sin 2\beta \sin(\Delta m_d \Delta t)\end{aligned}\quad (7.2.2)$$

where the \pm in the index refers to events where B_{tag} is a B^0 (+) and \bar{B}^0 (-). The probability distribution functions for mixed and unmixed events (Eqn 3.0.1) are modified in a similar manner

$$\begin{aligned}h_{\pm, tag=B^0} &\propto \left[\left(1 + \frac{1}{2}\Delta \mathcal{D} \right) \pm \langle \mathcal{D} \rangle (\cos \Delta m_d \Delta t) \right] \\ h_{\pm, tag=\bar{B}^0} &\propto \left[\left(1 - \frac{1}{2}\Delta \mathcal{D} \right) \pm \langle \mathcal{D} \rangle (\cos \Delta m_d \Delta t) \right],\end{aligned}\quad (7.2.3)$$

where the \pm in the index refers to mixed (-) and unmixed (+) events as before. The signal distributions for CP events given by Eqn 7.2.2 and flavor-eigenstate events given by Eqn 7.2.3 are convoluted with a resolution function $\mathcal{R}(\delta t; \hat{a})$ (as explained in Chapter 3) to yield the respective functions

$$\mathcal{F}_\pm = f_\pm(\Delta t_{true}; \Gamma, \Delta m_d, \sin 2\beta, \langle w \rangle, \Delta w) \otimes \mathcal{R}(\delta t; \hat{a}) \quad (7.2.4)$$

$$\mathcal{H}_{\pm, \text{tag}=B^0} = h_{\pm, \text{tag}=B^0}(\Delta t_{\text{true}}; \Gamma, \Delta m_d, \langle w \rangle, \Delta w) \otimes \mathcal{R}(\delta_t; \hat{a}) \quad (7.2.5)$$

$$\mathcal{H}_{\pm, \text{tag}=\bar{B}^0} = h_{\pm, \text{tag}=\bar{B}^0}(\Delta t_{\text{true}}; \Gamma, \Delta m_d, \langle w \rangle, \Delta w) \otimes \mathcal{R}(\delta_t; \hat{a}) \quad (7.2.6)$$

The probability distribution functions are normalized such that

$$\int_{-\infty}^{+\infty} (\mathcal{F}_+ + \mathcal{F}_-) d\Delta t = 1 \quad (7.2.7)$$

$$\int_{-\infty}^{+\infty} [\mathcal{H}_+(B_{\text{tag}}^0) + \mathcal{H}_-(B_{\text{tag}}^0) + \mathcal{H}_+(\bar{B}_{\text{tag}}^0) + \mathcal{H}_-(\bar{B}_{\text{tag}}^0)] d\Delta t = 1 \quad (7.2.8)$$

7.3 Background modeling

The probability distributions \mathcal{F}_{\pm} and \mathcal{H}_{\pm} of Eqn 7.2.6 must be modified by adding new terms that describe the time evolution of background sources. We recall from Sec. 4.6 that the backgrounds for the *CP* sample are very small and mostly combinatoric; the purity of the sample is 92%. The backgrounds for the flavor-eigenstate sample are also mostly combinatoric but constitute a larger fraction of the total; the purity of the flavor-eigenstate sample is 82%. The properties of the background in the *CP* and flavor-eigenstate sample are determined empirically from events in the m_{ES} sideband.

7.3.1 Likelihood function for *CP* eigenstates

Since each flavor tagging category has a physical source (i.e., a primary lepton or right-sign kaon), the background sources tend to have different properties depending on the flavor tag. For example, light charm continuum events rarely result in a candidate fulfilling the **Lepton** tag requirements. Analyses which suffer from continuum backgrounds, then, typically have a higher reconstructed signal purity in the **Lepton** category than in any other tag category. Therefore, the background parameterizations of the *CP* sample are allowed to be different based on the flavor tagging category of the B_{tag} . The events are then classified by their particular tagging category i , and by whether the B_{tag}

was a B^0 (+) or a \bar{B}^0 (-). We label the different background parameterizations for each (+/-, i) combination by an index j . The full likelihood for the CP sample is then

$$\begin{aligned} \mathcal{F}_{\pm,i} = & f_{i,\text{sig}}^{CP} \mathcal{F}_{\pm}(\Delta t; \Gamma, \Delta m_d, w_i, \sin 2\beta, \hat{a}_i) + \\ & f_{i,\text{peak}}^{CP} \mathcal{B}_{i,\text{peak}}^{CP}(\Delta t; \hat{a}_i) + \sum_{j=\text{bkg}} f_{i,j}^{CP} \mathcal{B}_{i,j}^{CP}(\Delta t; \hat{b}_i) \end{aligned} \quad (7.3.1)$$

There are three separate parameterizations of the background: one that describes peaking background (peak), one that describes combinatoric background assumed to have no lifetime (prmt), and one that describes a B meson background assumed to have the lifetime of the B^0 (life). Each background time distribution may share the signal resolution function parameters \hat{a}_i or a common set of background resolution function parameters \hat{b}_i . The parameterizations for each tagging category i and source are given by

$$\begin{aligned} \mathcal{B}_{i,\text{peak}}^{CP} &= \frac{1}{4} \Gamma_{B^0} e^{-\Gamma_{B^0} |\Delta t|} \otimes \mathcal{R}(\Delta t; \hat{a}_i) \\ \mathcal{B}_{i,\text{prmt}}^{CP} &= \frac{1}{2} \delta(\Delta t) \otimes \mathcal{R}(\Delta t; \hat{b}_i) \\ \mathcal{B}_{i,\text{life}}^{CP} &= \frac{1}{4} \Gamma_{B^0} e^{-\Gamma_{B^0} |\Delta t|} \otimes \mathcal{R}(\Delta t; \hat{b}_i) \end{aligned} \quad (7.3.2)$$

These parameterizations implicitly include assumptions that have been made about the properties of the various backgrounds. The absence of a $\sin(\Delta m_d \Delta t)$ term effectively sets any potential CP asymmetry in the peaking or lifetime backgrounds to zero. Additionally, the decay constant is chosen to be that of the B^0 meson for each tagging category in the peaking and lifetime backgrounds. In fact, the only tagging category dependence observed in the background sources comes from which set of resolution function parameters are used in the convolution (\hat{a}_i or \hat{b}_i). The systematic uncertainties that result from these assumptions are evaluated in Chapter 9. The background distributions are normalized for each tagging category i and source j such that

$$2 \int_{-\infty}^{+\infty} \mathcal{B}_{i,j}^{CP} d\Delta t = 1 \quad (7.3.3)$$

The factor of 2 comes from the fact that the background sources are independent of whether the tagging meson is a B^0 or \bar{B}^0 (in contrast to the signal probability distribution function \mathcal{F}_\pm).

The full likelihood for the CP sample is constructed from a weighted sum of the signal and background probability distribution functions. The weighting factors are based on the probability that the B^0 candidate is a signal or background event. This probability is determined from a separate fit to the m_{ES} spectrum as described in Sec. 4.4. For each decay mode of the CP sample, We first fit the m_{ES} distribution of the entire sample (tagged and untagged CP events passing the vertexing requirements) to the sum of a Gaussian ($\mathcal{S}(m_{ES})$) distribution for the signal and an ARGUS ($\mathcal{A}(m_{ES})$) distribution for the background. This fit determines the mean and width of the Gaussian and the ζ (see Eqn 4.4.3) parameter of the ARGUS function. Fixing these parameters, we then fit the events in each tagging category separately in order to determine the relative normalizations of the Gaussian and ARGUS for each tagging category. This determines the probability $p_i(m_{ES})$ of the event for tagging category i as

$$p_i(m_{ES}) = \frac{\mathcal{S}_i(m_{ES})}{\mathcal{S}_i(m_{ES}) + \mathcal{A}_i(m_{ES})} \quad (7.3.4)$$

We now construct the full likelihood as

$$\begin{aligned} \mathcal{F}_{\pm,i} = p_i(m_{ES}) & \left[(1 - \delta_{\text{peak}}) \mathcal{F}_\pm(\Delta t; \Gamma, \Delta m_d, w_i, \sin 2\beta, \hat{a}_i) + \delta_{\text{peak}} \mathcal{B}_{i,\text{peak}}^{CP}(\Delta t; \hat{a}_i) \right] \\ & + [1 - p_i(m_{ES})] \cdot \left[f_{\text{life}}^{CP} \mathcal{B}_{i,\text{life}}^{CP}(\Delta t; \hat{b}_i) + (1 - f_{\text{life}}^{CP}) \mathcal{B}_{i,\text{prmt}}^{CP}(\Delta t; \hat{b}_i) \right] \end{aligned} \quad (7.3.5)$$

where δ_{peak} is the fraction of peaking background determined from Monte Carlo simulation and f_{life}^{CP} is the relative fraction of lifetime to prompt background. The peaking background fraction is determined separately for each CP decay mode (see Table 4.9). We will discuss the number of free parameters in the fit after describing the likelihood for the flavor-eigenstate sample (which has some parameters in common with the CP likelihood).

7.3.2 Likelihood function for flavor-eigenstates

There are also three separate parameterizations of the backgrounds for the flavor-eigenstate sample corresponding to a peaking (peak), prompt (prmt), and lifetime (life) component. The parameterizations for each tagging category i are given by

$$\begin{aligned}
\mathcal{B}_{\pm,i,\text{peak}}^{\text{flav}} &= \frac{1}{4}\Gamma_{B^+} (1 \pm \mathcal{D}_i^{\text{peak}})e^{-\Gamma_{B^+}|\Delta t|} \otimes \mathcal{R}(\Delta t; \hat{a}_i) \\
\mathcal{B}_{\pm,i,\text{prmt}}^{\text{flav}} &= \frac{1}{2}(1 \pm \mathcal{D}_i^{\text{prmt}})\delta(\Delta t) \otimes \mathcal{R}(\Delta t; \hat{b}_i) \\
\mathcal{B}_{\pm,i,\text{life}}^{\text{flav}} &= \frac{1}{4}(1 \pm \mathcal{D}_i^{\text{life}})\Gamma_{\text{life}} e^{-\Gamma_{\text{life}}|\Delta t|} \otimes \mathcal{R}(\Delta t; \hat{b}_i)
\end{aligned} \tag{7.3.6}$$

where Γ_{B^+} refers to the decay constant of the B^+ and Γ_{life} refers to the decay constant that the fit prefers for the lifetime background. While the average dilutions $\langle \mathcal{D} \rangle$ of each background source are allowed to be different, the difference in the dilutions $\Delta \mathcal{D}$ for B^0 and \bar{B}^0 mesons are assumed to be zero for each source. Since the major component of the peaking background comes from charged B decays, the average dilutions for the peaking background $\mathcal{D}_i^{\text{peak}}$ are measured with the sample of fully reconstructed B^+ decays (see Sec. 4.7). The background distributions are each normalized such that

$$\int_{-\infty}^{\infty} (\mathcal{B}_{+,i}^{\text{flav}} + \mathcal{B}_{-,i}^{\text{flav}}) d\Delta t = 1 \tag{7.3.7}$$

The full likelihood for the flavor-eigenstate sample is constructed from a weighted sum of the signal and background probability distribution functions where the weighting is again done by fitting the m_{ES} distribution. Due to the high statistics of the flavor-eigenstate sample, the m_{ES} fit is performed for events in each tagging category that pass the vertexing requirements letting both the shape and normalizations of the Gaussian and ARGUS distribution float. The event-by-event tagging category dependent probability $p_i(m_{\text{ES}})$ is then used to weight each event. The full likelihood is constructed as

$$\begin{aligned}
\mathcal{H}_{\pm,i} &= p_i(m_{\text{ES}}) \cdot \left[(1 - \delta_{\text{peak}}) \mathcal{H}_{\pm}(\Delta t; \Gamma, \Delta m_d, w_i, \hat{a}_i) + \delta_{\text{peak}} \mathcal{B}_{\pm,i,\text{peak}}^{\text{flav}}(\Delta t; \hat{a}_i) \right] \\
&+ [1 - p_i(m_{\text{ES}})] \cdot \left[f_{i,\text{life}}^{\text{flav}} \mathcal{B}_{\pm,i,\text{life}}^{\text{flav}}(\Delta t; \hat{b}_i) + (1 - f_{i,\text{life}}^{\text{flav}}) \mathcal{B}_{\pm,i,\text{prmt}}^{\text{flav}}(\Delta t; \hat{b}_i) \right]
\end{aligned} \tag{7.3.8}$$

where δ_{peak} is the fraction of peaking background determined from Monte Carlo simulation to be 1.3% (Sec. 4.6) and $f_{i,\text{lif}}^{\text{flav}}$ is the relative fraction of lifetime to prompt background in each tagging category.

7.4 Free parameters of the likelihood fit

Variable description	Number of free parameters
$\sin 2\beta$	1
Signal dilutions	8
Signal resolution function	8
Background resolution function	3
B_{flav} background	13
B_{CP} background	1
Total	34

Table 7.1: Breakdown of the number of free parameters in the $\sin 2\beta$ maximum-likelihood fit.

We use an unbinned maximum-likelihood fit to the Δt distributions of the CP and flavor-eigenstate samples to determine $\sin 2\beta$ by maximizing

$$\mathcal{L}_{CP} + \mathcal{L}_{\text{mix}} \quad (7.4.1)$$

where the CP and mixing likelihoods are defined in Eqn 3.0.6 and 3.0.3 respectively. The fit has a total of 34 free parameters which are summarized in Table 7.1:

- **Value of $\sin 2\beta$**
- **Signal resolution function:** Eight parameters to describe the signal resolution function \hat{a}_i that are common to the CP and flavor-eigenstate signal and peaking background probability distribution functions. The signal resolution function consists of a sum of three Gaussians (Eqn. 6.4.2). The scale factor of the core Gaussian S_1 , the bias of the core Gaussian for

each tagging category $k_{1,i}$, the mean of the tail Gaussian k_2 , the fraction of the core Gaussian f_1 , and the fraction of the outlier Gaussian f_3 are the eight free parameters of the signal resolution function. The scale factor of the tail Gaussian S_2 is fixed to 3, the width of the outlier Gaussian σ_3 is fixed to 8 ps, and the mean of the outlier Gaussian is fixed to 0 ps. These values were obtained from studies of simulated B_{CP} decays where the maximum-likelihood fit was found to be more robust when the resolution function had less degrees of freedom. For example, the fit occasionally had trouble determining the mean of the outlier Gaussian, which contains only about 1% of the events.

- **Signal dilutions:** Eight parameters describe the measured average dilutions $\langle \mathcal{D}_i \rangle$ and dilution differences $\Delta \mathcal{D}_i$ in each tagging category. These dilutions are common to the signal CP and flavor-eigenstate probability distribution functions.
- **Background resolution function:** Three parameters are used to describe a common resolution function for all non-peaking backgrounds. This resolution function, modeled as the sum of a core and outlier Gaussian distribution, is written as

$$\mathcal{R}(\delta t, \hat{b}_i) = \frac{1}{\sqrt{2\pi}} \left[\frac{f_1^b}{S_1^b \sigma_{\Delta t}} \exp\left(-\frac{(\delta t - k_1^b \sigma_{\Delta t})^2}{2(S_1^b \sigma_{\Delta t})^2}\right) + \frac{(1 - f_1^b)}{\sigma_2^b} \exp\left(-\frac{\delta t^2}{\sigma_2^b}\right) \right] \quad (7.4.2)$$

The free parameters are the scale factor of the core S_1^b , the bias of the core k_1^b , and the fraction f_1^b of the core Gaussian. The width of the outlier Gaussian σ_2^b is fixed to 8 ps per simulated Monte Carlo studies.

- **Flavor-eigenstate background composition:** Thirteen parameters to describe the composition of the flavor-eigenstate background distributions. There are 4 average dilutions used to describe the lifetime $\mathcal{D}_i^{\text{life}}$ and 4 average dilutions used to describe the prompt $\mathcal{D}_i^{\text{prmt}}$ components of the flavor-eigenstate background sources (see Eqn 7.3.7). The relative

fractions of the lifetime to prompt component of the flavor-eigenstate background for each tagging category $f_{i,\text{life}}^{\text{flav}}$ are also free parameters. The average dilutions of the peaking background, fixed to values measured using a maximum-likelihood fit to the fully reconstructed B^+ control sample, are listed in Table 7.2.

- **CP background composition:** One parameter to describe the CP background properties. The fraction of prompt relative to lifetime background $f_{\text{life}}^{\text{CP}}$ (assumed to be the same for each tagging category) is free in the maximum-likelihood fit.

Category	N_{signal}	$\varepsilon(\%)$	$w(\%)$	$Q(\%)$
Lepton	2060 ± 48	9.9 ± 0.2	1.1 ± 0.3	9.5 ± 0.2
Kaon I	3710 ± 68	17.9 ± 0.3	7.7 ± 0.5	12.8 ± 0.4
Kaon II	4083 ± 73	19.7 ± 0.3	17.4 ± 0.6	8.3 ± 0.4
Inclusive	3870 ± 70	18.6 ± 0.3	27.7 ± 0.8	3.7 ± 0.3
Total	20771 ± 164	66.1 ± 0.6		34.3 ± 0.6

Table 7.2: Average efficiency ε , mistag fractions w , and effective tagging efficiency Q for each tagging category i in the control sample of fully reconstructed B^+ candidates.

7.5 External parameters of likelihood fit

The B^0 lifetime τ_{B^0} and $B^0-\bar{B}^0$ mixing frequency Δm_d are held fixed to their respective current world-average values in the maximum-likelihood fit for $\sin 2\beta$:

$$\begin{aligned}\tau_{B^0} &= (1.542 \pm 0.016) \text{ ps} \\ \Delta m_d &= (0.489 \pm 0.008) \text{ ps}^{-1}\end{aligned}$$

We have observed that the fitted value of $\sin 2\beta$ depends linearly on the fixed value of each of these parameters. The systematic error associated with this dependence is quantified in Sec. 9.3.

7.6 Validation studies

Studies have been performed using various high statistics samples of simulated B meson decays to validate the maximum-likelihood fitting procedure and to determine whether the procedure is capable of producing an unbiased estimate of $\sin 2\beta$. They are described below.

7.6.1 Study of simulated signal decays

The maximum-likelihood fit procedure has been validated using high statistics sample of simulated Monte Carlo decays of B mesons to flavor-eigenstates and CP eigenstates. The number of simulated decays to each CP final state corresponds to about 120 times the signal yield in data for the given mode. The number of simulated flavor-eigenstate decays used for this study corresponds to about 2 times the signal yield of the B_{flav} data sample. Since the CPU time required to perform the fits for such large samples is extensive, a fit to the B_{flav} sample was done separately to extract the dilutions and resolution function parameters. The results are shown in Table 7.3. On lower statistics simulated samples, this procedure was shown to have no effect on the fitted value of $\sin 2\beta$ determined from the CP sample alone.

The resolution function parameters and dilutions were also determined using information about the true generated decays in the simulated CP sample. The background terms in the likelihood function were set to zero explicitly since we only simulate signal decays. The results of the fit for $\sin 2\beta$ for various CP decay modes are shown in Table 7.4. For each mode, the fitted value of $\sin 2\beta$ differed by less than 3σ from the generated value. However, there appears to be a systematic shift of about $+0.015$ in the measured value of $\sin 2\beta$ compared to the generated value for each CP decay mode. This will be discussed further in Sec. 7.6.3.

Parameter	Result
Signal Resolution Function	
Scale (core)	1.179 ± 0.026
Scale (tail)	3.0 (fixed)
$\delta(\Delta t)$ Lepton (core)	-0.107 ± 0.032
$\delta(\Delta t)$ Kaon I (core)	-0.257 ± 0.027
$\delta(\Delta t)$ Kaon II (core)	-0.256 ± 0.024
$\delta(\Delta t)$ Inclusive (core)	-0.209 ± 0.024
$\delta(\Delta t)$ (tail)	-0.909 ± 0.176
f (tail)	0.095 ± 0.012
f (outlier)	0.002 ± 0.001
Signal dilutions	
$\langle \mathcal{D} \rangle$, Lepton	0.930 ± 0.006
$\langle \mathcal{D} \rangle$, Kaon I	0.820 ± 0.006
$\langle \mathcal{D} \rangle$, Kaon II	0.577 ± 0.008
$\langle \mathcal{D} \rangle$, Inclusive	0.382 ± 0.008
$\Delta \mathcal{D}$, Lepton	0.019 ± 0.011
$\Delta \mathcal{D}$, Kaon I	0.003 ± 0.010
$\Delta \mathcal{D}$, Kaon II	0.053 ± 0.012
$\Delta \mathcal{D}$, Inclusive	0.064 ± 0.013

Table 7.3: Fit results for the high statistics B_{flav} simulated Monte Carlo sample.

7.6.2 Study of simulated signal and background decays

Validation studies were also performed for each CP decay mode using a simulated sample of inclusive $B^0 \rightarrow J/\psi X$ decays. Since this sample includes sources of combinatoric and peaking background, the full CP likelihood fit was used, fixing the dilutions and resolution function parameters to the values measured in the B_{flav} simulated sample that are reported in Table 7.3. The results of the fit for $\sin 2\beta$ using the simulated sample of inclusive J/ψ decays are shown in Table 7.5. For each decay mode, the difference between the generated and fitted value of $\sin 2\beta$ was less than 3σ .

Mode	Generated $\sin 2\beta$	Fit $\sin 2\beta$	
		B_{flav}	Truth
$J/\psi K_S^0 (\pi^+\pi^-)$	0.703	0.716 ± 0.007	0.719 ± 0.007
$J/\psi K_S^0 (\pi^0\pi^0)$	0.703	0.718 ± 0.014	0.722 ± 0.014
$\psi(2S)K_S^0 (\pi^+\pi^-)$	0.703	0.724 ± 0.015	0.727 ± 0.015
$\chi_{c1}K_S^0 (\pi^+\pi^-)$	0.703	0.729 ± 0.021	0.734 ± 0.021
$J/\psi K_L^0$	0.703	0.706 ± 0.009	0.711 ± 0.009
B_{flav}	0.0	-0.009 ± 0.011	—

Table 7.4: Results of fits for $\sin 2\beta$ in high statistics simulated Monte Carlo samples of CP eigenstate decays. The two columns of $\sin 2\beta$ fit values correspond to fits using dilutions and resolutions either measured from the B_{flav} Monte Carlo sample or from using information about the generated decays in the simulated CP sample.

Mode	Inclusive J/ψ simulation		
	Generated $\sin 2\beta$	Fit $\sin 2\beta$	$\delta(\sin 2\beta)/\sigma(\sin 2\beta)$
$J/\psi K_S^0 (\pi^+\pi^-)$	0.703	0.685 ± 0.034	-0.4
$J/\psi K_S^0 (\pi^0\pi^0)$	0.703	0.778 ± 0.074	+1.1
$\psi(2S)K_S^0 (\pi^+\pi^-)$	0.703	0.406 ± 0.258	-1.1
$\chi_{c1}K_S^0 (\pi^+\pi^-)$	0.703	0.320 ± 0.193	-2.0

Table 7.5: Results of $\sin 2\beta$ fits for each CP decay mode using a high statistics simulated sample of inclusive $B^0 \rightarrow J/\psi X$ decays. The difference between the generated and fitted value $\delta(\sin 2\beta) = \sin 2\beta_{\text{gen}} - \sin 2\beta_{\text{fit}}$ divided by the error on $\sin 2\beta$ from the fit $\sigma(\sin 2\beta)$ is less than $\pm 3\sigma$ for all decay modes.

7.6.3 Determining the maximum-likelihood bias

The studies of Sec. 7.6.1 and 7.6.2 indicate a bias of about 0.015 and zero respectively for the maximum-likelihood fitting procedure using high statistics samples of simulated B_{CP} decays. It is more relevant to determine whether a bias exists for sample sizes corresponding to the size of the data sample that is used in this analysis. Consequently, 130 toy experiments were constructed where each toy consists of the same number of simulated tagged signal decays passing the vertexing requirements as found in the data for each CP decay

mode. Resolution function parameters were obtained from the simulated events for all of the experiments by fitting the residual Δt distribution $\Delta t = \Delta t_{\text{true}} - \Delta t$ to the sum of three Gaussian functions. The “true” dilutions of the sample were also obtained by comparing the measured flavor tag to the generated flavor of the B mesons. Each experiment was fit setting the background probability distribution functions of the CP likelihood to zero with $\sin 2\beta$ the only free parameter.

The residual $\sin 2\beta$ distribution, where the residual is the difference between the measured and generated values, was found to have a mean of 0.0124 ± 0.005 . This distribution is shown in Fig. 7.2 where the residual is fit to a Gaussian function. The pull of $\sin 2\beta$ (residual divided by the error on $\sin 2\beta$ returned by the likelihood fit) was found to be 1.07 ± 0.07 . This study was repeated fixing the dilutions and resolution function parameters to those obtained from a likelihood fit to a high statistics sample of simulated flavor-eigenstate decays (see Table 7.3). In this case, the bias of the residual is found to be 0.0138 ± 0.005 . Consequently, henceforth we correct the value of $\sin 2\beta$ returned by the maximum-likelihood fit by -0.014 . The systematic error associated with this correction will be discussed in Sec. 9.5.

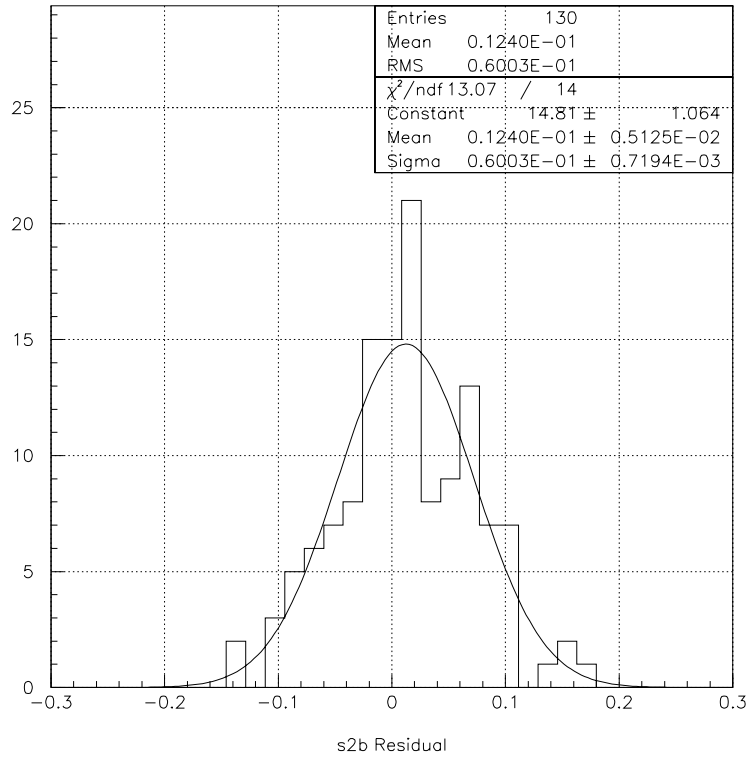


Figure 7.2: Residual distribution for $\sin 2\beta$ ($\sin 2\beta$ measured minus generated) found using 130 toy experiments of simulated B_{CP} decays where the number of fully reconstructed B mesons in each decay mode corresponds to the same number found in the B_{CP} data sample for that mode. The residual is found to have a bias of 0.0124 ± 0.005 .

Chapter 8

Fit results

As explained in Chapter 7, the value of $\sin 2\beta$, the dilution factors \mathcal{D}_i , signal resolution function parameters a_i , background fractions, and background time distribution parameters are determined from an unbinned maximum-likelihood fit to the Δt distribution of the B_{CP} and B_{flav} samples. The resolution function parameters and dilution factors are primarily determined by the B_{flav} sample. The value of $\sin 2\beta$ and the free parameter describing the relative fraction of prompt and lifetime background in the CP events are determined entirely by the CP sample.

In Sec. 8.1, we describe the results of fits to the m_{ES} distributions of the B_{CP} and B_{flav} samples for events in each tagging category that pass the vertexing requirements. Sec. 8.2 presents the results of the maximum-likelihood fit. We detail several cross checks performed to increase our confidence in the fitting procedure in Sec. 8.3. Additionally, we repeat the fit removing the assumption motivated in Sec. 1.7 that $|\lambda_{f_{CP}}| = 1$. These results are given in Sec. 8.4.

8.1 Data sample

Events with a reconstructed B meson must have a valid flavor tag, and satisfy the requirements $|\Delta t| < 20$ ps and $\sigma_{\Delta t} < 2.5$ ps in order to be included in

the likelihood fit for $\sin 2\beta$. Untagged events in the CP sample for each decay mode are used in the fits to the m_{ES} distributions to determine the parameters of the signal Gaussian and background ARGUS functions as described in Sec. 7.3.1. Table 8.1 lists the number of B^0 tagged, \bar{B}^0 tagged, and untagged signal ($m_{ES} > 5.27 \text{ GeV}/c^2$) events reconstructed in each CP decay mode after passing the vertexing requirements. There are 1506 signal CP events which are used to determine $\sin 2\beta$. The signal events of the B_{flav} after vertexing requirements for each tag category and flavor are listed for reference in Table 8.2.

Tag	$J/\psi K_S^0(\pi^+\pi^-)$			$J/\psi K_S^0(\pi^0\pi^0)$			$\psi(2S)K_S^0$			$\chi_{c1}K_S^0$			$\eta_c K_S^0$		
	B^0	\bar{B}^0	Tot	B^0	\bar{B}^0	Tot	B^0	\bar{B}^0	Tot	B^0	\bar{B}^0	Tot	B^0	\bar{B}^0	Tot
Lepton	70	71	141	10	14	24	17	14	31	5	4	9	9	6	15
Kaon I	124	135	259	27	19	46	13	20	33	6	15	21	17	24	41
Kaon II	133	150	283	26	28	54	28	20	48	12	10	22	13	24	37
Incl.	155	136	291	24	22	46	18	20	38	14	14	28	19	20	39
Tot tag	974			170			150			80			132		
No tag	465			105			79			35			80		
Total	1439			275			229			115			212		

Table 8.1: Event yields by tagging category and tag flavor for signal ($m_{ES} > 5.27 \text{ GeV}/c^2$) CP decay modes after vertexing requirements. Note that we have used Incl. as an abbreviation for Inclusive.

Tag	Flavor-eigenstate sample		
	B^0	\bar{B}^0	Tot
Lepton	1492	1411	2903
Kaon I	2929	2957	5886
Kaon II	3810	3521	7331
Inclusive	3878	3620	7498
Tot tag	23618		
No tag	13615		
Total	37233		

Table 8.2: Event yields by tagging category and tag flavor for signal ($m_{ES} > 5.27 \text{ GeV}/c^2$) flavor-eigenstate decays after vertexing requirements.

The m_{ES} distribution of all the tagged and untagged events passing the vertexing requirements in the CP decay modes, $J/\psi K_S^0(\pi^+\pi^-)$, $J/\psi K_S^0(\pi^0\pi^0)$,

$\psi(2S)K_S^0$, $\chi_{c1}K_S^0$, and $\eta_c K_S^0$, are fit together to a Gaussian plus an ARGUS function as described in Sec. 7.3.1. This fit yielded a Gaussian mean ($\mu_{m_{ES}}$) of 5280.2 ± 0.1 MeV/ c^2 , a Gaussian width ($\sigma_{m_{ES}}$) of 2.73 ± 0.06 MeV/ c^2 , and an ARGUS shape parameter (ζ) of -29 ± 6 . The events in each tagging category of each mode were then fit separately, with these parameters fixed, to determine the relative normalization of the Gaussian and ARGUS components. Table 8.3 gives the signal yield and purity results from these fits for each decay mode. Fig. 8.1 shows the m_{ES} distribution for the combined CP event sample for each tagging category after vertexing requirements overlaid with the results of the m_{ES} fit.

Mode	Parameter	Lepton	Kaon I	Kaon II	Inclusive	Total
All	$\mu_{m_{ES}}$ (MeV/ c^2)	5280.2 \pm 0.1 (fixed)				
	$\sigma_{m_{ES}}$ (MeV/ c^2)	2.73 \pm 0.06 (fixed)				
	ARGUS shape ζ	-29 \pm 6 (fixed)				
$J/\psi K_S^0 (\pi^+ \pi^-)$	Signal Yield	140 \pm 12	251 \pm 16	271 \pm 17	275 \pm 17	937 \pm 31
	Purity (%)	99.3 \pm 0.3	96.4 \pm 0.6	96.7 \pm 0.5	95.3 \pm 0.6	96.5
$J/\psi K_S^0 (\pi^0 \pi^0)$	Signal Yield	23 \pm 5	40 \pm 7	47 \pm 7	39 \pm 7	150 \pm 13
	Purity (%)	98 \pm 1	88 \pm 3	87 \pm 3	87 \pm 3	88.5
$\psi(2S)K_S^0$	Signal Yield	30 \pm 6	32 \pm 6	46 \pm 7	35 \pm 6	143 \pm 12
	Purity (%)	99 \pm 1	98 \pm 1	97 \pm 1	93 \pm 2	96.9
$\chi_{c1}K_S^0$	Signal Yield	9 \pm 3	19 \pm 5	20 \pm 5	27 \pm 5	75 \pm 9
	Purity (%)	98 \pm 2	94 \pm 3	94 \pm 3	96 \pm 2	94.5
$\eta_c K_S^0$	Signal Yield	14 \pm 4	28 \pm 6	23 \pm 6	29 \pm 6	95 \pm 11
	Purity (%)	92 \pm 4	72 \pm 6	64 \pm 7	74 \pm 5	73.3

Table 8.3: Signal yield and purity resulting from fit to the m_{ES} distribution of each tagging category in the CP eigenstate sample after vertexing requirements.

The m_{ES} distributions of tagged events in the flavor-eigenstate sample that have passed the vertexing requirements in each tagging category are fit with the Gaussian mean, width, and ARGUS shape floating. There are enough events in each tagging category of the flavor-eigenstate sample, as opposed to the CP sample, for these fit parameters to be well determined. The results from this fit are presented in Table 8.4 and displayed in Fig. 8.2.

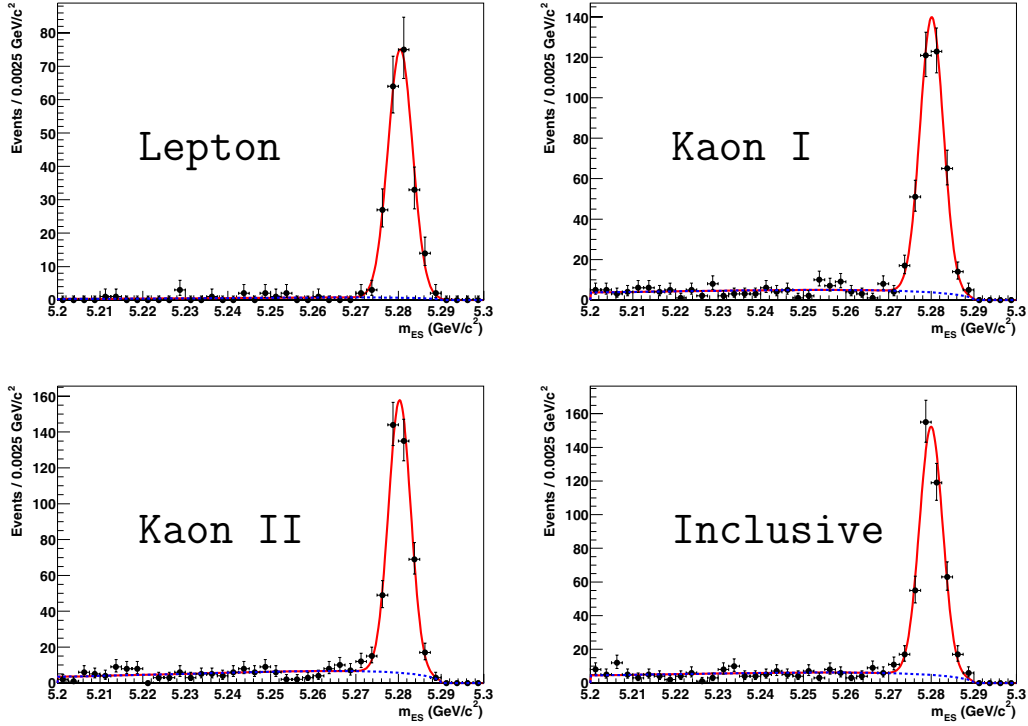


Figure 8.1: Distribution of m_{ES} for CP events passing vertexing requirements for (a) Lepton, (b) Kaon I, (c) Kaon II, and (d) Inclusive tagging categories overlaid with the fit result. The ARGUS component is shown as a dashed line.

Parameter	Lepton	Kaon I	Kaon II	Inclusive
$\mu_{m_{ES}}$ (MeV/c^2)	5280.30 ± 0.05	5280.20 ± 0.04	5280.20 ± 0.04	5280.20 ± 0.04
$\sigma_{m_{ES}}$ (MeV/c^2)	2.60 ± 0.04	2.64 ± 0.04	2.62 ± 0.03	2.60 ± 0.04
ARGUS shape ζ	-72 ± 7	-35 ± 2	-32 ± 2	-35 ± 2
Signal Yield	2979 ± 57	5450 ± 83	6489 ± 92	6535 ± 94
Purity(%)	0.956 ± 0.005	0.862 ± 0.005	0.826 ± 0.005	0.823 ± 0.005

Table 8.4: Signal yield, purity, Gaussian mean $\mu_{m_{ES}}$, width $\sigma_{m_{ES}}$, and ARGUS shape ζ resulting from fit to the m_{ES} distribution of each tagging category in the flavor-eigenstate sample after vertexing requirements.

8.2 Maximum-likelihood fit results

The results of the maximum-likelihood fit are displayed in Table 8.5 along with the correlation of each of the 34 free parameters with $\sin 2\beta$. The value of $\sin 2\beta$ obtained from the combined sample of B mesons reconstructed in

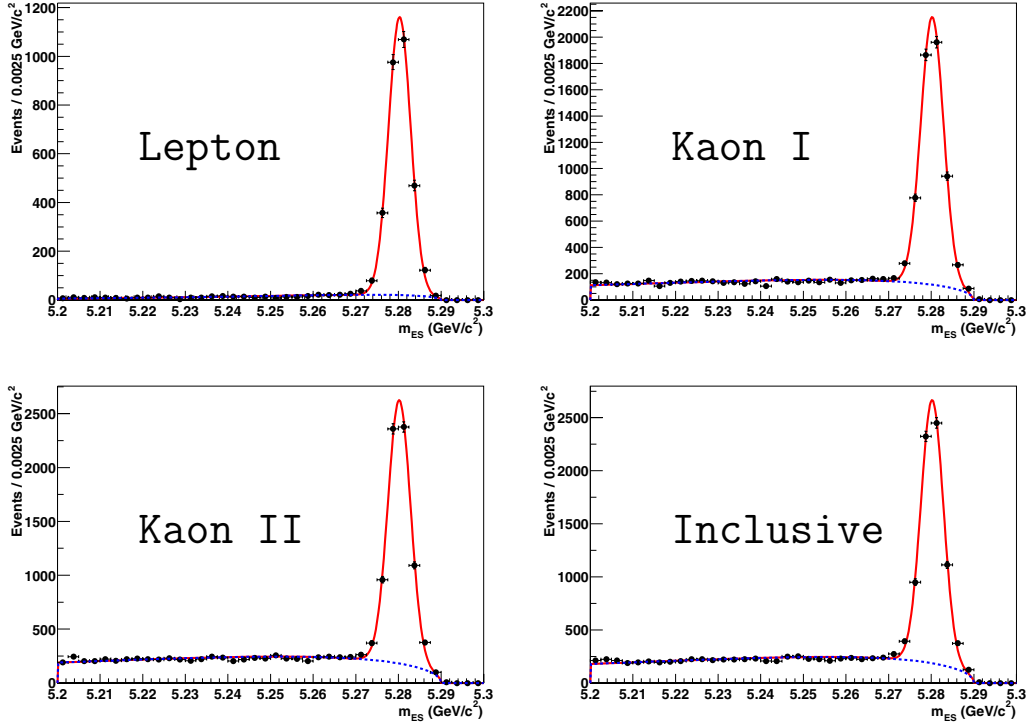


Figure 8.2: Distribution of m_{ES} for flavor-eigenstate events passing vertexing requirements for (a) Lepton, (b) Kaon I, (c) Kaon II, and (d) Inclusive tagging categories overlaid with the fit result. The ARGUS component is shown as a dashed line.

charmonium CP eigenstates with CP eigenvalue -1 is

$$\sin 2\beta = 0.755 \pm 0.074, \quad (8.2.1)$$

firmly establishing the existence of CP violation in the B system. This value includes the -0.014 correction discussed in Sec. 7.6.3 The largest correlation between $\sin 2\beta$ and any linear combination of the other free fit parameters is found to be 13%.

Parameter	Result	Corr. with $\sin 2\beta$
$\sin 2\beta$	0.755 ± 0.074	1.000
Signal Resolution Function		
Scale (core)	1.094 ± 0.048	0.020
Scale (tail)	3.0 (fixed)	
$\delta(\Delta t)$ Lepton (core)	0.039 ± 0.061	0.010
$\delta(\Delta t)$ Kaon I (core)	-0.234 ± 0.050	0.011
$\delta(\Delta t)$ Kaon II (core)	-0.232 ± 0.044	0.012
$\delta(\Delta t)$ Inclusive (core)	-0.219 ± 0.045	0.007
$\delta(\Delta t)$ (tail)	-1.020 ± 0.293	-0.007
f (tail)	0.106 ± 0.020	0.017
f (outlier)	0.003 ± 0.001	-0.010
Signal dilutions		
$\langle D \rangle$, Lepton	0.934 ± 0.013	-0.046
$\langle D \rangle$, Kaon I	0.801 ± 0.014	-0.066
$\langle D \rangle$, Kaon II	0.582 ± 0.016	-0.056
$\langle D \rangle$, Inclusive	0.367 ± 0.017	-0.048
ΔD , Lepton	0.029 ± 0.022	0.003
ΔD , Kaon I	0.021 ± 0.022	0.004
ΔD , Kaon II	0.078 ± 0.023	-0.007
ΔD , Inclusive	0.051 ± 0.025	0.006
Background properties		
τ , mixing bgd [ps]	1.325 ± 0.062	-0.001
$f(\tau = 0)$, CP bgd	0.639 ± 0.050	-0.024
$f(\tau = 0)$, mixing bgd, Lepton	0.289 ± 0.163	0.000
$f(\tau = 0)$, mixing bgd, Kaon I	0.630 ± 0.026	0.000
$f(\tau = 0)$, mixing bgd, Kaon II	0.657 ± 0.024	0.000
$f(\tau = 0)$, mixing bgd, Inclusive	0.683 ± 0.022	0.000
Background resolution function		
Scale (core)	1.398 ± 0.019	-0.003
$\delta(\Delta t)$ core	-0.045 ± 0.013	0.000
f (outlier)	0.016 ± 0.002	-0.001
Background dilutions		
$\langle D \rangle$, Lepton, $\tau = 0$	1.372 ± 0.630	0.002
$\langle D \rangle$, Kaon I, $\tau = 0$	0.649 ± 0.030	0.006
$\langle D \rangle$, Kaon II, $\tau = 0$	0.393 ± 0.024	0.006
$\langle D \rangle$, Inclusive, $\tau = 0$	0.158 ± 0.024	0.005
$\langle D \rangle$, Lepton, $\tau > 0$	0.170 ± 0.104	0.000
$\langle D \rangle$, Kaon I, $\tau > 0$	0.251 ± 0.048	0.000
$\langle D \rangle$, Kaon II, $\tau > 0$	0.279 ± 0.042	0.000
$\langle D \rangle$, Inclusive, $\tau > 0$	0.032 ± 0.046	0.000

Table 8.5: Maximum-likelihood fit results for the CP data sample. The global correlation coefficient for $\sin 2\beta$ is 13%.

The distribution of events as a function of Δt for the CP sample with $m_{ES} > 5.27 \text{ GeV}/c^2$ for B^0 and \bar{B}^0 tags is shown in Fig 8.3. Overlaid on the data are projections of the signal and background Δt distributions obtained from the fit, where the latter is normalized to the projected background level. The difference between the Δt distributions of B^0 and \bar{B}^0 tags is evident. The raw asymmetry in the number of B^0 and \bar{B}^0 tags normalized to the total number of tagged events in bins of Δt ,

$$\mathcal{A}(\Delta t) = \frac{N(B^0\text{tag}; \Delta t) - N(\bar{B}^0\text{tag}; \Delta t)}{N(B^0\text{tag}; \Delta t) + N(\bar{B}^0\text{tag}; \Delta t)} \quad (8.2.2)$$

is shown in Fig. 8.4 for the CP sample.

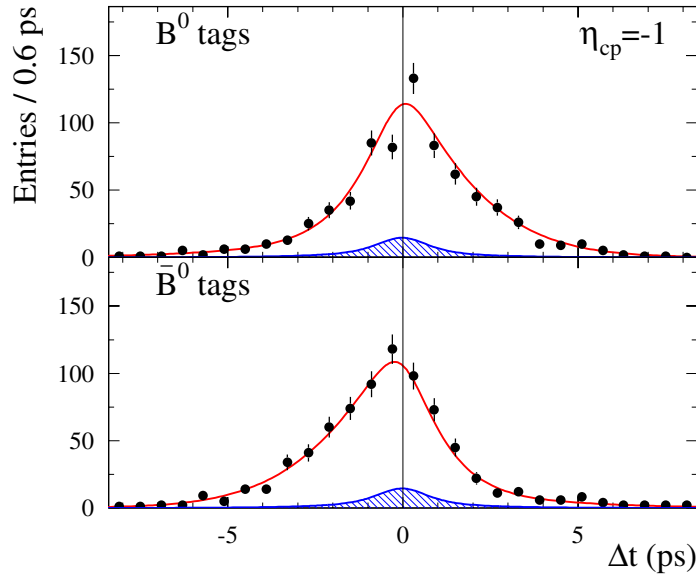


Figure 8.3: The distribution of events in the CP sample with $m_{ES} > 5.27 \text{ GeV}/c^2$ as a function of Δt for B^0 (top) and \bar{B}^0 (bottom) tags. The results of the likelihood fit are overlaid on the data for signal (solid line) and background (shaded histogram) contributions.

8.2.1 Goodness of fit

It is non-trivial to determine the goodness of the maximum-likelihood fit in the traditional manner of reporting the χ^2 of the fit to the data. It is not

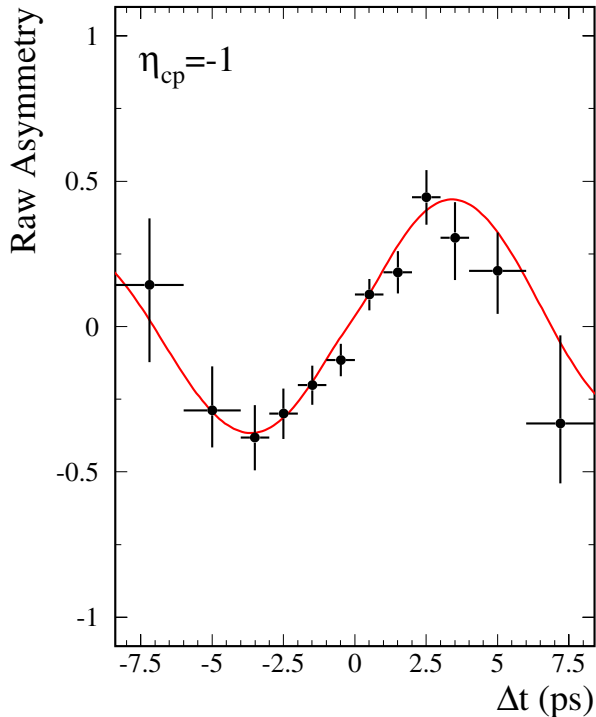


Figure 8.4: The raw asymmetry in the number of B^0 and \bar{B}^0 tags in the CP sample normalized to the total number of tagged events in bins of Δt . The data points are overlaid with the maximum-likelihood fit result.

obvious how to determine the number of degrees of freedom of the fits to all CP events shown in Figs. 8.3 and 8.4. These fits are projected over four discrete tagging categories and contain 34 free parameters but only two are primarily determined by the CP sample.

Consequently, we use samples of toy Monte Carlo ¹ (TMC) to evaluate the likelihood of the fit and its error. We construct 1000 toy experiments that contain exactly the same statistics as observed in our data set (same number of events in each tagging category for B^0 and \bar{B}^0 tags) and we use the same

¹The terminology “toy” is used to indicate that we construct data sets by randomly sampling from known probability distribution functions, not by simulating the reconstruction of B meson decays.

m_{ES} values for each event as found in the data. The free parameters of the probability distribution functions used to construct the likelihood are fixed to those obtained from the data for each tagging category. The value of $\sin 2\beta$ is determined by fitting the generated Δt distribution of each toy experiment in the same way that it is determined in data. Table 8.6 lists the mean expected statistical error and log likelihood from the ensemble of toy experiments, the values of the error and log-likelihood observed in data, and the fraction of toy Monte Carlo fits that returned a log-likelihood value less likely than that returned by the fit to data. Fig. 8.5 shows the statistical error on $\sin 2\beta$ and Fig. 8.6 shows the log likelihood distributions from the 1000 toy experiment fits for each CP decay mode.

We conclude that the errors returned by the fit in data for each CP mode are in good agreement with those predicted by the toy experiments. We also don't find any reason to be concerned with value of the maximum of the log-likelihood for any of the CP modes. The log-likelihood values in the data fall near the mean of the most probable regions found in the toy Monte Carlo experiments.

Sample	$\langle\sigma_{\text{TMC}}\rangle$	RMS σ_{TMC}	σ_{Data}	$\langle-\ln\mathcal{L}_{\text{TMC}}\rangle$	$-\ln\mathcal{L}_{\text{Data}}$	Frac.
$J/\psi K_S^0 (\pi^+ \pi^-)$	0.0816	0.005	0.084	-1513.0 ± 1.7	-1494.9	0.623
$J/\psi K_S^0 (\pi^0 \pi^0)$	0.2345	0.018	0.240	-495.1 ± 0.8	-511.5	0.263
$\psi(2S)K_S^0$	0.2113	0.025	0.235	-227.6 ± 0.7	-222.9	0.576
$\chi_{c1}K_S^0$	0.3138	0.060	0.396	-151.0 ± 0.6	-152.2	0.472
$\eta_c K_S^0$	0.3398	0.038	0.320	-579.4 ± 0.7	-601.5	0.151

Table 8.6: Comparison of the statistical error on $\sin 2\beta$ in data (σ_{Data}) with the average error on $\sin 2\beta$ in 1000 toy Monte Carlo (TMC) experiments ($\langle\sigma_{\text{TMC}}\rangle$) for each CP decay mode. The RMS of the σ_{TMC} distribution is shown as well. The value of the negative log-likelihood in data ($-\ln\mathcal{L}_{\text{Data}}$) and its average value in the toy experiments ($\langle-\ln\mathcal{L}_{\text{TMC}}\rangle$) is also compared. The last column lists the fraction of TMC experiments that were less likely than the data fit (the fraction with $\ln\mathcal{L}_{\text{TMC}} < \ln\mathcal{L}_{\text{Data}}$).

Sigma $\sin 2\beta$

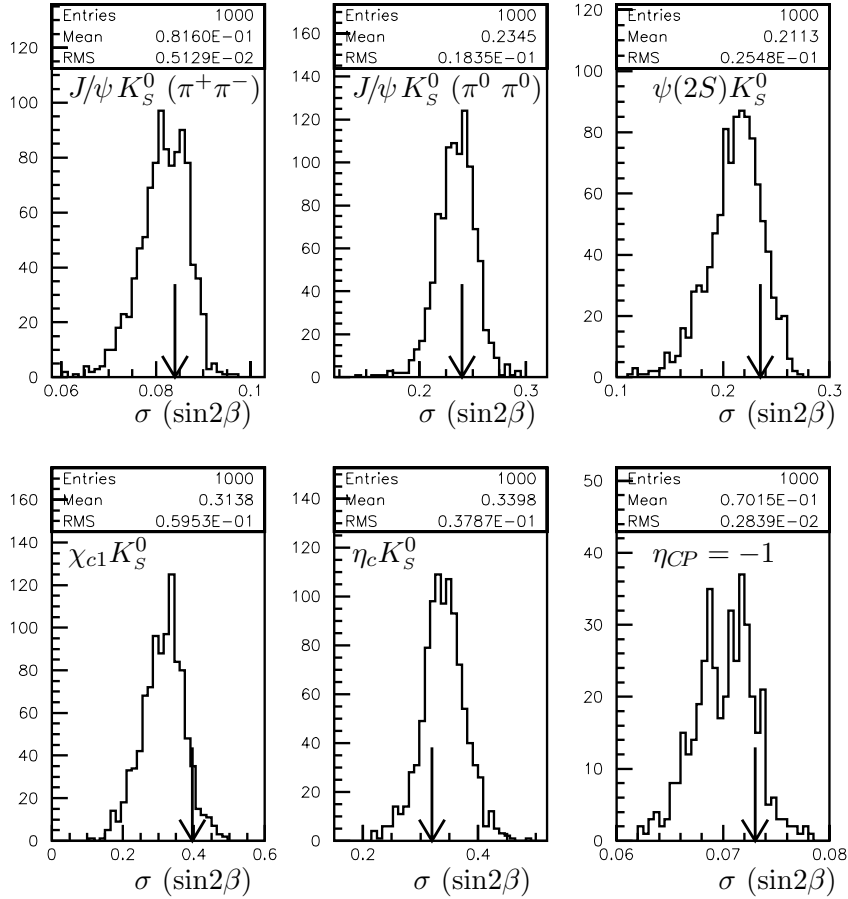


Figure 8.5: Distribution of $\sigma(\sin 2\beta)$ from fits to 1000 toy Monte Carlo experiments for each CP decay mode. The arrows indicate the value of the fit from the data.

8.2.2 Flavor tagging results

We evaluate the performance of the flavor tagging algorithm in the B_{flav} sample in Table 8.7. This Table summarizes results already shown in Table 8.2 (number of signal events) and 8.5 (average dilutions) for convenience. The effective tagging efficiency Q is found to be 28.1 ± 0.7 . We see that the Lepton

Minus ln L

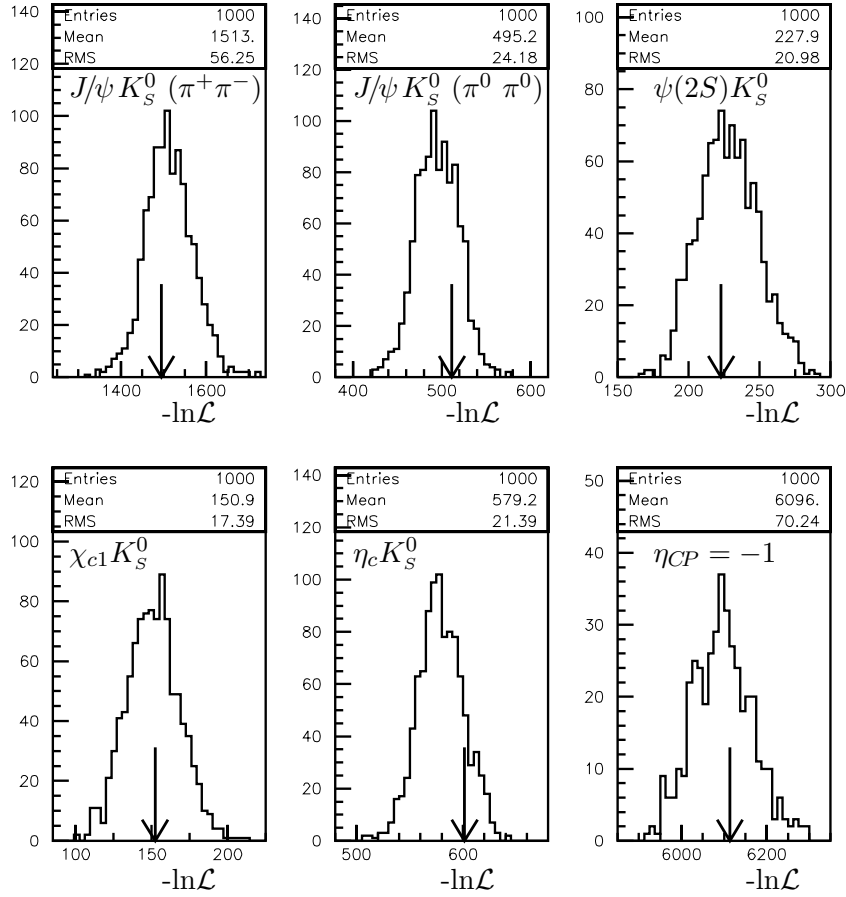


Figure 8.6: Distribution of log-likelihood from fits to 1000 toy Monte Carlo experiments for each CP decay mode. The arrows indicate the value of the fit from the data.

tag provides the cleanest sample (lowest mistag rate) but the Kaon I tag has the largest Q value of any category as expected because of the abundance of right sign kaons in B meson decays discussed in Sec. 5.2.2.

Category	N_{signal}	$\varepsilon(\%)$	$w(\%)$	$Q(\%)$
Lepton	2979 ± 57	9.1 ± 0.2	3.3 ± 0.6	7.9 ± 0.3
Kaon I	5450 ± 83	16.7 ± 0.2	9.9 ± 0.7	10.7 ± 0.4
Kaon II	6489 ± 92	19.8 ± 0.3	20.9 ± 0.8	6.7 ± 0.4
Inclusive	6535 ± 94	20.0 ± 0.3	31.6 ± 0.9	2.7 ± 0.3
Total	32700 ± 208	65.6 ± 0.5		28.1 ± 0.7

Table 8.7: Flavor tagging performance in data. The Kaon I tagging category provides the largest effective tagging efficiency Q .

8.2.3 $J/\psi K_L^0$ and $J/\psi K^{*0}$ results

As discussed in Sec. 3.2, B^0 decays to $J/\psi K_L^0$ and $J/\psi K^{*0}$ ($K^{*0} \rightarrow K_S^0 \pi^0$) are also used to measure $\sin 2\beta$. The details of the reconstruction and likelihood fit for these modes are outside the scope of this dissertation. However, we mention the results for completeness. Using 988 tagged B^0 decays to $J/\psi K_L^0$ with a purity of 55%, we find

$$\sin 2\beta_{J/\psi K_L^0} = 0.72 \pm 0.16 \quad (8.2.3)$$

A separate analysis [75] has determined that the fraction of the parity-odd orbital angular momentum component ($L = 1$) in the $B^0 \rightarrow J/\psi K^{*0}$ final state is $16.0 \pm 3.5\%$. After correcting for acceptance effects, this leads to an effective CP eigenvalue of $\eta_{CP} = 0.65 \pm 0.07$. Using 147 tagged B^0 decays to $J/\psi K^{*0}$ with a purity of 81%, we measure

$$\sin 2\beta_{J/\psi K^{*0}} = 0.22 \pm 0.52 \quad (8.2.4)$$

For the entire CP data sample that consists of 2641 tagged $J/\psi K_S^0$, $\psi(2S)K_S^0$, $\chi_{c1}K_S^0$, $\eta_c K_S^0$, $J/\psi K_L^0$, and $J/\psi K^{*0}$ ($K^{*0} \rightarrow K_S^0 \pi^0$) decays with a combined purity of 78%, we measure

$$\sin 2\beta = 0.741 \pm 0.067 \quad (8.2.5)$$

8.3 Cross checks

A variety of additional cross checks are performed to increase our confidence in the fit procedure. Some involve examining the consistency of the $\sin 2\beta$ values measured in various subsets of the data and some involve calibrating the procedure by fitting for $\sin 2\beta$ in control samples where $\sin 2\beta$ is expected to be zero a priori. These checks are described below.

8.3.1 CP decay mode

We fit for $\sin 2\beta$ in each decay mode of the B_{CP} sample independently to determine whether the results are consistent. Clearly, the value obtained when fitting the entire CP sample is dominated by the $J/\psi K_s^0$ ($\pi^+\pi^-$) decays. However, since the sum of the other decay modes contribute a weight of about 1/3 to the value of $\sin 2\beta$ measured with the entire data sample, this check is still meaningful. The values of $\sin 2\beta$ found for each decay mode are listed in Table 8.8. Plots of the number of signal events ($m_{ES} > 5.27 \text{ GeV}/c^2$) as a function of Δt for B^0 and \bar{B}^0 tags are shown for $J/\psi K_s^0$, $\psi(2S)K_s^0$, and $\chi_{c1}K_s^0$ in Fig. 8.7. The raw asymmetry for each of these modes as defined in Eqn 8.2.2 is displayed in Fig. 8.8. The Δt distributions of B^0 and \bar{B}^0 tagged events and the raw asymmetry for $\eta_c K_s^0$ are shown in Fig. 8.9. We determine the consistency of the $\sin 2\beta$ values for each mode by constructing a χ^2 as

$$\chi_{\text{modes}}^2 = \sum_i^{\text{modes}} \frac{(\sin 2\beta_i - \sin 2\beta_{CP})^2}{\sigma(\sin 2\beta_i)} \quad (8.3.1)$$

where $\sin 2\beta_{CP} = 0.755$ and i runs over each decay mode. With this definition, we calculate a χ^2 of 3.62 for 4 degrees of freedom which gives a probability of about 46%. A comparison of the $\sin 2\beta$ values measured for each CP decay mode compared to the value found for all the modes combined is shown in Fig. 8.10.

Sample	Yield(tag)	Purity	$\sin 2\beta$
<i>CP</i> sample	1399 ± 39	93.5	0.755 ± 0.074
$J/\psi K_S^0 (\pi^+ \pi^-)$	937 ± 31	96.5	0.820 ± 0.084
$J/\psi K_S^0 (\pi^0 \pi^0)$	150 ± 13	88.5	0.394 ± 0.241
$\psi(2S)K_S^0$	143 ± 12	96.9	0.691 ± 0.235
$\chi_{c1}K_S^0$	75 ± 9	94.5	1.014 ± 0.397
$\eta_c K_S^0$	95 ± 11	73.3	0.586 ± 0.320

Table 8.8: Values of $\sin 2\beta$ found for each *CP* decay mode. The quoted yield corresponds to tagged events returned by the likelihood fit that are therefore background subtracted.

8.3.2 Flavor tagging category

To determine whether any of the differences in the physical sources of the flavor tag described in Sec. 5.2 bias the measurement, we check that the values of $\sin 2\beta$ obtained in each tag category for the *CP* sample agree. The results for each tagging category are shown in Table 8.9. Fig. 8.11 and 8.12 display the Δt distribution of B^0 and \bar{B}^0 tagged events and the raw Δt asymmetry for each tagging category respectively. The amplitude of the raw asymmetry is clearly different for each category. However, we find consistent values of $\sin 2\beta$ for each category since the amplitude is the product of the dilution and $\sin 2\beta$ and each category has a different dilution. The asymmetry of the Δt distributions of B^0 and \bar{B}^0 tagged events is quite striking in the **Lepton** tagging category which has the lowest mistag rate, purest sample of reconstructed mesons, and lowest mean value of $\sigma_{\Delta t}$. The improved resolution on $\sigma_{\Delta t}$ (or $\sigma_{\Delta z}$) results from the high momentum prompt lepton track which provides a less biased estimate of the B_{tag} vertex than the other categories as explained in Chapter 6.

8.3.3 B^0 and \bar{B}^0 flavor tags

While the difference in the Δt distributions of B^0 and \bar{B}^0 tagged events in the *CP* sample provides an elegant visual confirmation of a *CP* asymmetry,

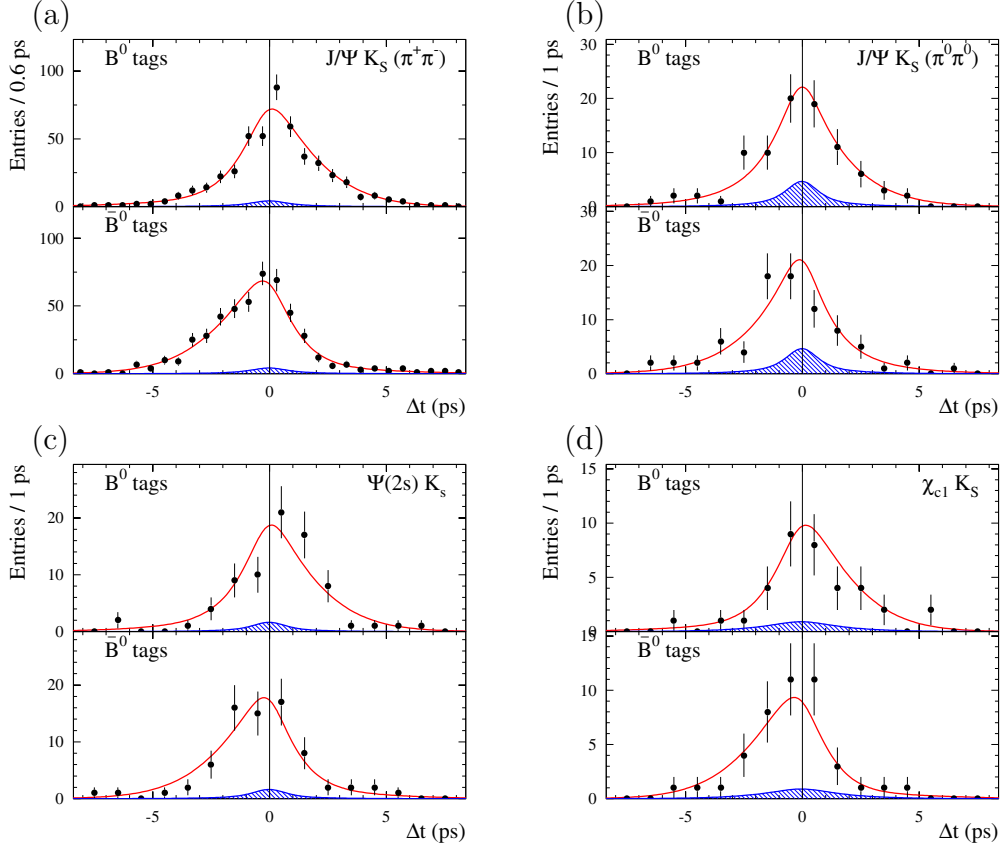


Figure 8.7: Distribution of events as a function of Δt for B^0 and \bar{B}^0 tagged decays with $m_{\text{ES}} > 5.27 \text{ GeV}/c^2$ for (a) $J/\psi K_S^0 (\pi^+ \pi^-)$, (b) $J/\psi K_S^0 (\pi^0 \pi^0)$, (c) $\psi(2S)K_S^0$, (d) $\chi_{c1}K_S^0$, and (e) $\eta_c K_S^0$. Results from the likelihood fit are overlaid for signal (solid line) and background (shaded histogram) for each mode.

Sample	Yield(tag)	Purity	$\sin 2\beta$
Lepton	217 ± 15	98.0	0.789 ± 0.113
Kaon I	370 ± 20	93.2	0.778 ± 0.119
Kaon II	407 ± 21	92.7	0.732 ± 0.171
Inclusive	406 ± 21	92.4	0.452 ± 0.282

Table 8.9: Value of $\sin 2\beta$ for each flavor tagging category for the CP sample. A consistent value is measured in all categories. The yields are for tagged events obtained with the likelihood fit and are therefore background subtracted.

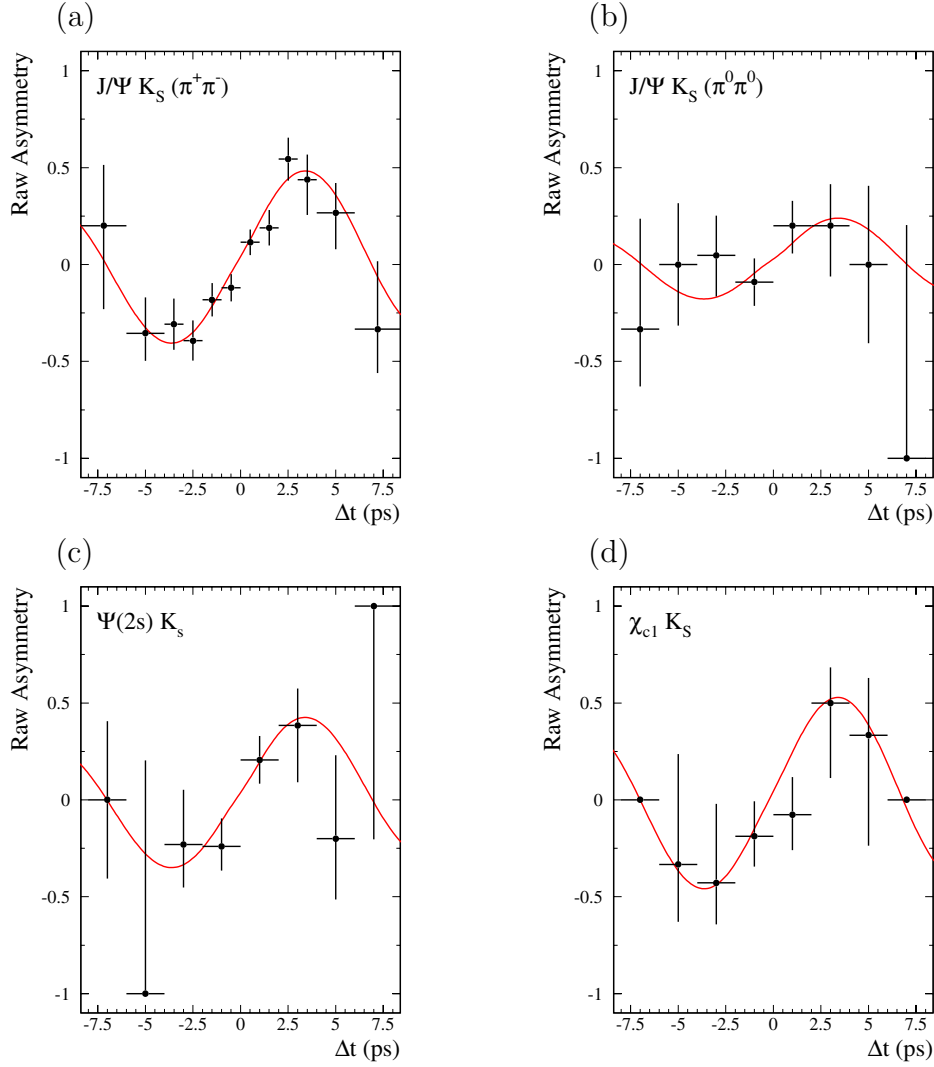


Figure 8.8: Raw Δt asymmetry for (a) $J/\psi K_S^0 (\pi^+ \pi^-)$, (b) $J/\psi K_S^0 (\pi^0 \pi^0)$, (c) $\psi(2S) K_S^0$, (d) $\chi_{c1} K_S^0$, and (e) $\eta_c K_S^0$. The data points are overlaid with the results from the maximum-likelihood fit in each case.

it was mentioned in Sec. 1.8 that can measure $\sin 2\beta$ using only one type of B meson flavor. This results from the fact that the Δt distribution of CP events (Eqn 3.0.4) for either tag is not symmetric with respect to $\Delta t = 0$.

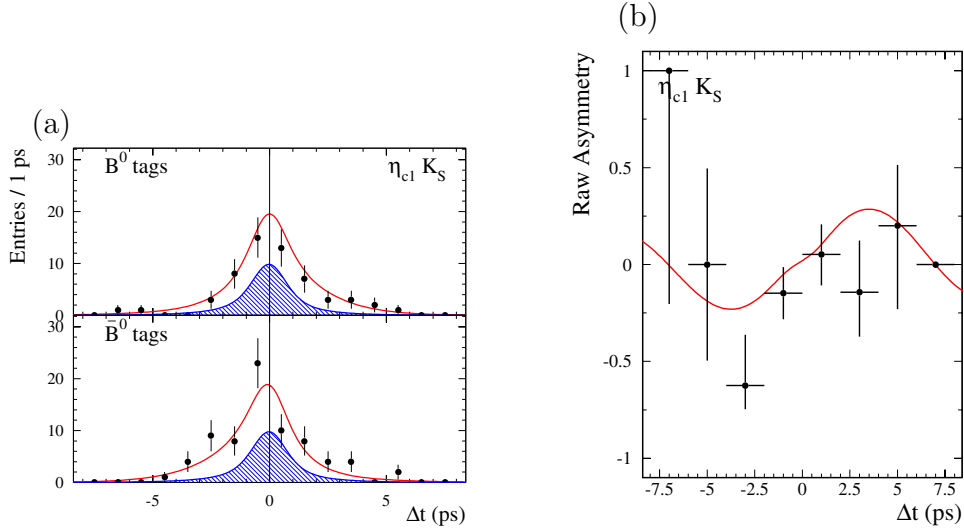


Figure 8.9: Distribution of (a) events as a function of Δt for B^0 and \bar{B}^0 tagged decays with $m_{ES} > 5.27 \text{ GeV}/c^2$, and (b) raw Δt asymmetry for $\eta_c K_S^0$. The data points are overlaid with the results from the maximum-likelihood fit for signal (solid line) and background (shaded histogram).

Consequently, we employ the same maximum-likelihood technique to measure $\sin 2\beta$ in the CP sample for B^0 and \bar{B}^0 tagged events separately. The results are shown in Table 8.10 and are found to be consistent for both flavor tags.

Sample	Yield(tag)	Purity	$\sin 2\beta$
B^0 -Tag	688 ± 27	94.1	0.754 ± 0.105
\bar{B}^0 -Tag	712 ± 28	93.3	0.739 ± 0.105

Table 8.10: Value of $\sin 2\beta$ for B^0 and \bar{B}^0 tagged events for the CP sample. A consistent value is measured for both types of flavor tags. The yields are obtained with the likelihood fit and are therefore background subtracted.

8.3.4 J/ψ reconstruction mode

All events in the CP sample (except for B mesons reconstructed as $\eta_c K_S^0$) contain a J/ψ candidate reconstructed as e^+e^- or $\mu^+\mu^-$. The invariant mass distribution of the lepton pair looks substantially different for those recon-

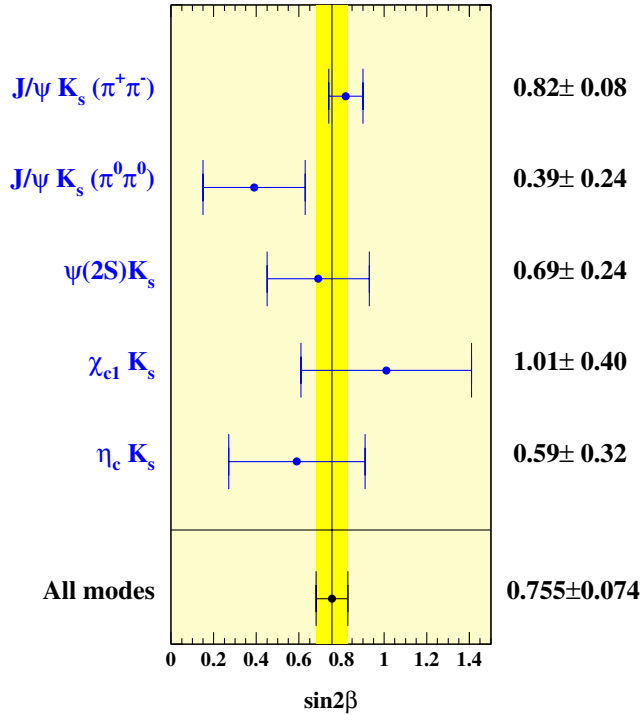


Figure 8.10: A comparison of the $\sin 2\beta$ values found in each CP decay mode with the one sigma band around the central value for all the modes combined. The errors are do not include systematic effects. The probability of the consistency of all the measured values is about 45% as explained in the text.

structed as e^+e^- due to energy loss from photon radiation as seen in Fig. 4.6. Additionally, the bremsstrahlung recovery algorithm is only used to attach photons to electron and positron tracks. While one does not really expect these differences to bias the $\sin 2\beta$ measurement, we check for consistency in the two J/ψ reconstruction modes. The results for $\sin 2\beta$ measured in the sample with $J/\psi \rightarrow e^+e^-$ and $J/\psi \rightarrow \mu^+ \mu^-$ are shown in Table 8.11 and found to be consistent.

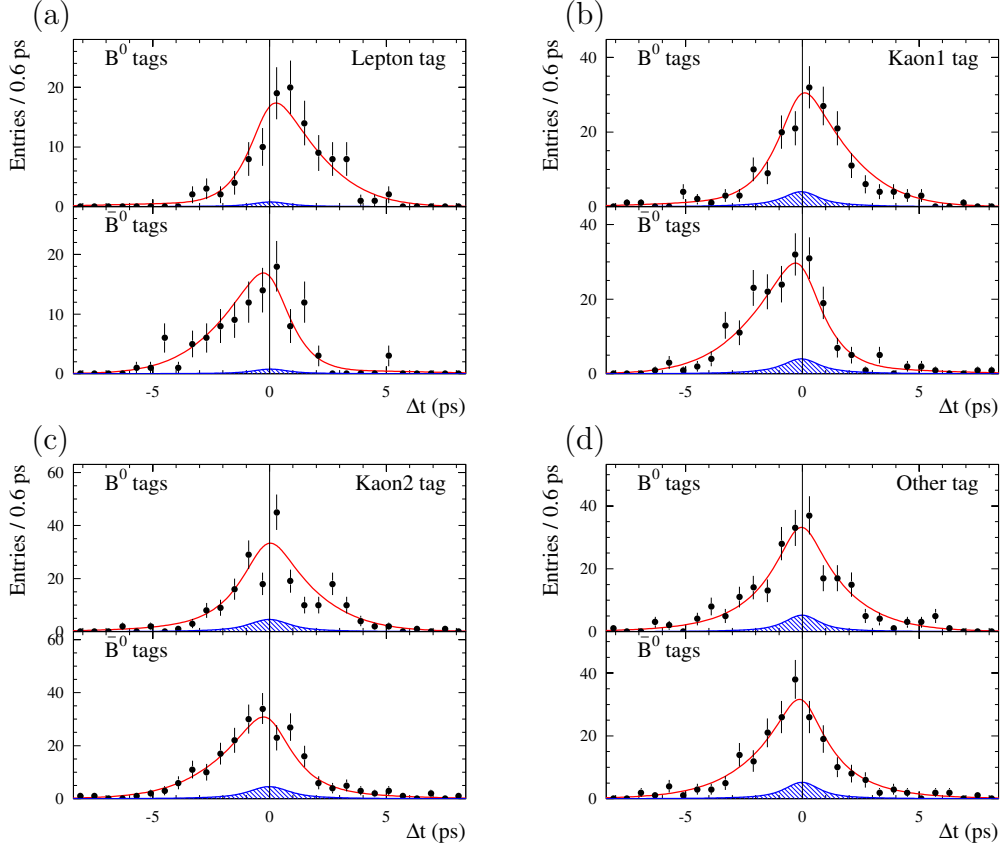


Figure 8.11: Distribution of events as a function of Δt for B^0 and \bar{B}^0 tagged decays in the CP sample with $m_{ES} > 5.27 \text{ GeV}/c^2$ for the (a) Lepton, (b) Kaon I, (c) Kaon II, and (d) Inclusive tagging categories. Results from the likelihood fit are overlaid for signal (solid line) and background (shaded histogram) for each category.

Sample	Yield(tag)	Purity	$\sin 2\beta$
$J/\psi \rightarrow e^+e^-$	623 ± 26	93.7	0.799 ± 0.099
$J/\psi \rightarrow \mu^+\mu^-$	681 ± 26	97.1	0.696 ± 0.104

Table 8.11: Value of $\sin 2\beta$ for $J/\psi \rightarrow e^+e^-$ and $J/\psi \rightarrow \mu^+\mu^-$ in the CP sample. A consistent value is measured for reconstruction of both modes. The yields are obtained with the likelihood fit and are therefore background subtracted.

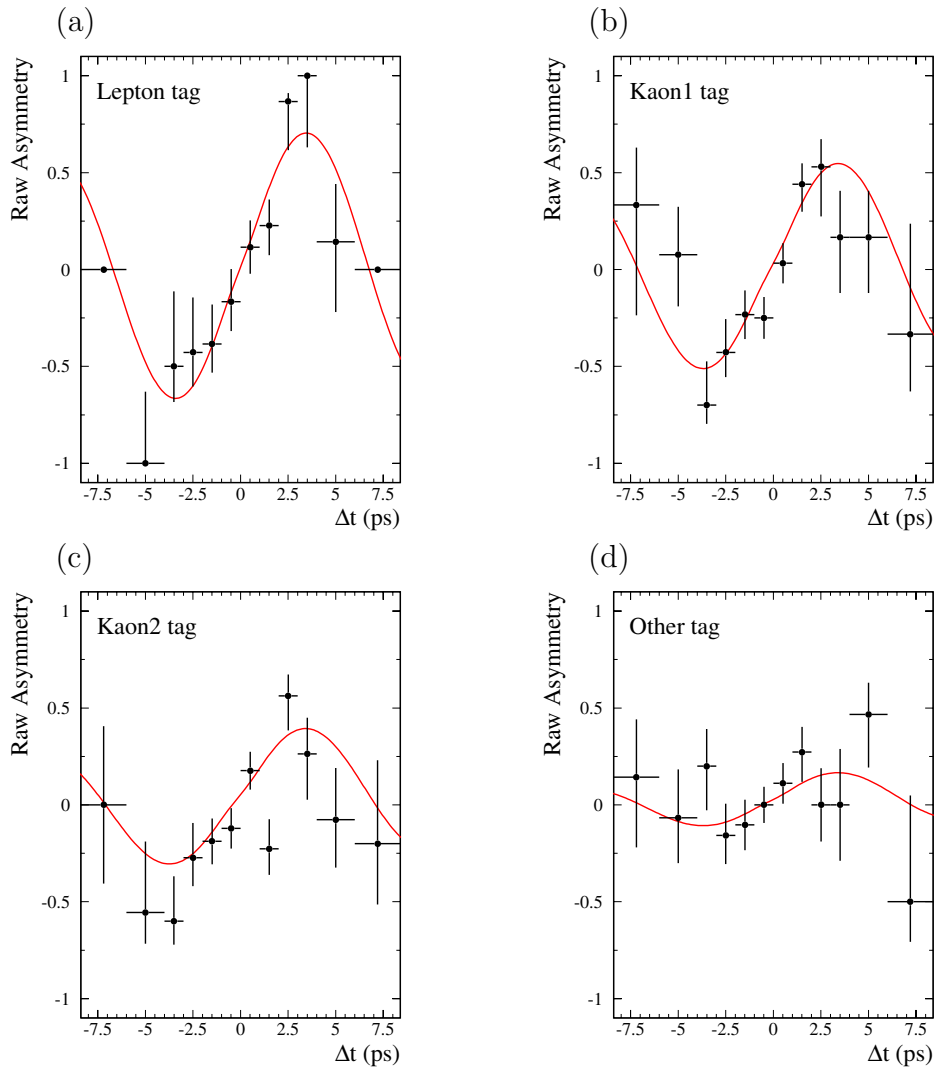


Figure 8.12: Raw Δt asymmetry for the (a) Lepton, (b) Kaon I, (c) Kaon II, and (d) Inclusive tagging categories. The data points are overlaid with the results from the maximum-likelihood fit in each case.

8.3.5 Run period

The data sample consists of about 88 million $\Upsilon(4S) \rightarrow B\bar{B}$ decays that were collected between 1999 and 2002. However, *BABAR* was not taking data continuously during that time span. There were different periods of a few

Run-block	Time period		Luminosity (fb^{-1})
	Begin	End	
Run1	October 1999	October 2000	20.1
Run2a	January 2001	June 2001	9.1
Run2b	July 2001	December 2001	26.4
Run2c	January 2002	June 2002	24.7

Table 8.12: Definitions and luminosity of different data taking periods.

months at a time when the machine was shut down so that repairs and upgrades could be made. Significant changes in the detector conditions (such as the global alignment of the SVT) were observed to occur when data taking was resumed after these periods. Corrections to the constants used in processing the data were made to account for this effect. Consequently, we break our data sample into four blocks (Run1, Run2a, Run2b, and Run2c) which correspond to discrete periods of contiguous data taking. The luminosity and definition of each run-block is given in Table 8.12. Table 8.13 displays the value of $\sin 2\beta$ that is measured for each run-block. We find that the probability of the χ^2 of a zeroth order polynomial fit to the $\sin 2\beta$ values from each run-block is 73%.

Sample	Yield	Purity	$\sin 2\beta$
Run 1	357 ± 19	93.3	0.628 ± 0.149
Run 2a	190 ± 14	94.4	0.866 ± 0.206
Run 2b	445 ± 22	94.2	0.761 ± 0.135
Run 2c	408 ± 21	93.9	0.824 ± 0.127

Table 8.13: Result of fitting for $\sin 2\beta$ in the CP sample for different data taking periods. The definitions of the run periods are displayed in Table 8.12. The yields are for tagged events and are obtained with likelihood fits and are therefore background subtracted.

Fig. 8.13 summarizes the results from the tagging category, flavor tag type, J/ψ reconstruction, and run-block subset cross checks of the CP data sample. None of the checks reveal inconsistencies with the value of $\sin 2\beta$ measured with

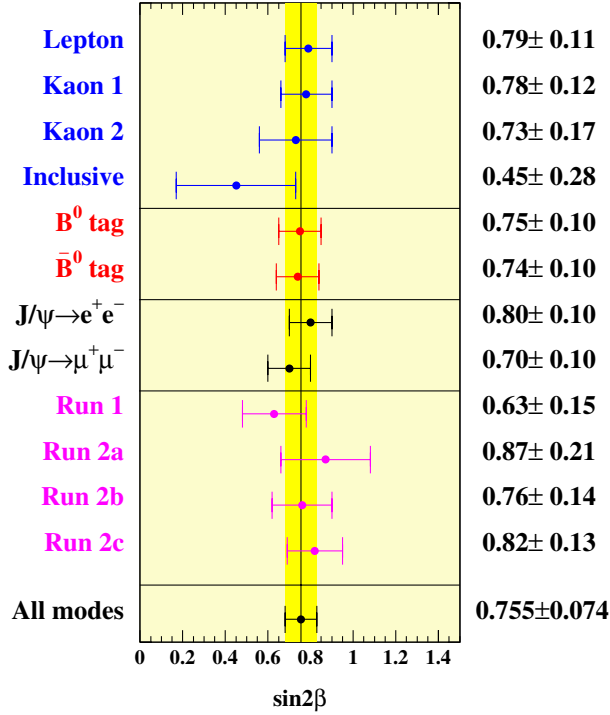


Figure 8.13: Comparison of $\sin 2\beta$ measured in various subsets of the full CP data sample. The subsets are grouped by horizontal lines according to tagging category, flavor tag type, J/ψ reconstruction, and run-block. Measurements of $\sin 2\beta$ from samples within a horizontal grouping are uncorrelated but those from different groups are highly correlated.

the full data sample.

8.3.6 Control samples

Sec. 4.7 discussed control samples of charged B meson decays to charmium plus a charged kaon and to $D^{(*)0}$ mesons plus a charged pion. Since charged final states are clearly not eigenstates of CP , we expect no CP asymmetries in these samples proportional to $\sin(\Delta m_d \Delta t)$ ². Consequently, we re-

²It is possible that there are direct CP violating asymmetries in these samples that are proportional to $\cos(\Delta m_d \Delta t)$ but they are predicted to be quite small in the SM.

peat the maximum-likelihood procedure to measure the effective value of $\sin 2\beta$, by which we mean the coefficient of the $\langle \mathcal{D} \rangle \sin(\Delta m_d \Delta t)$ term, in these samples and compare how different this effective value is from zero. Additionally, we recall from Eqn. 3.0.1 that the exponential behavior of the Δt distribution describing the decay of a neutral meson reconstructed in a flavor-eigenstate is modified only by a cosine (no sine) term that does not depend on $\sin 2\beta$. This allows us to check that the effective value of $\sin 2\beta$ in the flavor-eigenstate mixing sample is also consistent with zero. The effective values of $\sin 2\beta$ found in the various control samples are listed in Table 8.14. They are also displayed in Fig. 8.14. For each sample, the effective value of $\sin 2\beta$ is less than 1.5σ different from zero except for $\psi(2S)K^+$ where it is 2.1σ different from zero.

Control Sample	Yield(tag)	Purity	$\sin 2\beta$
$B^0 \rightarrow D^{(*)-}\pi^+/\rho^+/a_1^+$	19764 ± 160	84.2	0.021 ± 0.022
$B^- \rightarrow D^{(*)0}\pi^-$	13781 ± 131	87.0	0.017 ± 0.025
$B^0 \rightarrow J/\psi K^{*0}$	1678 ± 43	95.8	-0.009 ± 0.073
$B^+ \rightarrow \text{Charmonium } X$	6736 ± 87	93.8	0.021 ± 0.037
$B^+ \rightarrow J/\psi K^+$	5836 ± 81	93.8	0.047 ± 0.046
$B^+ \rightarrow \psi(2S)K^+$	555 ± 25	94.4	0.258 ± 0.121
$B^+ \rightarrow \chi_{c1}K^+$	345 ± 20	93.2	-0.194 ± 0.144
B_{flav}	21453 ± 166	85.0	0.017 ± 0.021

Table 8.14: Effective value of $\sin 2\beta$ measured in various control samples where no CP asymmetry is expected.

8.4 Fit for $|\lambda_{f_{CP}}|$

Recall that the form for the time-dependent asymmetry was simplified by making the assumption that $|\lambda_{f_{CP}}| = 1$ (see Eqn. 1.6.43). This assumption was well motivated by theoretical and experimental considerations that imply $q/p = 1$ in the B system and by the fact that the $b \rightarrow c\bar{c}s$ quark transition is dominated by a single weak phase (see Sec. 1.7). Nevertheless, we can measure

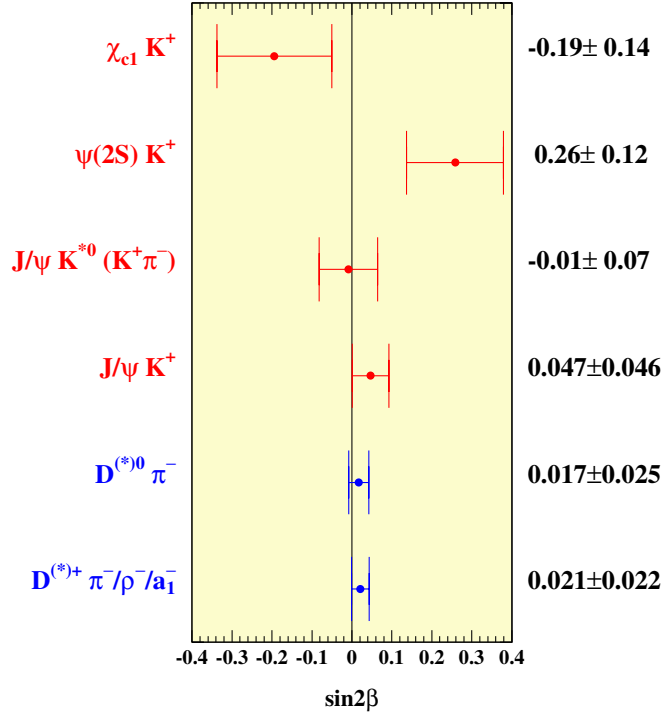


Figure 8.14: Comparison of effective value of $\sin 2\beta$ measured in various control samples. A zeroth order polynomial fit to the effective values of $\sin 2\beta$ measured in each control sample yields a value that is 1.5σ above zero.

$|\lambda_{f_{CP}}|$ from a fit to the $\eta_{CP} = -1$ sample, which has high purity and requires minimal assumptions about direct CP violation in backgrounds. This parameter is sensitive to the difference in the number of B^0 - and \bar{B}^0 -tagged events. To account for potential differences in reconstruction efficiency and tagging efficiency (depending on the tag category) for B^0 and \bar{B}^0 mesons, five additional free parameters were added to the maximum-likelihood fit. We measure

$$|\lambda_{f_{CP}}| = 0.948 \pm 0.051(\text{stat}) \pm 0.017(\text{syst}), \quad (8.4.1)$$

which is consistent with the SM expectation that $|\lambda_{f_{CP}}| = 1$. The coefficient of the $\sin(\Delta m_d \Delta t)$ term in Eqn. 1.6.43, which is equivalent to $\sin 2\beta$ when $|\lambda_{f_{CP}}| = 1$, is measured to be $0.759 \pm 0.074(\text{stat})$. Thus the measured value of

$\sin 2\beta$ is independent of whether $|\lambda_{f_{CP}}|$ is fixed or allowed to float. The sources of the systematic error for $|\lambda_{f_{CP}}|$ are the same as in the $\sin 2\beta$ measurement. These are described in detail in Chapter 9.

Chapter 9

Systematic uncertainties

The systematic uncertainties of the $\sin 2\beta$ measurement, whose results were presented in Chapter 8, can essentially be grouped into five categories according to their origin: the description and properties of the signal, the description and properties of the background, assumptions on fixed external parameters, detector reconstruction effects, and the limited statistics of Monte Carlo simulation used to validate the maximum-likelihood fitting procedure. Whenever possible, the effects of the systematic uncertainties are evaluated using the data sample. Otherwise, they are evaluated using Monte Carlo simulation.

By definition, a systematic uncertainty is independent of the size of the data sample used to make a measurement ¹. A large majority of the systematic uncertainties in this analysis arise from assumptions that have been made in the parameterizations of the signal and background Δt probability distribution functions (PDFs). These uncertainties are usually evaluated by making “reasonable” alternative assumptions and studying how they alter the measured value of $\sin 2\beta$. The difference between $\sin 2\beta$ measured with the standard (nominal) and new assumption is taken to be the systematic uncertainty.

¹If the systematic uncertainty is determined using data, as many are in this analysis, then its size will diminish with increased statistics until an asymptotic value is reached. This scaling with statistics merely indicates the experimenter’s inability to precisely determine the inherent size of the uncertainty.

The following presentation does not list the systematic uncertainties in order of importance but based on their category as defined above. All the uncertainties are summarized in Table 9.6 at the end of this Chapter for reference.

9.1 Signal parameters

The parameterization of the signal Δt probability distribution function for the CP sample relies on various assumptions that give rise to systematic uncertainties. The description assumes that the resolution and dilution of signal B_{CP} and B_{flav} events are the same since they are dominated (or determined) by the tagging B meson in the event. Additionally, the form of the resolution function assumed a specific model that was found to be adequate to describe simulated data.

9.1.1 Shared average signal dilutions

The average signal dilutions are assumed to be the same for the B_{flav} and B_{CP} probability distribution functions since the mistag rate should be independent of the reconstructed B meson. To evaluate the uncertainty associated with this assumption we use large samples of simulated B_{CP} and B_{flav} events. Average signal dilutions are obtained for both sets using knowledge of the generated flavor of the B_{tag} . The background probability distribution functions are removed from the fit and signal events are required to have $m_{ES} > 5.27$ GeV/ c^2 . The resolution function parameters are fixed to those obtained by fitting the residual distribution of the CP sample. We fit the CP sample for $\sin 2\beta$ varying the fixed dilutions extracted from the simulated B_{flav} sample by $\pm 1\sigma$. We repeat this procedure using the dilutions extracted from the simulated B_{CP} sample. The difference between the means of the $\sin 2\beta$ distributions constructed from both sets of fits is $(1.23 \pm 0.12) \cdot 10^{-2}$. The systematic uncertainty is taken to be $1.23 \cdot 10^{-2}$.

The difference between the means of the $\sin 2\beta$ distributions appears to be caused by a 3.4σ difference between the average mistag rates in the `Lepton` category for the simulated B_{CP} and flavor-eigenstate samples. It is not clear what causes this discrepancy. It is possible that the probability for swapping a B_{rec} and B_{tag} candidate is higher in the flavor-eigenstate sample when the B_{tag} decays semileptonically. For example, the B_{rec} might decay to $D^{*-}\pi^+$ and the B_{tag} to $D^{*-}e^+\nu_e$. One could imagine that the mistag rate is slightly different for these events compared to events in which the B_{tag} decays to the same final state but the B_{rec} decays to $J/\psi K_S^0$ since the probability for switching a B_{tag} and B_{rec} track is much smaller for the latter. Recall that two of the three variables used to determine the flavor-tag for the `Lepton` category, E_{90}^W and $\cos\theta_{miss}$ (see Sec. 5.2.1), use all the B_{tag} tracks (not just the lepton candidate) to assign a tag probability. This explanation has not been confirmed, however.

9.1.2 Shared signal resolution function parameters

To evaluate the assumption that the B_{CP} and B_{flav} events share the same resolution function, resolution function parameters are first obtained from fits to the Δt residual ($\delta t = \Delta t_{\text{true}} - \Delta t_{\text{meas}}$) for B_{CP} and B_{flav} simulated samples. The dilutions are fixed to those obtained using information about the true flavor of the B_{tag} . We then measure $\sin 2\beta$ in the simulated CP sample with a fit in which the background probability distribution functions are removed and signal events are required to have $m_{ES} > 5.27 \text{ GeV}/c^2$. The fits are performed 16 times by shifting the 8 resolution function parameters taken from the B_{CP} sample by $\pm 1\sigma$ from their nominal value. They are also done 16 times shifting the resolution function parameters taken from the B_{flav} sample. The difference in the means of the $\sin 2\beta$ distributions made from each set of parameters is found to be $(2 \pm 0.5) \cdot 10^{-3}$. The systematic uncertainty is taken to be $2 \cdot 10^{-3}$.

The outlier Gaussian is parameterized as having a fixed width of 8 ps and mean of 0 ps in the nominal fit. We vary the width of the outlier Gaussian

between 4 and 12 ps and the bias between -2 and +2 ps around the nominal fixed values respectively. The results of the variations in $\sin 2\beta$ are shown in Table 9.1 for these configurations. The systematic uncertainty is taken to be $5 \cdot 10^{-3}$.

Outlier Gaussian Width/Bias (ps)	$\delta \sin 2\beta$
8.0/0.0	–
4.0/0.0	–0.004
12.0/0.0	–0.002
8.0/–2.0	–0.001
8.0/+2.0	–0.003
Syst. Error	± 0.005

Table 9.1: Systematic uncertainty in $\sin 2\beta$ due to fixed width and bias of the Δt outlier Gaussian estimated from data by varying the width and bias of the model. $\delta \sin 2\beta$ is the difference of $\sin 2\beta$ for the specified fit and the reference fit with a Gaussian outlier with a width of 8 ps and zero bias.

A similar procedure was used to evaluate the systematic uncertainty due to the fixed value of the tail Gaussian scale factor in the nominal fit. The scale factor of the tail is varied between 2.0 and 5.0 around the nominal value of 3.0. The systematic uncertainty is found to be $2 \cdot 10^{-3}$.

9.1.3 Signal resolution function model

The resolution function is modeled as the sum of three Gaussian functions. To evaluate our sensitivity to this particular model, we perform the fit with an alternative description of the resolution function. Let $\mathcal{N}(t; \mu, \sigma)$ be a Gaussian distribution that is a function of an independent variable t with mean μ and width σ . The new resolution function $\mathcal{R}'(\delta t = \Delta t - \Delta t_{\text{true}})$ is the sum of a Gaussian of mean zero and the same Gaussian convoluted with an exponential

function:

$$\mathcal{R}'(\delta t; f_i, \sigma, \Gamma) = \sum_i^N \left[f_i \mathcal{N}(\delta t; 0, \sigma) + (1 - f_i) \int_{-\infty}^0 \Gamma e^{-\Gamma u} \mathcal{N}(\delta t - u; 0, \sigma) du \right] \quad (9.1.1)$$

where the sum is over the tagging categories and Γ is taken to be the decay constant of the B^0 meson. This particular function was well studied in a separate *BABAR* measurement of the B^0 and B^+ lifetimes where it was found to adequately describe the detector resolution [76]. The difference between the value of $\sin 2\beta$ obtained using this resolution function and the nominal one, $6 \cdot 10^{-3}$, is taken to be the systematic.

9.1.4 Resolution function for right and wrong tagged events

The likelihood fit implicitly assumes that the same resolution function parameters can be used for events that have been correctly flavor tagged (right tag) and those that have been incorrectly flavor tagged (wrong tag). It is not obvious that this should be true since the underlying physical processes that lead to wrong tags may also lead to larger biases in reconstructing the tag vertex, for example. The process for determining the impact of this effect on the $\sin 2\beta$ measurement described below is somewhat complicated. The idea is to compare the measured value of $\sin 2\beta$ in events that have been tagged correctly and incorrectly where common resolution function parameters are used with the value found in the same events where separate resolution function parameters are used for the correctly and incorrectly tagged events.

We use a high statistics sample of simulated Monte Carlo CP events to determine the systematic uncertainty. We determine the resolution function parameters of this sample (which we will refer to as the default parameters) by fitting the residual Δt distribution to the sum of three Gaussian functions. The sample is then split, using information about the generated flavor of the tagging meson, into a right tag and wrong tag subset. We measure $\sin 2\beta$ in

each subset fixing the resolution function parameters to their default values and setting background probability distribution functions to zero. Additionally, the average signal mistag rates of the right (wrong) tag sample are fixed to 0 (1). We get one value of $\sin 2\beta$ from this fit by taking the weighted average of $\sin 2\beta$ measured in the right and wrong tag subsets. The fit is repeated varying the default resolution function parameters by $\pm 1\sigma$ individually. We form a “default” distribution of $\sin 2\beta$ from these fits.

Then we determine the resolution function parameters of the right and wrong tag subsets separately (which we will refer to as the right-tag and wrong-tag parameters, respectively) by fitting the residual Δt distribution of each subset to the sum of three Gaussian functions. We measure $\sin 2\beta$ in the right tag subset fixing the resolution parameters to the right-tag values and we measure $\sin 2\beta$ in the wrong tag subset fixing the resolution parameters to the wrong-tag values. We get one value of $\sin 2\beta$ from this fit by taking the weighted average of $\sin 2\beta$ found in each subset. The fit is repeated varying the right and wrong-tag resolution function parameters by $\pm 1\sigma$. We form a distribution of $\sin 2\beta$ from these fits.

The difference in the mean of this distribution and the “default” distribution is found to be $2 \cdot 10^{-4}$ with an error of $8 \cdot 10^{-4}$. The systematic uncertainty is taken to be $8 \cdot 10^{-4}$.

9.2 Background parameters

The parameterization of the background probability distribution functions in the B_{CP} and B_{flav} sample rely on assumptions about the CP content of the backgrounds, the resolution function of the backgrounds, and the way in which signal and background probabilities are assigned. In the following sections, we evaluate the systematic uncertainties that result from these assumptions.

9.2.1 CP content of the background

The nominal fit assumes that there is no CP violation in the lifetime and peaking backgrounds in the CP sample. Thus, the parameterization of the Δt distributions of these backgrounds does not include a term that depends on $\sin(\Delta m_d \Delta t)$. To evaluate the systematic uncertainty, we modify the PDFs to include a term sensitive to CP violation but not dependent on $\sin 2\beta$:

$$\mathcal{B}' = e^{-\Gamma_{B^0} |\Delta t|} [1 \pm \eta_{\text{back}} \mathcal{D} \sin(\Delta m_d \Delta t)] \quad (9.2.1)$$

where η_{back} is the CP eigenvalue of the background, which is set to zero in the nominal fit (see Eqn. 7.3.3), and the value of \mathcal{D} used is described below.

For the lifetime background, we vary η_{back} between ± 1 taking the average dilutions in common with the CP signal PDF and find the systematic uncertainty (difference between $\sin 2\beta$ with these configurations and the nominal the fit) to be $0.5 \cdot 10^{-3}$.

For the peaking background, we fit for the effective asymmetry $\eta_{\text{back}} \mathcal{D}$ in each of the tagging categories. The difference between this fit and the nominal one is $12 \cdot 10^{-3}$, which we take to be the systematic uncertainty.

9.2.2 Lifetime of CP background

We assume that the Δt distribution of the CP background has the same lifetime as the B^0 meson (~ 1.5 ps). We vary the assumed lifetime from 0.7 to 2.0 ps and assign a systematic uncertainty of $2 \cdot 10^{-3}$. The range of these variations are justified based on the lifetime of the background found in simulated B_{CP} decays and on the known lifetime of charm and B mesons.

9.2.3 Fraction of peaking background

The peaking background fractions for each CP mode, listed in Table 4.9, were determined using large samples of Monte Carlo simulation of inclusive $B^0 \rightarrow J/\psi X$ decays. We vary the fraction of each peaking background fraction

by $\pm 1\sigma$ for all the CP decay mode simultaneously to also account for any systematic bias in the procedure used to measure these fractions. The systematic uncertainty is found to be $6.0 \cdot 10^{-3}$.

We repeat this procedure varying the amount of peaking background in the B_{flav} sample (see Sec 4.6.1) and find no change in the measured value of $\sin 2\beta$.

9.2.4 Signal probability determination

We evaluate the systematic effect of the measurement of the event-by-event probability determined by fitting the m_{ES} distribution on the value of $\sin 2\beta$. We measure a global probability for all events with $m_{ES} > 5.27 \text{ GeV}/c^2$. We assign this probability to all events in the signal region while the probability for all events with $m_{ES} < 5.27 \text{ GeV}/c^2$ is set to zero. We compare $\sin 2\beta$ measured using these probabilities (default fit) to $\sin 2\beta$ measured with fits where this signal probability is varied by one sigma. The signal probability for the CP sample and for the flavor-eigenstate sample is varied independently. The variation in $\sin 2\beta$ is reported in Table 9.2. The systematic uncertainty for the CP (B_{flav}) found to be $7 \cdot 10^{-3}$ ($1 \cdot 10^{-3}$).

Variation	$\delta \sin 2\beta$
$+\Delta CP$ prob	+0.007
$-\Delta CP$ prob	+0.006
$+\Delta B_{flav}$ prob	-0.001
$-\Delta B_{flav}$ prob	+0.001

Table 9.2: Change in $\sin 2\beta$ ($\delta \sin 2\beta$) resulting from variations in the event-by-event signal probability determination.

9.2.5 m_{ES} endpoint

The m_{ES} endpoint of the ARGUS component of the fit to the m_{ES} distribution is fixed to $5.291 \text{ GeV}/c^2$ in the nominal fit as described in Sec. 4.4.

We vary this by $\pm 0.002 \text{ GeV}/c^2$ to determine the systematic uncertainty. The magnitude of this variation is set by the $\sim 2 \text{ MeV}$ resolution of the energy of the beam in the c.m. frame as described in Sec. 2.1. The variation in the fitted value of $\sin 2\beta$ is shown in Table 9.3. We choose the largest variation ($1 \cdot 10^{-3}$) as the systematic uncertainty.

Variation	$\delta \sin 2\beta$
$E_{\text{beam}} = 5.289 \text{ GeV}/c^2$	+0.000
$E_{\text{beam}} = 5.281 \text{ GeV}/c^2$	+0.001

Table 9.3: Systematic uncertainty due to the m_{ES} endpoint of the ARGUS fit.

9.2.6 Background resolution function

The nominal fit assumes that the background Δt resolution function is adequately described using the sum of two Gaussians. We measure $\sin 2\beta$ using a background resolution function for the B_{CP} and B_{flav} likelihoods that is the sum of three Gaussians and find the difference with the nominal fit to be $6 \cdot 10^{-3}$.

9.2.7 Mixing component of background B_{flav} lifetime

The parameterization of the background B_{flav} lifetime does not include a $\cos(\Delta m_d \Delta t)$ contribution from mixing (see Eqn 7.3.7). To determine the systematic uncertainty, we assume that this background contribution mixes maximally with frequency Δm_d . The difference in $\sin 2\beta$ compared to the nominal fit is found to be $3 \cdot 10^{-3}$.

9.3 External parameters

In the nominal fit for $\sin 2\beta$, we fix the B^0 lifetime and the $B^0-\bar{B}^0$ mixing frequency Δm_d to the world averages of $\tau(B^0) = 1.542 \pm 0.016 \text{ ps}$ and

$\Delta m_d = 0.489 \pm 0.008 \text{ ps}^{-1}$. The dependency of $\sin 2\beta$ on the values of these fixed parameters is determined by varying them in the fit. The behavior is linear in each case (see Fig. 9.1). The slope of $\sin 2\beta$ versus $\tau(B^0)$ (Δm_d) is found to be -0.23 ps^{-1} (-0.40 ps) and the associated systematic uncertainty is taken to be $4 \cdot 10^{-3}$ ($3 \cdot 10^{-3}$). The systematic uncertainty on $\sin 2\beta$ due to uncertainties in $\tau(B^0)$ and Δm_d correspond to 1σ variations of the world average values. Table 9.4 summarizes the results obtained when Δm_d and (or) $\tau(B^0)$ are allowed to float in the fit.

Fit	$\delta \sin 2\beta$	$\sigma_{\sin 2\beta}$	Δm_d (ps^{-1})	$\tau(B^0)$ (ps)
Nominal	-	0.074	0.489	1.542
Float Δm_d	0.017	0.072	0.530 ± 0.008	-
Float $\tau(B^0)$	0.004	0.073	-	1.561 ± 0.016
Float Δm_d & $\tau(B^0)$	0.015	0.072	0.532 ± 0.008	1.534 ± 0.017

Table 9.4: Variation in $\sin 2\beta$ and its error when Δm_d and (or) $\tau(B^0)$ are free parameters in the likelihood fit.

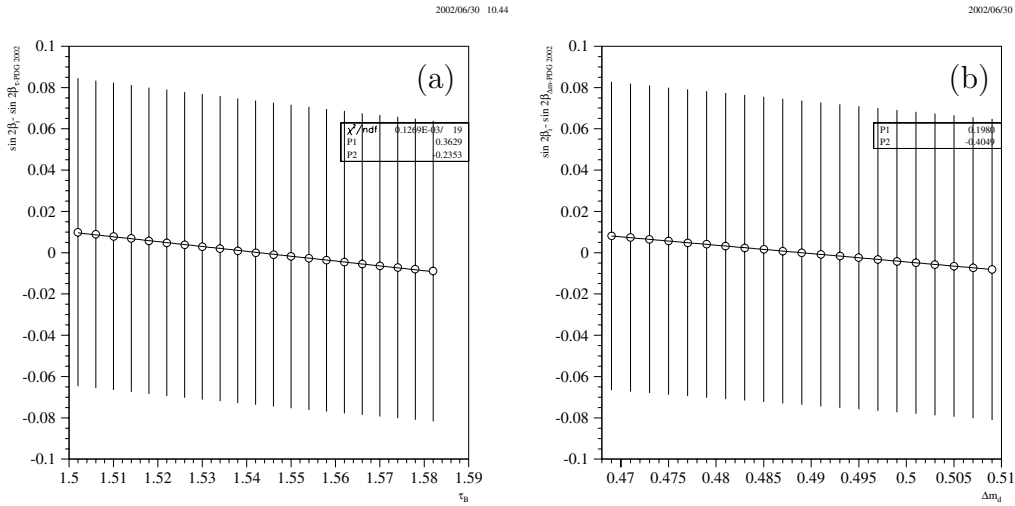


Figure 9.1: Dependence of $\sin 2\beta$ on (a) $\tau(B^0)$ and (b) Δm_d . The results are summarized in the text. Note that the errors are completely correlated for each data point.

9.4 Detector effects

Assumptions made about our knowledge of the location of the beam spot, length scale of the detector along the boost direction, and SVT alignment give rise to systematic uncertainties in the determination of $\sin 2\beta$.

9.4.1 Beam spot position

The vertexing algorithm uses the position of the beam spot as a constraint in determining the z location of the of the B_{tag} vertex. This constraint essentially comes from the y (vertical) position of the beam spot since its vertical size is only about $10 \mu\text{m}$. We evaluate the systematic uncertainty by varying the y position of the beam spot to ± 20 and $\pm 40 \mu\text{m}$ (the nominal position is usually $5 \mu\text{m}$) and by independently varying the width of the y position to 30 and $60 \mu\text{m}$. The systematic uncertainty is taken to be the maximal variation of $10 \cdot 10^{-3}$ that corresponds to shifting the y beam position by $+40 \mu\text{m}$.

9.4.2 SVT alignment

The misalignment of the SVT may cause a systematic uncertainty in our determination of $\sin 2\beta$. We have created different versions of the geometry representing the alignment of the silicon wafers with respect to each other that we use to reconstruct simulated decays. We evaluate how closely these geometries reflect the misalignment by comparing impact parameter measurements in the transverse and longitudinal plane as a function of azimuthal angle for tracks from dimuon events in data and the misaligned simulation. We choose a group of misalignments sets which accurately reproduce different azimuthal effects observed in data. We measure $\sin 2\beta$ in large samples of simulated B_{CP} decays that were generated with one alignment set and reconstructed with a separate alignment. We find that the systematic uncertainty corresponding to the average change in $\sin 2\beta$ is $10 \cdot 10^{-3}$.

9.4.3 Uncertainty on z scale

In Sec. 6.2, we described a check of the absolute scale z scale using proton tracks that has a precision of 0.2%. We evaluate the systematic uncertainty of the z scale by conservatively scaling the measured Δt and its error by 0.6% in data and Monte Carlo simulation. The effect on the measured value of $\sin 2\beta$ is estimated to be $1 \cdot 10^{-3}$.

9.5 Monte Carlo correction

In Sec. 7.6.3, the maximum-likelihood fit for $\sin 2\beta$ was found to be biased by 0.0138 ± 0.005 using 130 samples of simulated Monte Carlo B_{CP} decays with the same number of events in each decay mode as found in the data sample. As explained, we correct the measured value of $\sin 2\beta$ found in the data by -0.014. Studies have determined an effect which partially accounts for this bias.

A portion of the bias is due to a correlation between the mistag rate and the Δt resolution that is not modeled in the likelihood function. Figure 9.2 shows the dilution as a function of $\sigma_{\Delta t}$ for each tagging category using samples of simulated B_{CP} decays. These distributions were fit with a polynomial of the form

$$\mathcal{D} = \mathcal{D}_0 + S\sigma_{\Delta t} \quad (9.5.1)$$

The results of the fit are given in Table 9.5. The correlation is most apparent in the Kaon I and Kaon II tagging categories.

It is found that the mistag rate for kaon tags and the event-by-event error $\sigma_{\Delta t}$ both depend inversely on $\sqrt{\sum p_t^2}$, where p_t is the transverse momentum with respect to the z axis of tracks from the B_{tag} decay. The mistag rate dependence originates from the kinematics of the physics sources for wrong-sign kaons. These sources, listed in Sec. 5.2.2, produces a spectrum of charged tracks that have smaller $\sqrt{\sum p_t^2}$ than B decays that produce a correct tag. The Δt resolution dependence originates from the $1/p_t^2$ dependence of σ_z for the

individual contributing tracks (i.e., the larger the transverse momentum of a track the less the uncertainty in determining its z vertex).

We have studied the impact of ignoring the correlation on $\sin 2\beta$ with toy and simulated Monte Carlo. In both cases, we fit several data-size samples for $\sin 2\beta$ twice: once using average dilutions factors with no $\sigma_{\Delta t}$ dependence and once with the linear model given in Eqn 9.5.1. The results of these studies are shown in Fig. 9.3. The distribution of the difference of $\sin 2\beta$ with and without the linear model from the toy Monte Carlo has a mean value of $6 \cdot 10^{-3}$ with an RMS of $6 \cdot 10^{-3}$, indicating that ignoring the correlation leads to a small positive bias on $\sin 2\beta$. The same distribution using the simulated Monte Carlo sample has a mean and RMS of $4 \cdot 10^{-3}$. We assign a systematic uncertainty of $10 \cdot 10^{-3}$ which is the difference between the observed bias in the full simulation ($14 \cdot 10^{-3}$) and the portion of it that is understood ($4 \cdot 10^{-3}$).

As a cross-check, we have performed the fit on the B_{CP} and B_{flav} data samples incorporating the linear $\sigma_{\Delta t}$ dependence and floating both \mathcal{D}_0 and S . The measured value of $\sin 2\beta$ changed by $1 \cdot 10^{-3}$ and its error was unchanged.

Category	\mathcal{D}_0	S
Lepton	0.95 ± 0.01	-0.02 ± 0.02
Kaon I	0.92 ± 0.01	-0.20 ± 0.02
Kaon II	0.70 ± 0.01	-0.17 ± 0.02
Inclusive	0.45 ± 0.01	-0.10 ± 0.02

Table 9.5: Dilution as a function of $\sigma_{\Delta t}$ from the linear fits to simulated B_{CP} decays shown in Fig. 9.2.

9.6 Doubly-CKM-suppressed $b \rightarrow u$ transitions

In Eqn 1.8.3, we wrote down the time-dependent amplitude for one B meson to decay to a CP -eigenstate and one to decay to a state which uniquely tagged its flavor. This equation was the basis for the subsequent time-dependent

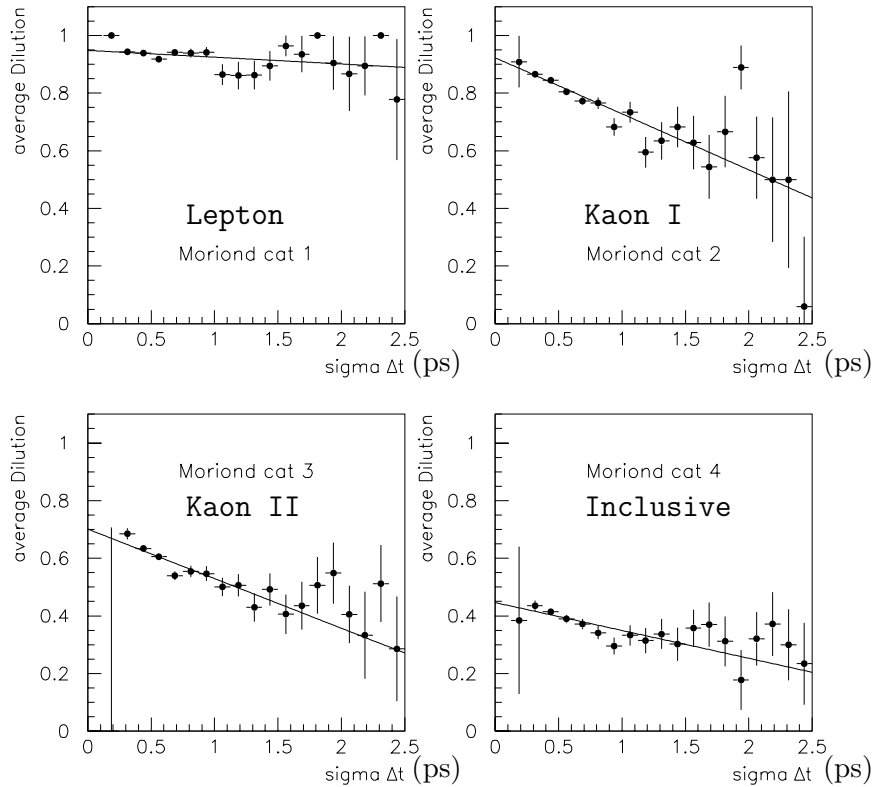


Figure 9.2: Dilution as a function of $\sigma_{\Delta t}$ from a large sample of simulated B_{CP} decays for the four tagging categories. The shape of the $\sigma_{\Delta t}$ distribution is shown in Fig. 6.6.

distributions that were developed for tagged B_{CP} and B_{flav} decays. However, the assumption that the final state uniquely tags the flavor of a B meson is not correct for all the final states that are used for tagging in this analysis. For example, we assume that the decay $D^-\pi^+$ is completely dominated by the favored B^0 decay amplitude and that the doubly-CKM (DCKM) suppressed decay amplitude for $\bar{B}^0 \rightarrow D^-\pi^+$ is negligible. The Feynman diagrams for these decays are displayed in Fig. 9.4. The CKM-favored B^0 amplitude and the DCKM-suppressed \bar{B}^0 amplitude interfere and alter the time-dependent

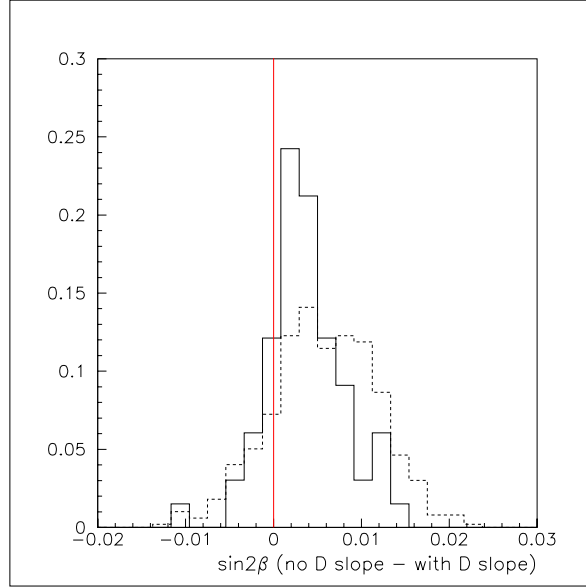


Figure 9.3: The difference in the value of $\sin 2\beta$ comparing fits with and without the linear $\sigma_{\Delta t}$ dilution dependence. The solid (dashed) distribution is from simulated (toy) Monte Carlo samples.

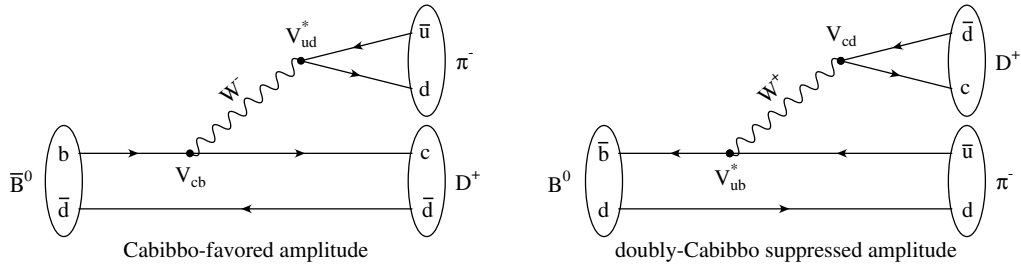


Figure 9.4: The CKM favored and suppressed Feynman diagrams for the final state $D^-\pi^+$

coherent evolution of the $B^0-\bar{B}^0$ system. In addition, the reconstructed B mesons in the flavor-eigenstate sample do not uniquely tag the B_{rec} flavor when we account for the DCKM decay amplitudes.

We need to determine how the neglected interference terms affect the measured value of $\sin 2\beta$. Following the work presented in Ref. [77], we denote the

amplitudes for various $B \rightarrow D\pi$ decays

$$\begin{aligned}
A(B^0 \rightarrow D^- \pi^+) &= a \\
A(\bar{B}^0 \rightarrow D^- \pi^+) &= ar e^{-i\gamma} e^{i\delta} \\
A(B^0 \rightarrow D^+ \pi^-) &= ar e^{+i\gamma} e^{i\delta} \\
A(\bar{B}^0 \rightarrow D^+ \pi^-) &= a
\end{aligned}$$

where a and r are real numbers and δ is the strong phase difference between the CKM-favored and DCKM-suppressed amplitude. We can estimate r as

$$r = \frac{V_{ub}V_{cd}^*}{V_{ud}V_{cb}^*} = 0.020 \pm 0.004 \quad (9.6.1)$$

It can also be shown [77] that the probability distribution function for a tagged event in which a B meson decays to a CP -eigenstate is given by

$$\begin{aligned}
R_{\pm} \propto & e - \Gamma|\Delta t| \left\{ (1 + r^2) - 2r \cos(2\beta + \gamma \pm \delta) \right. \\
& - \cos \Delta m_d \Delta t [2r \sin(2\beta) \sin(2\beta + \gamma \pm \delta)] \\
& \left. \pm \sin \Delta m_d \Delta t [(1 - r^2) \sin(2\beta)] \right\}
\end{aligned}$$

We recover the signal probability distribution given by Eqn 1.8.3 in the limit that $r \rightarrow 0$. We note that semileptonic B decays do not suffer from DCKM-suppressed $b \rightarrow u$ contributions so $r = 0$ for these events. Events in the lepton category are almost all (95%) from semileptonic B_{tag} decays. A fraction of events in the other tag categories also contain semileptonic B_{tag} decays that are unaffected by DCKM decays (11% to 19%).

It can be shown [78] that the bias on $\sin 2\beta$ when the interference terms from the DCKM-suppressed tag-side decays are ignored can be written as

$$\Delta \sin 2\beta \approx -r \sin(\gamma - 1.0) \cos \delta \quad (9.6.2)$$

By studying toy Monte Carlo samples generated with different conservative values of strong phase shifts and $r = 0.02$, we assign a systematic uncertainty of $8 \cdot 10^{-3}$.

9.7 Total systematic uncertainty

Adding in quadrature the uncorrelated systematic uncertainties from uncertainties in the signal parameters (Sec. 9.1), background parameters (Sec. 9.2), external parameters (Sec. 9.3), detector effects (Sec. 9.4), simulated Monte Carlo statistics (Sec. 9.5), and DCKM-suppressed decays (Sec. 9.6), we find the total systematic uncertainty is $30 \cdot 10^{-3}$. This is more than a factor of two less than the statistical error of $74 \cdot 10^{-3}$. A summary of all the systematic uncertainty contributions is given in Table 9.6.

9.8 Additional validation studies

The $\sin 2\beta$ measurement was repeated using alternative vertexing, tagging, and reconstruction configurations. These alternative configurations do not represent additional systematic sources of uncertainty. They merely represent different methods we might have employed in the measurement that are useful in comparison with the nominal fit to ensure robustness of the analysis procedure. The different configurations are listed below:

- Determine the B_{CP} vertex using a mass constrained charmonium candidate;
- Use the charmonium candidate vertex for the B_{CP} vertex;
- Remove the K_s^0 mass constraint;
- Remove bremsstrahlung photons from the charmonium candidate;
- Do not use constraints from the beam momentum in determining Δz ;
- Do not use constraints from the beam spot in determining Δz ;
- Do not veto tracks consistent with originating from photon conversions in tracking material when determining the B_{tag} vertex;

Source		CP sample
Signal parameters		
Shared B_{CP}/B_{flav} dilutions	[9.1.1]	± 0.012
Shared B_{CP}/B_{flav} Δt res fcn	[9.1.2]	± 0.002
Δt resolution fcn outliers	[9.1.2]	± 0.005
Δt resolution fcn tail scale factor	[9.1.2]	± 0.002
Δt resolution fcn model	[9.1.3]	± 0.006
Δt right/wrong sign res	[9.1.4]	± 0.0008
Background parameters		
CP background CP content (lifetime)	[9.2.1]	± 0.012
CP background CP content (Peak)	[9.2.1]	± 0.005
CP background τ	[9.2.2]	± 0.002
Fraction of CP peaking background	[9.2.3]	± 0.006
Fraction of B_{flav} peaking background	[9.2.3]	0
Signal probability: CP sample	[9.2.4]	± 0.007
Signal probability: B_{flav} sample	[9.2.4]	± 0.001
M_{ES} endpoint	[9.2.5]	± 0.001
Background resolution	[9.2.6]	± 0.006
B_{flav} background mixing contrib.	[9.2.7]	± 0.003
External parameters		
B^0 lifetime	[9.3]	± 0.004
Δm_d	[9.3]	± 0.003
Detector effects		
Beam spot	[9.4.1]	± 0.010
SVT alignment	[9.4.2]	± 0.010
z scale + boost	[9.4.3]	± 0.001
Monte Carlo correction	[9.5]	-0.014 ± 0.010
DCKM-suppressed decays	[9.6]	± 0.008
Total systematic uncertainty		± 0.030
Statistical error		± 0.074

Table 9.6: Summary of contributions to the systematic uncertainty on $\sin 2\beta$.

- Compute Δt as $\Delta z / \langle \gamma \beta \rangle$ (“boost approximation”);
- Use a different vertexing algorithm (“FvtClusterer”).

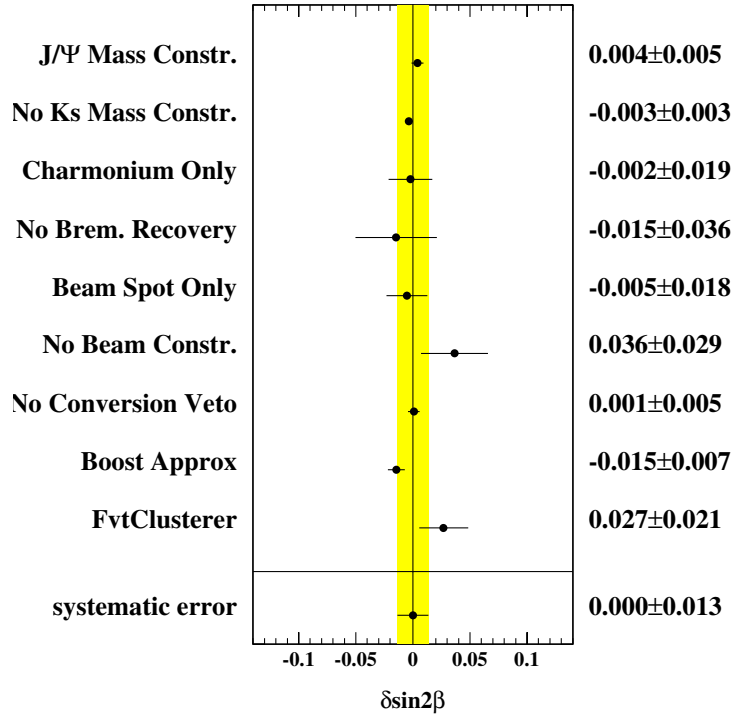


Figure 9.5: Variation in $\sin 2\beta$ ($\delta(\sin 2\beta)$) compared to the nominal fit for various alternative vertexing, tagging, and reconstruction configurations. The band around zero corresponds to the quadrature systematic error of the Δt resolution function description and SVT misalignment.

For the first four configurations listed, the resolution function and dilution parameters were fixed to their values determined in the nominal fit (listed in Table 8.5) and no B_{flav} sample was used. For the remaining five items, the B_{flav} data sample was processed with the alternative configurations and was used in the full maximum-likelihood fit for consistency. Only events that were common to the nominal data sample and the sample processed with the alternative configurations were used in the likelihood fit. The difference between the value of $\sin 2\beta$ measured with the new configuration compared to the nominal fit is shown in Fig. 9.5. The statistical error on the difference was computed using the *kin* method that is described in detail in Ref. [79].

Chapter 10

Conclusion

Using a data sample of about 88 million $\Upsilon(4S) \rightarrow B\bar{B}$ decays collected at the PEP-II asymmetric-energy B Factory at SLAC between 1999 and 2002, we have observed a CP violating asymmetry in the proper time distribution of neutral B meson decays. We fully reconstruct one neutral B meson in the CP decay modes $J/\psi K_S^0$, $\psi(2S)K_S^0$, $\chi_{c1}K_S^0$, and $\eta_c K_S^0$, or in flavor-eigenstate decay modes and determine the flavor of the other neutral B meson at the time it decays mainly by using the charge of identified leptons and kaons. The value of the CP violating asymmetry amplitude $\sin 2\beta$ is determined from a simultaneous maximum-likelihood fit to the time-difference distribution of the flavor-eigenstate sample and a sample of about 1506 tagged neutral B meson decays to CP -eigenstate modes. We find

$$\sin 2\beta = 0.755 \pm 0.074(\text{stat}) \pm 0.030(\text{syst}), \quad (10.0.1)$$

demonstrating CP violation in the neutral B meson system. We also measure $\sin 2\beta$ in events with neutral B mesons that decay to $J/\psi K_L^0$ and $J/\psi K^{*0}$ ($K^{*0} \rightarrow K_S^0 \pi^0$) final states with CP eigenvalue -1 and 0.65 ± 0.07 respectively. Using the entire CP sample, we measure

$$\sin 2\beta = 0.741 \pm 0.067(\text{stat}) \pm 0.034(\text{syst}), \quad (10.0.2)$$

The results of this measurement have been published in Physics Review Letters [50].

The Belle collaboration in Japan has also recently updated their measurement of $\sin 2\beta$ with a similarly sized data sample of B^0 mesons collected at the $\Upsilon(4S)$ resonance. They find [51] $\sin 2\beta = 0.719 \pm 0.074(\text{stat}) \pm 0.035(\text{syst})$, which is in good agreement with the *BABAR* measurement. Fig. 10.1 displays the various measurements of $\sin 2\beta$ compared to the current world-average of 0.734 ± 0.055 .

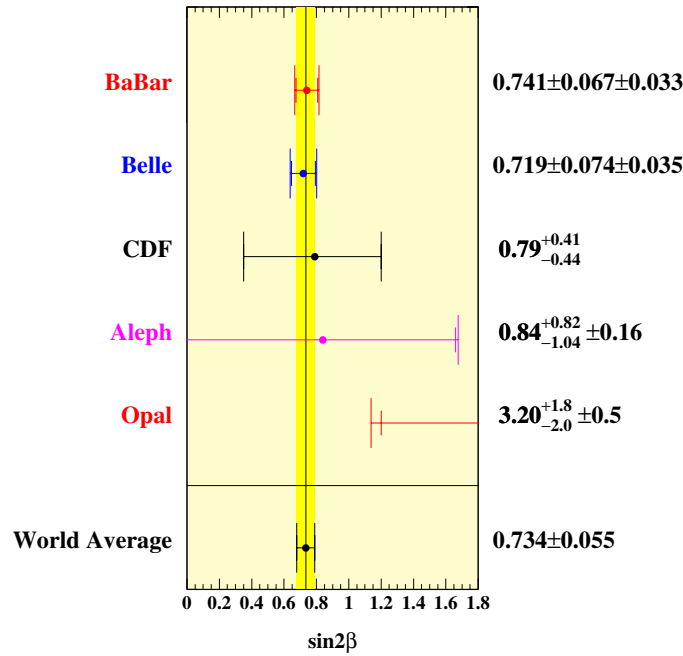


Figure 10.1: Comparison of $\sin 2\beta$ measurements with the current world-average. The results from *BABAR* and Belle dominate the world-average and are in good agreement.

10.1 Interpretation

Important conclusions may be drawn from our (along with Belle's) measurement of $\sin 2\beta$ concerning CP violation in the Standard Model. The result firmly establishes the existence of CP violating effects in the neutral B^0 meson system. Further, the Kobayashi-Maskawa (KM) mechanism of CP violation has successfully passed its first precision test [80]. This implies that the KM mechanism is most likely the dominant source of CP violation in flavor changing processes. In Sec. 1.9, we reviewed the constraints on the apex of the unitarity triangle in the $(\bar{\rho}, \bar{\eta})$ plane from the CP conserving observables Δm_d , $|V_{ub}/V_{cb}|$, and Δm_s , as well as from the CP violating parameter ϵ_K . It was also shown how a measurement of $\sin 2\beta$ constrains this vertex up to a four-fold ambiguity. In Fig. 10.2a, the four solutions for β corresponding to our measured value of $\sin 2\beta$ are displayed in the $(\bar{\rho}, \bar{\eta})$ plane. We overlay these solutions with the other constraints in Fig. 10.2b and find that one solution for β is in excellent agreement with the other constraints.

A combined fit to the CP conserving and CP violating constraints shown in Fig. 10.2b finds that all processes are consistent with one value of the single CKM phase $\delta_{\text{CKM}} = 59^\circ \pm 13^\circ$ [11]. Alternative models to the KM mechanism have been proposed that assume ϵ_K is small because all CP violating effects are small. These models are naturally motivated within a supersymmetric framework [81]. However, the observation that δ_{CKM} is of order one excludes this idea unless one resorts to fine-tuning. Additionally, minimal left-right-symmetric models with spontaneous CP violation [82] are excluded [80].

10.2 Future measurements

Since 1999, the *BABAR* collaboration has published the result of its $\sin 2\beta$ measurement in journals on five separate occasions using a larger data sample for each publication. This abnormally fast reporting rate indicates that

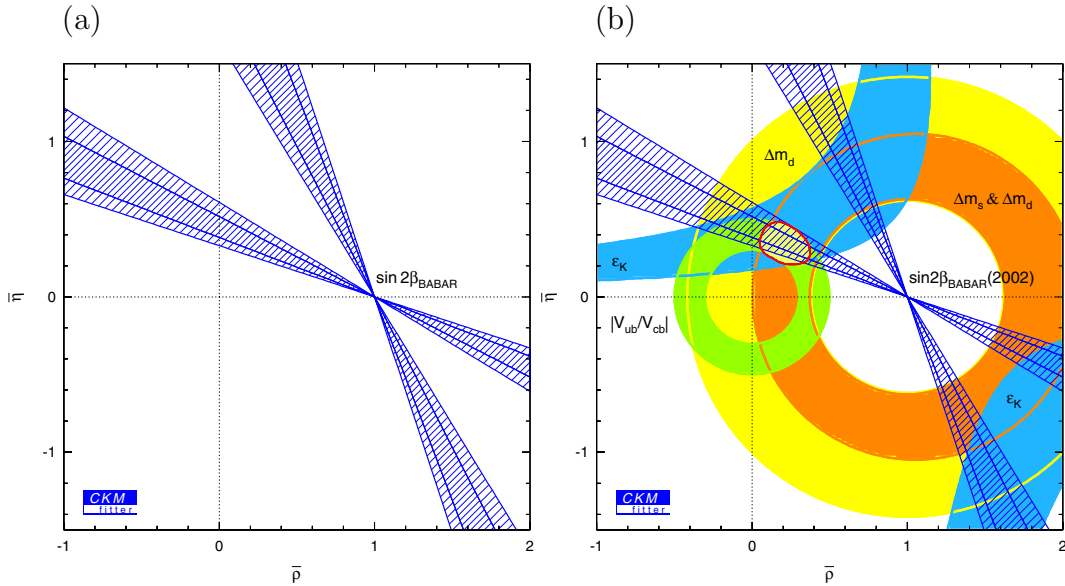


Figure 10.2: A comparison of (a) the four solutions of β in the $(\bar{\rho}, \bar{\eta})$ using our measured value of $\sin 2\beta$; and (b) the solutions overlaid with other CP -conserving and CP -violating constraints on the apex of the unitarity triangle. The inner-hatched (outer-hatched) band corresponds to the $\pm 1\sigma$ ($\pm 2\sigma$) uncertainty in β . We see that one solution for β is in good agreement with the other constraints. The constraints in the $(\bar{\rho}, \bar{\eta})$ plane from other measurements are discussed in detail in Sec. 1.9.

relatively minor ($\sim 20\%$) decreases in the uncertainty of $\sin 2\beta$ still provided enough new information to be considered relevant by the physics community at large. It appears that this phase has ended since the precision ($\sim 10\%$) of the latest result provides a strong case for the consistency of the KM mechanism. It is necessary to investigate at what data sample size the improved precision in the result again makes it compelling to report. The next major milestone for the detector is the accumulation of 500 fb^{-1} that is projected to occur around the end of 2006.

Fig. 10.3 shows the statistical error for each *BABAR* measurement as a function of luminosity assuming the usual \sqrt{N} dependence, where N is the number of signal events used to make the measurement. We see that successive measurements have always beaten the \sqrt{N} scaling. This occurred primarily be-

cause new CP final states were added, the reconstruction efficiency of $J/\psi K_s^0$ increased, the effective tagging efficiency increased, and the Δt resolution increased with improved understanding of the local SVT alignment. However, as it becomes increasingly more difficult to significantly beat this scaling, we assume that the only future improvement will be a 4% relative increase in Q . We then find that the statistical error on $\sin 2\beta$ using data sample of 500 fb^{-1} would be 0.026.

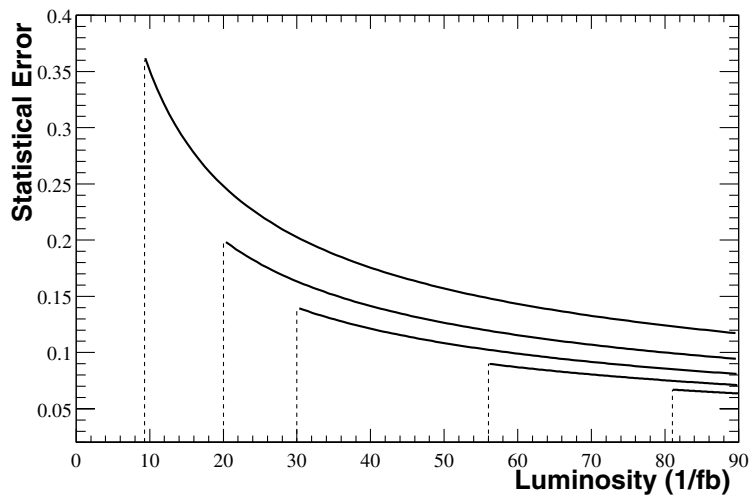


Figure 10.3: Statistical error on $\sin 2\beta$ from each *BABAR* measurement as a function of integrated luminosity. Successive measurements improved on the expected scaling of the statistical error due to improvements in the analysis procedure.

More guesswork is required to estimate the size of the systematic error with 500 fb^{-1} of data. Many of the systematic uncertainties scale with the square root of the data size until they reach an intrinsic asymptotic value. For example, this analysis quoted an uncertainty of 0.012 due to the assumption that there is no CP violation in the lifetime background of the CP sample. With 500 fb^{-1} of data, we could remove this assumption and include the CP eigenvalue of this background as a free parameter in the likelihood fit. This would clearly lessen the systematic error and shift some of it to the statistical error. Other

systematic uncertainties that could be decreased are due to the finite statistics of the Monte Carlo simulation, the assumption that the CP and B_{flav} samples share the same resolution function parameters, and the dependence on Δm_d and $\tau(B^0)$. It seems, however, that the asymptotic level of the systematic uncertainty from the SVT alignment, knowledge of the beam spot, and dilutions of the CP sample is about 0.02. At 500 fb^{-1} then, we estimate a systematic error of $0.02 - 0.03$.

We project that the statistical and systematic errors will be nearly the same with a data sample of 500 fb^{-1} (assuming no major changes to the analysis procedure). This implies that $\sin 2\beta$ would be measured to a precision of about 5%. It seems then that the most logical next step is to repeat this measurement with a 500 fb^{-1} data sample thereby improving the precision by a factor of two.

Appendix A

Spectroscopy of charmonium

This appendix is meant to serve as a reference for the η_c , J/ψ , $\psi(2S)$, and χ_{c1} charmonium mesons that are used to fully reconstruct decays of B mesons to CP eigenstates in this analysis.

The simultaneous discovery of a narrow vector meson, the J/ψ , in November of 1974 by experimental groups at SLAC and Brookhaven National Laboratory sparked tremendous excitement in the particle physics community [83, 84]. The leaders of the groups were jointly awarded the Nobel Prize for their discovery. At SLAC, the J/ψ was discovered as an enhancement in the e^+e^- cross section at a center of mass energy of about 3.1 GeV as shown in Fig. A.1. The excitement was generated primarily because the width of the J/ψ resonance was observed to be ~ 70 keV, about a factor of 1000 smaller than a typical hadronic width. The J/ψ was immediately interpreted as the lowest bound state of a new quark and antiquark, $c\bar{c}$ [85]. A second narrow resonance at 3.7 GeV, called the ψ' or $\psi(2S)$, was discovered about 10 days later by the SLAC group [86]. The large cross section observed in the e^+e^- channel at SLAC implied that the J/ψ and $\psi(2S)$ should have the same $J^{PC} = 1^{--}$ quantum numbers as the photon.

The J/ψ and $\psi(2S)$ have a relatively long lifetime because they are not massive enough to decay to two open charm mesons. They must decay through

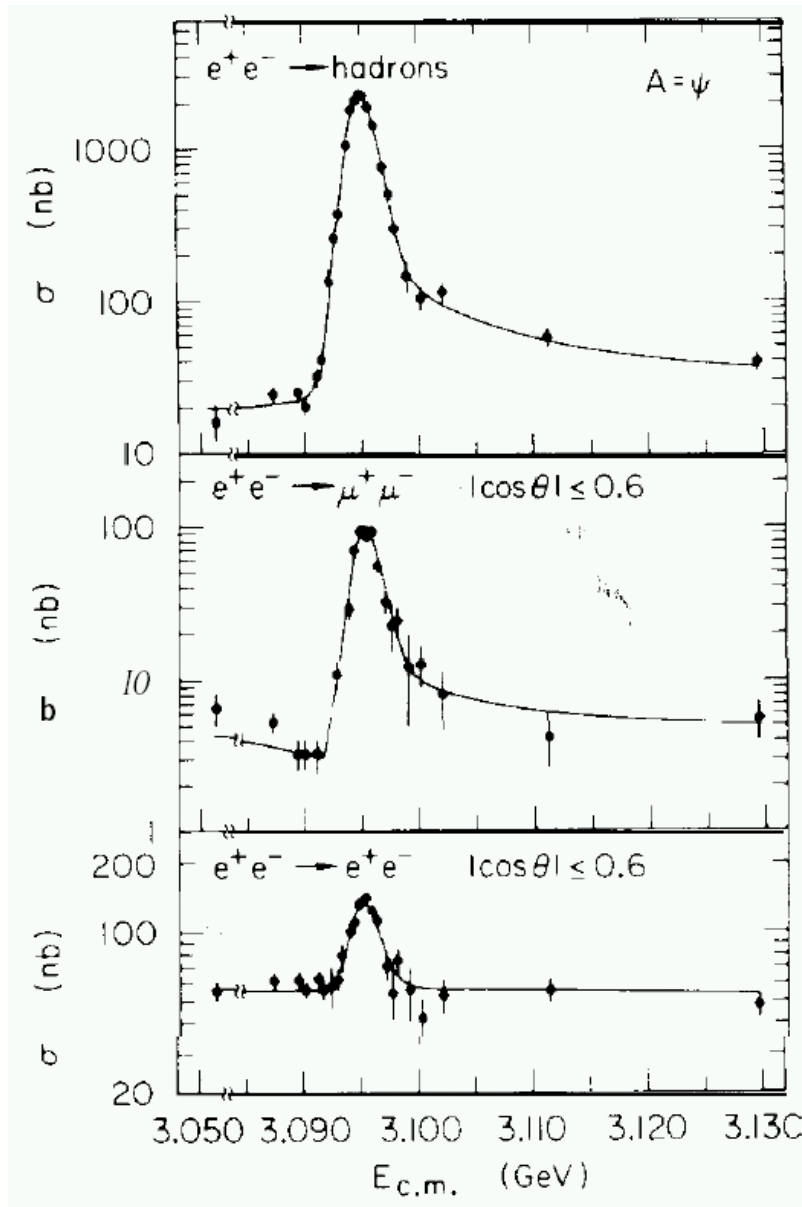


Figure A.1: Energy dependence of the cross-sections for (top) $e^+e^- \rightarrow \text{hadrons}$, (middle) $e^+e^- \rightarrow \mu^+ \mu^-$, and (bottom) $e^+e^- \rightarrow e^+e^-$ interactions near the J/ψ resonance. The observed widths are dominated by the intrinsic energy spread of the electron and positron beams, not by the true width of the J/ψ . (Fig. from B. Richter's 1976 Nobel Lecture [87])

annihilation of the $c\bar{c}$ pair which is suppressed due to a phenomenological se-

lection rule invented independently by Okubo, Zweig, and Iizuka [88] (OZI). The OZI rule postulates that disconnected quark diagrams are suppressed relative to connected ones. We note that the lowest gluonic intermediate state that has the right quantum numbers to couple to a 1^{--} particle has three gluons [89]. Since none of the gluons belong to the singlet representation of color $SU(3)$ (and the J/ψ is a color singlet) exchange of one gluon is excluded, and two gluon exchange is forbidden by charge conjugation conservation in strong decays. Consequently, the J/ψ and $\psi(2S)$ are narrow because conservation of energy and momentum force them to decay only through OZI suppressed channels.

The present experimental status of the spectroscopy of charmonium ($c\bar{c}$ bound states) is shown in Fig. A.2. This system can be described well using perturbative QCD methods and it has been studied extensively. The states are labeled by their spectroscopic classification $n^{2S+1}L_J$ where n is the radial excitation level, S is spin, L is orbital angular momentum, and J is total angular momentum. The η_c , J/ψ , and $\psi(2S)$ have $L = 0$, while the χ_{c1} has $L = 1$. The spin of the $c\bar{c}$ state is 0 for η_c , and 1 for $J/\psi, \psi(2S)$, and χ_{c1} . These charmonium mesons all have a CP -eigenvalue equal of 1 except for η_c which has a CP -eigenvalue of -1. However, the CP eigenvalue of a B^0 decay to any of these mesons and a K_s^0 is the same (-1). This is because the orbital angular momentum of the final state must be a P -wave ($L = 1$) for all the decays except for $B^0 \rightarrow \eta_c K_s^0$ (where $L = 0$) in order to conserve angular momentum¹. Table A.1 summarizes the properties of these $c\bar{c}$ mesons.

¹Recall that the parity of the final state goes like $(-1)^L$

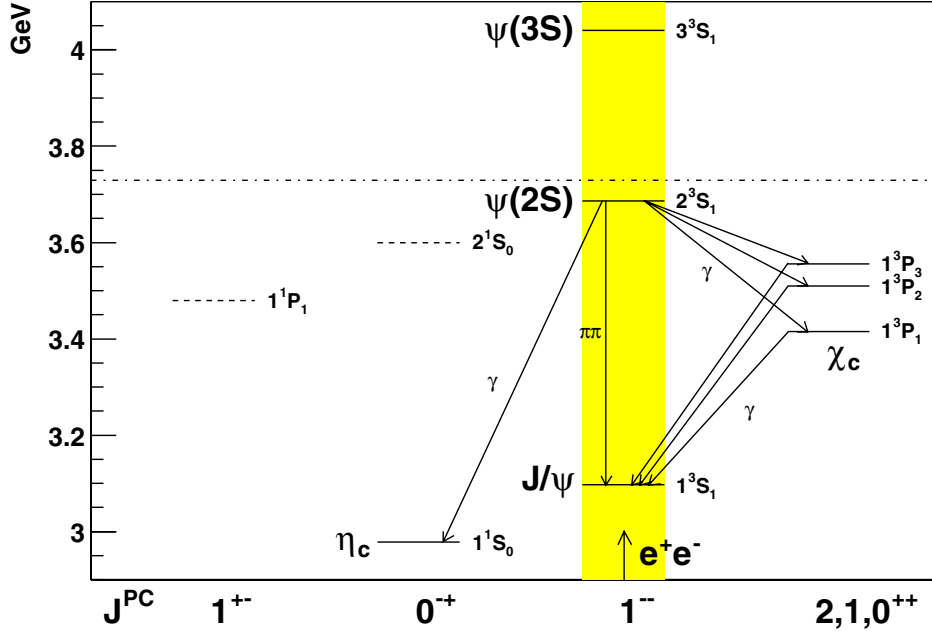


Figure A.2: The observed spectroscopy of charmonium mesons. The yellow band represents the meson which have the same quantum numbers as the photon and can therefore be directly produced by e^+e^- annihilation. The dot-dash line shows the threshold for decay to two open charm mesons. The spectroscopic classification $n^{2S+1}L_J$ and J^{PC} assignments are discussed in the text. The lines connecting different states represent decay by γ or $\pi\pi$ emission as indicated.

Particle	J^{PC}	Mass(MeV/ c^2)	Γ (MeV)	Decay Mode	Fraction(%)
η_c	0^{-+}	2979.7 ± 1.5	16.0 ± 3.6	$K\bar{K}\pi$	5.5 ± 1.7
J/ψ	1^{--}	3096.9 ± 0.04	0.087 ± 0.005	e^+e^-	5.93 ± 0.10
				$\mu^+ \mu^-$	5.88 ± 0.10
				hadrons	87.7 ± 0.5
χ_{c1}	1^{++}	3510.51 ± 0.12	0.92 ± 0.13	$J/\psi\gamma$	31.6 ± 3.2
				hadrons	< 3
$\psi(2S)$	1^{--}	3685.96 ± 0.09	0.300 ± 0.025	e^+e^-	0.73 ± 0.04
				$\mu^+ \mu^-$	0.70 ± 0.09
				$J/\psi \pi^+ \pi^-$	30.5 ± 1.6

Table A.1: Properties of the $\eta_c, J/\psi, \chi_{c1}$, and $\psi(2S)$ charmonium mesons.

Appendix B

BABAR author list

This appendix lists the authors in the *BABAR* collaboration.

The *BABAR* Collaboration,

B. Aubert, R. Barate, D. Boutigny, J.-M. Gaillard, A. Hicheur, Y. Karyotakis,
J. P. Lees, P. Robbe, V. Tisserand, A. Zghiche

Laboratoire de Physique des Particules, F-74941 Annecy-le-Vieux, France

A. Palano, A. Pompili

Università di Bari, Dipartimento di Fisica and INFN, I-70126 Bari, Italy

J. C. Chen, N. D. Qi, G. Rong, P. Wang, Y. S. Zhu

Institute of High Energy Physics, Beijing 100039, China

G. Eigen, I. Ofte, B. Stugu

University of Bergen, Inst. of Physics, N-5007 Bergen, Norway

G. S. Abrams, A. W. Borgland, A. B. Breon, D. N. Brown, J. Button-Shafer,
R. N. Cahn, E. Charles, M. S. Gill, A. V. Gritsan, Y. Groysman, R. G. Jacobsen,
R. W. Kadel, J. Kadyk, L. T. Kerth, Yu. G. Kolomensky, J. F. Kral, C. LeClerc,
M. E. Levi, G. Lynch, L. M. Mir, P. J. Oddone, T. J. Orimoto, M. Pripstein,

N. A. Roe, A. Romosan, M. T. Ronan, V. G. Shelkov, A. V. Telnov, W. A. Wenzel
*Lawrence Berkeley National Laboratory and University of California, Berkeley, CA
94720, USA*

T. J. Harrison, C. M. Hawkes, D. J. Knowles, S. W. O’Neale, R. C. Penny,
A. T. Watson, N. K. Watson
University of Birmingham, Birmingham, B15 2TT, United Kingdom

T. Deppermann, K. Goetzen, H. Koch, B. Lewandowski, M. Pelizaeus, K. Peters,
H. Schmuecker, M. Steinke
*Ruhr Universität Bochum, Institut für Experimentalphysik 1, D-44780 Bochum,
Germany*

N. R. Barlow, W. Bhimji, J. T. Boyd, N. Chevalier, P. J. Clark, W. N. Cottingham,
C. Mackay, F. F. Wilson
University of Bristol, Bristol BS8 1TL, United Kingdom

C. Hearty, T. S. Mattison, J. A. McKenna, D. Thiessen
University of British Columbia, Vancouver, BC, Canada V6T 1Z1

S. Jolly, P. Kyberd, A. K. McKemey
Brunel University, Uxbridge, Middlesex UB8 3PH, United Kingdom

V. E. Blinov, A. D. Bukin, A. R. Buzykaev, V. B. Golubev, V. N. Ivanchenko,
A. A. Korol, E. A. Kravchenko, A. P. Onuchin, S. I. Serednyakov, Yu. I. Skovpen,
A. N. Yushkov
Budker Institute of Nuclear Physics, Novosibirsk 630090, Russia

D. Best, M. Chao, D. Kirkby, A. J. Lankford, M. Mandelkern, S. McMahon,
R. K. Mommsen, D. P. Stoker
University of California at Irvine, Irvine, CA 92697, USA

K. Arisaka, C. Buchanan
University of California at Los Angeles, Los Angeles, CA 90024, USA

H. K. Hadavand, E. J. Hill, D. B. MacFarlane, H. P. Paar, Sh. Rahatlou, G. Raven,
U. Schwanke, V. Sharma

University of California at San Diego, La Jolla, CA 92093, USA

J. W. Berryhill, C. Campagnari, B. Dahmes, N. Kuznetsova, S. L. Levy, O. Long,
A. Lu, M. A. Mazur, J. D. Richman, W. Verkerke

University of California at Santa Barbara, Santa Barbara, CA 93106, USA

J. Beringer, A. M. Eisner, M. Grothe, C. A. Heusch, W. S. Lockman, T. Pulliam,
T. Schalk, R. E. Schmitz, B. A. Schumm, A. Seiden, M. Turri, W. Walkowiak,
D. C. Williams, M. G. Wilson

*University of California at Santa Cruz, Institute for Particle Physics, Santa Cruz,
CA 95064, USA*

J. Albert, E. Chen, G. P. Dubois-Felsmann, A. Dvoretzkii, D. G. Hitlin, I. Narsky,
F. C. Porter, A. Ryd, S. Yang

California Institute of Technology, Pasadena, CA 91125, USA

S. Jayatilke, G. Mancinelli, B. T. Meadows, M. D. Sokoloff

University of Cincinnati, Cincinnati, OH 45221, USA

T. Barillari, F. H. Blanc, P. Bloom, W. T. Ford, U. Nauenberg, A. Olivas,
P. Rankin, J. Roy, J. G. Smith, W. C. van Hoek, L. Zhang

University of Colorado, Boulder, CO 80309, USA

J. L. Harton, T. Hu, A. Soffer, W. H. Toki, R. J. Wilson, J. Zhang

Colorado State University, Fort Collins, CO 80523, USA

R. Aleksan, S. Emery, A. Gaidot, P.-F. Giraud, G. Hamel de Monchenault,
W. Kozanecki, M. Langer, G. W. London, B. Mayer, G. Schott, B. Serfass,
G. Vasseur, Ch. Yèche, M. Zito

*DAPNIA, Commissariat à l'Énergie Atomique/Saclay, F-91191 Gif-sur-Yvette,
France*

D. Altenburg, T. Brandt, J. Brose, T. Colberg, M. Dickopp, R. S. Dubitzky,
A. Hauke, E. Maly, R. Müller-Pfefferkorn, R. NOGOWSKI, S. Otto,
K. R. Schubert, R. Schwierz, B. Spaan, L. Wilden

*Technische Universität Dresden, Institut für Kern- und Teilchenphysik, D-01062
Dresden, Germany*

D. Bernard, G. R. Bonneaud, F. Brochard, J. Cohen-Tanugi, S. T’Jampens,
Ch. Thiebaux, G. Vasileiadis, M. Verderi

Ecole Polytechnique, LLR, F-91128 Palaiseau, France

A. Anjomshoaa, D. J. BARD, R. Bernet, A. Khan, D. Lavin, F. Muheim,
S. Playfer, J. E. Swain, J. Tinslay

University of Edinburgh, Edinburgh EH9 3JZ, United Kingdom

M. Falbo

Elon University, Elon University, NC 27244-2010, USA

C. Borean, C. Bozzi, L. Piemontese, A. Sarti

Università di Ferrara, Dipartimento di Fisica and INFN, I-44100 Ferrara, Italy

E. Treadwell

Florida A&M University, Tallahassee, FL 32307, USA

F. Anulli,¹ R. Baldini-Ferroli, A. Calcaterra, R. de Sangro, D. Falciai,
G. Finocchiaro, P. Patteri, I. M. Peruzzi,² M. Piccolo, A. Zallo

Laboratori Nazionali di Frascati dell’INFN, I-00044 Frascati, Italy

S. Bagnasco, A. Buzzo, R. Contri, G. Crosetti, M. Lo Vetere, M. Macri,
M. R. Monge, S. Passaggio, F. C. Pastore, C. Patrignani, E. Robutti, A. Santroni,
S. Tosi

Università di Genova, Dipartimento di Fisica and INFN, I-16146 Genova, Italy

¹Also with Università di Perugia, I-06100 Perugia, Italy

²Also with Università di Perugia, I-06100 Perugia, Italy

S. Bailey, M. Morii

Harvard University, Cambridge, MA 02138, USA

G. J. Grenier, U. Mallik

University of Iowa, Iowa City, IA 52242, USA

J. Cochran, H. B. Crawley, J. Lamsa, W. T. Meyer, S. Prell, E. I. Rosenberg, J. Yi

Iowa State University, Ames, IA 50011-3160, USA

M. Davier, A. Höcker, H. M. Lacker, S. Laplace, F. Le Diberder, V. Lepeltier,
A. M. Lutz, T. C. Petersen, S. Plaszczynski, M. H. Schune, L. Tantot, G. Wormser

Laboratoire de l'Accélérateur Linéaire, F-91898 Orsay, France

R. M. Bionta, V. Brigljević, D. J. Lange, M. Mugge, K. van Bibber, D. M. Wright

Lawrence Livermore National Laboratory, Livermore, CA 94550, USA

A. J. Bevan, J. R. Fry, E. Gabathuler, R. Gamet, M. George, M. Kay, D. J. Payne,
R. J. Sloane, C. Touramanis

University of Liverpool, Liverpool L69 3BX, United Kingdom

M. L. Aspinwall, D. A. Bowerman, P. D. Dauncey, U. Egede, I. Eschrich,
G. W. Morton, J. A. Nash, P. Sanders, G. P. Taylor

University of London, Imperial College, London, SW7 2BW, United Kingdom

J. J. Back, G. Bellodi, P. Dixon, P. F. Harrison, H. W. Shorthouse, P. Strother,
P. B. Vidal

Queen Mary, University of London, E1 4NS, United Kingdom

G. Cowan, H. U. Flaecher, S. George, M. G. Green, A. Kurup, C. E. Marker,
T. R. McMahon, S. Ricciardi, F. Salvatore, G. Vaitsas, M. A. Winter

*University of London, Royal Holloway and Bedford New College, Egham, Surrey
TW20 0EX, United Kingdom*

D. Brown, C. L. Davis

University of Louisville, Louisville, KY 40292, USA

J. Allison, R. J. Barlow, A. C. Forti, P. A. Hart, F. Jackson, G. D. Lafferty,
A. J. Lyon, N. Savvas, J. H. Weatherall, J. C. Williams

University of Manchester, Manchester M13 9PL, United Kingdom

A. Farbin, A. Jawahery, V. Lillard, D. A. Roberts

University of Maryland, College Park, MD 20742, USA

G. Blaylock, C. Dallapiccola, K. T. Flood, S. S. Hertzbach, R. Kofler,
V. B. Koptchev, T. B. Moore, H. Staengle, S. Willocq

University of Massachusetts, Amherst, MA 01003, USA

R. Cowan, G. Sciolla, F. Taylor, R. K. Yamamoto

*Massachusetts Institute of Technology, Laboratory for Nuclear Science, Cambridge,
MA 02139, USA*

M. Milek, P. M. Patel

McGill University, Montréal, QC, Canada H3A 2T8

F. Palombo

Università di Milano, Dipartimento di Fisica and INFN, I-20133 Milano, Italy

J. M. Bauer, L. Cremaldi, V. Eschenburg, R. Kroeger, J. Reidy, D. A. Sanders,
D. J. Summers, H. Zhao

University of Mississippi, University, MS 38677, USA

C. Hast, P. Taras

*Université de Montréal, Laboratoire René J. A. Lévesque, Montréal, QC, Canada
H3C 3J7*

H. Nicholson

Mount Holyoke College, South Hadley, MA 01075, USA

C. Cartaro, N. Cavallo, G. De Nardo, F. Fabozzi,³ C. Gatto, L. Lista, P. Paolucci,
D. Piccolo, C. Sciacca

*Università di Napoli Federico II, Dipartimento di Scienze Fisiche and INFN,
I-80126, Napoli, Italy*

J. M. LoSecco

University of Notre Dame, Notre Dame, IN 46556, USA

J. R. G. Alsmiller, T. A. Gabriel

Oak Ridge National Laboratory, Oak Ridge, TN 37831, USA

B. Brau

Ohio State Univ., 174 W.18th Ave., Columbus, OH 43210

J. Brau, R. Frey, M. Iwasaki, C. T. Potter, N. B. Sinev, D. Strom, E. Torrence

University of Oregon, Eugene, OR 97403, USA

F. Colecchia, A. Dorigo, F. Galeazzi, M. Margoni, M. Morandin, M. Posocco,
M. Rotondo, F. Simonetto, R. Stroili, G. Tiozzo, C. Voci

Università di Padova, Dipartimento di Fisica and INFN, I-35131 Padova, Italy

M. Benayoun, H. Briand, J. Chauveau, P. David, Ch. de la Vaissière, L. Del Buono,
O. Hamon, Ph. Leruste, J. Ocariz, M. Pivk, L. Roos, J. Stark

*Universités Paris VI et VII, Lab de Physique Nucléaire H. E., F-75252 Paris,
France*

P. F. Manfredi, V. Re, V. Speziali

Università di Pavia, Dipartimento di Elettronica and INFN, I-27100 Pavia, Italy

L. Gladney, Q. H. Guo, J. Panetta

University of Pennsylvania, Philadelphia, PA 19104, USA

C. Angelini, G. Batignani, S. Bettarini, M. Bondioli, F. Bucci, G. Calderini,
E. Campagna, M. Carpinelli, F. Forti, M. A. Giorgi, A. Lusiani, G. Marchiori,

³Also with Università della Basilicata, I-85100 Potenza, Italy

F. Martinez-Vidal, M. Morganti, N. Neri, E. Paoloni, M. Rama, G. Rizzo,
F. Sandrelli, G. Triggiani, J. Walsh

Università di Pisa, Scuola Normale Superiore and INFN, I-56010 Pisa, Italy

M. Haire, D. Judd, K. Paick, L. Turnbull, D. E. Wagoner

Prairie View A&M University, Prairie View, TX 77446, USA

G. Cavoto,⁴ N. Danielson, P. Elmer, C. Lu, V. Miftakov, J. Olsen, A. J. S. Smith,
A. Tumanov, E. W. Varnes

Princeton University, Princeton, NJ 08544, USA

F. Bellini, D. del Re, R. Faccini,⁵ F. Ferrarotto, F. Ferroni, M. Gaspero,
E. Leonardi, M. A. Mazzoni, S. Morganti, G. Piredda, F. Safai Tehrani, M. Serra,
C. Voena

*Università di Roma La Sapienza, Dipartimento di Fisica and INFN, I-00185 Roma,
Italy*

S. Christ, G. Wagner, R. Waldi

Universität Rostock, D-18051 Rostock, Germany

T. Adye, N. De Groot, B. Franek, N. I. Geddes, G. P. Gopal, E. O. Olaiya,
S. M. Xella

*Rutherford Appleton Laboratory, Chilton, Didcot, Oxon, OX11 0QX, United
Kingdom*

M. V. Purohit, F. X. Yumiceva

University of South Carolina, Columbia, SC 29208, USA

K. Abe,⁶ D. Aston, R. Bartoldus, N. Berger, A. M. Boyarski, O. L. Buchmueller,
M. R. Convery, D. P. Coupal, D. Dong, J. Dorfan, W. Dunwoodie, R. C. Field,
T. Glanzman, S. J. Gowdy, E. Grauges-Pous, T. Hadig, V. Halyo, T. Himel,

⁴Also with Università di Roma La Sapienza, Dipartimento di Fisica and INFN, I-00185 Roma, Italy

⁵Also with University of California at San Diego, La Jolla, CA 92093, USA

⁶Also with University of British Columbia, Vancouver, BC, Canada V6T 1Z1

T. Hryn'ova, M. E. Huffer, W. R. Innes, C. P. Jessop, M. H. Kelsey, P. Kim,
M. L. Kocian, U. Langenegger, D. W. G. S. Leith, S. Luitz, V. Luth, H. L. Lynch,
H. Marsiske, S. Menke, R. Messner, D. R. Muller, C. P. O'Grady, V. E. Ozcan,
A. Perazzo, M. Perl, S. Petrak, B. N. Ratcliff, S. H. Robertson, A. Roodman,
A. A. Salnikov, T. Schietinger, R. H. Schindler, J. Schwiening, G. Simi, A. Snyder,
A. Soha, J. Stelzer, D. Su, M. K. Sullivan, H. A. Tanaka, J. Va'vra, S. R. Wagner,
M. Weaver, A. J. R. Weinstein, W. J. Wisniewski, D. H. Wright, C. C. Young

Stanford Linear Accelerator Center, Stanford, CA 94309, USA

P. R. Burchat, C. H. Cheng, T. I. Meyer, C. Roat

Stanford University, Stanford, CA 94305-4060, USA

R. Henderson

TRIUMF, Vancouver, BC, Canada V6T 2A3

W. Bugg, M. Krishnamurthy, S. M. Spanier

University of Tennessee, Knoxville, TN 37996, USA

J. M. Izen, I. Kitayama, X. C. Lou

University of Texas at Dallas, Richardson, TX 75083, USA

F. Bianchi, M. Bona, D. Gamba

*Università di Torino, Dipartimento di Fisica Sperimentale and INFN, I-10125
Torino, Italy*

L. Bosisio, G. Della Ricca, S. Dittongo, L. Lanceri, P. Poropat, L. Vitale,
G. Vuagnin

Università di Trieste, Dipartimento di Fisica and INFN, I-34127 Trieste, Italy

R. S. Panvini

Vanderbilt University, Nashville, TN 37235, USA

Sw. Banerjee, C. M. Brown, D. Fortin, P. D. Jackson, R. Kowalewski, J. M. Roney

University of Victoria, Victoria, BC, Canada V8W 3P6

H. R. Band, S. Dasu, M. Datta, A. M. Eichenbaum, H. Hu, J. R. Johnson, R. Liu,
F. Di Lodovico, A. K. Mohapatra, Y. Pan, R. Prepost, S. J. Sekula, J. H. von
Wimmersperg-Toeller, J. Wu, S. L. Wu, Z. Yu
University of Wisconsin, Madison, WI 53706, USA

H. Neal
Yale University, New Haven, CT 06511, USA

Bibliography

- [1] S.L. Glashow, Nucl. Phys. **22**, 579 (1961);
S. Weinberge, Phys. Rev. Lett. **19**, 1264 (1967);
A. Salam, in *Proceedings of the 8th Nobel Symposiom*, ed. N. Swartholm,
Almquist and Wiksells, Stockholm (1968).
- [2] M. Kobayashi and T. Maskawa, Prog. Theor. Phys. **49**, 652 (1973).
- [3] The so called *strong CP problem* and its proposed solutions are reviewed by
R. D. Peccei in *CP Violation*, ed. C. Jarlskog, World Scientific Publishing
Company (1989).
- [4] J. H. Christenson, J. W. Cronin, V. L. Fitch and R. Turlay, Phys. Rev.
Lett. **13**, 138 (1964).
- [5] G. D. Barr *et al.* [NA31 Collaboration], Phys. Lett. B **317**, 233 (1993);
L. K. Gibbons *et al.*, Phys. Rev. Lett. **70**, 1203 (1993).
- [6] M. Gell-Mann, Phys. Lett. **8**, 214 (1964).
- [7] G. Zweig, CERN-TH-412
- [8] F. Abe *et al.* [CDF Collaboration], Phys. Rev. D **50**, 2966 (1994).
- [9] K. Kodama, *et al.* [DONUT Collaboration], Phys. Lett. B **504** 218 (2001).
- [10] Q. R. Ahmad *et al.* [SNO Collaboration], Phys. Rev. Lett. **87**, 071301
(2001) [arXiv:nucl-ex/0106015];

- Q. R. Ahmad *et al.* [SNO Collaboration], Phys. Rev. Lett. **89**, 011301 (2002) [arXiv:nucl-ex/0204008];
- K. Eguchi *et al.* [KamLAND Collaboration], Phys. Rev. Lett. **90**, 021802 (2003) [arXiv:hep-ex/0212021].
- [11] Particle Data Group, K. Hagiwara *et al.*, Phys. Rev. D **66**, 010001 (2002).
This reference is used for all measured physical parameters, unless explicitly stated otherwise.
- [12] D. J. Gross and F. Wilczek, Phys. Rev. Lett. **30**, 1343 (1973).
H. D. Politzer, Phys. Rev. Lett. **30**, 1346 (1973).
- [13] E. Noether, Nachr. v. d. Ges. d. Wiss. zu Göttingen 235 (1918)
- [14] M. E. Peskin and D. V. Schroeder, *An Introduction to Quantum Field Theory*, Addison-Wesley Publishing Company (1995).
- [15] There are many reviews of this subject. See, for example, W. Bernreuther, Lect. Notes Phys. **591**, 237 (2002) [arXiv:hep-ph/0205279].
A. D. Dolgov, Phys. Rept. **222**, 309 (1992).
V. A. Rubakov and M. E. Shaposhnikov, Usp. Fiz. Nauk **166**, 493 (1996) [Phys. Usp. **39**, 461 (1996)] [arXiv:hep-ph/9603208].
- [16] T. Saeki *et al.*, Phys. Lett. B **422**, 319 (1998) [arXiv:astro-ph/9710228].
T. Sanuki *et al.*, Astrophys. J. **545**, 1135 (2000) [arXiv:astro-ph/0002481].
J. Alcaraz *et al.* [AMS Collaboration], Phys. Lett. B **461**, 387 (1999) [arXiv:hep-ex/0002048].
- [17] A. G. Cohen, A. De Rujula and S. L. Glashow, Astrophys. J. **495**, 539 (1998) [arXiv:astro-ph/9707087].
- [18] A. D. Sakharov, Pisma Zh. Eksp. Teor. Fiz. **5**, 32 (1967) [JETP Lett. **5**, 24 (1967 SOPUA,34,392-393.1991 UFNAA,161,61-64.1991)].

- [19] See, for example, A. G. Cohen, D. B. Kaplan and A. E. Nelson, *Ann. Rev. Nucl. Part. Sci.* **43**, 27 (1993) [arXiv:hep-ph/9302210].
- [20] M. E. Shaposhnikov, *JETP Lett.* **44**, 465 (1986) [*Pisma Zh. Eksp. Teor. Fiz.* **44**, 364 (1986)].
- [21] W. Buchmuller, Z. Fodor and A. Hebecker, *Nucl. Phys. B* **447**, 317 (1995) [arXiv:hep-ph/9502321].
Z. Fodor, J. Hein, K. Jansen, A. Jaster and I. Montvay, *Nucl. Phys. B* **439**, 147 (1995) [arXiv:hep-lat/9409017]. K. Rummukainen, M. Tsypin, K. Kajantie, M. Laine and M. E. Shaposhnikov, *Nucl. Phys. B* **532**, 283 (1998) [arXiv:hep-lat/9805013].
- [22] E. Fermi, *Nuovo Cim.* **11**, 1 (1934).
- [23] T. D. Lee and C. N. Yang, *Phys. Rev.* **104**, 254 (1956).
- [24] C. S. Wu, E. Ambler, R. W. Haywood, D. D. Hoppes, and R. P. Hudson, *Phys. Rev.* **105**, 1413 (1957).
- [25] L. D. Landau, *Nucl. Phys.* **3**, 127 (1957).
T. D. Lee, R. Oehme and C. N. Yang, *Phys. Rev.* **106**, 340 (1957).
- [26] V. L. Fitch, *Rev. Mod. Phys.* **53**, 373 (1981).
- [27] N. Cabibbo, *Phys. Rev. Lett.* **10**, 531 (1963).
- [28] S. L. Glashow, J. Iliopoulos and L. Maiani, *Phys. Rev. D* **2**, 1285 (1970).
- [29] G. C. Branco, L. Lavoura, and J. P. Silva, *CP Violation*, Clarendon Press (1999).
- [30] P. F. Harrison and H. R. Quinn [BABAR Collaboration], SLAC-R-0504
Papers from Workshop on Physics at an Asymmetric B Factory (BaBar

Collaboration Meeting), Rome, Italy, 11-14 Nov 1996, Princeton, NJ, 17-20 Mar 1997, Orsay, France, 16-19 Jun 1997 and Pasadena, CA, 22-24 Sep 1997

- [31] L. Wolfenstein, Phys. Rev. Lett. **51**, 1945 (1983).
- [32] L. L. Chau and W. Y. Keung, Phys. Rev. Lett. **53**, 1802 (1984);
J. D. Bjorken, Phys. Rev. D **39**, 1396 (1989);
C. Jarlskog and R. Store, Phys. Lett. B **208**, 268 (1988);
J. L. Rosner, A. I. Sanda, and M. P. Schmidt, in *Proceedings of the Workshop on High Sensitivity Beauty Physics at Fermilab*, Fermilab, November 11-14, 1987, edited by A. J. Slaughter, N. Lockyer, and M. Schmidt (Fermilab, Batavia, 1988), p.165; C. Hamzaoui, J. L. Rosner, and A. I. Sanda, *ibid.*, p. 215.
- [33] V. F. Weisskopf, and E. P. Wigner, *Zeitschrift für Physik* **63**, 54 (1930).
- [34] See, for example, Y. Nir, In *The third family and the physics of flavor* (ed L. Vassilian). Stanford Linear Accelerator Center, Stanford, California (1993).
- [35] G. Buchalla, A. J. Buras, and M. E. Lautenbacher, Rev. Mod. Phys. **68**, 1125 (1996), hep-ph/9512380.
- [36] A. J. Buras, hep-ph/9905437.
- [37] A. J. Buras, W. Slominski and H. Steger, Nucl. Phys. **B245**, 369 (1984).
- [38] J. D. Richman, *Prepared for Les Houches Summer School in Theoretical Physics, Session 68: Probing the Standard Model of Particle Interactions, Les Houches, France, 28 Jul - 5 Sep 1997*
- [39] I. I. Bigi and A. I. Sanda, Cambridge Monogr. Part. Phys. Nucl. Phys. Cosmol. **9**, 1 (2000).

- [40] "PEP-II: An Asymmetric B Factory", Conceptual Design Report, SLAC-418, LBL-5379 (1993).
- [41] N. Isgur, M. B. Wise, Phys. Lett. B **232** 113 (1989), and Phys. Lett. B **237**, 527 (1990);
 E. Eichten and B. Hill, Phys. Lett. B **234**, 511 (1990);
 M. E. Luke, Phys. Lett. B **252**, 447 (1990).
- [42] M. Paulini [CDF Collaboration], arXiv:hep-ex/0302016.
- [43] L. Lellouch, Nucl. Phys. PS **94**, 142 (2001).
- [44] A. Hocker, H. Lacker, S. Laplace and F. Le Diberder, Eur. Phys. J. C **21**, 225 (2001) [arXiv:hep-ph/0104062].
- [45] C. Dib, I. Dunietz, F. J. Gilman and Y. Nir, Phys. Rev. D **41**, 1522 (1990).
 I. Dunietz and J. L. Rosner, Phys. Rev. D **34**, 1404 (1986).
 I. I. Bigi and A. I. Sanda, Nucl. Phys. B **281**, 41 (1987).
- [46] K. Ackerstaff *et al.* [OPAL collaboration], Eur. Phys. J. C **5**, 379 (1998) [arXiv:hep-ex/9801022].
- [47] R. Barate *et al.* [ALEPH Collaboration], Phys. Lett. B **492**, 259 (2000) [arXiv:hep-ex/0009058].
- [48] T. Affolder *et al.* [CDF Collaboration], Phys. Rev. D **61**, 072005 (2000) [arXiv:hep-ex/9909003].
- [49] "KEKB B-Factory Design Report", KEK Report 95-7, (1995).
- [50] B. Aubert *et al.* [BABAR Collaboration], Phys. Rev. Lett. **89**, 201802 (2002) [arXiv:hep-ex/0207042].
- [51] K. Abe *et al.* [Belle Collaboration], Phys. Rev. D **66**, 071102 (2002) [arXiv:hep-ex/0208025].

- [52] B. Aubert *et al.* [BABAR Collaboration], Nucl. Instrum. Meth. A **479**, 1 (2002) [arXiv:hep-ex/0105044].
- [53] R. Giles *et al.* [CLEO Collaboration], Phys. Rev. D **29**, 1285 (1984).
- [54] D. Boutigny *et al.*, SLAC-R-0443 69 (1994).
- [55] V. Re *et al.*, Nucl. Instrum. Meth. **409**, 354 (1998).
- [56] P. Billoir, Nucl. Instrum. Meth. **225**, 225 (1984).
- [57] G. Sciolla *et al.* [BABAR Drift Chamber Collaboration], Nucl. Instrum. Meth. A **419**, 310 (1998).
- [58] I. Adam *et al.* [DIRC Collaboration], Nucl. Instrum. Meth. A **433**, 121 (1999).
- [59] J. Brose [BABAR Collaboration], Nucl. Instrum. Meth. A **379**, 495 (1996).
- [60] H. Albrecht *et al.* [ARGUS Collaboration], Nucl. Instrum. Meth. A **275**, 1 (1989).
- [61] R. Sinkus and T. Voss, Nucl. Instrum. Meth. A **391**, 360 (1997).
- [62] F. Anulli *et al.* [BaBar Collaboration], Nucl. Instrum. Meth. A **494**, 455 (2002).
- [63] R. Santonico and R. Cardarelli, Nucl. Instrum. Meth. **187**, 377 (1981).
- [64] G. C. Fox and S. Wolfram, Phys. Rev. Lett. **41**, 1581 (1978).
- [65] See, for example, *Statistical and Computational Methods in Data Analysis*, Siegmund Brandt, North Holland Publishing.
- [66] ARGUS Collaboration, H. Albrecht *et al.*, Phys. Lett. B **241**, 278 (1990)
- [67] B. Aubert *et al.* [BABAR Collaboration], arXiv:hep-ex/0203040.

- [68] D. Boutigny *et al.* [BABAR Collaboration], SLAC-R-0457
- [69] H. Albrecht *et al.* [ARGUS Collaboration], Z. Phys. C **62**, 371 (1994).
- [70] J. Beringer *et al.*, *BTagger: A Multivariate Tagging Algorithm with Categories Based on the B_{tag} Decay*, BABAR Analysis Document 317 (2002).
- [71] S. Metzler *et al.*, *Measurements of B Lifetimes at BABAR*, BABAR Analysis Document 65 (2000).
- [72] F. Martinez-Vidal *et al.*, *The BABAR Vertexing* BABAR Analysis Document 102 (2001).
- [73] R. J. Barlow, **Statistics**, John Wiley and Sons (1989).
- [74] H. Cramer, **Mathematical Methods of Statistics**, Princeton University Press (1946).
- [75] B. Aubert *et al.* [BABAR Collaboration], Phys. Rev. Lett. **87**, 241801 (2001) [arXiv:hep-ex/0107049].
- [76] B. Aubert *et al.* [BABAR Collaboration], Phys. Rev. Lett. **87**, 201803 (2001) [arXiv:hep-ex/0107019].
- [77] M. Baak, O. Long, *The Effect of Tag-Side Doubly-Cabibbo-Suppressed Decays on Time-Dependent Asymmetry Measurements* BABAR Analysis Document 572 (2003).
- [78] O. Long, M. Baak, R. N. Cahn and D. Kirkby, arXiv:hep-ex/0303030.
- [79] S. Versillé, F. Diberder, *The Kin Variable*, BABAR Note 406 (1998).
S. Versillé, F. Diberder, *The Kin Variable and CP Thinking Revisited*, BABAR Note 421 (1998).
- [80] Y. Nir, Nucl. Phys. Proc. Suppl. **117**, 111 (2003) [arXiv:hep-ph/0208080].

- [81] K. S. Babu and S. M. Barr, Phys. Rev. Lett. **72**, 2831 (1994) [arXiv:hep-ph/9309249].
 S. A. Abel and J. M. Frere, Phys. Rev. D **55**, 1623 (1997) [arXiv:hep-ph/9608251].
 G. Eyal and Y. Nir, Nucl. Phys. B **528**, 21 (1998) [arXiv:hep-ph/9801411].
 K. S. Babu, B. Dutta and R. N. Mohapatra, Phys. Rev. D **61**, 091701 (2000) [arXiv:hep-ph/9905464].
- [82] P. Ball, J. M. Frere and J. Matias, Nucl. Phys. B **572**, 3 (2000) [arXiv:hep-ph/9910211].
 P. Ball and R. Fleischer, Phys. Lett. B **475**, 111 (2000) [arXiv:hep-ph/9912319]. S. Bergmann and G. Perez, Phys. Rev. D **64**, 115009 (2001) [arXiv:hep-ph/0103299].
- [83] J. J. Aubert *et al.*, Phys. Rev. Lett. **33**, 1404 (1974).
- [84] J. E. Augustin *et al.*, Phys. Rev. Lett. **33**, 1406 (1974).
- [85] See, for example, Sec. 2.13 in F. Halzen, A. Martin, *Quarks and Leptons*, John Wiley & Sons (1984).
- [86] G. S. Abrams *et al.*, Phys. Rev. Lett. **33**, 1453 (1974).
- [87] B. Richter in *Nobel Lectures in Physics 1971-1980*, ed. Stig Lundqvist, World Scientific Publishing Company (1992).
- [88] S. Okubo, Phys. Lett. **5**, 165 (1963).
 J. Iizuka, Suppl. Progr. Theor. Phys. **37-38**, 21.
 G. Zweig, Unpublished. CERN Preprints, Th 401, 412 (1964).
- [89] See, for example, Chapter 9 in E. Leader, E. Predazzi, *An Introduction to Gauge Theories and the 'New Physics'*, Cambridge University Press (1982).
- [90] A. Boyarski *et al.*, Phys. Rev. Lett. **34**, 1357 (1975).